From Polythiophenes to Functional Materials: Development of Complex Architectures through Polymer Analogous Modifications

Von der Fakultät Chemie der Universität Stuttgart zur Erlangung der Würde eines Doktors der Naturwissenschaften (Dr. rer. nat.) genehmigte Abhandlung

Vorgelegt von

Peter Reinold

aus Ulm

Hauptberichterin:	Prof. Dr. Sabine Ludwigs
Mitberichter:	Prof. Dr. René Peters
Prüfungsvorsitzender:	Prof. Dr. Elias Klemm
Tag der mündlichen Prüfung:	6. September 2018

Institut für Polymerchemie der Universität Stuttgart

2018

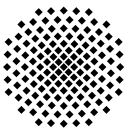

Universität Stuttgart

Erklärung über die Eigenständigkeit der Dissertation

Ich versichere, dass ich die vorliegende Arbeit mit dem Titel

From Polythiophenes to Functional Materials: Development of Complex Architectures through Polymer Analogous Modifications

selbständig verfasst und keine anderen als die angegebenen Quellen und Hilfsmittel benutzt habe; aus fremden Quellen entnommene Passagen und Gedanken sind als solche kenntlich gemacht.

Declaration of Authorship

I hereby certify that the dissertation entitled

From Polythiophenes to Functional Materials: Development of Complex Architectures through Polymer Analogous Modifications

is entirely my own work except where otherwise indicated. Passages and ideas from other sources have been clearly indicated.

Peter Reinold

Summary

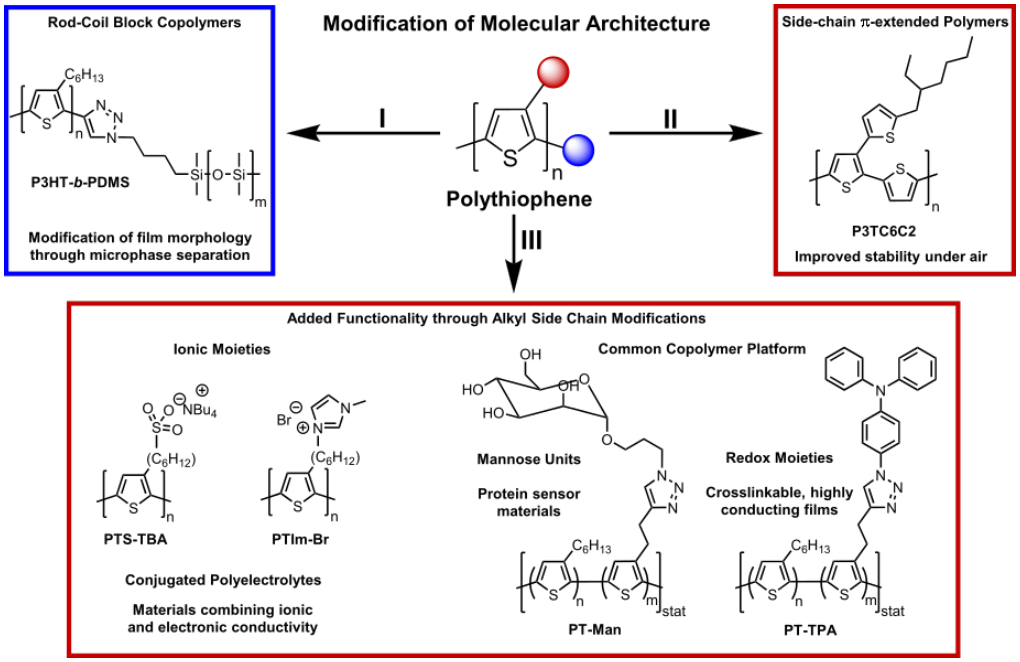

The work presented in this dissertation was concerned with modifying the molecular architecture of regioregular poly(3-alkylthiophene)s (**P3AT**s). Three main synthetic approaches were pursued, relying mainly on polymer analogous functionalizations, yielding materials with tailor-made functionalities for applications in organic electronics and energy storage.[1]

First, the effect of an additional attached poly(dimethylsiloxane) (**PDMS**) coil-type block to the otherwise unmodified rod-like poly(3-hexylthiophene) (**P3HT**) was studied. Such a combination promises improved stability of thin films under mechanical strain, which is highly important for applications like bendable displays or plastic microelectronics.[2] The modification was shown to significantly influence the film morphology of these materials through microphase separation. A copper(I)-catalyzed alkyne-azide click chemistry (CuAAC) based grafting-to approach was used to synthesize **P3HT-*b*-PDMS**.[3] Temperature-dependent absorption spectroscopy, organic field effect transistor (OFET) measurements as well as atomic force microscopy (AFM) were used to compare the block copolymer to the semicrystalline **P3HT** precursor homopolymer.

Extending the π-system of linear polythiophenes by alkylthiophene groups in the side chains was shown to influence the structure formation of the resulting materials in earlier work, while additionally lowering the positions of the frontier orbitals.[4–7] Such materials promise improved stability against atmospheric conditions in applications like organic

solar cells or field effect transistors. However, solubility issues occured in earlier attempts, which were mostly alleviated by the introduction of branched instead of linear alkyl side chains. The approach presented here tested the limits of this method, further decreasing side chain length to a 2-ethylhexyl group, leading to the polymer **P3TC6C2**. The material was compared to its longer side-chain analogues and **P3HT**. Thermal properties were evaluated by a combination of DSC, TGA and WAXS measurements, as well as temperature-dependent absorption spectroscopy. Furthermore, electrochemical and chemical doping experiments were conducted. OFET measurements were performed to determine charge carrier mobilities and significant improvements compared to existing analogues were found.

The main part of this thesis dealt with the concept of side-chain terminal modification, which was used to introduce additional functionalities to the polythiophene materials. Ionic moieties were incorporated to yield conjugated polyelectrolytes, combining electronic and ionic conductivity mechanisms in single materials.[8] The cationically substituted model system **PTIm-Br** was synthesized by polymer analogous functionalization of a bromine-substituted precursor polymer and compared against the anionic derivative **PTS-TBA**.[9, 10] Aggregation phenomena in solution and thin films were evaluated spectroscopically. The electronic conductivities and thin film absorption spectra of chemically doped films were further investigated and clear differences between the two systems were found, which could be partly explained by the stabilizing and destabilizing effects of the pendant ionic groups.[11]

Extending beyond this simple bromine-based side-chain modification approach, a polythiophene copolymer-based platform bearing alkyne moieties was developed.[12] The system provided facile functionalization with different functional molecules *via* CuAAC. Based on this highly modular synthetic platform, the conjugated redox polymers **PT-TPA** and **PT-spTPA**, bearing redox-active triphenylamine units, were synthesized.[13] The materials could be crosslinked in thin films upon chemical or electrochemical oxidation. The CRPs were studied in electrochemical doping experiments under spectroscopic control to elucidate the crosslinking and doping mechanism. *In-situ* conductance experiments showed that charge transport was largely dominated by the polythiophene backbones. The crosslinking reaction rendered the films completely insoluble in all tested solvents and even extended electrochemical cycling of a crosslinked film in a THF-based electrolyte was possible, which would rapidly dissolve the as-cast films. Chemical doping experiments led to conductivity values up to 8 S/cm with $FeCl_3$ and oxidation of the pendant groups enabled the crosslinking reaction, for which a similar mechanism as for electrochemical doping could be confirmed. These materials thus are promising for applications in which

stable redox switching and high conductivity in direct contact to organic solvents are crucial, including polymer batteries or redox sensors. Demonstrating the broad applicability of the alkyne-functionalized copolymer platform, the same approach was furthermore utilized for the synthesis of polythiophenes bearing α-D-mannose units (termed **PT-Man**) as protein sensor materials. The strong interaction between these sugar moieties and the protein Concanavalin A (**Con A**) was employed as a model system to investigate the applicability of such materials in sensor devices based on electrolyte-gated field effect transistors (EGOFETs).[14, 15] Functionalization of the precursor polymers in homogeneous solutions as well as on the surface of predeposited thin films on transistor substrates was performed and the conditions optimized. EGOFET measurements at *Laboratoire ITODYS*, Paris, showed superior stability of the surface-functionalized films. The devices were able to detect analytes with high sensitivity and it was possible to discriminate between salts and proteins in the electrolyte. However, selectivity of the sensor for **Con A** still has to be optimized, since also the addition of human serum albumin (**HSA**) led to a significant response, presumably due to unspecific hydrophobic interactions between the film surface and the proteins.

Zusammenfassung

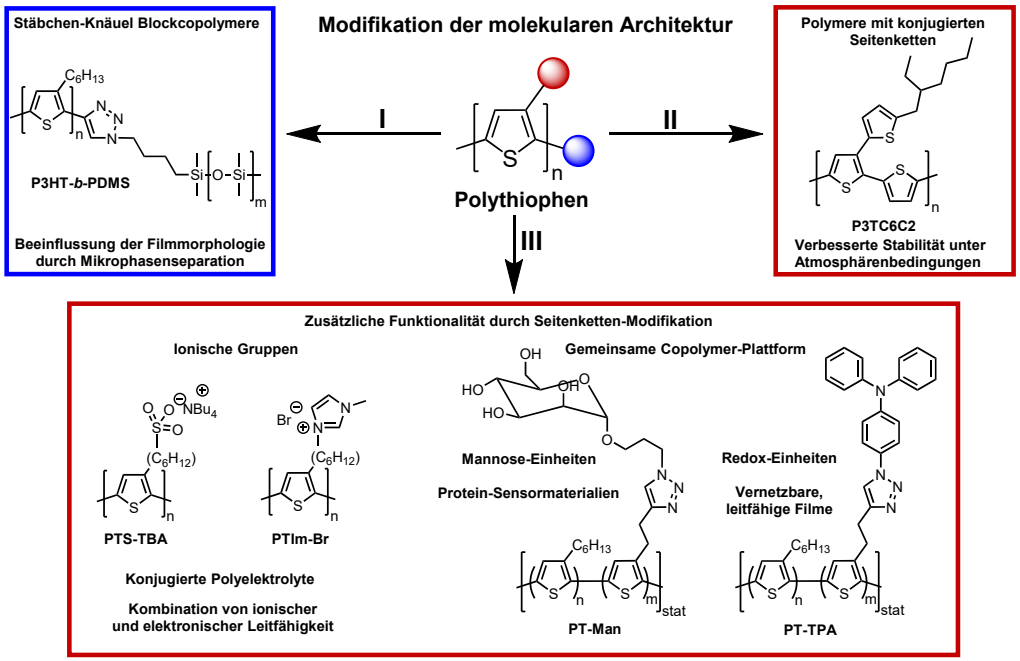

Die vorliegende Arbeit beschäftigte sich mit der Modifikation der molekularen Architektur von regioregulären Poly(3-alkylthiophen)en (**P3AT**s). Drei hauptsächlich auf polymeranalogen Funktionalisierungen basierende synthetische Ansätze wurden dabei verfolgt, welche zu Materialien mit maßgeschneiderten Funktionalitäten für Anwendungen in der organischen Elektronik und in der Energiespeicherung führten.[1]

Zunächst wurde der Effekt von angeknüpften knäuelförmigen Poly(dimethylsiloxan) (**PDMS**) Blöcken an ansonsten unmodifiziertes stäbchenförmiges Poly(3-hexylthiophen) (**P3HT**) untersucht. Diese Kombination von Polymerblöcken verspricht verbesserte Stabilität von Dünnfilmen unter mechanischer Belastung, was interessant für Anwendungen wie biegbare Displays oder Plastik-Mikroelektronik ist.[2] Es wurde gezeigt, dass die Modifikation die Filmmorphologie der Materialien durch Mikrophasenseparation signifikant beeinflusste. Ein „grafting-to"-Ansatz basierend auf Kupfer(I)-katalysierter Alkin-Azid Click-Chemie (CuAAC) wurde zur Herstellung von **P3HT-*b*-PDMS** genutzt.[3] Temperaturabhängige Absorptionsspektroskopie, Messungen an organischen Feldeffekt-Transistoren (OFETs), sowie Rasterkraftmikroskopie (AFM) wurden verwendet, um die Eigenschaften des Blockcopolymers mit denen des semikristallinen **P3HT** Vorläufer-Homopolymers zu vergleichen.

Eine Vergrößerung des π-Systems von linearen Polythiophenen durch Alkylthiophen-Gruppen in den Seitenketten führte in früheren Arbeiten zu einer starken Beeinflussung

der Strukturbildung der Materialien, während zusätzlich die Energieniveaus der Grenzorbitale zu tieferen Werten verschoben wurden.[4–7] Dies verspricht verbesserte Resistenz der Materialien gegenüber atmosphärischen Bedingungen in Anwendungen wie organischen Solarzellen oder Feldeffekt-Transistoren. Jedoch stellte die Löslichkeit in früheren Versuchen ein Problem dar, welches größtenteils durch die Einführung von verzweigten anstelle von linearen Seitenketten behoben werden konnte. Der hier gezeigte Ansatz lotete die Grenzen dieser Methode aus, indem die Seitenkettenlänge weiter zu einer 2-Ethylhexyl-Gruppe verkürzt wurde, wodurch das Polymer **P3TC6C2** entstand. Das Material wurde mit den Analoga mit längeren Seitenketten, sowie mit **P3HT** verglichen. Die thermischen Eigenschaften wurden mit einer Kombination von DSC-, TGA- und WAXS-Messungen, sowie temperaturabhängiger Absorptionsspektroskopie untersucht. Weiterhin wurden elektrochemische und chemische Dotierungs-Experimente durchgeführt. Ladungsträger-Beweglichkeiten wurden mittels OFET-Messungen bestimmt und deutliche Verbesserungen im Vergleich zu den existierenden Analoga wurden gefunden.

Der Hauptteil dieser Arbeit beschäftigte sich mit dem Konzept der Modifikation der Seitenketten-Enden, welches genutzt wurde um die Polythiophen-Materialien mit zusätzlichen Funktionalitäten zu versehen. Ionische Gruppen wurden eingebaut, was zu konjugierten Polyelektrolyten führte, welche elektronische und ionische Leitfähigkeits-Mechanismen im gleichen Material vereinen.[8] Das kationisch substituierte Modellsystem **PTIm-Br** wurde mittels polymeranaloger Funktionalisierung eines Bromid-modifizierten Vorläuferpolymers hergestellt und mit dem anionischen Derivat **PTS-TBA** verglichen.[9, 10] Aggregations-Phänomene in Lösung und Dünnfilmen wurden spektroskopisch untersucht. Die elektronischen Leitfähigkeiten und Absorptionsspektren der chemisch dotierten Filme wurden weiter untersucht und deutliche Unterschiede zwischen den beiden Systemen wurden gefunden, welche größtenteils durch die stabilisierenden und destabilisierenden Effekte der ionischen Seitengruppen erklärt werden konnten.[11]

Als Alternative zu diesem einfachen Bromid-basierten Ansatz der Seitenketten-Modifikation wurde eine synthetische Plattform, basierend auf Alkin-funktionalisierten Polythiophen-Copolymeren, entwickelt.[12] Das System erlaubt die einfache Modifikation mit unterschiedlichen funktionellen Molekülen durch CuAAC. Basierend auf dieser modularen synthetischen Plattform wurden die konjugierten Redoxpolymere **PT-TPA** und **PT-spTPA** entwickelt, welche redoxaktive Triphenylamin-Einheiten in der Seitenkette trugen.[13] Die Materialien konnten in Dünnfilmen durch chemische oder elektrochemische Oxidation vernetzt werden. Elektrochemische Dotierungs-Experimente unter spektroskopischer Kontrolle wurden zunächst genutzt um den Vernetzungs- und Dotierungsmechanismus aufzuklären. Gekoppelte *in-situ* Leitfähigkeitsmessungen zeigten, dass der Ladungstransport

größtenteils durch das Polythiophen-Rückgrat bestimmt wurde. Die Vernetzungsreaktion führte zu einer vollständigen Unlöslichkeit der Filme in allen getesteten Lösungsmitteln und sogar längeres elektrochemisches Schalten eines vernetzen Films in einem THF-basierten Elektrolyten war möglich, welcher einen unvernetzten Film sofort auflöste. Chemische Dotierungs-Experimente führten zu Leitfähigkeiten bis zu 8 S/cm mit $FeCl_3$ und die Oxidation der Seitengruppen ermöglichte die Vernetzungsreaktion, für welche ein ähnlicher Mechanismus wie für die elektrochemische Dotierung bestätigt werden konnte. Diese Materialien sind deshalb vielversprechend für Anwendungen, in denen zuverlässige Redox-Eigenschaften und hohe Leitfähigkeiten in direktem Kontakt zu organischen Lösungsmitteln Grundvoraussetzungen sind, beispielsweise für Polymer-Batterien oder Redox-Sensoren. Um die breite Anwendbarkeit des Alkin-funktionlisierten Vorläuferpolymers zu demonstrieren, wurde der gleiche Ansatz weiterhin für die Synthese von α-D-Mannose-funktionalisierten Polythiophenen (**PT-Man**) als Protein-Sensormaterialien angewandt. Die starke Interaktion zwischen diesen Zuckereinheiten und dem Protein Concanavalin A (**Con A**) wurde als Modellsystem genutzt, um die Anwendbarkeit solcher Materialien in Sensoren basierend auf Elektrolyt-geschalteten Feldeffekt-Transistoren (EGOFETs) zu testen.[14, 15] Die Vorläuferpolymere wurden sowohl in Lösung funktionalisiert als auch durch heterogene Funktionalisierung der Oberfläche von Dünnfilmen auf Transistorsubstraten. EGOFET-Messungen am *Laboratoire ITODYS*, Paris, zeigten eine bessere Stabilität der oberflächenfunktionalisierten Filme. Die Sensoren waren in der Lage, Analyten mit hoher Sensitivität zu erkennen und zwischen Salzen und Proteinen im Elektrolyt zu unterscheiden. Jedoch muss die Selektivität der Sensoren für **Con A** weiter optimiert werden, da auch die Zugabe von humanem Serum-Albumin (**HSA**) zu einem signifikanten Signal führte, vermutlich aufgrund von hydrophoben Wechselwirkungen zwischen der Filmoberfläche und den Proteinen.

Danksagung

Die vorliegende Arbeit wurde zwischen Oktober 2014 und März 2018 am *Institut für Polymerchemie* der *Universität Stuttgart* angefertigt. Ich möchte mich im Folgenden bei all denen bedanken, die durch praktische Zusammenarbeit im Labor, durch theoretische Diskussionen, im Rahmen von Kooperationen und auch außerhalb der Universität maßgeblich zu ihrem Gelingen beigetragen haben.

Zunächst gilt mein Dank *Prof. Dr. Sabine Ludwigs* für die Aufnahme in den Arbeitskreis, die exzellente Betreuung und die Möglichkeit, innerhalb eines faszinierenden und aktuellen Forschungsbereichs auch eigene Ideen zu verfolgen und im Labor mit ausgezeichneter Ausstattung umzusetzen. Viele wertvolle wissenschaftliche Diskussionen und Ratschläge ermöglichten mir eine große fachliche Weiterentwicklung.

Prof. Dr. René Peters danke ich für die freundliche Übernahme des Mitberichts. Bei *Prof. Dr. Elias Klemm* möchte ich mich für die Übernahme des Prüfungsvorsitzes bedanken.

Dr. Klaus Dirnberger möchte ich für die vielen hilfreichen Gespräche danken, welche durch seinen unerschöpflichen Erfahrungsschatz der Polymerchemie in höchstem Maße zum Gelingen dieser Arbeit beigetragen haben.

Kirsten Bruchlos möchte ich insbesondere für die gelungene Kooperation zu konjugierten Triphenylamin-Redoxpolymeren danken.

Weiterhin möchte ich all denjenigen danken, die im Rahmen von Kooperationen mit anderen Arbeitsgruppen beteiligt waren:

Prof. Dr. Benoît Piro, *Khue Nguyen*, sowie *Alexandra Tibaldi* vom *Laboratoire ITODYS* in Paris möchte ich für die freundliche Aufnahme in die Arbeitsgruppe während meiner Aufenthalte in Paris und die Hilfe bei der Durchführung der EGOFET-Messungen danken.

Prof. Dr. Joachim Maier und *Dr. Rotraut Merkle* vom *Max Planck Institut für Festkörperforschung* in Stuttgart danke ich für die erfolgreiche Kooperation während der gemeinsamen Forschung zur ionischen und elektronischen Leitfähigkeit von konjugierten Polyelektrolyten, sowie der Arbeit an der diesbezüglichen Veröffentlichung.

Prof. Dr. Albert Jeltsch und *Jun.-Prof. Dr. Tomasz Jurkowski* vom *Institut für Biochemie* der *Universität Stuttgart* gebührt mein Dank für die Nutzungserlaubnis für das MALDI-TOF-Spektrometer.
Prof. Dr. Michael Buchmeiser danke ich für die Möglichkeit, HT-GPC-Messungen am *Institut für Polymerchemie* durchzuführen.
Prof. Dr. Frank Gießelmann, *Dr. Nadia Kapernaum*, *Carsten Müller* und *Marc Harjung* vom *Institut für Physikalische Chemie* möchte ich für die Nutzungserlaubnis und die Einführung für das WAXS-Spektrometer danken.
Prof. Dr. Thomas Schleid und *Christian Funk* vom *Institut für Anorganische Chemie* danke ich für die TGA-Messungen.

Ich möchte mich insbesondere bei meinen Labor- und Bürokollegen *Martin Scheuble*, *Florian Fischer*, *Miriam Goll*, *Justus Back*, *Christian Rothe*, *Daniel Trefz*, *Philipp Gutbrod*, *Kirsten Bruchlos*, *Yannic Gross*, *Jochen Kuhlmann*, *Carsten Dingler* und *Matthias Wieland* für die großartige Zeit innerhalb und außerhalb des Labors und die Unterstützung bei wissenschaftlichen Fragestellungen aller Art bedanken.

Den von mir betreuten Forschungspraktikanten, Bachelor- und Masterstudenten *Daniel Rose*, *Diana Zelenic*, *Kai Mundsinger*, *Katharina Schmitt*, *Tim Hierlemann* und *Marc Schnierle* danke ich für die erfolgreiche Zusammenarbeit. *Dr. Roman Tkachov* und *Moritz Katzmaier* danke ich weiterhin für diverse Synthesen und Messungen zu konjugierten Polyelektrolyten, die ebenfalls maßgeblich zum Gelingen dieser Arbeit beigetragen haben.

Corinne Rost-Schmidt gilt mein Dank für die Durchführung von GPC-Messungen, die Bestellung der Arbeitsmaterialien und Chemikalien und viele weitere Hilfestellungen im Labor. *Beatrice Omiecienski* und *Anke Schrogl* danke ich für die exzellente Administration der Arbeitsgruppe und Hilfe bei Fragestellungen aller Art. *Simon Tannert* möchte ich für die Erstellung und Weiterentwicklung vieler Origin-Scripts sowie Hilfestellung bei diversen IT-Problemen danken. *Yannic Gross* danke ich noch einmal besonders für die Zusammenarbeit bei der Auswertung von Transistormessungen und der Erstellung des LaTeX-Headers.

Meinen Eltern danke ich für die bedingungslose Unterstützung während meines Studiums und während der Promotionsphase.

Mein letzter und größter Dank gebührt Karishma.

Contents

1 Introduction

Arguably, the most important and at the same time most difficult challenge humanity will face during the course of this century will be the transition of the world's energy system to a sustainable supply primarily based on renewable resources like solar, wind, water and biomass energy.[16, 17] This is mandatory both because of health and environmental protection concerns as well as resource scarcity reasons. A continuation of the current energy generation methods is expected to lead to an increase in average global temperatures by up to 9.5 °C if only conventional deposits of fossil fuels are exploited and burned and is expected to render whole regions of the earth uninhabitable due to droughts, floodings related to rising sea levels, thunderstorms and other extreme weather phenomena.[18] At the same time, millions of deaths around the world each year can be related to air pollution, especially in megacities.[19] On the other hand, (fossil) energy sources like oil, natural gas and coal as well as uranium ores are limited resources, which becomes apparent in the fact that highly costly extraction methods like hydraulic fracturing ("fracking") or tar sands extraction already have become necessary to exploit many deposits. Since the world's population is expected to grow to at least 9 billion until the year 2100, all of these problems will only intensify, if the *status quo* is not changed.[20] The 2015 Paris climate agreement marks a turning point in this regard, in which all of the United Nations member states pledged themselves to take measures to decrease their emissions of greenhouse gases and limit global warming to a maximum of 2 °C compared to pre-industrial values.[21]

Laying the groundwork for these huge concerted efforts requires the development of new technologies in many disciplines, including all natural sciences and engineering. In particular, new, cheaper energy generation technologies, especially decentralized ones, are highly desirable. Furthermore, the significant fluctuations in energy generation from sources like sunlight and wind with daytime and season as well as ever rising numbers of mobile technologies, like electric vehicles and consumer electronics, will lead to a demand for stationary and mobile, affordable, high-performance energy storage solutions.[22] Lastly, technologies like autonomous cars, smart grids, RFID chips and wearable electronics will require huge numbers of cheap microprocessors. In many of these applications, low prices and properties like flexibility and light-weight are more important than high computing performance which opens the way for printed solutions ("plastic electronics").[23] Furthermore, since conventional top-down approaches in microelectronics manufacturing are expected to reach physical limits within the next years (10 nm half pitch sizes are already state of the art in 2017), new bottom-up manufacturing approaches, based on the self-assembly of molecular structures are highly desirable.[24, 25]

In the last decades, polymer chemistry has been revolutionized by the discovery of a new class of materials which might offer solutions for many of these applications: conjugated polymers (CPs).[1]

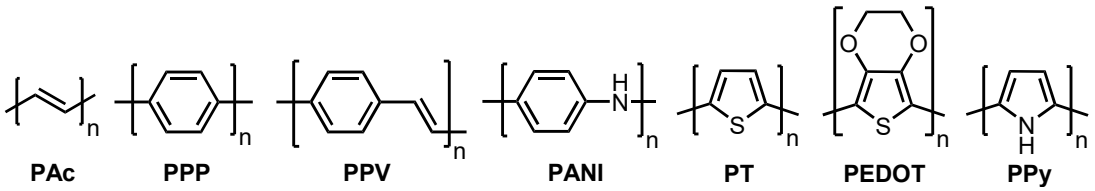

Figure 1.1: The classic types of conjugated polymers: polyacetylene (**PAc**), poly(*para*-phenylene) (**PPP**), poly(*para*-phenylene vinylene) (**PPV**), polyaniline (**PANI**), polythiophene (**PT**), poly(3,4-ethylenedioxythiophene) (**PEDOT**) and polypyrrole (**PPy**).

Compared to state of the art commodity polymers like polypropylene (**PP**), polystyrene (**PS**) or poly(ethylene terephthalate) (**PET**), to name a few, this modern class of macromolecules is able to conduct electricity due to the fully conjugated π-systems present on the polymer chains.[1] Even though such a behavior was already predicted after the discovery of the ring current present on aromatic rings by means of NMR spectroscopy and *Natta* had already reported on the polymerization of acetylene in 1958, which led to infusible and insoluble material, the first somewhat controlled synthesis of polyacetylene (**PAc**) films was reported by the *Shirakawa* group in 1974.[26] However, when these films were probed for conductivity, only values of 10^{-8}-10^{-4} S/cm were found. Breakthroughs occured in the years around 1977, when the groups of *Shirakawa*, *Heeger* and *MacDiarmid* reported on conductivity increases of several orders of magnitude when polyacetylene was treated with small quantities of oxidation agents like halogens or AsF_5, a process quickly referred to as doping in analogy to inorganic semiconductors.[27–29] For this discovery, the three scientists were awarded the *Nobel Prize* in chemistry in the year 2000. The reasons for the low conductivities in pristine CPs and the underlying mechanisms of doping will be discussed in the following chapter. The concept was soon adapted to other conjugated systems, predominantly aromatic and heteroaromatic conjugated polymers. Notable examples, which together with polyacetylene today can be seen as the "basic" types of CPs representing the foundation for all further developments in the field, are poly(*para*-phenylene) (**PPP**), poly(*para*-phenylene vinylene) (**PPV**), polyaniline (**PANI**), polythiophene (**PT**), poly(3,4-ethylenedioxythiophene) (**PEDOT**) and polypyrrole (**PPy**) (see Figure 1.1). For all of these materials, highly sophisticated synthesis methods have been developed, allowing to fine-tune the molecular, optical and electronic properties over a wide range.[30] This has led to the development of a multitude of different applica-

tions in electronic devices including, but not limited to the fields of energy generation and storage, organic microelectronics and sensors. In the following, an introduction on fundamental structure-property relationships in conjugated polymers, concerning their optoelectronic properties, as well as an introduction to thin film transistor devices will be given. Furthermore, the evolution of synthetic methods for polythiophene-based materials with highly controlled molecular properties will be summarized and synthetic approaches for advanced, application-specific hybrid materials relevant for this thesis will be discussed. In addition, each main chapter of this thesis will start with a brief introduction detailing the state of the art in literature methods for the respective application.

1.1 Fundamental Theory

The unique properties of CPs are, as mentioned before, mainly based on the large π-systems extending along the polymer backbones.

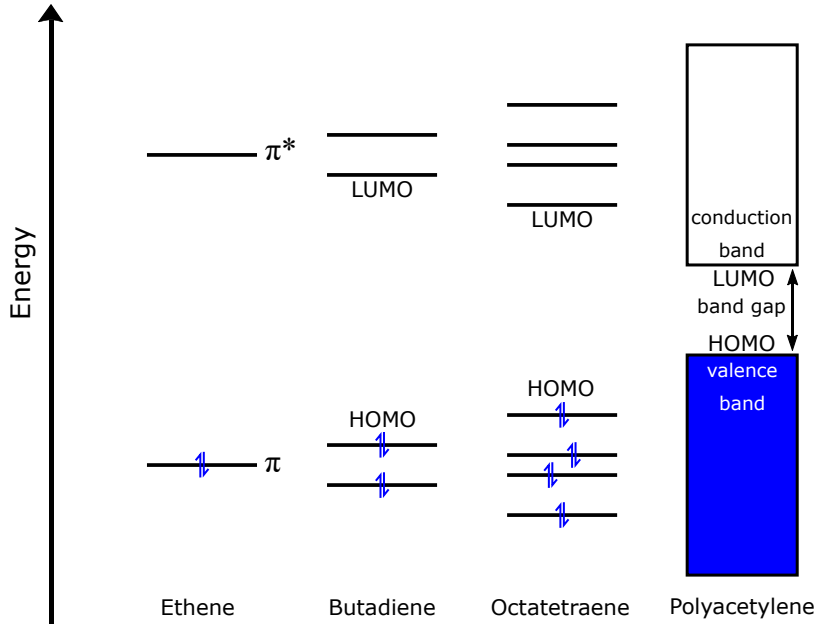

Figure 1.2: Molecular Orbital (MO) energy diagram detailing the origin of valence and conduction band structures in large conjugated π-systems like polyacetylene.

In the least complex case, polyacetylene, such a system consists entirely of a fully unsaturated alkyl chain.[31] Here, all carbon atoms are sp^2-hybridized and thus possess three sp^2 and one p_z orbital each. In the molecular orbital theory, double bonds are formed by the combination of a σ-bond and a π-bond, which result from the interaction of two sp^2 orbitals and two p_z orbitals of neighbouring carbon atoms, respectively. The

smallest possible system containing a carbon-carbon double bond is ethene. In the Linear Combination of Atomic Orbitals (LCAO) theory, the interaction of the p_z orbitals leads to a split into an energetically lower bonding (π) and a higher antibonding (π^*) molecular orbital (Figure 1.2).[32] The π orbital contains both of the bond's electrons, thus it is called the highest occupied molecular orbital (HOMO), while the π^* orbital is called the lowest unoccupied molecular orbital (LUMO). If the unsaturated chain is elongated and more and more π-bonds interact with each other due to delocalization, both the bonding and antibonding MOs are split again into two bonding and two antibonding orbitals each. Notably, the energy difference between the new HOMO and LUMO levels is now lower.

The interaction of n p_z orbitals always leads to n molecular orbitals in the π-system. For octatetraene, already four completely filled bonding orbitals and four empty antibonding orbitals exist. For very long unsaturated chains, the high numbers of π and π^* orbitals blur into an energy level diagram which closely resembles the one typically applied for metals and inorganic semiconductors, containing a valence band (consisting of π orbitals) and a conduction band (consisting of π^* orbitals).[33] The energy level difference between the upper limit of the valence band and the lower limit of the conduction band is called "band gap". In theory, for infinitely long chains, the band gap would approach zero and the material would behave like a "synthetic metal" at room temperature. However, this is not the case in undoped conjugated polymers, which typically show conductivities comparable to isolators or bad semiconductors.[34] Notably, it was found that the temperature-dependence of conductivity in CPs even follows semiconductor theory, *i.e.* higher temperatures lead to higher conductivity due to thermal excitation of charge carriers from the valence band into the conduction band.[28] In a metal-like material, increases in temperature would lead to higher resistance due to increased brownian motion and thus more frequent collisions involving charge carriers.[33] The main reason for this is that the extended π-systems in conjugated polymers do not exhibit perfect conjugation. In other words, neighbouring bonds partly retain their characteristics as single and double bonds. In polyacetylene, this means that an alternation in bond lengths is found. These phenomena are caused by the so-called "*Peierls* distortion", which is also known for other "one-dimensional crystals" in physics.[35] In the MO energy diagram, this effect leads to a widening of the band gap and it is energetically more favorable for charge carriers to remain localized on individual bonds, *i.e.* to stay in the valence band, as compared to moving along the π-system (in the conduction band).

1.1.1 Conductivity Mechanisms and Doping

The low conductivities of pristine conjugated polymers were very unsatisfactory and greatly hindered their application in electronic devices in the first years following their discovery. The conductivity σ of a material can be expressed as

$$\sigma = n \cdot e \cdot \mu$$

with the number of charge carriers n, the elemental charge e and the charge carrier mobility μ. Thus, either the number or the mobility of charge carriers (or both) must be very low in pristine CPs.

However, it was quickly found that *trans*-polyacetylene exhibited significantly higher conductivity values compared to all other neutral CPs, including *cis*-polyacetylene.[34] This phenomenon can be explained when considering a unique property of the *trans*-**PAc** backbone: due to the imperfect conjugation and alternation in bond lengths the two mesomeric boundary structures are not only theoretical but may both exist in the same π-system. This leads to two macroscopically indistinguishable structures which may quickly alternate between each other. This alternation process is prone to produce defects, *e.g.* when commencing simultaneously from both chain ends in opposite directions. Such defects manifest themselves in the form of singular charge carriers which are produced at certain positions along the chain, called "solitons" in physics, which correspond to radicals in chemical terminology (see Scheme 1.1).[36]

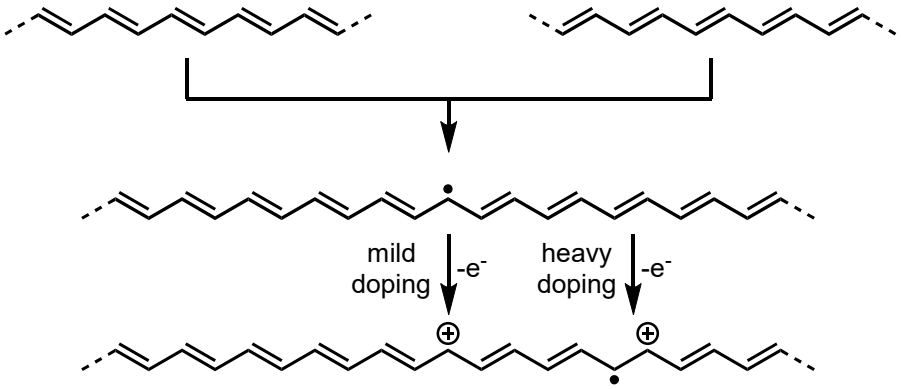

Scheme 1.1: Formation of soliton (radical) defects on *trans*-polyacetylene chains. Mild and heavy oxidative doping leads to cationic or radical cationic species by removal of the soliton or an electron from a π-bond, respectively.

These solitons may move much more freely along the π-system. In the MO band theory, they can be seen as located in mid-gap states, from which excitation to the conduction

band is much less energy-intensive. The comparably high conductivity of pristine *trans*-**PAc** can be mainly attributed to these soliton charge carriers. However, solitons are spontaneous defects, *i.e.* the charge balance of the whole π-system is not altered. Thus, they must always be generated as pairs of uncharged radicals in a single π-system which leads to a high probability of recombination with formation of a π-bond, greatly limiting the total number of solitons which can be simultaneously present on a single polymer chain. The major accomplishment of *Shirakawa*, *Heeger* and *MacDiarmid* was the finding that the addition of oxidation or reduction agents, "dopants", leads to the generation of positively ("holes", p-type carriers) or negatively (electrons, n-type carriers) charged species along the backbone.[29] The resulting charges are counterbalanced by oppositely charged ions formed from the dopant. Alternatively, electrochemical experiments can be performed to dope conjugated polymers.[37] Here, charges are counterbalanced by ions of the conducting salt which enter the polymer bulk from the electrolyte solution, usually accompanied by a shell of solvent molecules.

If polyacetylene is heavily doped, not only neutral solitons can be converted into carbocations or carbanions but even π-bonds may be broken, leading to the formation of radical cations or anions.[36] Due to electrostatic repulsion, these "charged solitons" can not easily recombine and thus can exist in higher numbers simultaneously. This led to increases in conductivity values over several orders of magnitude and for AsF_5-doped **PAc**, which is still one of the reference materials in terms of CP conductivities today, values up to 560 S/cm could be obtained.[29] However, the repulsion also limits both the allowed distance between two charged solitons as well as their mobility along the polymer chains. In aromatic CPs like **PPP** or **PT**, neutral solitons can not be generated by the same mechanisms present for polyacetylene since the resulting quinoid form is energetically less favorable than the aromatic form, *i.e.* the local aromatization energy prevents the solitons from forming spontaneously. However, the formation of charged species can still be enforced by strong oxidation or reduction agents (Scheme 1.2). These charged species are typically called "polarons" for aromatic CPs, since here, the introduction of a charge is always accompanied by the local formation of a quinoid repeating unit which leads to a localized structural deformation (polarisation) of the material, analogous to inorganic crystals.[38] Since polarons in aromatic CPs are usually generated by the oxidation or reduction of double bonds, they are charged radical species. The activation energies associated with the transition from aromatic to quinoid forms, which are required upon movement of these polaron species, strongly hinder their mobility along the polymer chains, leading to typically lower conductivities of aromatic CPs compared to polyacetylene. If these radical cation or anion species are even further oxidized or reduced, bipolaron

species may form which chemically can be described as dications or dianions.[37] Despite the electrostatic repulsion, a bipolaron is still the most stable system to accomodate two charges on a set of repeating units, since it can be achieved with the lowest possible number of quinoid structures. However, for some aromatic CPs, including polythiophene, the generation of bipolaron species, indicative of very high doping levels, is often associated with less favorable electronic properties or even irreversible degeneration of the backbone through side reactions.[39]

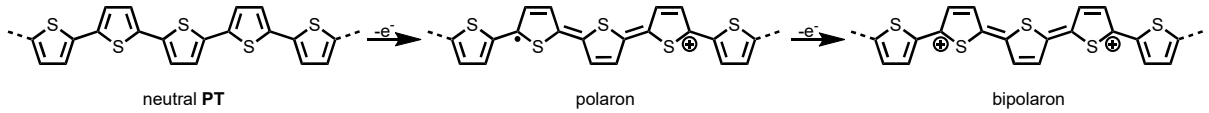

Scheme 1.2: Generation of positively charged, quinoid polaron and bipolaron species by oxidative doping of polythiophene.

Small quantities of chemical dopants already cause a significant increase in measured conductivities, as shown in Figure 1.4 a for poly(3-hexylthiophene) (**P3HT**) thin films doped oxidatively with the small molecule acceptor dopant 2,3,5,6-tetrafluoro-7,7,8,8-tetracyanoquinodimethane (**F_4TCNQ**) (Figure 1.3 details the process of the sequential "spin-doping" method used).[40] **F_4TCNQ** has a LUMO level at -5.24 eV, as measured *via* UPS and IPES, enabling facile electron transfer from **P3HT** (HOMO ~ 5.0 eV).[40–42] Its reduced form, the radical anion **$F_4TCNQ^{-\bullet}$**, has been shown to form a stable charge-transfer complex with polythiophenes both in solution and in thin films.[41, 43–46]

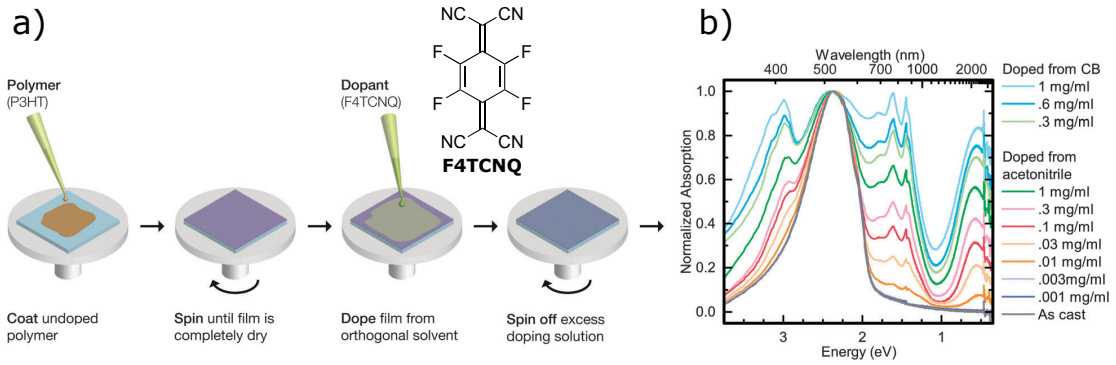

Figure 1.3: a) Sequential method for chemical doping of polythiophene thin films.[40] b) UV/Vis spectra of **P3HT** films doped with different concentrations of **F_4TCNQ** using this method. Adapted with permission from [40], © 2016, The Royal Society of Chemistry.

At higher dopant concentrations, conductivity values tend to saturate, approaching a maximum. The measured values of conductivity of polythiophenes doped with **F_4TCNQ** are

among the highest reported, with **P3HT** films reaching conductivities up to ~10 S/cm.[40, 47] Similar phenomena are observed when **P3HT** films are charged in an electrochemical cell using cyclic voltammetry (CV) coupled with *in-situ* conductance measurements on interdigitated microarray electrodes (Figure 1.4 b). Charges are induced into the polymer film through electrochemical oxidation starting from the onset at 0 V against the internal ferrocene/ferrocenium (Fc/Fc^+) standard, manifesting in a positive current in the cyclic voltammogram (grey curve). From the onset values of this oxidation wave in the CV, the HOMO level of **P3HT** can be approximated as

$$E_{HOMO}[\text{eV}] \quad = \quad -(E_{ox}[V] + 5.1) = -5.1\, eV$$

using −5.1 eV as the formal potential of Fc/Fc^+ in the *Fermi* scale.[48] From the respective reduction wave, the LUMO level can be determined using the formula

$$E_{LUMO}[\text{eV}] \quad = \quad -(E_{red}[V] + 5.1)$$

Simultaneously, upon charging the polymer film, conductance values (red curve) increase significantly, before reaching a "plateau value" for the rest of the charging process.[37, 49] Mainly two effects play a role here. Firstly, the number of charge carriers a single chain (segment) can hold simultaneously is limited by coulombic repulsion as well as the structural distortion induced by the (bi)polarons. For polythiophenes, the maximum obtainable doping levels lie on the order of 0.25 to 0.33, *i.e.* every third to fourth repeating unit bears on average one charge.[37] However, these values are believed to lie substantially lower in many cases. Secondly, hopping effects between chains and also between segments of different lengths on a single chain can be assumed to be rate-determining for the macroscopically observed conductivity.[50] Since hopping takes place predominantly between isoenergetic sites in the polymer bulk, the broad plateau of maximum conductance is believed to originate from the superposition of hopping events between chain segments with different oxidation potentials, *i.e.* different "effective conjugation lengths" (see also chapter 1.1.2).

Since in aromatic conjugated polymers, the introduction of charges through doping (both by chemical and electrochemical oxidation or reduction) causes structural changes to

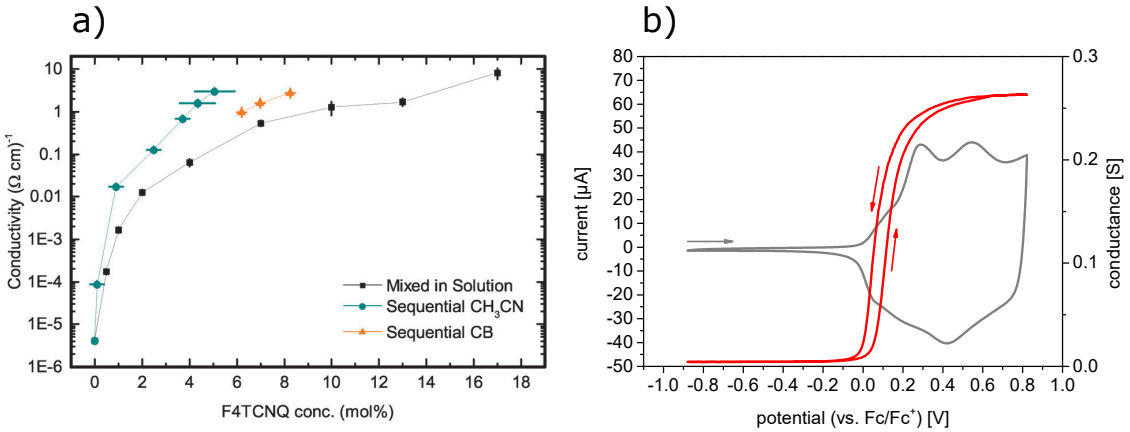

Figure 1.4: a) Conductivities of **P3HT** films doped with varying concentrations of the small molecule acceptor dopant **F_4TCNQ**.[40] The dopant was either added to the polymer solution prior to spin coating (black points) or deposited onto the dried film from separate solutions (teal and orange points). Adapted with permission from [40], © 2016, The Royal Society of Chemistry. b) Conductance profile of a **P3HT** film upon electrochemical oxidation *via* cyclic voltammetry (CV) (data measured by *Dr. Miriam Goll*).

the backbone π-system, the processes can in many cases be conveniently followed by optical absorption spectroscopy.[51–53] These phenomena are commonly referred to as electrochromic properties of CPs. In the MO band model, both polarons and bipolarons correspond to a set of mid-gap states (shown schematically for **P3HT** in Figure 1.5). Compared to the neutral polymer, in which optical excitation requires an energy equal to the band gap (ΔE_g), these exhibit lower excitation energies and thus lead to optical absorption at higher wavelengths.

This often results in visible color changes of the materials, which is for example applied in electrochromic windows. These phenomena will be shown exemplarily for p-type doping (oxidation) of polythiophene thin films in the following (Figure 1.6). Other simple linear CPs show qualitatively similar behavior in their respective wavelength ranges. For more sophisticated backbone constructions like donor-acceptor copolymers, the spectra become more complex due to the occurrence of charge-transfer effects between the different building blocks. In the neutral state, poly(alkylthiophene) films typically feature a relatively narrow main absorption band with a maximum around 500-550 nm.[54] For films exhibiting at least some degree of chain order in the bulk, π-π interactions cause additional shoulder bands resulting in a more or less significant fine structure. These effects will be further explained in the next chapter. Oxidation first leads to the formation of polaronic (radical cation) species in the π-system. The growing concentrations of polarons, accompanied

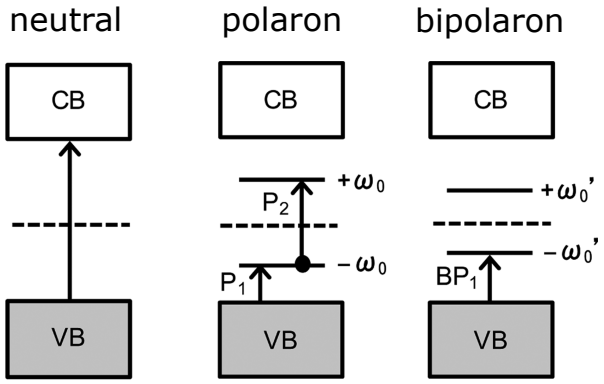

Figure 1.5: Schematic representation of mid-gap states formed through the generation of polaronic and bipolaronic species in poly(3-hexylthiophene) (**P3HT**). The arrows denote allowed transitions. Adapted with permission from [53], © 2015, American Chemical Society.

with a decrease in neutral species, lead to a decreasing absorption of the neutral band, an isosbestic point and the development of a broad band in the region between approximately 600 and 1100 nm, as well as a very broad absorption above 1200 nm.[53] These two bands can be related to the two allowed transitions P_2 and P_1, respectively (Figure 1.5). Electron paramagnetic resonance (EPR) studies have been used to directly correlate these optical features to the occurrence of radical species.[52]

Upon further oxidation, while the neutral species band still keeps decreasing, the higher energy polaron band absorption (600 and 1100 nm) eventually saturates and then starts to slowly decrease. Meanwhile, the low energy band (above 1200 nm) broadens, shows a slight blue-shift and increases significantly in absorption. This new band corresponds to the transition BP_1. Again, an isosbestic point and the vanishing of EPR activity confirm the interconversion of polaron to bipolaron species (Figure 1.5 b).[52]

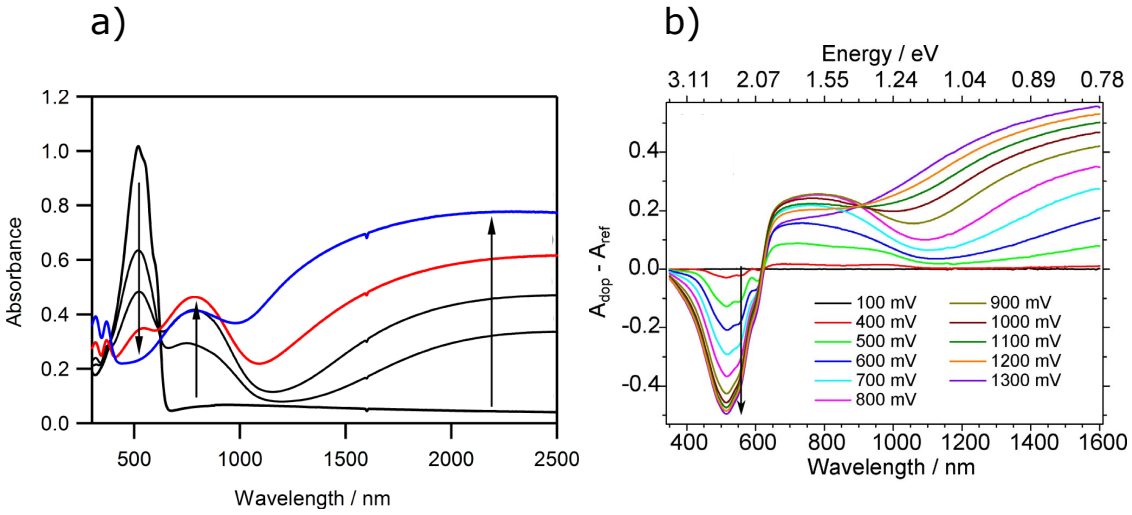

Figure 1.6: Development of optical absorption spectra of poly(3-hexylthiophene) (**P3HT**) thin films upon a) chemical doping with iron(III) chloride and b) electrochemical doping (differential plots against the neutral film reference spectrum).[52, 53] The neutral band (500-500 nm) decreases while the polaron (600-1100 nm) and bipolaron (above 1200 nm) bands increase consecutively. The spectra in a) from black to red correspond to the neutral film as well as films doped at a concentration of 10 mmol/L for 2, 4 and 304 s. The blue spectrum corresponds to a film doped at 50 mmol/L for 120 s. Potentials from cyclic voltammetry measurements are given *vs.* Ag/AgCl. Adapted with permission from [53], © 2015, American Chemical Society and [52], © 2016, Wiley-VCH Verlag GmbH & Co. KGaA.

1.1.2 Conformation, Chain-chain Interactions and Influences on Optical Properties

In the previous chapter the generation of mobile charge carriers by doping has been shown to be the prerequisite for electrical conductivity in conjugated polymers. The fundamentals presented to this point however paint a greatly simplified picture, which is only valid on a molecular level, when considering idealized single chains without any intra- or intermolecular forces. In any real application, the backbones are surrounded by a matrix of chemical species, like solvent molecules or a bulk consisting of other chains. In contrast to metals or conductive inorganic crystals, which possess highly spatially defined lattices, CPs, like other polymers, show much more complex ordering behavior due to the entropy induced by their chainlike structure (high numbers of possible conformations) and their inherently inhomogeneous nature (*e.g.* polydispersity). Mainly two factors have to be considered concerning charge transport in such systems. Firstly, a perfectly planar conformation is not the energetically most stable. Thus, CP backbones almost always

show a certain degree of twisting, especially if they carry sterically demanding substituents or if their degree of regioregularity is low (see chapter 1.2.1). This twisting leads to a shortening of the so-called "effective conjugation length" and to less favorable electronic properties. The effective conjugation length is determined through the average number of repeating units in a chain segment which show full delocalization of their π-system. For polythiophenes in solution, this value has been proposed to typically lie somewhere between 10 and 20 repeating units (see Figure 1.7), however, the length of individual segments varies greatly due to the local conformation of the chain.[55, 56] This overlap of many slightly different conjugation lengths causes both the bands found in optical spectroscopy as well as electrochemical features (*e.g.* redox waves in cyclic voltammetry) to be typically broader and less defined compared to small molecules.[37, 57]

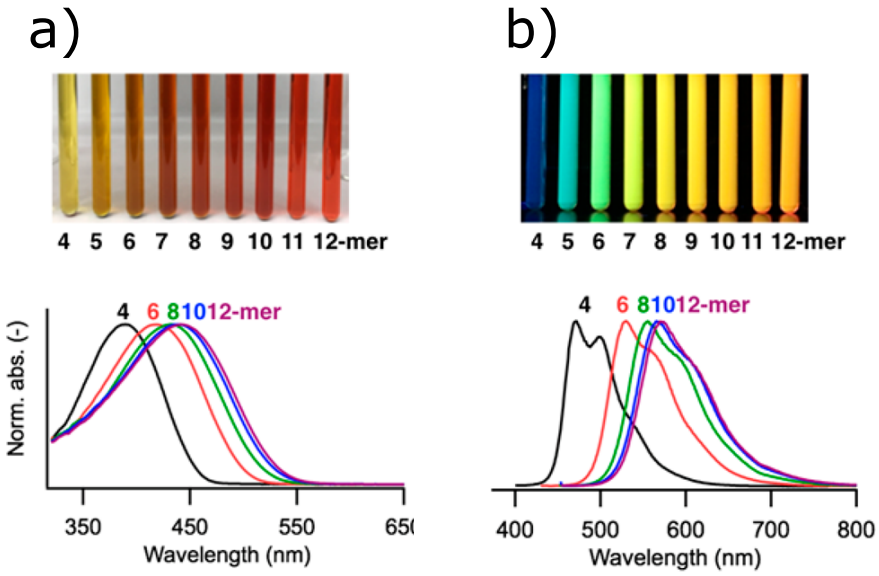

Figure 1.7: a) Optical absorption and b) photoluminescence spectra of a series of 3-hexylthiophene (**3HT**) oligomers in chloroform solution.[56] The blue-shifts of the spectra converge towards the 12-mer. Adapted with permission from [56], © 2017, American Chemical Society.

Secondly, charge transport from chain to chain has to occur *via* carrier hopping which is typically less effective compared to movement along the backbone and can be considered as a bottleneck.[50] Interchain packing effects, based on π-π interactions, decrease the average hopping distance perpendicular to the π-system, facilitate hopping events and thus can partly alleviate this drawback. In addition, more tightly packed chains assume a more planar conformation, which also has positive effects on the charge transport along the chain.[57] Reversely, this means that highly regioregular chains without sterically

demanding substituents, which can be planarized more easily, tend to show superior packing properties.

UV/Vis spectroscopy of CP solutions and thin films is a powerful tool to elucidate these effects, since both chain twisting and π-π interactions have been shown to greatly influence the optical properties. In the following, these effects will be shown for **P3HT** as a prototypical polythiophene.[57] It has to be noted that the information obtained through this method alone can only provide a rough assessment, since it is averaged over the whole solution or polymer bulk in the beam path and thus the local situations on the molecular level can greatly differ.

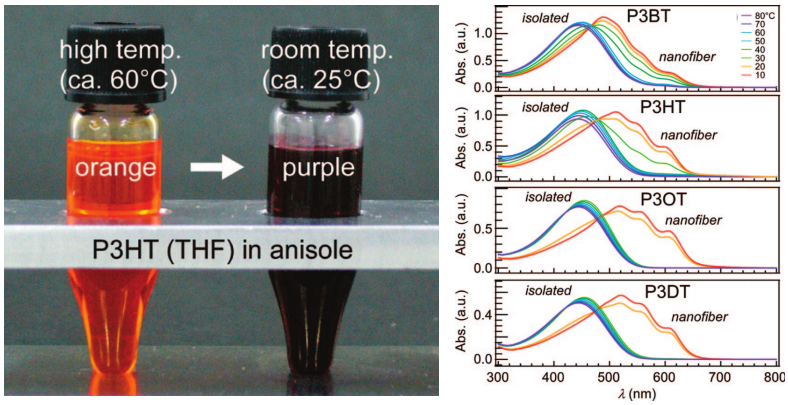

Figure 1.8: Color change of an anisole solution of a THF *Soxhlet* fraction of **P3HT** from bright orange to dark purple upon cooling from 60 to 25 °C.[58] Absorption spectral changes upon slow cooling of solutions of **P3AT**s with different alkyl chain lengths from butyl (**P3BT**) to decyl (**P3DT**), allowing the generation of nanofibers. The solubilizing effect of longer alkyl chains is immediately apparent. Adapted with permission from [58], © 2008, American Chemical Society.

In solutions of low concentrations in a good solvent like chloroform, **P3HT** can be found as free, "isolated" chains and the solutions show a bright orange color. The associated spectra thus fully reflect the influences of chain twisting. A single band without any fine structure is seen under these conditions. Going from regioirregular to highly regioregular polymers, this band shows a bathochromic shift from 420 to 454 nm, caused by the elongation of the effective conjugation length.[59] Similar effects were found when the effect of chain length for regioregular **P3HT** batches was studied. For short chains (3 and 5 kg/mol), the bathochromic shift was more pronounced (λ_{max} changes from 421 to 438 nm), since here, the conjugation length is most influenced. For higher molecular weights, the effect diminishes, since chain lengths become greater than the longest possible fully conjugated segment (λ_{max} = 441, 447 nm for 11 and 26 kg/mol, respectively).[60]

Upon decreasing the solvent quality for **P3HT**, *e.g.* using solvents like ethyl acetate or anisole instead of chloroform, as well as at high polymer concentrations or decreased temperatures, the solution spectra become more complex (Figure 1.8).[58] Under these conditions, the polymer chains can not anymore exist in their fully isolated form and start to interact intra- and intermolecularly by forming aggregates. Using controlled conditions, like specialized solvent mixtures or slow cooling protocols, self-assembly into supramolecular structures like nanofibers can be achieved. Macroscopically, aggregation manifests as a color change of the solutions from orange over dark red to purple. The main band ususally shows a slight red-shift caused by a high degree of planarization through interchain packing. Additionally, a more or less significant fine structure caused by superimposing absorption bands develops, which result in shoulders which broaden the main band to higher wavelengths, typically with maxima at approximately 515, 560 and 605 nm. Very similar features are also seen in thin film spectra of the polymer, with maxima around 520, 550 and 610 nm.[61] The appearance of these shoulders, as well as their respective ratios, strongly depend on the molecular properties of the used polymer batch (regioregularity, molecular weight and the presence of bulky substituents), as well as film deposition conditions (method, solvent, concentration, temperature, drying time, preaggregation in solution). The shoulder bands can be related in increasing order of wavelengths to transitions from the ground state to the 2^{nd} and 1^{st} vibrational levels, (0-2 and 0-1), as well as to the vibrational ground state of the first excited state (0-0) (Figure 1.9). Corresponding transition bands can be found in the photoluminescence spectra, at higher wavelengths due to their respective *Stokes* shift. *Spano et al.* developed a model which allows to correlate the ratio between the 0-0 and the 0-1 transitions to the occurrence of interchain and intrachain aggregates.[62, 63]

Both in aggregated **P3HT** solutions and in thin films increases in temperature lead to breaking of the ordered structures through increased molecular movement.[61] Thermal activation successively overpowers the aromatization energies which hold the backbones in a planarized state and causes twisting. These effects lead to gradual vanishing of the fine structure, as well as a blue-shift of the main band. At high temperatures, the polymer chains are again found freely dissolved in solution, or in a melted, optically "solution-like" state in thin films.

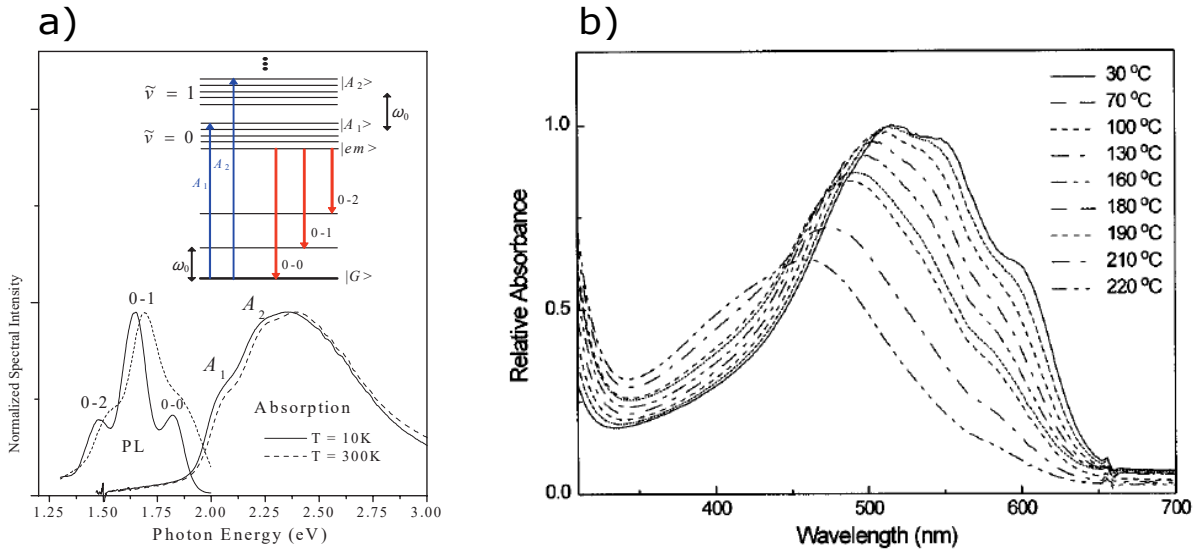

Figure 1.9: a) Absorption and photoluminescence (PL) spectra of solid-state **P3HT**. $A_{0\text{-}0}$ and $A_{0\text{-}1}$ are labeled as A_1 and A_2, respectively, the global absorption maximum (A_3 or $A_{0\text{-}2}$) is omitted.[62, 63] According to *Spano's* model, the low intensity of the $A_1/A_{0\text{-}0}$ absorptions and 0-0 emission bands point at a predominantly intermolecular aggregation in this case. b) Absorption spectral changes of a **P3HT** film upon heating from 30 to 220 °C.[61] Adapted with permission from [62], © 2009, American Institute of Physics and [61], © 1996, American Chemical Society.

1.1.3 Organic Field Effect Transistors, EGOFETs, OECTs

The connected world we enjoy today, with smart mobile devices, the internet and supercomputers, was made possible mainly by the invention of integrated circuits (ICs) based on silicon technology. In the last decades, these have undergone an extremely rapid shrinking process, which can be described by *Moore's* Law.[64] The central electric elements of any IC are transistors, which essentially function as switches blocking or allowing current flow based on their switching state. This is accomplished by employing semiconducting materials in a three-contact setup. In any modern field effect transistor (FET), the semiconductor is directly contacted by the "source" and "drain" electrodes, with a certain spacing between these contacts, called the "channel".[65] The third contact, the "gate" is placed above or below the channel area and is separated from the semiconductor by an isolating material with high dielectric constant, called the "gate dielectric".

In the off-state of the transistor, applying a voltage bias between the source and drain electrodes induces no or only negligible flow of current through the channel since the semiconducting material acts as an insulator. Upon applying an additional potential of suitable polarity between the source and the gate electrodes, an electric field is induced

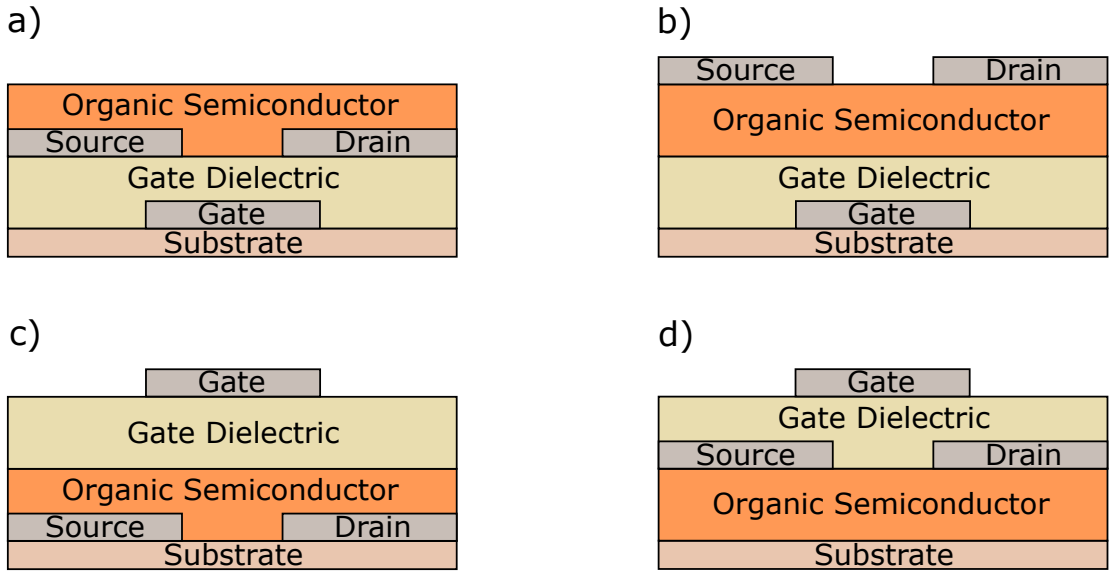

Figure 1.10: Schematic cross-sections of four principal layer structures of organic field effect transistors (OFETs): a) bottom-gate/bottom-contact, b) bottom-gate/top-contact, c) top-gate/bottom-contact and d) top-gate/top-contact.

throughout the gate dielectric and the semiconductor. This leads to accumulation of charge carriers (electrons for n-type and "holes" for p-type semiconductors) in a thin layer at the interface between the semiconductor and the dielectric. In this "on-state", the source-drain bias now causes a current flow, dependent on the abundance and mobility of charge carriers present in the channel. Higher gate fields induce more carriers, thus, source-drain currents can be modulated by the gate field in certain limits. This behavior can be measured by recording the current-voltage characteristics for such devices, called the "output" and "transfer" curves. Output characteristics are determined by increasing the potential between the source and drain electrodes (V_{sd}) at a fixed gate potential (V_g) and measuring the dependent source-drain current I_{sd}. This process is then repeated for different potential steps of V_g (Figure 1.11 a).

At a given gate potential, I_{sd} will initially rise nearly linearly with increasing V_{sd}. This is called the "linear regime".[66] At higher source-drain potentials the currents slowly start to saturate ("saturation regime"), since all charge carriers present in the channel are fully utilized and this limits the flowing currents regardless of the applied V_{sd}. Higher I_{sd} values can only be reached by increasing the number of charge carriers through the gate potential. Here the transfer characteristics come into play. Transfer curves are recorded at fixed source-drain voltages by measuring the current response to increases in gate potentials (Figure 1.11 b and c). This can easily be imagined as a "cross-cut" through different output curves at a certain V_{sd}. Since typically the values for I_{sd} increase by

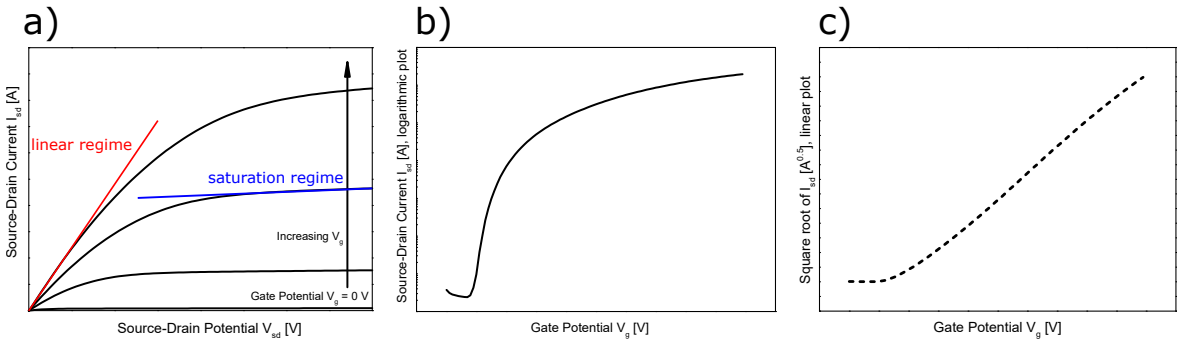

Figure 1.11: Characteristic curves obtained when measuring *I-V* behavior of FETs: a) Output curves for increasing gate potentials V_g, b) logarithmic plot of transfer curve at a fixed source-drain potential V_{sd}, c) linear plot of square root of the same transfer curve.

many orders of magnitude, transfer curves are usually plotted on the logarithmic scale. Additionally, the square root graph of the transfer curves is calculated and plotted on a linear scale. From the slope of a linear fit to this plot, field effect mobilities μ can be determined, the exact method depending whether the transfer curve was measured in the linear or the saturation regime.[65] Throughout this thesis, all mobilities were determined in the saturation regime, the associated formula is given as

$$\mu_{sat} = \frac{2l}{C_{diel} w} \left(\frac{\partial \sqrt{|I_{sd}|}}{\partial V_g} \right)^2$$

with the channel length l and total width w, as well as the capacitance of the gate dielectric $C_{diel} = 1.5 \cdot 10^{-4}$ As/Vm for our standard bottom-gate/bottom-contact substrates. For **P3HT** transistors for example, field effect mobilities lie in the range of 10^{-5}-10^{-2} $cm^2V^{-1}s^{-1}$, depending on the molecular weight, regioregularity (see chapter 1.2.1) and processing conditions used.[57, 67, 68] The x-axis zero-intercept of the same linear fit gives the so-called "threshold voltage" V_{th}, the minimal source-drain potential required for a measurable current flow.

The most common type of transistor today is the so called metal-insulator-semiconductor field effect transistor (MISFET).[65] These devices consist of layered, three-dimensional structures of the individual components. In traditional microelectronics the contacts are either metals like copper or gold or heavily n-doped silicon, the gate dielectric usually consists of silicon oxide while the semiconductor is weakly p-doped silicon. The integrated circuits, which today consist of billions of such multilayer structures, are produced in highly sophisticated processes including many successive steps of applying photoresists,

lithography and etching. With the discovery of semiconductor-like behavior of many conjugated polymers (and also conjugated small molecules like rubrene or pentacene), these materials were quickly proposed as alternatives to silicon and as early as 1987 the first organic field effect transistor (OFET) was produced, employing a polythiophene as the active layer.[69] The field has grown tremendously in the last decades and huge numbers of different polymers and small molecules have been tested for their performances in OFET devices.[65] Like in organic photovoltaics, research on p-type materials has been favored and these typically show better performance than pure n-type materials. Devices rivaling silicon-based transistors with mobilities in the order of $10^1\,\mathrm{cm^2V^{-1}s^{-1}}$ have been realized for example with the small molecule rubrene and recently also with polymeric semiconductors.[70] Many transistor geometries have been tested, most of which had already proven successful in traditional silicon technology. The four most-used, named after the positions of the source, drain and gate contacts relative to the semiconductor layer, are depicted schematically in Figure 1.10. As gate dielectric, usually the SiOx substrate itself or polymers like **PMMA** or **CYTOP™** (Figure 1.12) are employed. While SiOx possesses a relative permittivity (dielectric constant, ϵ_r) of 3.9, with polymers, lower values of $\epsilon_r = 3.6$ (P**MMA**) or even 2.1 (perfluorinated polymers like **CYTOP™**) can be reached.[71, 72] In addition, the water absorptivity of these materials is exceptionally low (**PMMA**: 0.3 w%, **CYTOP™**: <0.01 w%), which allows them to function as an additional layer of encapsulation against atmospheric conditions in the case of a top-gate geometry.

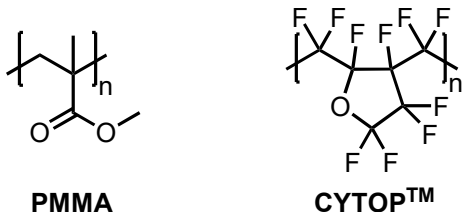

PMMA **CYTOP™**

Figure 1.12: Structures of polymers frequently used as the dielectric layer in organic field effect transistors.

With printed OFETs, it is not yet possible to reach the nanometer-scale structure sizes which can be obtained by modern lithography processes in traditional silicon technology. Lithographic patterning recently enabled OFET channel lengths in top-gate geometry as low as 500 nm.[73] Thus, these devices can for now not be seen as valid alternatives for applications like microprocessors, in which computing performance and energy efficiency are the most important factors. However, in contrast to metal/silicon-based systems, integrated circuits based on organic materials can be created by potentially much cheaper

solution deposition methods like spin coating or blade coating or by printing processes.[23] The substrates can be flexible materials like polymer foils or even paper, opening potential applications of such devices both for low-cost use cases like throw-away chips (RFID tags, medical tests, etc.) as well as wearable electronics. Like in other organic electronics devices, long-term stability under atmospheric conditions is still a concern, since due to their chemical nature, the active layers can undergo unwanted oxidative side reactions. Reliable oxygen-proof encapsulation methods and the development of air-stable semiconductor materials are thus highly important.[74]

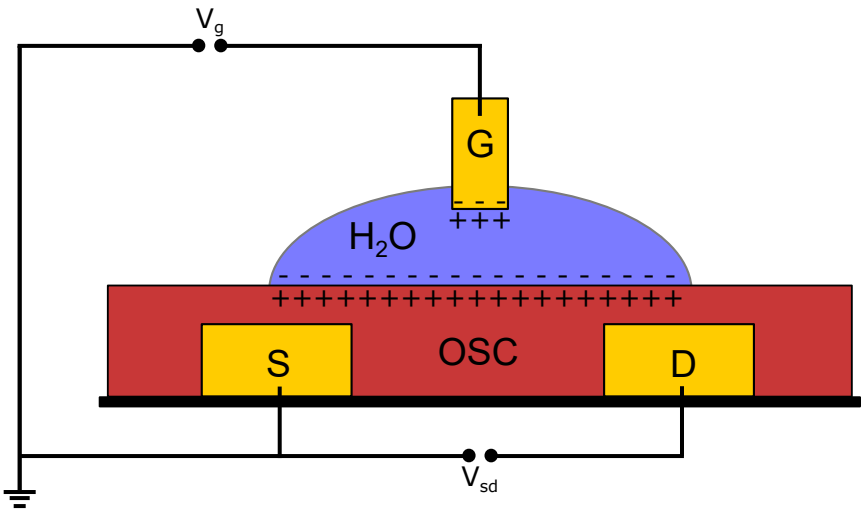

Figure 1.13: Schematic representation of an electrolyte-gated organic field effect transistor (EGOFET). Upon application of a potential between the gate (G) and source (S) electrodes, capacitances form both on the gate electrode and organic semiconductor (OSC) surfaces (depicted for a p-type OSC).

Electrolyte-gated organic field effect transistors (EGOFETs) represent a special type of the top-gate OFET, in which the insulating gate dielectric is replaced by a liquid electrolyte droplet, often based on ultrapure water or buffer solutions.[15, 75, 76] The gate electrode typically consists of a polished gold wire with a well-controlled cross sectional area, which is immersed into the droplet. The low dielectric constant of the electrolyte allows the transistor to operate at low enough gate potentials (<1 V) to exclude the risk of electrochemical reactions of the electrolyte (*e.g.* water splitting). However, electrochemical reactions of the semiconductor with the electrolyte or diffusion of electrolyte and any dissolved species into the semiconductor films are potentially possible and need to be considered as sources of error.

In an EGOFET device, charges will build up as double layers at the gate electrode interface and at the semiconductor interface. Depending on the diameter ratio of these

surfaces, each of these capacitances can be more or less contributing to the transistor characteristics. Based on this concept, sensor devices can be built, in which either the gate surface (*e.g.* thiol SAMs on gold surfaces) or the semiconductor surface (click chemistry, amide linkages, etc.) can be functionalized with (bio)molecules possessing affinity to a given analyte dissolved in the electrolyte.[75, 77] The resulting concentration of analyte molecules on the functionalized surface influences the respective capacitance and thus changes the source-drain currents at a given gate potential, which can be read out as a sensor signal. Many biomolecules, *e.g.* proteins, have net negative charge at neutral pH values, which can be expected to significantly alter the negative charge concentration induced on the surface of a p-type OSC.[14]

For both normal OFETs as well as EGOFETs, chemical reactions of the organic semiconductor layer or intrusion of the electrolyte are highly unwanted and usually have a substantial impact on transistor performance and stability. However, the possibility for controlled electrochemical or chemical redox reactions can also be seen as an advantage of conjugated polymers in certain specialized transistor applications, compared to silicon technology. A prime example is the organic electrochemical transistor (OECT).[79] Its structure is very similar to the EGOFET, however, the OSC layer is on purpose created from hydrophilic conjugated polymer systems like **PEDOT/PSS** or conjugated polyelectrolytes (see chapter 1.2.3) and open to the intrusion of electrolyte (Figure 1.14 a).

In contrast to most OFET types, which usually operate in accumulation mode (charge carriers are accumulated by application of the gate field), most OECTs are depletion mode transistors, *i.e.* the channel is most conducting when the gate potential is zero, and charge carriers are depleted by application of higher V_g values (Figure 1.14 b). This is realized by employing active materials in their doped state, in which they show their highest conductivity. In the case of **PEDOT/PSS**, the poly(styrene sulfonate) (**PSS**) anions counterbalance the positive polarons present in the doped state of **PEDOT**. The applied gate field moves ions from the electrolyte into the channel. Due to the polymeric nature of **PSS**, the sulfonate anions are not able to leave the polymer bulk. Thus, the electrolyte counterions form net neutral species with **PSS**, thus destabilizing charge carriers on the backbone and forcing a dedoping process. This leads to diminished and finally negligible conductivity, corresponding to the off-state of the transistor. Compared to traditional organic transistors, OECTs offer much higher transconductances, *i.e.* small changes in gate potentials induce very high changes in source-drain currents. However, their switching speeds are lower, since ion motion in and out of the active layer is a slow process compared to accumulation of charge carriers.[80] Like EGOFETs, OECTs can

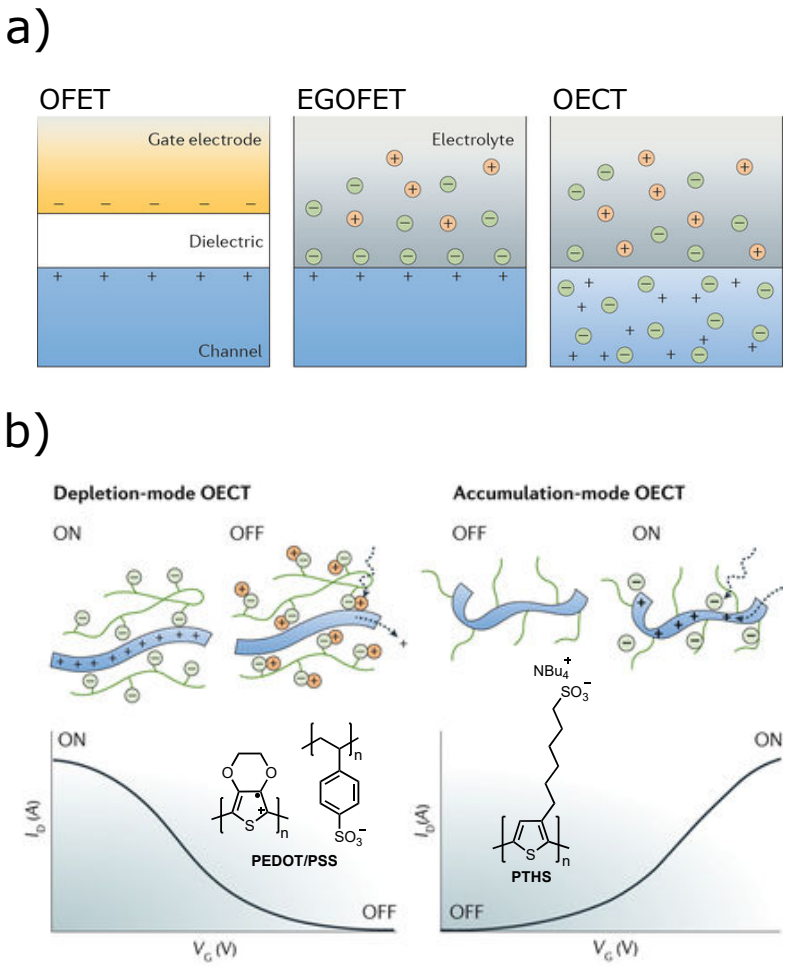

Figure 1.14: a) Comparison of the different operating regimes of organic field effect transistors (OFETs), electrolyte-gated organic field effect transistors (EGOFETs) and organic electrochemical transistors (OECTs). b) Processes occuring in depletion-mode and accumulation-mode OECTs upon application of a gate field and the resulting influence on the source-drain voltage. Structures of **PEDOT/PSS** and the conjugated polyelectrolyte **PTHS** as representative examples for the two different types of OECTs.[78]. Adapted with permission from [78], © 2018, Macmillan Publishers Ltd.

operate in direct contact with (aqueous) solvent systems and can be used as sensors for various types of analytes.[81]

1.2 Developments in Polythiophene Chemistry

Of all classes of conjugated polymers, polythiophenes and their derivatives are probably the most well-investigated today. Especially poly(3-hexylthiophene) (**P3HT**) has gained a reputation as the "working horse" in many applications in organic electronics, including organic photovoltaics (OPV) and field effect transistors (OFETs), among others, since it combines structural simplicity and processability with still very competitive electronic properties.[57, 82, 83] Another notable example is poly(3,4-ethylenedioxythiophene) (**PEDOT**). Due to its high-lying HOMO level (-4.3 eV as determined by electrochemical experiments against the internal standard Fc/Fc^+ at -5.1 eV in the *Fermi* scale), this polymer can exist in its doped state with remarkable stability even under environmental conditions if a suitable counterion like poly(styrene sulfonate) (**PSS**) is used.[48, 84] The electronic conductivities of such **PEDOT/PSS** systems have been reported to reach up to 3065 S/cm, making these materials highly relevant for conductive coatings, interfacial layers or thermoelectrics.[85–89]

In this chapter, a brief overview of the synthetic developments which are most relevant for this thesis will be given: the introduction of highly controlled polymerization methods for poly(alkylthiophenes) (**P3AT**s), polymer analogous functionalizations, block copolymers, side-chain π-extensions, as well as the addition of ionic, redox and sensor functionalities. Other important aspects in polythiophene chemistry, like three-dimensional, hyperbranched systems or donor-acceptor copolymers, will not be covered in-depth in this chapter since they are beyond the scope of this thesis. The reader is instead referred to literature review articles covering these topics.[90, 91] Although this chapter mainly focuses on polythiophene-based materials, many of the underlying concepts can be and have been adapted to other conjugated polymer types.

1.2.1 Highly Controlled Polymerization Methods

Only a few years after the discovery of electrical conductivity in doped polyacetylene, the first methods to synthesize polythiophenes from simple monomers, both by chemical and electrochemical methods, were developed.[27, 30, 92, 93]

Electrochemical polymerization typically results in the formation of insoluble polymer films on the working electrodes. This is arguably the fastest method to produce polythiophene films on various conducting substrates and has been used for applications ranging from simple coatings to highly complex sensor devices.[93] However, film quality, especially if very thin films are desired, is often not competitive with film deposition methods

from solution, since polymerization starts at individual nucleation points throughout the substrate, leading to inhomogeneous films. Investigations of the chemical structure are difficult, owing to the insolubility of the films which prohibits some powerful analytic methods like NMR spectroscopy. Since all polymers which will be presented in this work were synthesized chemically, the reader is referred to literature where electrochemical polymerization methods and mechanisms have been reviewed in great detail.[37, 93]
Early chemical polymerization methods initially consisted of either oxidative polymerization of thiophene with strong oxidation agents like iron(III) chloride or transition metal catalyzed polycondensation of 2,5-dihalothiophene monomers.[94, 95] Oxidative polymerization was shown to follow a similar mechanism to electropolymerization and lead to short, partly insoluble, charged polymer species which had to be dedoped prior to further use. Early cross-coupling methods led to more defined products, however, molecular weights were still low and broadly distributed.[92] For all early polythiophenes, solubility issues presented a major challenge. This was changed when *Eisenbaumer et al.* discovered that attachment of alkyl chains (butyl or higher) in a β-position of the thiophene ring led to good solubility of such poly(3-alkylthiophene)s (**P3AT**s) even at higher molecular weights.[96] However, this asymmetric substitution of the repeating units brought about a new challenge which did not have to be considered earlier: the occurence of head-to-head (HH), head-to-tail (HT) and tail-to-tail (TT) linkages (Figure 1.15).[97]

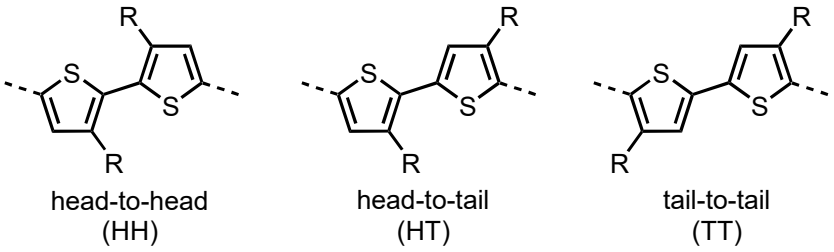

Figure 1.15: Possible linkages between repeating units in poly(3-alkylthiophene)s (**P3AT**s).

If these different linkages occur randomly throughout the polymer chain, the polymer is called "regiorandom". This is the case for **P3AT**s synthesized by uncontrolled polymerization methods like oxidative polymerization. If the amount of strictly HT-linked repeating units is increased, the "regioregularity" of the polymer improves. **P3AT**s with >95% of HT linkages are commonly termed "regioregular". The degree of regioregularity can be determined by proton NMR spectroscopy, in which the different linkages lead to triads with slightly different chemical shifts, most easily visible for the β-proton signal in the aromatic region.[98, 99]

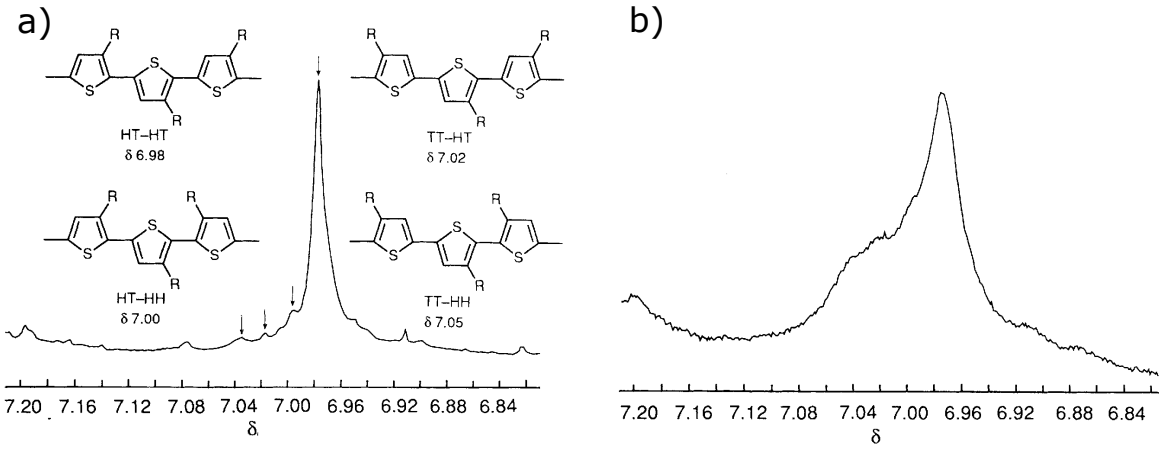

Figure 1.16: a) Aromatic region of a proton NMR spectrum of poly(3-dodecylthiophene) (**P3DDT**), synthesized by an early variant of the controlled *Kumada*-type polymerization.[98] Signals corresponding to the four different structural triads formed by combinations of HH, HT and TT linkages. b) Spectrum of a similar polymer synthesized by oxidative polymerization with $FeCl_3$. Adapted with permission from [98], © 1992, The Royal Society of Chemistry.

Regioregularity of polythiophenes has a significant effect on the electronic properties of the materials.[67, 100] While the introduction of alkyl chains in itself presents a decrease in electroactive volume in the polymer bulk, regioirregular linkages additionally lead to twisting of the polymer backbone due to steric interactions. This causes a shortening of the effective conjugation lengths and thus less efficient charge transport by delocalization along the polymer backbone. Additionally, planarization of the π-systems is energetically less favorable and thus interchain π-π stacking is decreased, leading to less efficient charge transport between the chains. Thus, until the early 1990s, it was not trivial to combine high charge carrier mobility and conductivity as well as facile solution processability in a single polythiophene material. In 1992, the groups of *Rieke* and *McCullough* independently discovered two related methods to produce highly regioregular **P3AT**s.[98, 101] The *McCullough* group used asymmetrically substituted monomers, in which only one of the α-positions was halogenated. Selective lithiation with LDA in the open position and subsequent *Grignard* reagent formation allowed for a regioselective polymerization reaction with Ni catalysts. *Rieke* found that the addition of active zinc to 2,5-dibromo-3-hexylthiophene (**3HTBr$_2$**) resulted, remarkably, in the regioselective generation of a single intermediate species which was then polymerized with $Pd(PPh_3)_4$, yielding highly regioregular **P3HT**.

Both methods still suffered from the necessity of cryogenic temperatures for the formation of the active monomer species. This drawback was eliminated a few years later, again by the *McCullough* group, through the invention of the *Grignard* Metathesis Polymerization (GRIM, Scheme 1.3).[102] In this polymerization method, like in *Rieke*'s protocol, **3HTBr$_2$** is used as the monomer. The formation of the active species takes place *via* a *Grignard* transfer reaction using *e.g.* *t*BuMgCl or *i*PrMgCl and can be carried out at room temperature. However, compared to the active zinc route, this reaction is less regioselective, leading to a ratio of the two possible isomers of ~3/1 - 4/1 under typically used conditions. The preferred generation of the 5-metalated species can be most probably ascribed to steric hindrance between the bulky *Grignard* transfer reagent and the alkyl side chain of the monomer. The influence of reaction times and conditions has been studied in great detail by *Thelakkat et al.*[103] Although the exclusive formation of one intermediate can be enforced by using an asymetrically substituted *Yokozawa*-type monomer, 2,5-dibromo-3-alkylthiophene still remains the monomer of choice for most applications.[104] This is due to the fact that, despite the ~3/1 ratio, the 5-metalated intermediate is almost exclusively incorporated into the polymer backbone when Ni(dppp)Cl$_2$ is used as the castalyst.[105, 106] This can be ascribed to the higher reaction rates for the polymerization of this species, compared to couplings involving the 2-metalated monomer, most probably caused both by the electronic and steric influence of the position of the alkyl chain.
The mechanism of the GRIM polymerization has been investigated in great detail.[107] The generally accepted mechanism starts by the formation of the respective activated monomers through *Grignard* transfer reaction. When the Ni catalyst is added, dimers form from two monomers due to catalyst insertion. Since bromine terminal groups are typically found on the starting terminus of polymer chains which were synthesized *via* GRIM, this first coupling must occur in a tail-to-tail fashion, which might be preferred since it offers the least steric hindrance.[104] After reductive elimination, the Ni catalyst and the dimer form an associated pair, which is the reason why GRIM polymerization, in this context often referred to as *Kumada* Chain Transfer Polymerization (KCTP), shows pseudo-living chain growth. From the state of the associated pair, oxidative addition of the catalyst to the chain end is far more probable than addition to another monomer. The catalyst complex can be visualized as "hopping" over the last added repeating unit and immediately inserting into its thiophene-Br bond. From this point, chain growth proceeds through repeated cycles of transmetalation, reductive elimination and oxidative addition, until the reaction is quenched by addition of protic solvents, acids or endcapping reagents. GRIM/KCTP has become the state-of-the-art method for producing poly(alkylthiophene) derivatives since its invention and has been successfully employed for the synthesis of

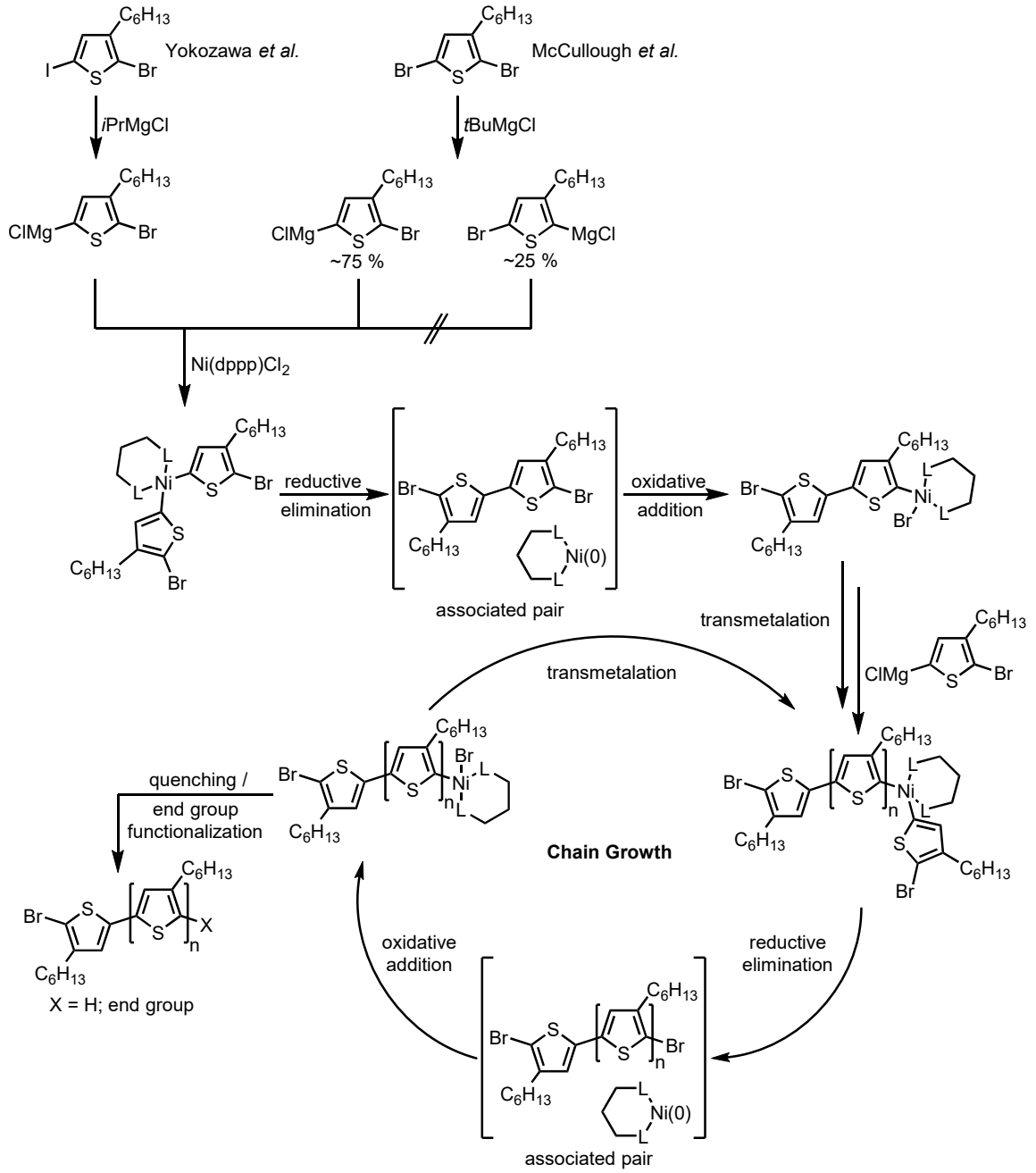

Scheme 1.3: Proposed mechanism of the *Grignard* Metathesis (GRIM) or *Kumada* Chain Transfer Polymerization (KCTP) starting from the respective *Yokozawa* or *McCullough* monomers.[107]

functionalized side-chain derivatives, surface-initiated polymerization, block copolymers as well as polymer brushes.[108] Apart from polythiophenes, the method has also proven successful for the synthesis of other conjugated polymers.[108]

1.2.2 Polymer Analogous Functionalization of Polythiophenes

In parallel with the development of highly controlled polymerization methods for polythiophenes, a multitude of synthetic protocols to functionalize the side chains or backbones was developed. Notable examples include the post-polymerization bromination of the free β-positions of **P3AT**s followed by cross-coupling reactions, originally developed by *Holdcroft*, as well as the displacement of terminal bromine groups on the side chains (Scheme 1.4).[109–112]

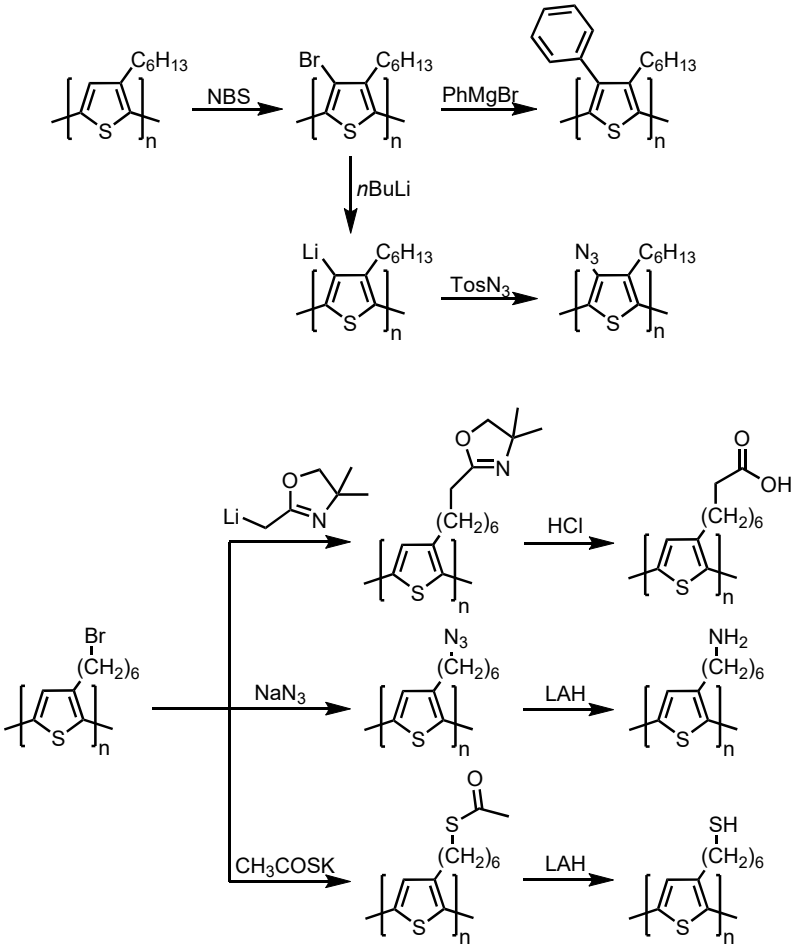

Scheme 1.4: Illustrative examples of polymer analogous methods which have been successfully employed for the functionalization of polythiophene materials.[109, 111] Many intermediate and final products of these conversions represent platforms which can be used for further functionalizations with more complex molecules.

During recent years several reactions have been identified in organic chemistry which feature exceptionally reproducible high yields with high selectivity, broad applicability (solvent and functional group tolerance), atom economy, facile workup procedures and

non-harmful, inert byproducts. These reactions, which include cycloaddition reactions as well as nucleophilic substitutions on strained ring systems, among others, have been summarized under the term "click chemistry" by *Sharpless*, *Kolb* and *Finn* in 2001.[113] One of these reactions, the copper(I) catalyzed alkyne-azide cycloaddition (CuAAC) originally developed by the groups of *Sharpless* and *Meldal*, has gained exceptional popularity, especially for synthetically challenging tasks often occuring in polymer chemistry, biochemistry and materials science.[114–118] These include polymer analogous functionalizations with highly complex (bio)molecules, block or graft polymers, heterogeneous reactions on (particle) surfaces, as well as crosslinking reactions.[119–123]

In the context of conjugated polymers and more specifically polythiophenes, CuAAC has been successfully employed for a multitude of functionalizations, both on side chains and on chain ends, *e.g.* for the formation of p-type/n-type hybrids, sensor materials, telechelic polymers, macroinitiators or for connection of preformed homopolymer blocks.[12, 14, 124–136]

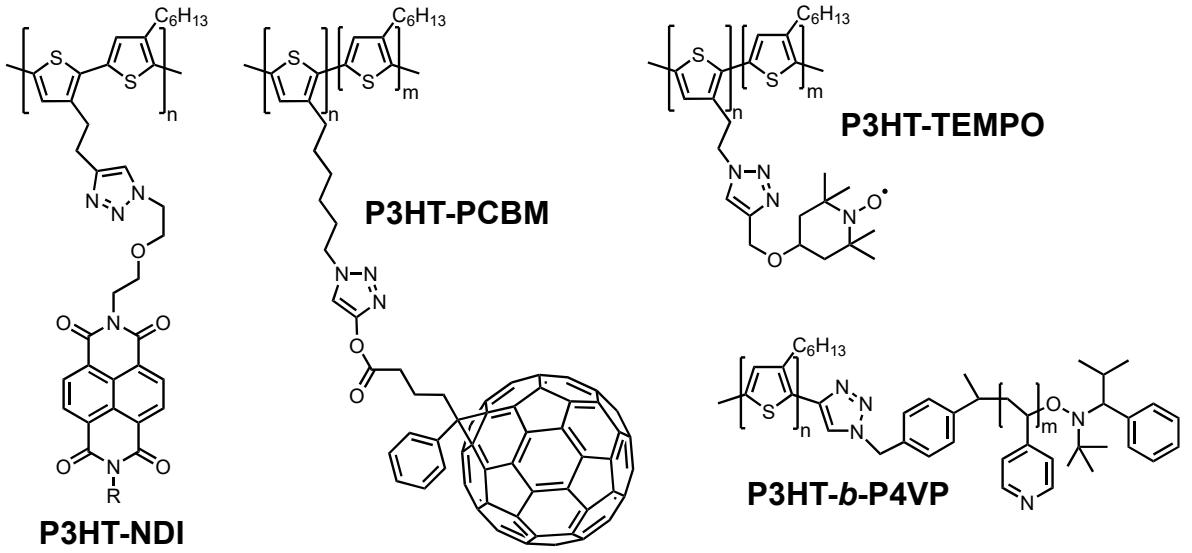

Figure 1.17: Examples of polythiophene hybrid materials functionalized by polymer analogous CuAAC methods: p-type/n-type hybrids with naphthalene bisimide (**P3HT-NDI**) and fullerene pendants (**P3HT-PCBM**), polythiophene bearing stable nitroxide group (**P3HT-TEMPO**), block copolymer incorporating **P3HT** and poly(4-vinylpyridine) (**P4VP**) blocks (**P3HT-*b*-P4VP**).[12, 124, 132, 137]

Building on *Holdcroft*'s work, *Swager et al.* extended the approach to the β-positions (Scheme 1.4).[138]. Polythiophenes have also been heterogeneously grafted to surfaces of silicon oxide or graphene oxide and incorporated into polymer/inorganic nanocomposites.[139–142] CuAAC functionalization of **PEDOT** films has been performed by the groups of *Larsen* and *Bäuerle* as well as our group.[84, 143, 144]

Based on the 1,3-dipolar cycloaddition between azides and alkynes found by *Huisgen* in the 1960s, in CuAAC the formation of regiospecifically substituted triazole rings is facilitated and accelerated by a copper(I) catalyst.[145] The generally accepted mechanism of this catalysis is shown in Scheme 1.5. Since the process is still relatively new and the identification of the involved species is not trivial, many details are still investigated. However, kinetic measurements and density functional theory (DFT) calculations strongly suggest the involvement of two Cu(I) centers in the transition state.[146, 147]

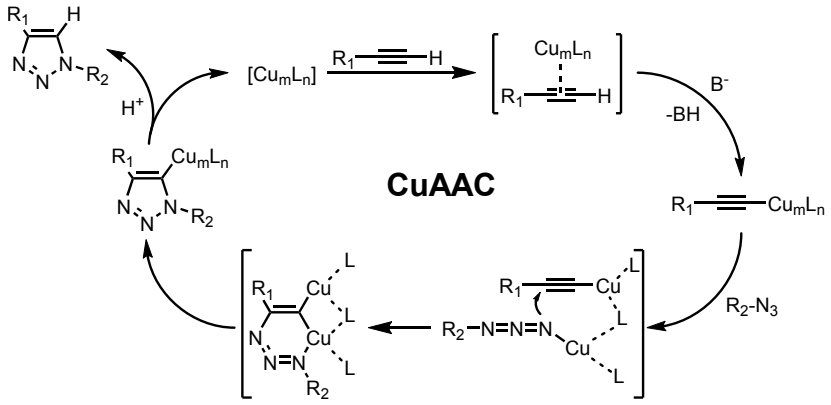

Scheme 1.5: Proposed mechanism of the copper(I) catalyzed alkyne-azide cycloaddition (CuAAC) reaction.[146, 147]

The copper(I) species can be either employed directly, for example in the form of the respective halide salts like CuBr or CuI, or it can be generated *in situ* through the reduction of Cu(II) by reducing agents like sodium ascorbate. Since Cu(I) is relatively unstable in many solvents under atmospheric conditions, degassed solvents, strict exclusion of oxygen and stabilizing ligands are needed. The addition of Cu(0) powder can be beneficial since traces of Cu(II) generated through oxidation can be conveniently converted back to Cu(I) through comproportionation. The choice of ligand type strongly depends on the solvent used. In aqueous systems, typically copper halide salts in conjunction with amine bases like triethylamine or N,N-diisopropylethylamine (DIPEA) are used. For organic solvents, where solubility issues of copper salts are common, special soluble preformed Cu(I) catalysts like $Cu(MeCN)_4PF_6$ have been developed. The main role of the ligand is to solubilize the Cu(I) species, to stabilize it against oxidation and to prevent the formation of polynuclear copper acetylides which show much lower reactivity. Additionally, the ligand may act as a base and facilitate the coordination of the catalyst to the terminal alkyne by deprotonation. The formed acetylide can now be more easily attacked by an azide moiety activated through another copper center. An intermediate six-membered ring incorporating one of the copper centers is formed. This leads to a high regioselectivity for

the 1,4-isomer upon the final triazole ring formation. In the last step of the catalytic cycle, the newly formed ring is protonated again and the initial copper catalyst is recovered.

1.2.3 Molecular Architectures with Added Functionality

Block Copolymers

Block copolymers are a highly interesting class of polymeric materials, since they not only combine the properties of the individual homopolymers they consist of, but possess unique properties based on their tendency to self-assemble into micellar structures in solution or to nano- and micrometer size structures in thin films.[148] This self-assembly is strongly dependent on the degree of miscibility of the individual polymer blocks. Conjugated polymer backbones typically exhibit rod-like conformation and strong interchain π-π stacking interactions which lead to a high tendency for aggregation phenomena and thus, especially when paired with flexible nonconjugated blocks, often show self-assembly phenomena. Two main types of block copolymers containing conjugated polymer blocks are known: rod-rod and rod-coil copolymers.[149, 150]

Most modern approaches of polythiophene-based block copolymer synthesis are only possible due to controlled polymerization methods like GRIM. In addition to producing highly regioregular polythiophene backbones with superior electronic properties this pseudo-living chain growth reaction enables end group functionalization either by *in-situ* endcapping or post-polymerization functionalization. Rod-rod copolymers of polythiophenes can be synthesized mostly analogous to other "living" polymerization methods like anionic polymerization or controlled radical polymerizations, in which a second type of monomer can be added after the chain growth of the first block has ended due to monomer depletion.[149]

Since, unlinke in rod-rod copolymers, both blocks of rod-coil copolymers can not be built up by the same polymerization method, grafting-from approaches using a macroinitiator or post-polymerization grafting-to methods are required to synthesize rod-coil copolymers. Such synthetic approaches are dependent on suitable functionalities to be present as end groups of the individual blocks. As shown by *Jeffries-El* and *McCullough*, GRIM-polymerized polythiophenes can be end-functionalized *in-situ* by adding a suitably substituted *Grignard* reagent after the monomers have been fully consumed.[151, 152] Several end groups have been introduced *via* this method, like alkyl, alkenyl, alkynyl and several differently substituted aryl groups. Owing to the sensitivity of the *Kumada* reaction, protonic groups like alcohols or amines have to be protected. It was found that for alkenyl and

alkynyl *Grignard* reagents predominantly monofunctionalized polythiophene chains were produced, however, for all other end groups, a significant amount of difunctionalization was detected, *i.e.* both chain ends were bearing a functionalization.[151] This was explained by a detachment of the Ni catalyst from the chain end after reaction with the endcapping reagent followed by insertion into the thiophene-Br bond on the opposite terminus of the same or another chain (Scheme 1.6). For unsaturated end groups like alkenyl or alkynyl, the predominant monofunctionalization can be explained by a coordinative interaction with the nickel catalyst, which retains it in close proximity to the chain end.

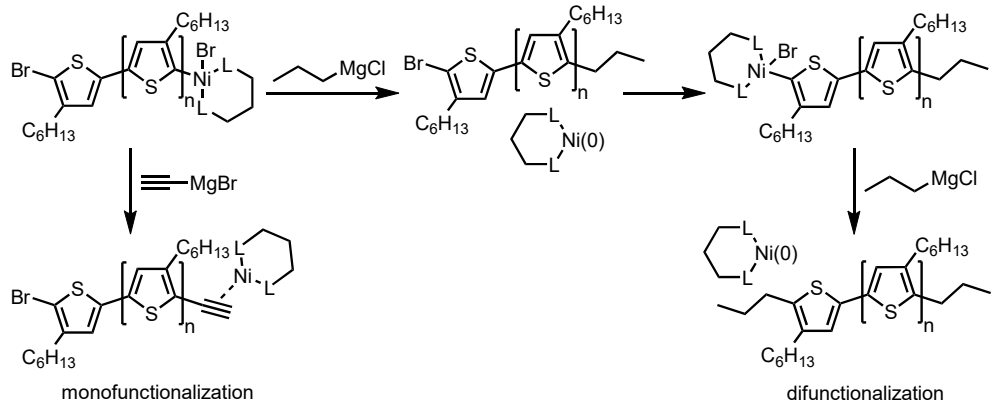

Scheme 1.6: Mechanisms of mono- and difunctionalization upon *in-situ* endcapping of polythiophenes synthesized *via* GRIM polymerization with saturated and unsaturated *Grignard* reagents.

Another possible method for end group introduction is polymer analogous functionalization, which utilizes the bromine groups present on the starting terminus of GRIM-polymerized polythiophene chains. While this is in theory a convenient method to produce libraries of differently end-functionalized materials from the same polymer batch, in practical applications it suffers from side reactions leading to mixtures of Br/H- and H/H-terminated chains which are often encountered after quenching a GRIM reaction. These limitations can be overcome by external initiation methods, in which the desired functionality is introduced already in the initiation step as part of a tailor-made catalyst system (Scheme 1.7).[153, 154] As an alternative, a non-functional blocking group can be introduced on the starting terminus, preventing the abovementioned difunctionalization upon *in-situ* endcapping.

Rod-coil block copolymers combine the individual properties of a stiff, electroactive conjugated polymer block and a flexible coil-like nonconjugated block, often leading for example to a lower degree of aggregation of the materials in solution and thus easier processability while preserving or even improving the electronic performance.[150]

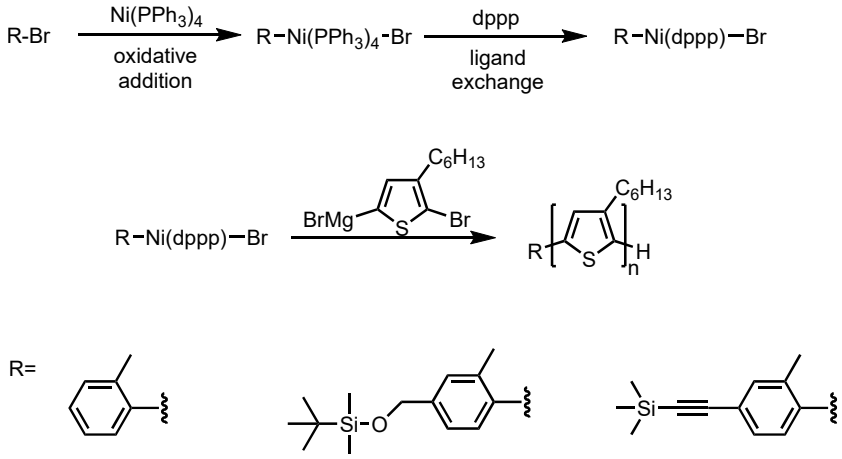

Scheme 1.7: Mechanism of external initiation for the polymerization of **P3AT**s with several functionalized *ortho*-tolyl moieties. The desired functionality is first integrated into the Ni catalyst system which is then used for the polymerization reaction. The method leads to exclusively monofunctionalized polymers which can then be employed for the synthesis of block copolymers through suitable procedures.[154]

They are able to self-assemble into unique structures both in solutions and in thin films due to stacking interactions and the often highly immiscible nature of the blocks. Examples of coil-type polymers which have been combined successfully with polythiophene blocks include polystyrene (**PS**), poly(vinylpyridine) (**PVP**) derivatives, poly(acrylic acid) (**PAA**), poly(methyl methacrylate) (**PMMA**), poly(ethylene glycol) (**PEG**), poly-(dimethylsiloxane) (**PDMS**) and poly(N-isopropylacrylamide) (**PNIPAM**), to name a few.[130, 132, 133, 155–159]

Amphiphilic block copolymers of **P3HT** with poly(2-vinylpyridine) (**P2VP**) or poly(4-vinylpyridine) (**P4VP**) coil blocks have shown especially impressive phase separation behavior in thin films, as found by the groups of *Thelakkat* and *Su* for linear polymers (Figure 1.18), as well as *Kim et al.* for graft copolymers.[129, 132, 155] By changing the weight fractions of the individual blocks, different long-range oriented morphologies could be generated, from spherical micelles over cylinders to lamellae and nanofibers.

Poly(vinylpyridine) blocks offer the additional advantage that they can be protonated, which greatly facilitates separation of the block copolymer from residual unreacted **P3HT** homopolymer. Similar approaches can be employed for **P3HT-*b*-PAA** materials, where first an ester-protected derivative of the coil block, like poly(*tert*-butyl acrylate) (**P*t*BA**), is attached to the rod block.[130] Acidolysis of the ester bond and subsequent deprotonation of the acid group then enable facile separation of the block copolymer.

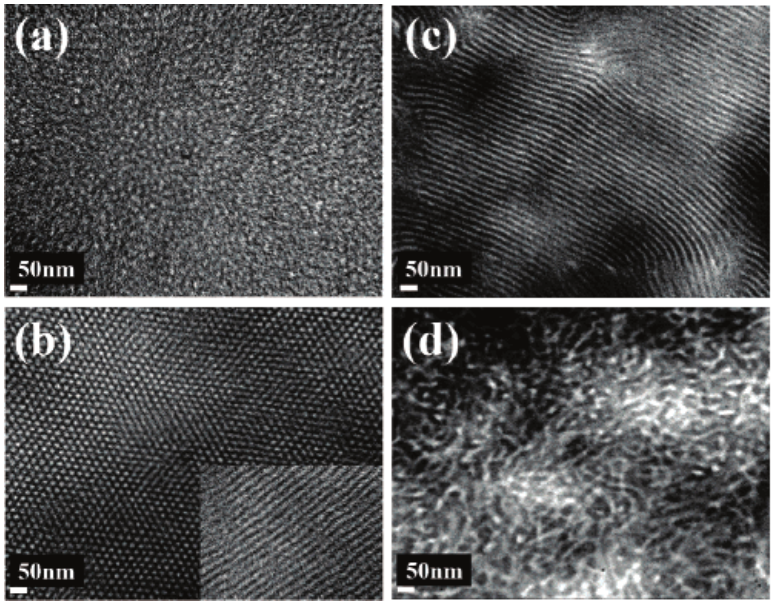

Figure 1.18: Transmission electron microscopy (TEM) images of **P3HT-*b*-P2VP** block copolymer films: a) disordered micelles, b) hexagonal close-packed cylinders, c) lamellae, and d) nanofibers. From a) to d) the weight fractions of the **P3HT** blocks are 14, 25, 41 and 70 w%, respectively.[155] Adapted with permission from [155], © 2007, American Chemical Society.

Apart from inducing self-assembly, certain coil blocks are able to introduce additional functions to the materials, which open up new possible applications. For example, *Balsara et al.* could show that **P3HT-*b*-PEG** materials feature simultaneous ionic and electronic conductivity, as well as decent cycling stability, making them attractive as cathode materials in lithium ion or all-polymer batteries.[134] *Kuila et al.* synthesized thermoresponsive **P3HT-*b*-PNIPAM** materials with highly solvatochromic properties which showed increases in photoluminescence intensity of one order of magnitude when heated above their lower critical solution temperature (LCST) in aqueous solutions (Figure 1.19).[159] This was explained by the breaking of π-stacked structures upon collapsing of the **PNIPAM** blocks.

The combination of a polythiophene (**PT**) and a poly(dimethylsiloxane) (**PDMS**) backbone in a single block copolymer material can be seen as one of the most prototypical rod-coil approaches. Regioregular poly(alkylthiophene)s like **P3HT** still are viewed as the "working horses" among p-type semiconducting polymers for applications in organic electronics, especially for organic photovoltaics (OPV) and field effect transistors (OFETs).[57] They exhibit strong π-π interactions in many solvents as well as in thin films, making them ideal candidates as core blocks for block or graft copolymers. **PDMS** materials on

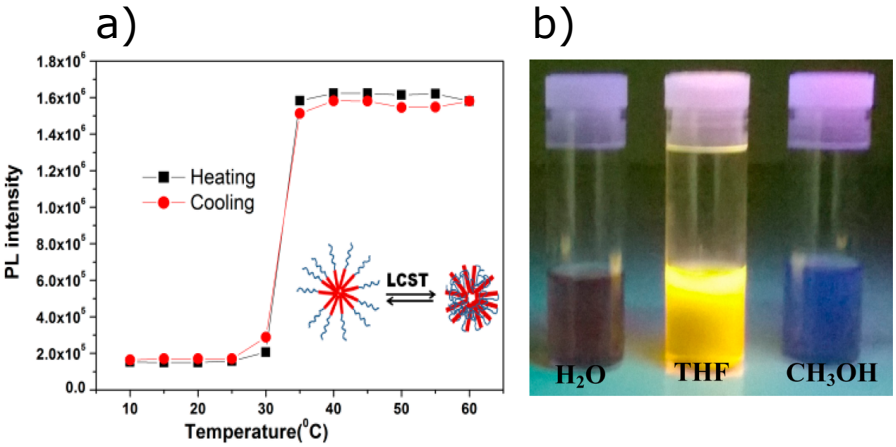

Figure 1.19: a) Temperature-dependent photoluminescence intensity of **P3HT-*b*-PNIPAM** polymers synthesized by *Kuila et al.*[159] b) **P3HT-*b*-PNIPAM** solutions in three different solvents under UV illumination at room temperature. Adapted with permission from [159], © 2015, American Chemical Society.

the other hand represent the opposite in terms of properties and applications.[160] They are typical insulators and, depending on the molecular weights, temperature and the degree of crosslinking, can be found in a wide range of states, ranging from oils with low viscosity to comparably rigid elastomeric materials. **PDMS** oils typically show viscoelastic behavior. Intermolecular forces between the individual chains are very low and the backbones are highly flexible while exhibiting heat resistance due to the strong and highly inert Si-O bonds. Such "silicone" materials are often used for hydrophobic surface treatment, as lubricants and anti-foaming agents, as well as for glue systems, lithography resins or contact lenses.

Combining two polymer classes with such orthogonal properties in the form of block copolymers can be expected to lead to hybrid materials with highly interesting new properties and a wide range of possible applications in which the electronic performance and mechanical flexibility may be utilized. If the polythiophene blocks are able to form pathways through the insulating matrix by means of which charge transport can occur, films of these polymers promise high durability during repeated bending strain in electronic devices, like foldable displays, thin film solar cells, transistors and batteries, as well as actuators.[161] Such applications are already foreshadowed by some promising studies on **PT/PDMS** blend materials for transistors and electromechanical devices, which have been found to exhibit comparable or even improved performances in comparison to the respective homopolymer systems.[2, 162, 163] As a recent example, *Yang et al.* produced

P3HT/PDMS blend films with a w/w ratio of 1/9, capable of reaching field effect mobilities up to 0.045 $cm^2V^{-1}s^{-1}$ (Figure 1.20).

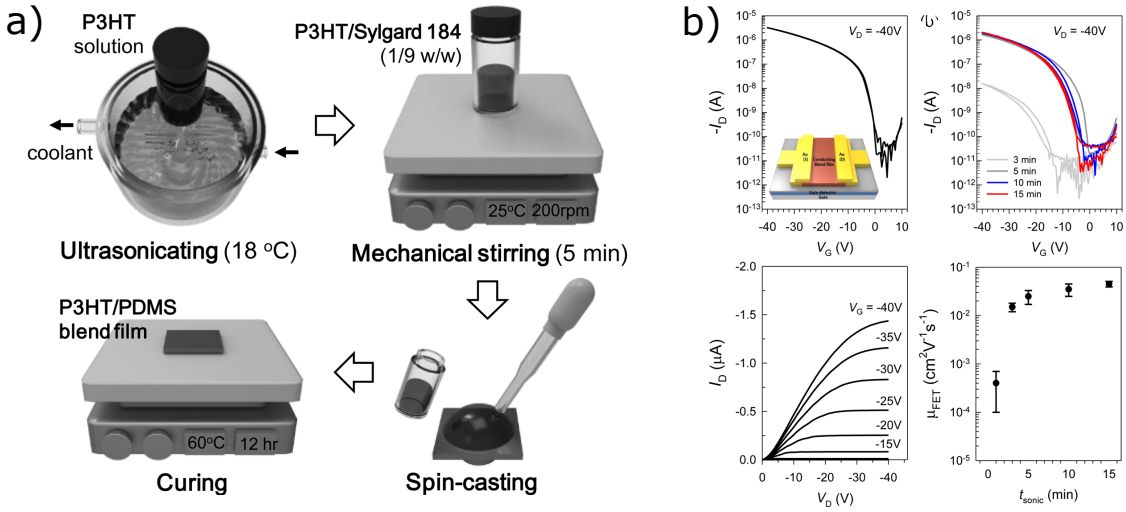

Figure 1.20: a) Process used by *Yang et al.* for the deposition of **P3HT/PDMS** blend films with high field effect mobilities.[162] **P3HT** solutions were first preaggregated by ultrasonication, mixed with a **PDMS** precursor, spin cast onto transistor substrates and thermally cured to form a flexibe **PDMS** matrix around the **P3HT** aggregates. b) Dependence of transistor performance on ultrasonication times. Adapted with permission from [162], © 2015, American Chemical Society.

However, literature reports on successful synthesis protocols for the formation of **PT-*b*-PDMS** copolymers remain relatively scarce, especially in comparison to polythiophene block or graft copolymers with coil blocks based on vinylic monomers, like polystyrene derivatives or polyacrylates. This can most likely be mainly attributed to two factors. On the one hand, from a synthetic standpoint, attachment of a **PDMS** block to a polythiophene backbone is not straightforward. Controlled radical polymerization, arguably the most advanced approach for polythiophene block copolymer formation, is not possible here, excluding such grafting-from methods utilizing a suitable macroinitiator.[132, 156] Most known synthesis methods for **PT-*b*-PDMS** polymers thus rely on grafting-to approaches which are especially prone to non-quantitative yields of the polymer-analogous reactions on chain ends. Secondly, the two homopolymers exhibit very comparable solubility behavior in organic solvents, largely excluding separation of excess homopolymers from the block copolymer based on solubility properties, which is often possible for amphiphilic copolymers.

To the best of my knowledge, the first successful synthesis of a **P3HT-*b*-PDMS** polymer was achieved by *Manners et al.* in 2011 (Scheme 1.8).[158] They synthesized a chlorosilane-

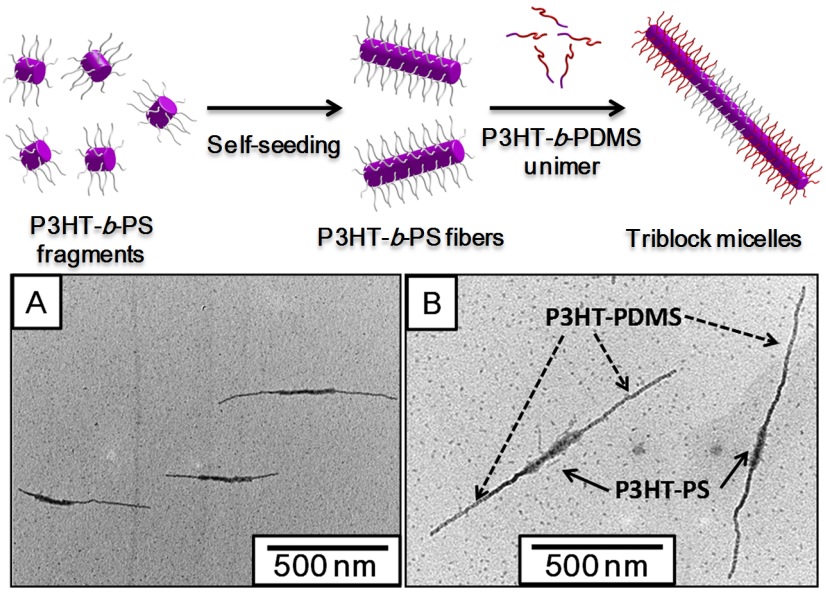

Figure 1.21: Crystallization-driven self-assembly (CDSA) of **P3HT-*b*-PS** and **P3HT-*b*-PDMS** into hybrid micelles. **P3HT-*b*-PS** was first self-seeded in a bad solvent (BuAc) before addition of aggregate-free **P3HT-*b*-PDMS** dissolved in THF and slow evaporation of this solvent in air.[3] Adapted with permission from [3], © 2014, American Chemical Society.

terminated, regioregular **P3HT** derivative over several polymer-analogous steps, which was then used to terminate a living anionic ring opening polymerization of **PDMS**. The materials were applied in crystallization-driven self-assembly (CDSA) studies in solution and cylindrical micelles with controlled lengths between 40 and 320 nm could be obtained. An improved method was later introduced by the same group, this time based on copper(I) catalyzed click chemistry between alkyne-terminated **P3HT** and azide-terminated **PDMS** homopolymers, respectively.[3] Similar approaches were also shown to be viable for other block combinations, *e.g.* of polyselenophene and polystyrene, as well as poly(ferrocenylsilane) and **PDMS**.[164, 165] The polymers were again investigated in CDSA experiments in conjunction with **P3HT-*b*-PS**, leading to the formation of hybrid micelles consisting of **PS**-containing cores and **PDMS**-containing outer fragments (Figure 1.21). Recently, **P3HT-*b*-PDMS** copolymers were synthesized by *Ogino et al.*, in this case by connecting the two blocks *via* a hydrosilylation reaction.[166] The materials were studied for their performance in organic solar cells in conjunction with **PCBM** as acceptor and efficiencies up to $\eta = 3.24\%$, superior to the pure homopolymer **P3HT** (2.45%), were found.

In chapter 3 of this dissertation, results of own work on **P3HT-*b*-PDMS** block copolymers will be shown, focusing on optimization of the linking procedure through CuAAC, the

influence of the **PDMS** block concerning microphase separation during thin film formation, as well as the optoelectronic properties of the materials.

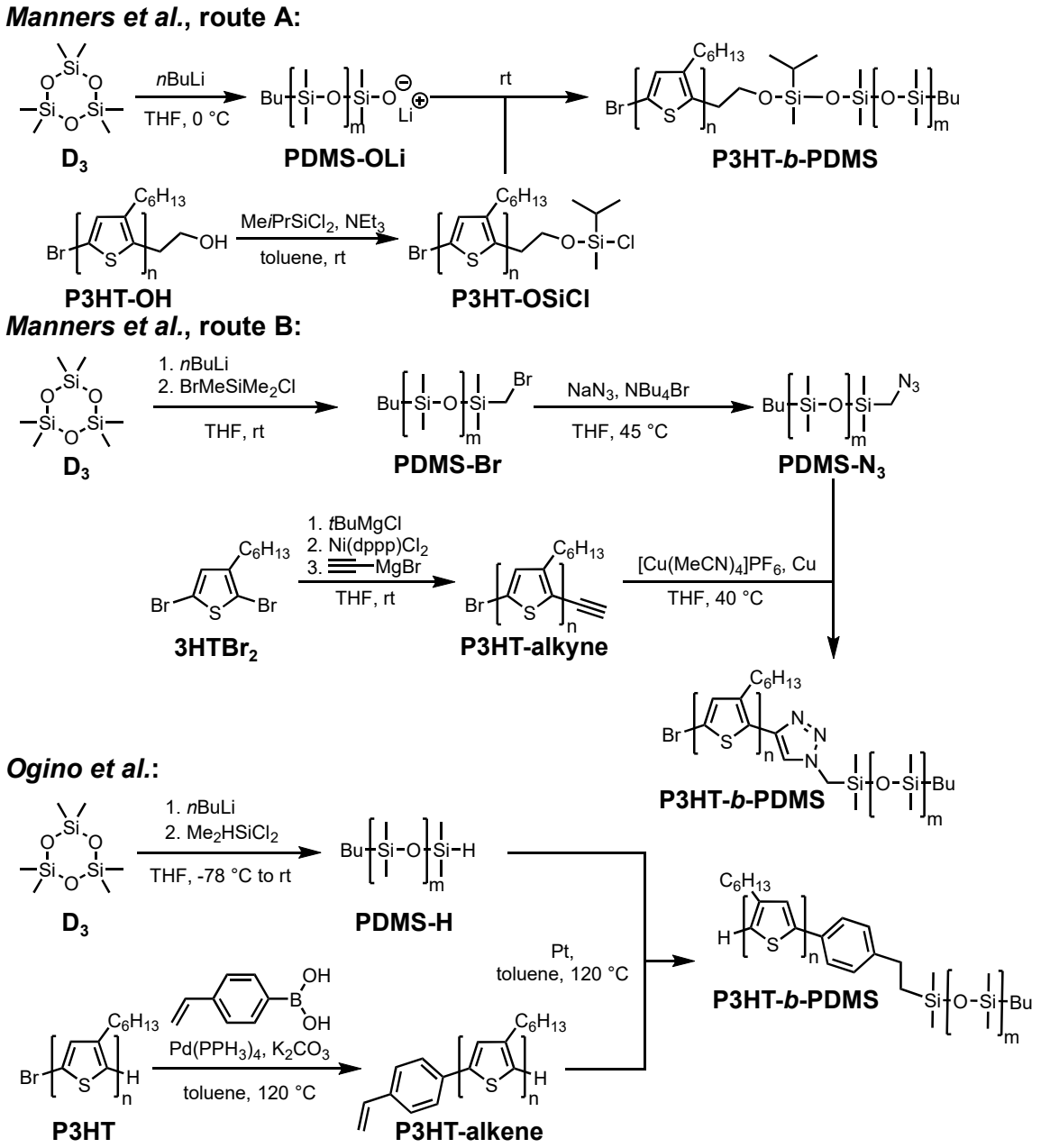

Scheme 1.8: Three different routes used for the synthesis of **P3HT-*b*-PDMS** block copolymers by the groups of *Manners* and *Ogino*.

Side-chain π-extensions

As has been shown in the previous chapters, synthesis methods for linear polythiophenes greatly evolved over the last decades, allowing the production of highly defined regioregular materials with superior electronic performance due to their high tendency for molecular order and crystallization in thin films. However, due to their linear nature, large scale order typically introduces a preferred orientation of chains in films of these polymers, leading to anisotropy of the electronic performance with better charge transport in chain direction.[167] In search for high-performance thiophene-based materials with isotropic conduction properties, many groups, including ours, have focused on the development of oligomeric and polymeric two- and threedimensional branched systems. These approaches range from exactly defined dendrimers built up in highly complex multistep reaction/purification procedures to more practically applicable polymerizations incorporating branched monomers into molecularly disperse systems (Figure 1.22).

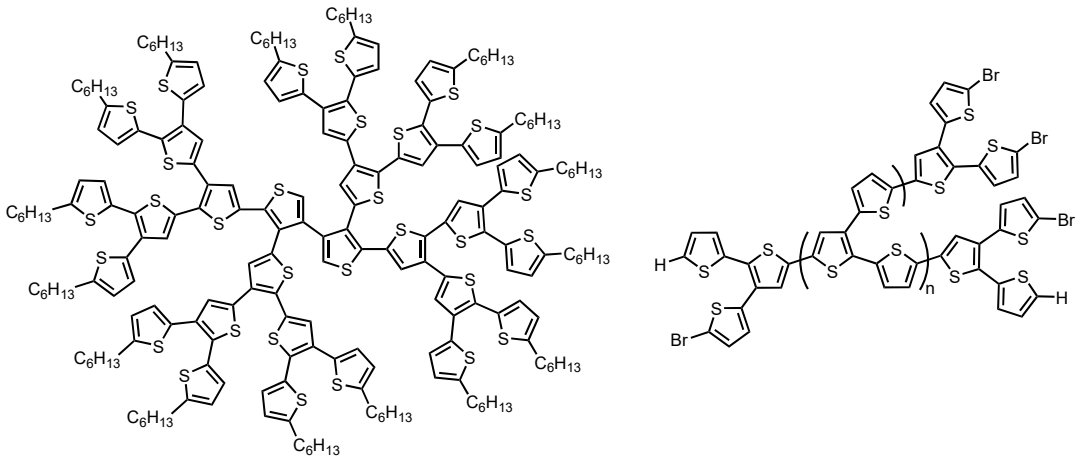

Figure 1.22: Examples of a dendrimer (**30T**) consisting of branched 2,2':3',2"-terthiophene (**3T**) units, synthesized through a multistep reaction/purification procedure by *Advincula et al.* and a molecularly disperse hyperbranched dendrimer (**P(3TBr3)**), synthesized through a Ni-catalyzed *Kumada* polymerization by our group.[168, 169]

Electrochemical, oxidative chemical and metal-catalyzed synthesis procedures were applied for these polymerizations.[169–171] An extensive literature overview on branched systems can be found in a recent review article from our group.[90] Several trends which hold true for the majority of these approaches can be identified: Compared to their linear analogues, branched polymers often possess low molecular weights and the production of systems

with higher molecular weights is challenging even using cross-coupling methods. Branched systems show lowered tendency to aggregate in solution and to crystallize in thin films, caused by the steric hindrance associated with the branching points. This is beneficial for solubility and handling and often allows to omit side chains, but also usually leads to inferior electronic properties. Furthermore, twisting between aromatic units at the branching points occurs, leading to imperfect conjugation along the branches. Lastly, the extension of the linear π-systems by sp^2 side groups influences the position of the HOMO and LUMO energy levels, in most cases lowering both, thus allowing for bandgap engineering and leading to materials with higher stability against oxidation and thus potentially improved durability under atmospheric conditions.

In order to combine the advantages of branched (oxidation stability, band gap engineering) and linear materials (high molecular weights, planarization, stacking), several groups have investigated so-called "side-chain π-extended" linear polythiophenes. In these systems, branched monomers are incorporated in which all connection points but the two necessary for linear polymerization are blocked, often by alkyl chains. This leads to linear materials which bear either aromatic groups or vinylene extensions in conjugation to the backbone π-system. In the following, a non-exhaustive overview on the important developments in this field will be given. An extensive review article by *Jeng et al.*, focusing on the applications on π-extended polythiophenes in organic photovoltaics, is recommended for further reading.[172]

Although originally synthesized to demonstrate the versatility of their newly developed β-bromination / cross coupling postpolymerization approach, a library of phenyl- and thiophene-extended polythiophenes by *Holdcroft et al.* represent early examples of such materials (see also Scheme 1.4, **Ph-PHT** to **2-Th-PHT**).[109] Red-shifts of the absorption and emission spectra, along with suppressed π-π stacking, compared to the parent **P3HT**, were found in most cases. *Li et al.* as well as *Jeng et al.* investigated the effects of vinylene spacers between the backbone and several types of aromatic pendants, including donor-type phenyl (**PT-vinPh**), thiophene (**PT-vinTh**) and carbazole (**PT(tCz)$_m$(DBT)$_n$**), as well as acceptor-type benzothiazole moieties (**PT-vinPhThz**).[173, 174] Broadening and increases in intensity of the absorption spectra were found to varying degrees for the materials with donor-type pendants. The phenylene-vinylene moieties led to the appearance of a second absorption band in the UV region in addition to the backbone main band which was slightly red-shifted compared to **P3HT**. This additional band was also found for the thienylene-vinylene derivatives, where it was shifted to above 400 nm, strongly overlapping with the main band and thus broadening the overall visible absorption. HOMO levels dropped slightly by about 0.2 eV, compared to **P3HT** (-5.1 eV).

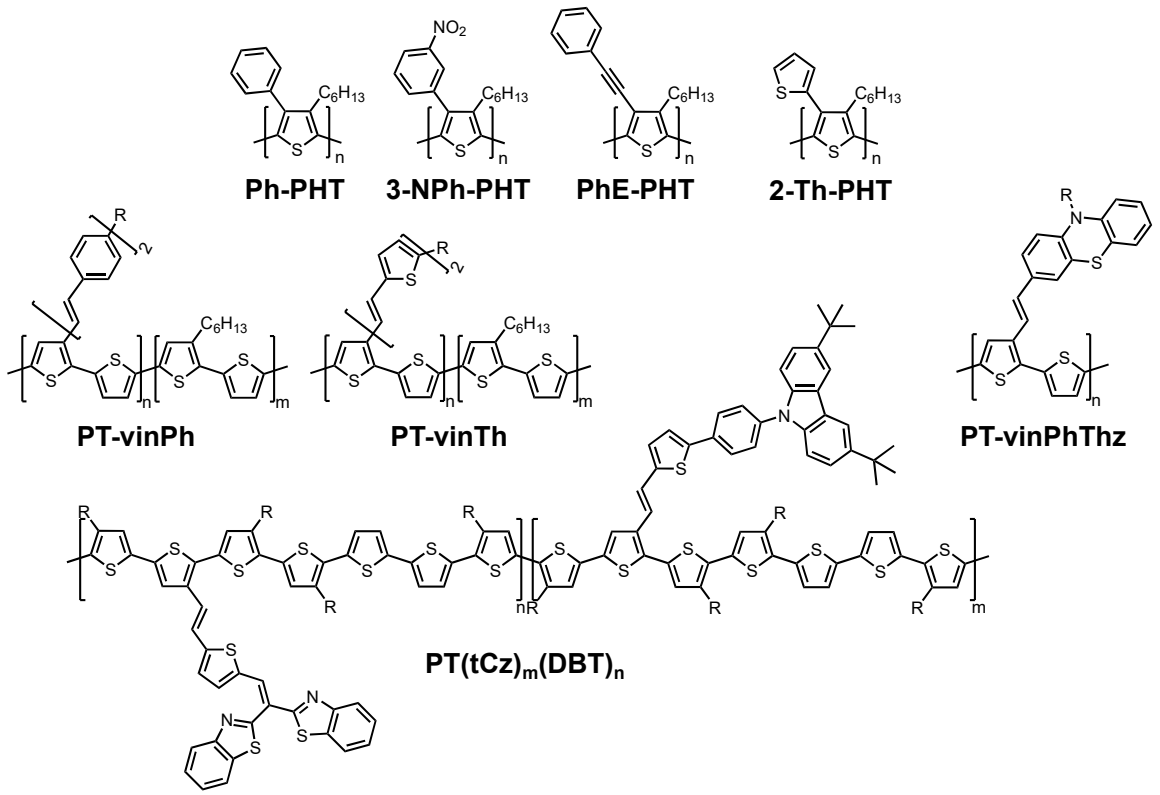

Figure 1.23: Examples of side-chain π-extended polythiophenes developed by the groups of *Holdcroft*, *Li* and *Jeng*.[109, 173, 174]

Efficiencies in OPV devices reached up to 3.18% and hole mobilities of $6.8 \cdot 10^{-3}\,cm^2V^{-1}s^{-1}$ were measured, indicating decent performance of these materials in organic transistor devices as well. From the polythiophenes with vinylene-linked carbazole moieties to the acceptor-type benzothiazole derivatives, HOMO levels were tunable from -5.39 to -5.26 eV while LUMO values shifted from -3.13 to -3.32 eV, leading to a narrowing of the bandgap from 2.26 to 1.94 eV. *Wang et al.* studied structurally related **PT**s bearing terthiophene pendant groups linked by a vinylene spacer unit, with the side-chain oligothiophene arranged either parallel or perpendicular to the backbone.[175] Their properties resembled the materials by *Li et al.*, exhibiting a broadened two-band absorption which was much more red-shifted in case of the perpendicular pendant group. However, the perpendicular orientation led to lower HOMO levels (-5.25 eV), a slightly broader band gap and better packing in thin films.

Chen et al. studied biaxially extended two-dimensional polythiophenes (**PT-Th$_m$**, Figure 1.24).[176] Here, side-chain (oligo)thiophene moieties were directly coupled to the main backbone without a conjugated spacer unit, with the branches on neighbouring repeating units facing away from each other. To prevent excessive steric hindrance, non-functionalized

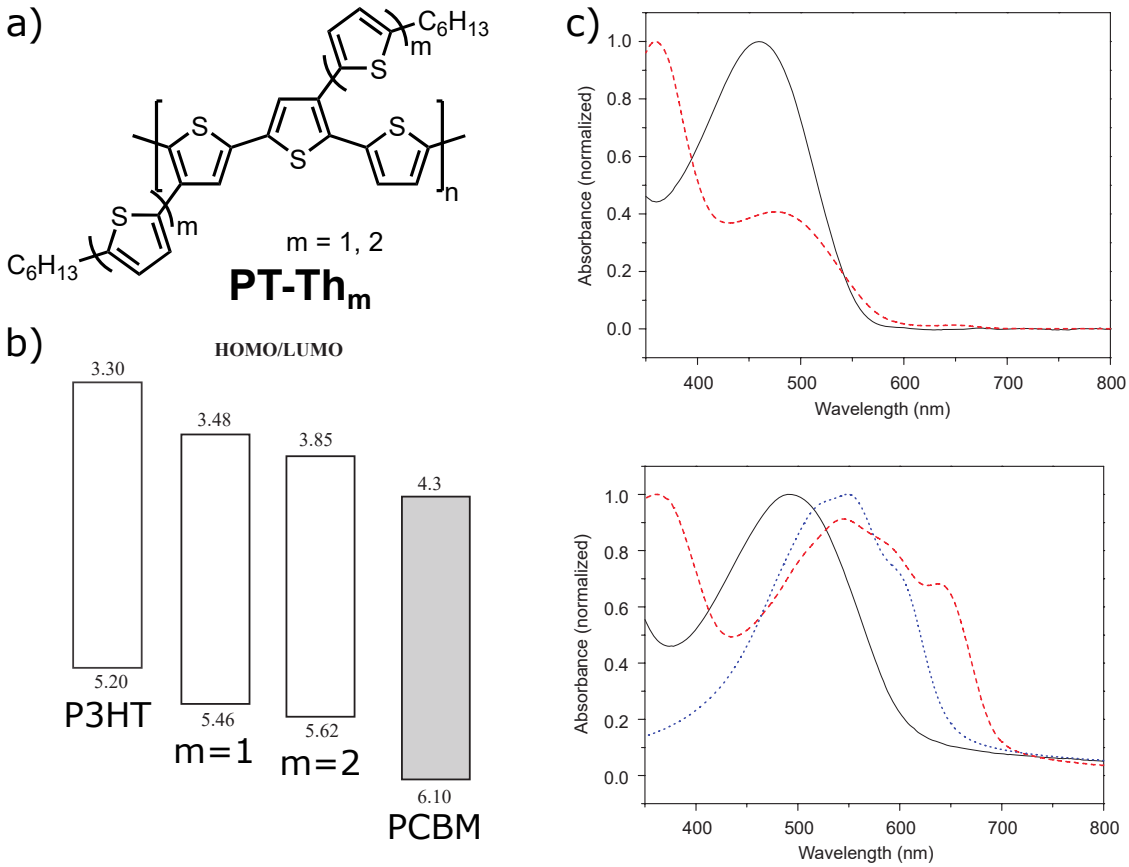

Figure 1.24: a) Structure of biaxially extended two-dimensional polythiophenes **PT-Th$_m$** synthesized by *Chen et al.*[176] b) Energy level diagram comparing the frontier orbital energies of these materials with **P3HT** and the acceptor phenyl-C61-butyric acid methyl ester **PC$_{61}$BM** used for the investigated organic solar cells. c) Solution (top) and thin film (bottom) absorption spectra of **P3HT** (blue) and biaxially extended polymers **PT-Th$_m$** with m=1 (black) and m=2 (red). Adapted with permission from [176], © 2009, Elsevier B.V.

thiophene spacers were incorporated into the backbone. Low HOMO levels between -5.19 and -5.51 eV along with narrow band gaps of around 2.55 eV were determined electrochemically if the side chains consisted of only one alkylthiophene unit.[177] Shorter thiophene spacers along the backbone led to a higher degree of twisting and thus to lower HOMO values due to shortening of the effective conjugation lengths. Hole mobilities reached up to $1.54 \cdot 10^{-2}$ cm^{2}V^{-1}s^{-1} and PCEs in solar cells up to 2.44%. Qualitatively similar values (HOMO = -5.62 eV, $\mu = 4.6 \cdot 10^{-3}$ cm^{2}V^{-1}s^{-1}, PCE = 1.3%) were found when the side chains were elongated to two thiophenes.[176] The introduction of thiophene-thiophene branching points within the side chains led to lower HOMO values (-5.33 eV), band gaps in the range of 2.6 eV and inferior electronic properties ($\mu = 4.5 \cdot 10^{-5}$ cm^{2}V^{-1}s^{-1}, PCE = 1.3-2.8%),

again due to steric hindrance inducing twisting, which could be partly alleviated by longer non-functionalized spacer units.[178] When vinylene spacers were introduced into the backbone π-system after every second thiophene, OPV and OFET performances increased significantly to $\mu = 0.12\,cm^2V^{-1}s^{-1}$, PCE = 4.0% for simple alkylthiophene side-chains and $\mu = 1.79{\cdot}10^{-3}\,cm^2V^{-1}s^{-1}$, PCE = 2.7% for the branched pendants.[179] Concerning the OPV performance of these biaxially extended polythiophenes it has to be noted that although the same solvent (*o*DCB) was used in all cases to deposit the blend, the donor/acceptor ratio varied from 1/1 to 1/3, which might have an influence on the measured PCE values.

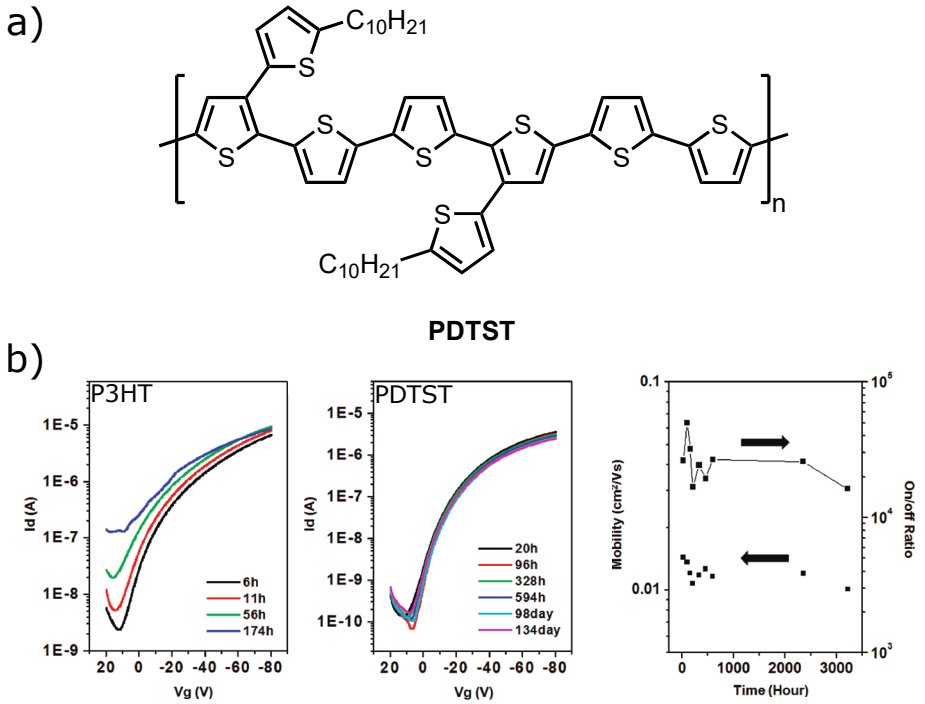

Figure 1.25: a) Structure of π-extended sexithiophene-based polymer **PDTST**, developed by *Park et al.*[180] b) Comparison of transistor transfer characteristics of **P3HT** and **PDTST** under ambient conditions as a function of time, highlighting the superior air stability of the polymer which can be ascribed to the lowered HOMO level at -5.21 eV. Adapted with permission from [180], © 2010, American Chemical Society.

Side-chain π-extended quater- and sexithiophene-based polymers (**PDTST**), in which the side chains faced towards each other were investigated by *Park et al.* (Figure 1.25). In agreement with the trends observed by *Chen et al.*, steric twisting lowers the HOMO levels to -5.21 eV and -5,27 eV with narrow band gaps of 1.65 and 1.75 eV, allowing OFET device performance to remain stable over >90 days of exposure to atmospheric conditions, retaining field effect mobilities of up to $0.05\,cm^2V^{-1}s^{-1}$ on substrates bearing

octadecyltrichlorosilane (**ODTS**) self-assembled monolayers.[180] PCE values of up to 3.2% were measured for the best materials of this class in conjunction with **$PC_{71}BM$** as acceptor.[181]

Building on earlier work by *Yamashita et al.*, who synthesized polymers with related structures by uncontrolled oxidative polymerization, our group investigated several derivatives of side-chain π-extended polythiophenes bearing alkylthiophene groups on every second thiophene repeating unit.[5, 7, 182] Due to their high regioregularity, which was achieved through Ni-catalyzed cross coupling polymerizations, these materials showed a very high tendency for π-stacking along with the lowered frontier orbital levels. The molecular and optoelectronic properties of this class of materials will be shown in the following.

With the goal of combining the advantages of hyberbranched polythiophenes based on the 2,2':3',2"-terthiophene (**3T**) unit as a core structural motif, as well as linear polythiophenes like **P3HT**, *Dr. Thomas Richter* from our group performed early work on such materials, which were termed **P3TC6** and **P3TC16**.[4, 5] The number denotes the length of the linear alkyl side chain blocking the α-positions of the side-chain thiophene units. **P3TC6** could only be obtained in a soluble form by $FeCl_3$-mediated oxidative polymerization and even for this product, a comparably low molecular weight of 5.9 kg/mol with a PDI of 1.8 was found. *Soxhlet* extraction and preparative size exclusion chromatography were necessary for removal of oligomeric species from the bimodally distributed crude polymer. Attempts to synthesize the polymer by a transition metal catalyzed polymerization were unsuccessful due to precipitation of insoluble material. This already highlights the high importance of alkyl chain length optimization for linear **P3AT**s in general, but especially if side-chain π-extensions are involved. In contrast, the **P3TC16** derivative could be obtained both by oxidative and cross coupling polymerization. A GRIM approach was not possible, since the required dibrominated monomer could not be obtained in pure form. Instead, the free α-position of a monobrominated monomer was deprotonated using LDA and a *Negishi*-type zinc-organic intermediate was produced by reaction with $ZnCl_2$. The polymerization reaction could be induced by addition of $Ni(dppp)Cl_2$, yielding polymers with molecular weights ranging from 5.4 to 31.6 kg/mol ($\overline{M_n}$) and PDI values generally in the range of 2.0 to 2.4, which were fully soluble in CB, *o*DCB and TCB, and partly soluble upon heating in THF and $CHCl_3$. No signs of a pseudo-living polymerization mechanism were found, which was partly attributed to the high viscosities of the solutions during polymerization.

P3TC16 showed temperature-dependent optical absorption properties in solution and thin films typical for highly aggregating linear **P3AT**s, with increases in temperature causing breakup of aggregates due to thermal energy overpowering the rotational barriers between

thiophene units. HOMO and LUMO levels were determined at -5.6 and -3.1 eV by cyclic voltammetry, significantly lower than the ones typically found for **P3HT** (approximately -5.1 and -2.8 eV, respectively), promising increased stability of these side-chain π-extended derivatives.

Motivated by the high tendency of the materials for π-π interactions and the favorable frontier orbital levels, the polymer was subsequently tested in organic field effect transistors and solar cells. High charge carrier mobilities up to $1.5 \cdot 10^{-2}\,cm^2V^{-1}s^{-1}$ could be reached under optimized conditions, with the initial values of as-cast polymer films in the range of $4.5 \cdot 10^{-4}\,cm^2V^{-1}s^{-1}$. In OSCs in conjunction with the fullerene acceptor **$PC_{60}BM$** (**P3TC16:$PC_{60}BM$** = 1:1 w/w, spin coated from 20 mg/mL *o*DCB solution), the polymer reached high open circuit voltages (V_{OC}) of up to 715 mV, but only moderate efficiencies of $\eta = 1.54\%$. Recently, *Sini*, *Schubert* and *Neher* compared the performance of **P3TC16** with several other polythiophene derivatives as donor materials in all polymer solar cells with naphthalene and perylene bisimide acceptors and found improved photocurrents and external quantum efficiency (EQE) values compared to the respective cells with **P3HT** as the donor material.[183]

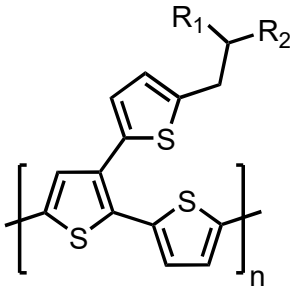

	R_1=	R_2=
P3TC6	H	C_4H_9
P3TC16	H	$C_{14}H_{29}$
P3TC12C8	C_8H_{17}	$C_{10}H_{21}$
P3TC10C6	C_6H_{13}	C_8H_{17}
P3TC8C4	C_4H_9	C_6H_{13}

Figure 1.26: Structures of side-chain π-extended polythiophenes studied in earlier work in our group.[5, 7]

An extensive study on the effect of different lengths of branched alkyl side chains on similar systems was conducted by *Dr. Martin Scheuble* in the following years during his PhD thesis, motivated by the favorable effect of branched instead of linear alkyl chains which had been shown for other conjugated polymer systems.[6, 7, 184] The polymers were termed **P3TCxCy** with x denoting the length of the longest linear segment of the respective side chain and y the length of the branch which was always attached in the 2-position of the alkyl chains. Three separate polymers, **P3TC12C8**, **P3TC10C6** and **P3TC8C4** were produced by combination of a specifically developed convergent approach for monomer

synthesis, followed by a *Negishi*-type polymerization analogous to **P3TC16**. All three polymers showed molecular weights between 16.7 and 19.5 kg/mol ($\overline{M_n}$), PDI values below 2.0 and high degrees of regioregularity, as determined by NMR spectroscopy. Frontier orbital levels were very comparable to **P3TC16**, with HOMO and LUMO values of -5.6 and -3.0 eV for all three derivatives, corresponding to an electrochemical band gap of 2.6 eV, showing that the length and type of alkyl side chain has no significant effects in this regard (Figure 1.27 a). The thermal properties of the polymers in bulk, solutions as well as thin films were investigated by a combination of differential scanning calorimetry, wide angle X-ray scattering and optical absorption as well as *Raman* measurements. Decreases in side chain length led to increases of temperatures for melting transitions, with values ranging from 182 to 210 °C for the longest and shortest chains, respectively (Figure 1.27 b). Aggregation in solutions was found to be severely influenced by side chain length, with **P3TC8C4** showing significant fine structure in UV/Vis spectra at room temperature in *o*DCB solution while only a small shoulder at ~583 nm was barely visible for **P3TC12C8** (Figure 1.27 c). For all three derivatives, any spectral evidence of aggregation phenomena fully vanished upon heating of the solutions to 80 °C. Thin film spectra of all polymers at rt were very similar, with only subtle differences upon heating up to 240 °C. Powder XRD experiments revealed intermolecular distances of 22-25 Å in direction of the alkyl chains, increasing with their respective lengths, and ~4.6 Å in π-π stacking direction (Figure 1.27 d). Upon heating, these distances widened and around the melting temperatures, loss of order, primarily in the direction of the alkyl chains, was detected.

Morphological investigations on as-cast and solvent-vapor annealed films by means of POM, AFM and TEM measurements showed that it was possible to induce long-range order by slow, controlled crystallization of the polymers. However, these effects were more prominent for the longer side-chain derivatives, due to the better solubility of these materials. TEM measurements revealed intermolecular distances comparable to the ones found in bulk powder, and a "face-on" morphology, in which the backbones are lying flat parallel to the substrate surface, was postulated based on the observed contrast between amorphous and crystalline regions.

The significantly lower field effect mobilities, compared to **P3TC16**, observed in bottom-gate/bottom-contact transistor measurements were attributed to this preferred morphology. Charge transport in a polymer lying face-on in the channel requires charge hopping in direction of the alkyl chains, which is less favorable compared to the π-π stacking direction.[67] Mobilities however clearly increased with decreasing lengths of side chains and values up to $1.2 \cdot 10^{-5}$ $cm^2V^{-1}s^{-1}$ could be reached under optimized conditions for **P3TC8C4**,

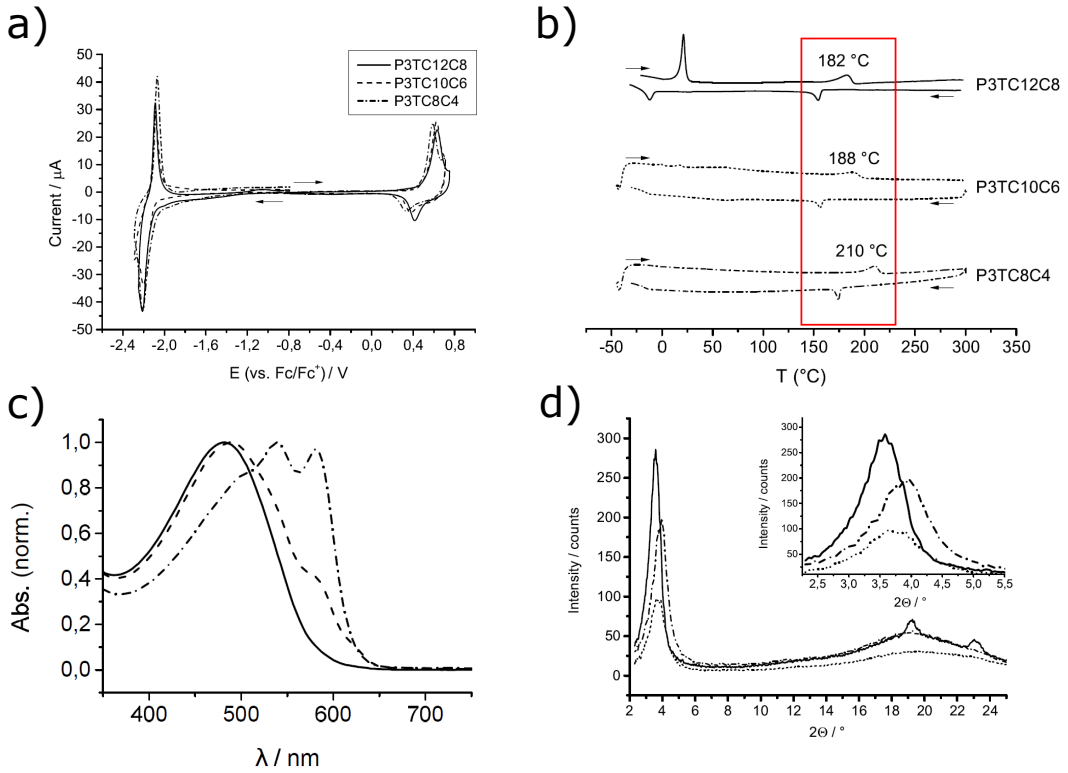

Figure 1.27: Comparison of electrochemical, thermal and crystallographic properties of **P3TCxCy** derivatives from earlier work by *Dr. Martin Scheuble*: a) Cyclic voltammetry measurements, b) melting transitions in DSC measurements, c) optical absorption of 3 mg/mL *o*DCB solutions at 25 °C, d) WAXS diffractograms at room temperature.[6, 7] Adapted with permission from [7], © 2015, American Chemical Society.

while **P3TC12C8** and **P3TC10C6** only showed $1.5 \cdot 10^{-7}$ $cm^2V^{-1}s^{-1}$ and $1.7 \cdot 10^{-6}$ $cm^2V^{-1}s^{-1}$ under similar conditions (annealed for 1 h at 120 °C after deposition).

In chapter 4, the **P3TCxCy** family of materials will be extended to a derivative with the shortest side-chain to date, termed **P3TC6C2** and its aggregation-related and optoelectronic properties will be compared to the existing analogues.

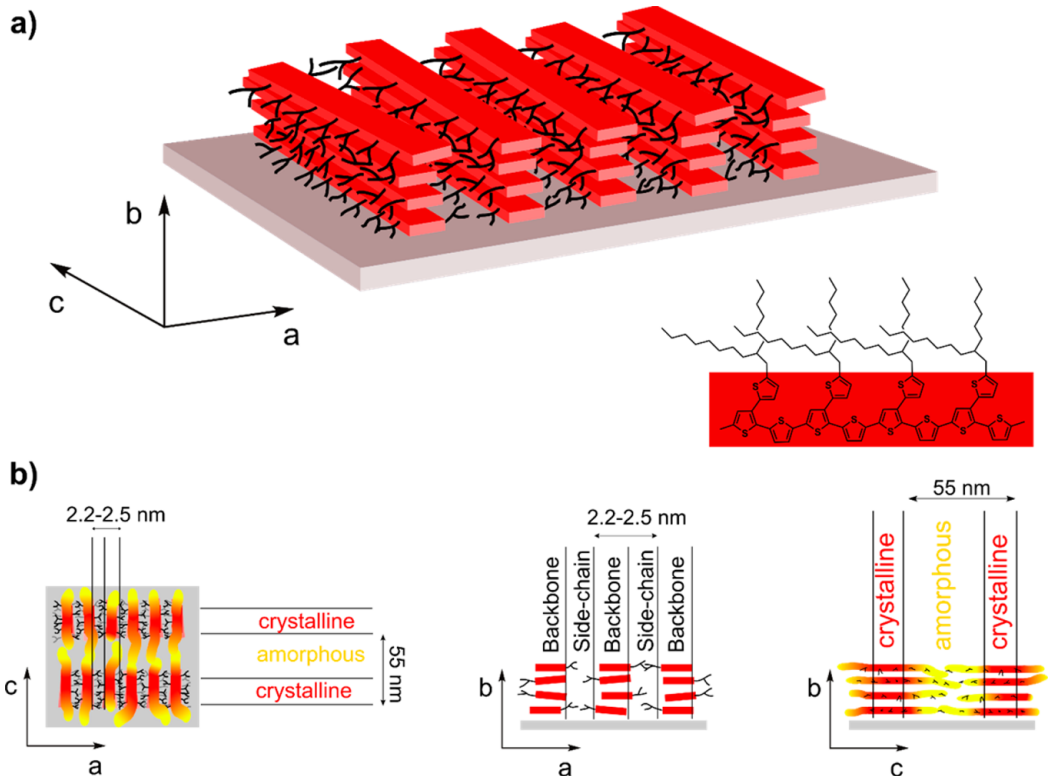

Figure 1.28: a) Schematic representation of the postulated "face-on" morphology found in **P3TCxCy** thin films. b) Views from the differenct crystallographic directions with the respective interchain distances. Crystalline regions are depicted in red, amorphous regions in yellow.[7] Adapted with permission from [7], © 2015, American Chemical Society.

Ionic Functionalities

Conjugated polyelectrolytes (CPEs) are a class of hybrid materials, which combine the individual properties of conjugated polymer backbones and ionic polyelectrolyte-like pendant groups.[8, 185] Early synthetic developments in this field were mainly motivated by the expected solubility of such materials in more environmentally benign, "green chemistry" solvents like water or alcohols, compared to pure conjugated polymers which can in many cases only be fully dissolved in chlorinated solvents. However, it was quickly found that the unique properties of CPE materials opened a wide range of possible applications, from layer-by-layer deposition processes over ion and biomolecule sensing to interlayers and active layers in optoelectronic devices.[186–190] Initially, conjugated polyelectrolytes were synthesized either by oxidative chemical polymerization or electropolymerization of monomers already bearing the ionic pendant groups, leading to a low degree of control over the molecular and electronic properties of the polymers.[191, 192] With the development

of highly controlled transition metal catalyzed polymerization methods like GRIM, it is now possible to produce highly regioregular CPEs with high molecular weights and low polydispersities, as well as exactly controlled contents of ionic pendant groups. In the following, a short overview on the most important aspects of the field will be given and the reader is referred to conclusive review articles for deeper insights.[8, 185, 193]

The first combination of a conjugated backbone and charged pendant groups can be traced back to 1987, when *Wudl* and *Heeger* prepared polythiophene films bearing sodium sulfonate moieties *via* electropolymerization.[194] Conductivities of the undoped films ranged from 10^{-7} (dry) to 10^{-2} S/cm (ambient conditions), and upon doping with bromine vapor, values up to ~10 S/cm could be reached.[195] *Wudl et al.* also introduced the concept of "self-doping" related to these materials, which describes the stabilization of positive charges on the polymer backbone by the sulfonate anions. Chemical or electrochemical p-type doping of such polymers leads to expulsion of the cationic counterion (in this case Na^+) from the thin films, a process which was also termed "cation popping".[196] Soon after these initial discoveries, the free sulfonic acid forms of these polymers were found to exhibit backbone oxidation, even in the absence of external dopants and without any electrochemical charging. These phenomena quickly became known as "auto-doping" or "self-acid-doping" and have since been proven for a number of acid-bearing CPEs.[191, 193]

As chemical polymerization protocols evolved, precursor methods were developed in which suitably functionalized, nonionic conjugated polymers were first synthesized and purified.[8] In a following step, polymer analogous reactions were used to convert these functionalities into ionic pendant groups. These methods possess the advantage that the precursor polymers, due to their predictable solubility behavior, can be much more easily characterized in terms of properties like regioregularity, molecular weights and polydispersities, allowing for much better control of these parameters in the final CPE materials. In recent years, combination of such approaches with modern synthesis methods for conjugated polymers have led to highly complex materials. Prime examples are the amphiphilic all-conjugated rod-rod block copolymers developed by *Scherf et al.*, consisting of a hydrophobic polyfluorene block and a hydrophilic polythiophene-based CPE block.[197]

The early developments induced a high level of interest in the field and in quick succession, large numbers of different combinations of conjugated backbone types and ionic pendant groups were introduced and characterized.[185] Sulfonate moieties were applied to materials based on **PEDOT**, **PPP** or **PPV** backbones, to name just a few.[198–200] Further often encountered anionic moieties include carboxylates or phosphonates.[201, 202] Quaternization reactions, which are well known *e.g.* from synthesis protocols for ionic liquids, also allowed to attach a multitude of cationic substituents, of which ammonium, pyridinium and

imidazolium moieties are most investigated.[203, 204] Most relevant for this dissertation is the imidazolium-substituted material **PMHT-Br** (termed **PTIm-Br** by us in chapter 5.1), which was first synthesized by *Vohlídal et al.* (Figure 1.29).[10]

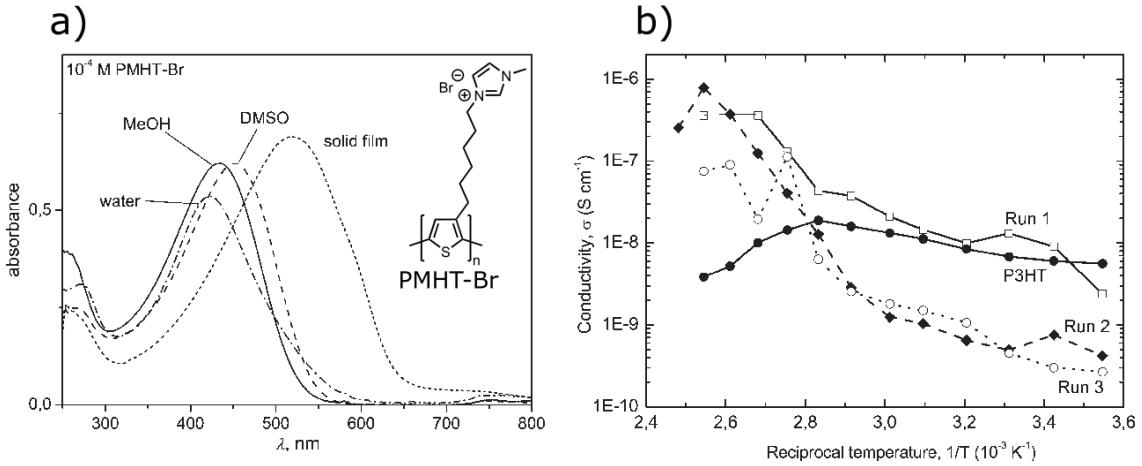

Figure 1.29: a) Optical absorption spectra of **PMHT-Br** in different solvents and as thin film. b) Temperature-dependent conductivity of **PMHT-Br** compared to the reference material **P3HT**. Adapted with permission from [10], © 2010, Wiley Periodicals, Inc.

The group studied in this first report mainly the molecular and optical properties of the materials in solution and thin films. Additionally, electrical conductivities in the undoped state were measured, with the materials reaching maximum values in the order of 10^{-10} to 10^{-6} S/cm. The same group later employed the polymer for the formation of hybrid materials with silver nanoparticles.[205] *Maes et al.* studied the solution and thin film behavior as well as the thermal properties of similar systems upon "diluting" the concentration of ionic groups on the polymer backbone by copolymerisation with 3-hexylthiophene monomers.[206]

In bulk or thin films conjugated polyelectrolytes exhibit mixed conductivity behavior, incorporating both electronic charge transport, which is mainly governed by the conjugated backbones, as well as ion movement through pathways incorporating the ionic pendant groups.[207] This makes CPE materials promising candidates for applications as interlayers in optoelectronic devices like organic light emitting diodes (OLEDs) or solar cells (OSCs, see Figure 1.30 a).[190] For example, *Bazan et al.* reached power conversion efficiencies up to $\eta = 6.5\%$ in OSCs incorporating interlayers based on ammonium-substituted polythiophene homopolymers and block copolymers.[208] More recently, *Bazan* and *Heeger* demonstrated that values up to $\eta = 8.2\%$ were possible with a hole-transport layer (HTL)

consisting of a narrow-bandgap sulfonate-based CPE, slightly higher than for similar cells employing the reference material **PEDOT/PSS** (7.9%) as the HTL.[209]
The possibility for ion movement within the layers allows counterions to redistribute upon creation of electric fields and thus helps to avoid the generation of trapped charges within the materials. Additionally, since the charged pendant groups in many cases enable dissolution in "green" solvents like methanol or water, which are orthogonal to those typically used for conjugated polymers, multilayer deposition involving CPEs is highly facilitated. Improvements in contact resistances between films and metal electrodes have been reported as well.[190] Recently, conjugated polyelectrolytes have also been considered as active layers in organic field effect transistors. This at first seems counter-intuitive since transistors operate based on the generation of stable electric fields in the channel and redistribution of these fields through ion movement would be highly detrimental. However, for some CPE materials, these limitations are less severe, since under typical OFET on-state conditions, no considerable ion movement is observed. A good example are the regioregular tetrabutylammonium sulfonate-substituted polythiophenes (**PTHS**) introduced by the *Thelakkat* group, for which charge carrier mobilities up to $1.2 \cdot 10^{-2}\,cm^2V^{-1}s^{-1}$ were found in diode geometry.[9] The ionic moieties enabled film preparation from aqueous solutions and seemed to have a rather low impact on the device performance, compared to the parent **P3HT**. The same material (termed **PTS-TBA** by us) will be studied for its electronic conductivity upon chemical doping in chapter 5.1. In some specialized transistor applications, like organic electrochemical transistors (OECTs) however, the oxidation state of the polymeric semiconductor film is changed electrochemically and thus movement of counterions between the thin films and the electrolyte solution is enforced. Here, CPE materials possess large advantages compared to the usually very hydrophobic unfunctionalized conjugated polymers since they are effectively facilitating these transport phenomena (Figure 1.30 b). While often blends of conjugated polymers and polyelectrolyte counterions like **PEDOT/PSS** are used for such applications, CPE materials have emerged in recent years as viable alternatives.[79, 211] The material **PTHS** was also employed in accumulation mode OECTs in collaboration with the *Malliaras* group.[210]
Due to their amphiphilic nature, CPEs exhibit very interesting properties in solutions in many solvents, especially in polar ones like DMSO, DMF, alcohols or water. In general, the optical spectra of free chains resemble the ones of the parent conjugated polymer backbones. In addition, in most solvents a complex interplay between the attractive π-π stacking interactions of the conjugated backbones and the "shielding" ionic pendant groups can be observed.[212] However, the situation is more difficult, since the formation

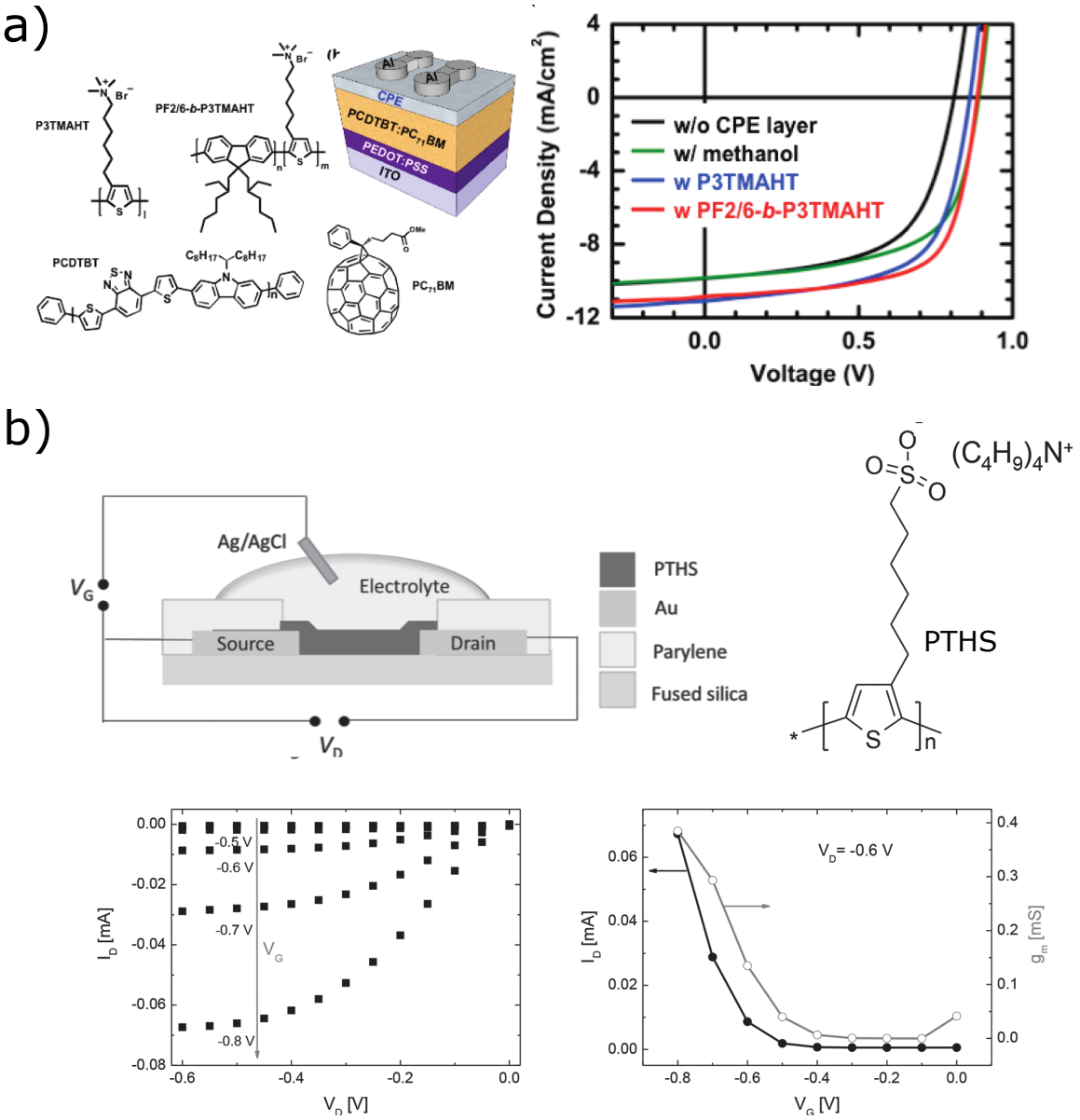

Figure 1.30: a) Organic photovoltaic device by *Bazan et al.*, incorporating interlayers consisting of conjugated polyelectrolytes **P3TMAHT** or **PF2/6-*b*-P3TMAHT**.[208] Corresponding I/V curves in comparison to the reference device without interlayer. Adapted with permission from [208], © 2011, American Chemical Society. b) Accumulation mode OECT with sulfonate-functionalized polythiophene **PTHS** as the active layer, developed by *Malliaras et al.*[210] Corresponding output and transfer curves including the transconductance g_m as function of the gate field. Adapted with permission from [210], © 2014, Wiley-VCH Verlag GmbH & Co. KGaA.

of aggregates specifically caused by the interaction of ions has also been shown in some cases.[213, 214] Studies of solution optical absorption and emission properties in the presence of surfactants have proven very useful to elucidate these complex interactions.[215–218] The choice of counterion often has a strong influence on aggregation behavior in solution and thin film structures, as well as on the electronic properties of films.[219, 220]

Redox Functionalities

Besides conjugated polymers, a second class of semiconducting polymers exists: redox polymers.[221, 222] Redox polymers are macromolecules with a fully isolating backbone which feature electroactive sites capable of accepting and donating electrons. Each of these sites can be individually charged and discharged, often leading to very high obtainable doping levels, fast and stable redox switching at defined potentials and highly localized charges. Applications of this class of compounds are thus mainly found in the fields of organic battery materials, sensor devices and electrocatalysis.[222–224] Redox polymers are typically synthesized by polymerizing redox-active monomers. The electroactive units can be either integrated directly into the polymer backbone or as pendant groups, the latter variant being typically synthesized *via* polymerization methods like (controlled) radical polymerization of vinyl monomers.[225, 226] Popular examples include polymers containing stable free nitroxide radicals like 2,2,6,6-tetramethylpiperidinyloxyl (**TEMPO**), organosulfur compounds which utilize disulfide formation, carbonyls (especially quinone derivatives), triarylamines and carbazoles as well as metal complexes with cyclopentadienyl, porphyrin and bipyridine ligands, so-called metallopolymers (Figure 1.31).[227–230]

Because redox polymers contain individual electroactive groups separated by insulating molecular structures, charge transport typically takes place *via* a hopping mechanism.[231] In many instances, *in-situ* conductance measurements revealed profiles indicative of a behavior similar to mixed-valence salts, in which conductivity is lowest when all redox units are either neutral or fully charged and highest when exactly half of the units contain a charge.[232, 233] Obviously, the presence of charge carriers is a prerequisite for conductivity. However, at very high doping levels, movement of carriers is impeded by electrostatic repulsion since there are no or only very few neutral sites to which a carrier can hop. Thus, conductivity is highest when there is a free position for every charge in the system, *i.e.* when the numbers of neutral and charged redox units are equal. In view of this mechanism, most redox polymers show relatively poor conductivity in a narrow potential window which constitutes a major drawback for many applications, especially as electrode materials. Mixtures of the active polymer compounds with highly conducting

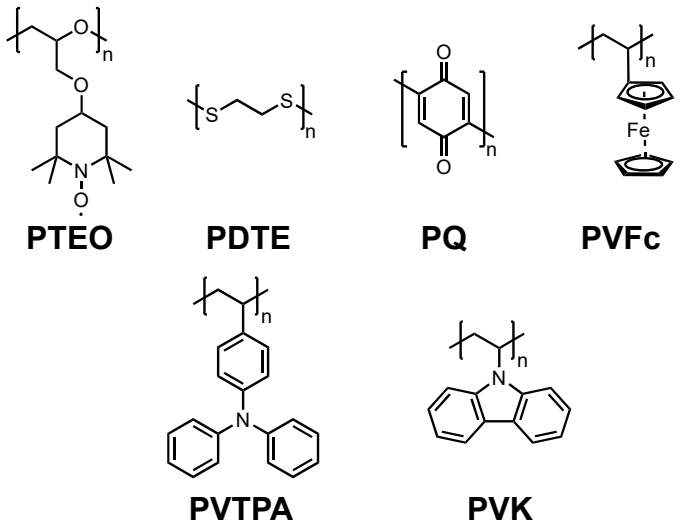

Figure 1.31: Illustrative examples of different classes of backbone and side-chain redox polymers: stable nitroxide radicals (**PTEO**), disulfide (**PDTE**) and quinone groups (**PQ**), metal complexes (*e.g.* ferrocene, **PVFc**), triphenylamines (**PVTPA**) and carbazoles (**PVK**) can be integrated as redox sites.[229, 230]

materials like carbon or metal additives, conjugated polymers and binder polymers are thus typically used. In practical battery applications, up to 80% of the electrode can consist of conductive additives.[228] This in turn lowers the amount of active material and therefore the specific capacity of the electrodes. Conjugated polymers in contrast exhibit high conductivities in broad potential windows, since charge transport along the chains can take place *via* delocalization (in the limits of the effective conjugation lengths). However, their obtainable (stable) doping levels are relatively low, since the average distances between individual charges on a backbone are ususally a few repeating units.[37] Higher doping levels can be enforced, but pose the risk of decreasing conductivity through the generation of bipolaron species and irreversible degradation of the materials through side reactions. This has been shown to manifest in self-discharge phenomena and poor cycling stability.[234] In addition, conjugated polymers are oxidized and reduced in broad potential ranges due to the superposition of redox processes of conjugated segments of different lengths. This makes their charging behavior less predictable, which constitutes a drawback for potential applications in energy storage devices.

The individual properties of conjugated polymers and redox polymers can be combined by the synthesis of so-called conjugated/conducting redox polymers (CRPs) in which redox-active pendant groups are attached to fully conjugated polymer backbones (Figure 1.32).[13, 236] Such an approach can be expected to lead to materials which combine high

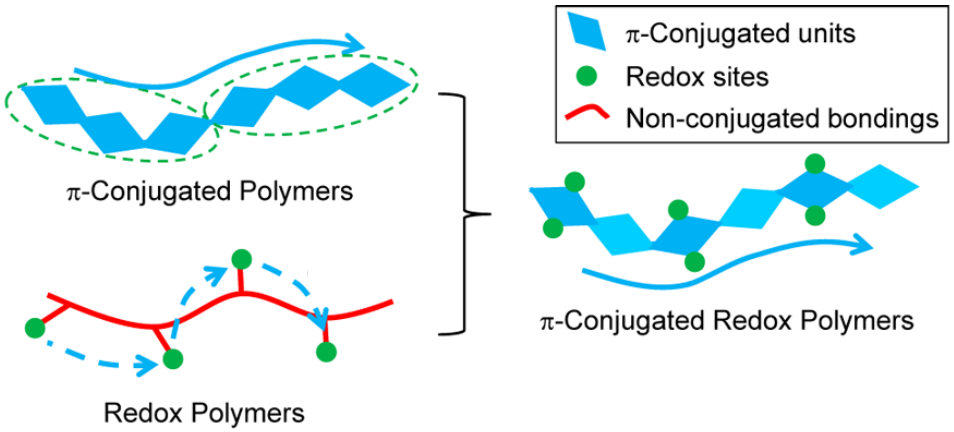

Figure 1.32: Sketch detailing the concept of conjugated redox polymers: combination of extended backbone π-systems with individual redox units is expected to lead to materials with good conductivity, high charge storage potential and stable redox chemistry.[235] Adapted with permission from [235], © 2015, American Chemical Society.

charge storage potential, stable and predictable redox switching and high conductivity in the doped state. In literature, especially the combination of p-type polymers with acceptor pendant groups like fullerene or naphthalene bisimide ("double-cable" polymers tested mainly for their performance in organic photovoltaics) and conjugated metallopolymers with pendant or backbone-integrated metal complexes are popular.[37, 124, 237–243] *Wolf et al.* attached **TEMPO** units to polythiophene backbones *via* CuAAC with the aim of developing materials (**P3HT-TEMPO**) for radical batteries with improved conductivity characteristics.[137] However, signs of backbone degradation due to radical side reactions were found. *Goodenough et al.* reported on **PPy** derivatives bearing ferrocene pendant groups (**PPy-Fc**) as electrode materials for lithium ion batteries.[244] The charge capacities compared to the pure conjugated polymer could be increased and the system showed a sharper switching potential at 3.5 V vs. Li^+/Li. Carbon black as a conductive additive as well as additional binder polymers were not necessary. *Sjödin et al.* combined a **PPy** backbone with hydroquinone pendant groups (**PPy-HQ**).[236] Block and graft copolymer approaches combining conjugated and redox polymer blocks have also been reported.[245, 246]

Additionally, conjugated (co)polymers in which redox processes are highly localized to specific sites along the backbone, *e.g.* by bad delocalization due to twisting, can be seen as conjugated redox polymers. A good example is the well-investigated n-type donor-acceptor copolymer **P(NDI2OD-T$_2$)**, which has been proposed as a battery material in addition to its wide-spread adoption as one of the reference n-type materials for organic photovoltaics

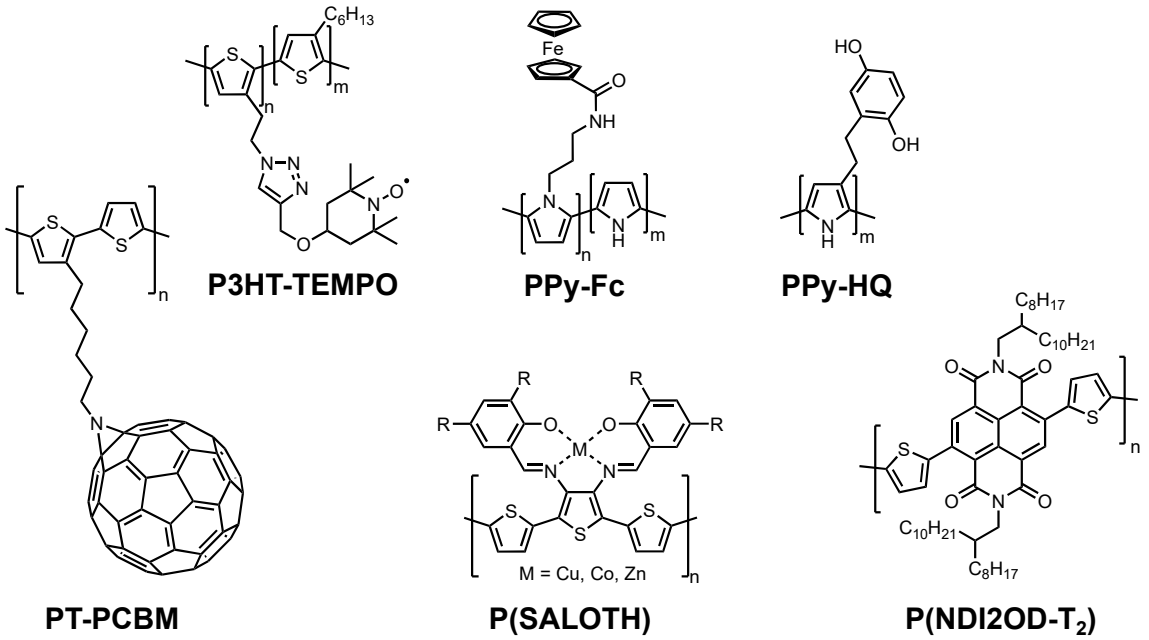

Figure 1.33: Structures of conjugated polymers bearing a variety of different redox moieties: fullerene acceptors (**PT-PCBM**), stable TEMPO radicals (**P3HT-TEMPO**), ferrocene (**PPy-Fc**) and salen metal complexes (**P(SALOTH)**) and hydroquinones (**PPy-HQ**).[137, 236, 238, 244, 247] Structure of the n-type donor-acceptor copolymer **P(NDI2OD-T$_2$)** which features highly localized redox processes due to twisting between the naphthalene bisimide and thiophene units.[235, 248]

and transistor devices.[235, 248] For the CRP concept to work ideally, the oxidation and reduction potentials of the redox groups should lie within the conducting potential window of the backbone, in which it is typically (moderately) p- or n-doped, a concept called redox matching.[236] This not only allows for efficient charge transport to and from the redox units, but has also been shown to lead to higher conductivity, since the redox units can take part in charge transport. This is best illustrated by a study of *Swager et al.*, in which a thiophene-functionalized and an **EDOT**-functionalized **Co(salen)** complex were polymerized, forming backbone-integrated conjugated metallopolymers (Scheme 1.34).[247] For **Th/Co(salen)**, two distinct waves corresponding to the oxidation of the **Co(salen)** complex and the thiophene backbone were found. Conductivity in these systems was correlated to the onset of oligothiophene oxidation and was below 40 S/cm. In **EDOT/Co(salen)** however, redox matching occured between the metal complex and the **EDOT** backbone, which led to overlapping oxidation waves and significantly higher conductivities up to 250 S/cm (Scheme 1.34 b). The contribution of the metal complex to the overall conductivity was proven by the addition of pyridine-based ligands which

reacted with the system and shifted the cobalt redox couple to lower potentials, thus neutralizing the redox matching. In cyclic voltammograms, this led to distinct waves and conductivity values were significantly lower, reaching only about 80 S/cm.

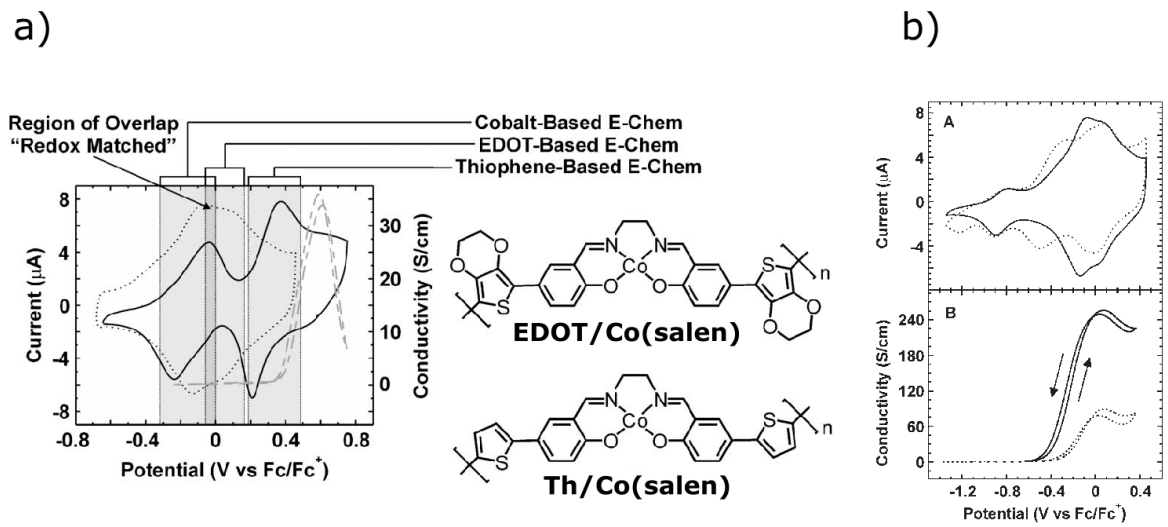

Figure 1.34: a) Cyclic voltammograms of **Th/Co(salen)** (solid line) and **EDOT/Co(salen)** (dotted line). Low conductivity of non-redox-matched system **Th/Co(salen)** (dashed line).[247] b) Cyclic voltammograms and conductivity measurements of **EDOT/Co(salen)** before (solid) and after (dotted) addition of pyridine ligands, lowering potentials of the metal complex redox couple. Adapted with permission from [247], © 2005, The Royal Society of Chemistry.

Depending on the location of the electroactive centers relative to the backbone π-system (as pendant groups or part of the main chain), inner-sphere and outer-sphere mechanisms of this conductivity contribution can be distinguished, as has been shown by *Swager et al.* for conjugated metallopolymers (Figure 1.35).[247] In inner-sphere redox matched systems, orbital overlap between the redox units and the conjugated segments of the backbone allows for shuttling of charges between metal complexes through the π-system. For outer-sphere systems, the redox sites may only contribute to the conductivity through hopping events of charges between each other and to the backbone π-system, for the latter of which redox matching is a prerequisite.

Apart from independent redox switching and taking part in charge transport processes, some redox pendants are able to provide the redox polymer or conjugated redox polymer they are attached to with additional functionality. A good example is the class of triarylamines and carbazoles which are well known to readily dimerize to their respective dimers upon electrochemical or chemical oxidation. If such units are fixed to a polymeric

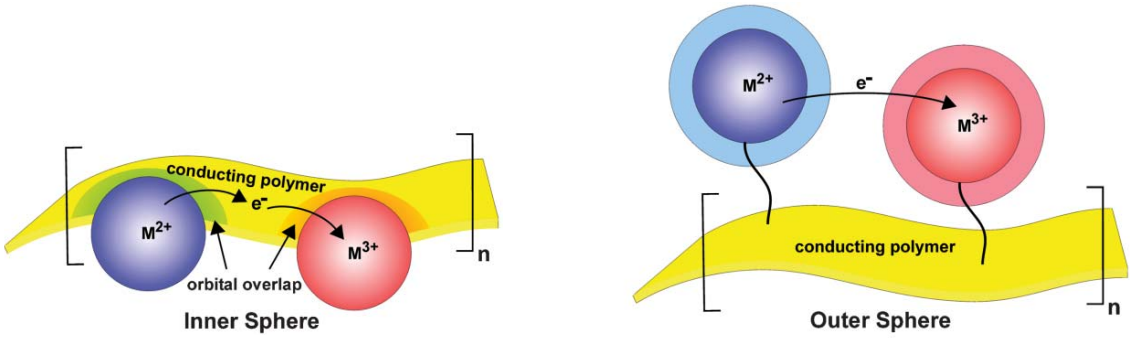

Figure 1.35: Inner and outer sphere mechanisms of conductivity contribution in redox matched conjugated metallopolymers.[247] Adapted with permission from [247], © 2005, The Royal Society of Chemistry.

backbone, these reactions cause crosslinking, stabilizing the material against dissolution. Most notably, the dimers still show stable and reliable redox switching behavior. Our group recently investigated the coupling mechanism and the potential-dependent conductance behavior of several triphenylamine (**TPA**) systems in detail.[233, 249] The underlying mechanisms are essentially identical to the inital steps of electropolymerization (see Scheme 1.9 and Figure 1.36).[37] In the first cycle of a cyclic voltammetry experiment, oxidation of the **TPA** units to their radical cations ($\mathbf{TPA^{+\bullet}}$) occurs which then readily dimerize to tetraphenylbenzidine (**TPB**) under elimination of two protons. The **TPB** unit is immediately reoxidized over the radical cation $\mathbf{TPB^{+\bullet}}$ to the dication $\mathbf{TPB^{2+}}$ which is then discharged in the backward scan. In the 2nd and all further cycles **TPB** is then only charged and discharged in a two-electron process. *In-situ* conductance measurements clearly showed a mixed-valence conductance behavior with two distinct maxima of conductance corresponding to half-filled states of $\mathbf{TPB^{+\bullet}}$ and $\mathbf{TPB^{2+}}$, respectively.

This type of coupling chemistry can also be used to build up hyperbranched architectures from multifunctional monomers or to couple polymer chains to (particle) surfaces in heterogeneous reactions.[250–255] Electrochemical and chemical oxidation of the respective aromatic monomers is possible.[171, 256, 257]

The fact that the electroactive crosslinks can be individually charged and discharged reliably in predictable, narrow potential windows makes such materials promising candidates for all-polymer energy storage devices. In combination with a doped conjugated polymer backbone, conducting additives which diminish the electrode capacities could be potentially reduced or fully avoided. Redox polymers based on triphenylamine and carbazole as active components are already established as state of the art polymer battery materials.[229, 230] Fully crosslinked polytriphenylamine (**PTPA**) could be oxidized up

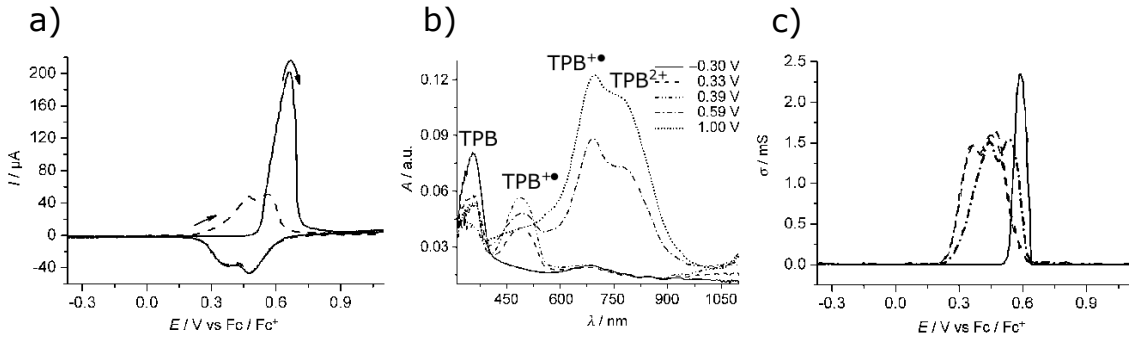

Figure 1.36: a) 1st (solid) and 2nd (dashed) cycles of a cyclic voltammogram of a triphenylamine redox polymer.[233] b) Solution UV/Vis spectra recorded *in situ* during the 2nd cycle (dimerized **TPB** state). c) Conductance profiles of thin films for the 1st (solid) and 2nd (dashed) forward and backward scans. Adapted with permission from [233], © 2010, Wiley-VCH Verlag GmbH & Co. KGaA.

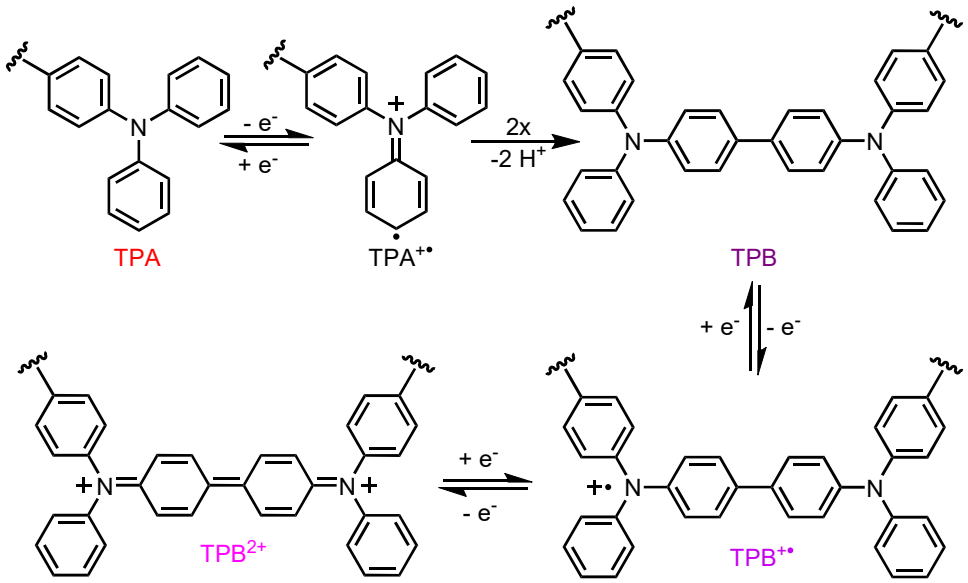

Scheme 1.9: Mechanism of the coupling reaction of two triphenylamine (**TPA**) units to tetraphenylbenzidine (**TPB**) and subsequent two-electron charging process to $\mathbf{TPB^{2+}}$.

to a doping level of 95% by *Yang et al.*, leading to a high charge storage capacity of 103 mAh/g.[258] After 1000 cycles at a rate of 20 C, still 90 mAh/g were measured. *Wang et al.* employed electrospun **PTPA** fibers in organic pseudo-capacitors.[259] *Zhang et al.* were able to reach up to 129 mAh/g with a structurally related derivative (**PDDP**), optimized for weight-specific capacity.[260] Poly(vinyl carbazole) (**PVK**) was used by *Song et al.* in conjunction with **PEDOT/PSS** as a replacement for carbon-based conducting additives and as the binder polymer, allowing essentially the construction of an all-polymer energy

storage device.[261] In chapter 5.3 of this thesis, crosslinkable, highly conducting conjugated redox polymers based on the combination of **TPA** units attached to a polythiophene backbone will be presented.

Functionalities Towards Sensor Applications

A chemical sensor is often defined as a composite device capable of eliciting a response which quantifies or at least qualitatively indicates the presence of an analyte.[262] Such a system is usually built up of at least three components: a) a receptor unit which shows affinity to the given type of analyte, preferably with high selectivity, b) a component which transduces reception events into some kind of measurable response and c) an applicable form of signal readout. Conjugated polymers are predestined materials for such applications, since they are organic compounds, thus, they can be functionalized with almost any type of receptor unit imaginable, given a suitable synthesis procedure. As explained earlier, CP backbones combine several optical (absorption and fluorescence) and electronic properties (redox behavior, conductivity), changes of which can be used as signals.[262]

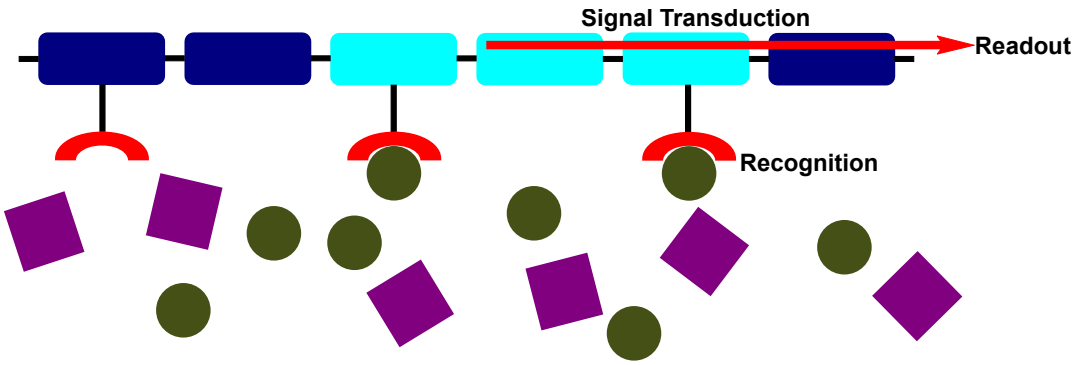

Figure 1.37: Working principle of a chemical sensor based on conjugated polymers: Pendant recognition groups allow specific recognition of an analyte, which produces a signal, often through changes in the optical or electronic properties of the backbone. This signal can be read out by a suitable spectroscopic or electrochemical method.

Often, already very small changes in the chemical environment of such systems induce a measurable response. This is a consequence of the inherent signal amplification and transduction pathways of CPs which are related to their polymeric nature. Since typically not only one but many individual repeating units bearing multiple receptor moieties are involved in analyte detection and most signal responses are tied to changes in effective conjugation lengths, the changes in the chemical environment of the backbone induced

through all recognition events add up. Concerning the electronic properties of CPs, already the introduction of a small amount of charges into the π-system causes large jumps in conductivity, often over several orders of magnitude, and also these properties can be significantly influenced by changes in backbone conformation or film structure upon analyte reception. Signal readout in CP-based sensors is usually based on established methods, like optical spectroscopy, electrochemical experiments, or measurements of conductivity values or transistor characteristics.

Among the first sensor materials based on conjugated polymer backbones were crown-ether-modified polythiophenes, which allowed the detection of alkali ions in several different solvents.[262] Depending on the type of crown ether, it was even possible to discriminate between the different alkali ions based on size. One of the most elegant approaches is the one presented by *Marsella* and *Swager* in 1993, in which the crown ethers were arranged in such a way along a bithiophene repeating unit of the backbone that ion complexation led to significant backbone twisting (see Figure 1.38). The degree of twisting was highly dependent on the size of the ion.[263] The signal was read out as a shift of the corresponding λ_{max} values of the polymer UV/Vis spectra in solution.

Building on these early results, a high number of metal-ion-sensitive sensor materials were produced, which usually relied on the selective complexation of the metal ions through suitable ligands which were attached as pendant groups or integrated into the backbone, or on the selective interaction of the complexes with free ions in the solution. The sensor response was in most cases recorded as changes in either the redox potentials or the conductivity of the materials. Such concepts were applied for example for cobalt, ruthenium or aluminium ions complexed by salen, bipyridyl or phthalocyanine ligands, to name just a few.[262, 264, 265]

Moving from metal-organic recognition to biochemical sensory problems imposes new challenges, mainly concerning the compatibility of the sensor materials with the conditions used to stabilize biomolecules (especially aqueous buffer solutions). As shown earlier, the inter- and intrachain interactions between conjugated polymer backbones usually have a profound effect on the optical properties of the materials, like light absorption and fluorescence. If these interactions are specifically and predictably influenced by the presence or absence of a biomolecule in the same solution, the resulting changes in optical properties, *e.g.* visible color changes or fluorescence quenching, can be potentially read out as sensor signals.[187–189] Water-soluble conjugated polyelectrolytes (CPEs) are predestined materials for such applications, since aqueous media like buffer solutions are prerequisites for many relevant analytes. In the most basic cases, concentrations of external small ion species, *i.e.* salts, can be detected through CPEs, as has been shown for example by

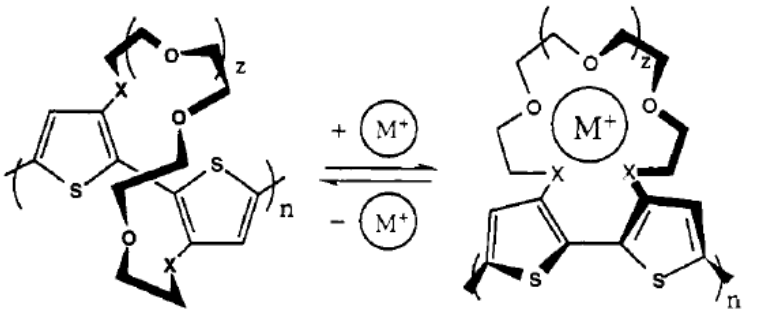

polymer	λ_{max} (nm)	$\Delta\lambda_{max}$ (nm)		
		K^+	Na^+	Li^+
6	497	22	91	46
7	510	10	63	15
8	524	45	30	13
11	434	–4	3	3
12	432	1	3	4

Figure 1.38: Working principle of an alkali ion sensor system based on crown-ether-modified polythiophenes. Complexation of an ion leads to twisting of the backbone to a certain degree, depending on the size of the complexed ion. The signal can be read out as a shift in λ_{max} values. Entries 6-12 correspond to materials with different crown ethers and different contents of crown-ether-substituted bithiophene repeating units on a single chain. Adapted with permission from [263], © 1993, American Chemical Society.

Bunz, *Schanze* or *Leclerc*, for Pb^{2+}, Cu^{2+} and I^- ions (Figure 1.39 a), respectively.[266–268] However, sensing possibilities can be extended much further to small biomolecules like adenosine triphosphate (**ATP**, Figure 1.39 b) or even macromolecules like **DNA** or proteins.[187, 269–272] For such complex analytes, it is often necessary to combine ionic functionalities which induce water solubility with specific recognition groups as pendants on the conjugated polymer backbones.[187]

If the electronic properties of the conjugated polymer thin films are used as a signal, biochemical sensor materials can be designed without the need for solubilizing groups. Two notable examples include purine and pyrimidine base sensors developed by *Bäuerle et al.*, which used changes in the redox behavior of the polythiophene as the signal, as well as an avidin sensor material synthesized by *Piro et al* (Figure 1.40).[75, 273] In their approach, the interaction between the attached biotin moieties and the free avidin in solution influenced the characteristics of an electrolyte-gated organic field effect transistor (EGOFET) with the material as the active layer.

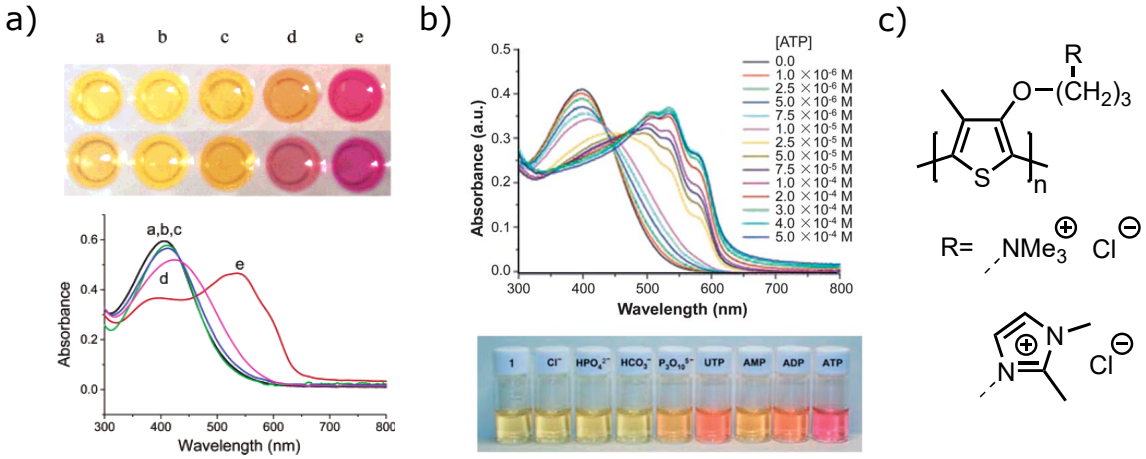

Figure 1.39: a) Iodide-specific visual sensing assay developed by *Leclerc et al.*, based on aqueous solutions of a 1,2-dimethylimidazolium chloride functionalized polythiophene.[268] a: Pure polymer solution, b to e: solutions containing equal concentrations of NaF, NaCl, NaBr and NaI. 2nd row: Solutions after ageing for four days. Corresponding solution absorption spectra. Adapted with permission from [268], © 2003, American Chemical Society. b) Trimethylammonium chloride functionalized derivative of the same backbone as a sensor for **ATP** and other small biomolecule phosphates (1: Pure polymer in water).[269] Adapted with permission from [269], © 2005, Wiley-VCH Verlag GmbH & Co. KGaA. c) Structures of the polymers used.

In chapter 5.4 of this dissertation, work on another polythiophene-based biochemical sensor system will be shown. As a model to test the applicability of such a system as the active layer in an EGOFET sensor, the interaction between the protein Concanavalin A (**Con A**) and α-D-mannose units fixed to the polythiophene backbone will be used. The fundamentals on this interaction and examples for its successful application in conjugated-polymer-based sensing devices will be shown in the following.

Con A is a lectin found in jack beans (*Canavalia ensiformis*).[274] Lectins are proteins which bind carbohydrate moieties with high selectivity. They play a crucial role in recognition events between individual cells and proteins or carbohydrates, or in the binding of viruses and bacteria. Many lectins found in nature are toxins, like ricin or *Shiga* toxin. It is believed that legume lectins like **Con A** are also a part of the defense system of certain plants against predators, however, in the amounts consumed in a typical diet they are not harmful to the human body. **Con A** was the first lectin which was commercially available in its pure form and it is thus used in a plethora of applications in biology and biochemistry today. One of its most important applications is lectin

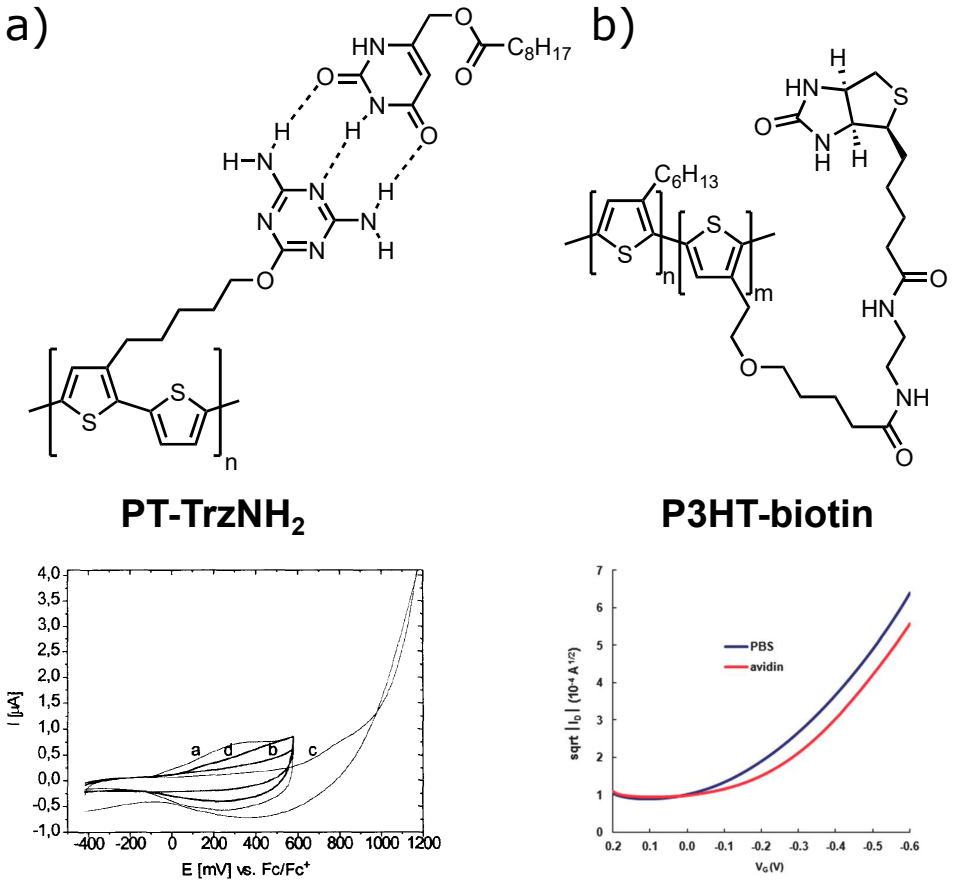

Figure 1.40: a) Structure of pyrimidine base sensor material **PT-TrzNH$_2$** developed by *Bäuerle et al.*. Cyclic voltammograms of electropolymerized **PT-TrzNH$_2$** films in monomer-free electrolyte (a), in electrolyte containing uracil (b), monomer-free electrolyte, scanning up to 1.2 V vs. Fc/Fc$^+$ to regenerate the sensor (c), scan in monomer-free electrolyte after regeneration (d).[273] Adapted with permission from [273], © 1999, Elsevier Science S.A. b) Avidin sensor material **P3HT-biotin**, synthesized by *Piro et al.* Changes in EGOFET characteristics between pure PBS buffer (blue) and PBS buffer containing free avidin (red).[75] Adapted with permission from [75], © 2013, The Royal Society of Chemistry.

affinity chromatography, in which it is bound to a stationary phase and used to purify glycoproteins or other glycosylated biomolecules.[275]

At neutral pH values, **Con A** is a predominantly tetrameric protein, a homotetramer in which all four subunits are identical, each having a molecular weight of 26.5 kDa.[276] Each of the four subunits is able to complex Mn^{2+} or Ca^{2+} ions which is essential for sugar binding. In the presence of these metal ions, **Con A** possesses high affinity and selectivity for terminal α-D-mannosyl and α-D-glucosyl moieties and each of the four subunits possesses one coordination site for a sugar derivative. This property makes it an

optimal model system for new sensor approaches alongside other high-affinity biochemical interactions like biotin-avidin binding.[277] Moreover, due to structural similarities of **Con A** and other more harmful lectins, sensitive and selective sensor materials are highly interesting candidates for the detection of neurotoxins of both natural (bacteria) and synthetic origin. Such sensors are of high importance in food industry, water quality monitoring, clinical diagnostics or bioweapons detection.[278]

For the design of potential sensor materials for **Con A** detection, polymer backbones are optimal scaffolds for the attachment of α-D-mannose groups, since such a "polydentate" glycopolymer ligand system is able to reach much higher binding affinities compared to monovalent sugar ligands.[279] This enhancement in binding affinities through oligomeric or polymeric structures, the "cluster glycoside effect", is utilized by nature for example in the presentation of large numbers of sugar moieties on cell surfaces in the form of glycans.[280, 281]

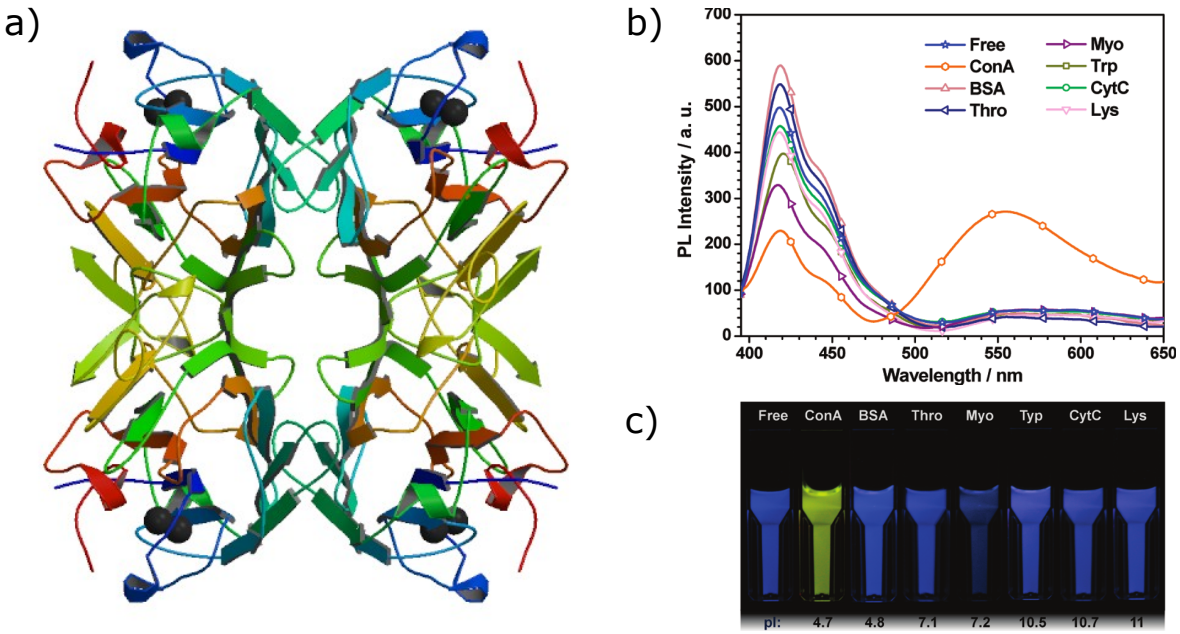

Figure 1.41: a) Crystallographic structure of Concanavalin A bearing Ca^{2+} ions (black spheres) in each of the four identical subunits. b), c) Specific optical detection of **Con A** through a two-component fluorescence assay based on α-D-mannose-functionalized conjugated polyelectrolytes developed by *Liu et al.*[14] Adapted with permission from [14], © 2010, American Chemical Society.

Conjugated polymer backbones extend the possibilities even further, since they not only present a passive scaffold holding the sugar moieties, but feature unique optical and electrochemical properties which can be used for signal transduction, amplification and

readout. When optical properties like absorption or fluorescence of conjugated polymers are used as the sensor signal, the corresponding materials have to be soluble in aqueous solutions at neutral pH. Especially conjugated polyelectrolytes (CPEs) and conjugated polymers bearing oligo(ethylene oxide) side chains have proven to be very useful for fluorescence quenching or *Förster* resonance energy transfer (FRET) approaches of **Con A** detection by the groups of *Bunz* and *Liu*, among others.[14, 282–284]

As an alternative, film properties of the functionalized conjugated polymers, composites with materials like carbon nanotubes or gold nanoparticles as well as directly surface-grafted sugar units can be used to read out the sensor signal.[285, 286] Besides standard electrochemical, impedimetric and transistor approaches an often-used method is the (electrochemical) quartz crystal microbalance (EQCM / QCM).[287] Here, mass changes of the polymer film upon binding of **Con A** are indirectly measured through a decrease in oscillation frequency of a quartz crystal, enabling very sensitive protein detection.[278] Recently, EQCM in conjunction with mannose-functionalized polythiophenes has been used to detect *E. coli* cells with high sensitivity (down to 50 cells per mL) by *Zeng et al.*[288] In this approach, bound **Con A** on the film surface improved the selectivity and sensitivity significantly, due to interaction with lipopolysaccharides (LPS) on the cell surface of the bacteria (Figure 1.42).

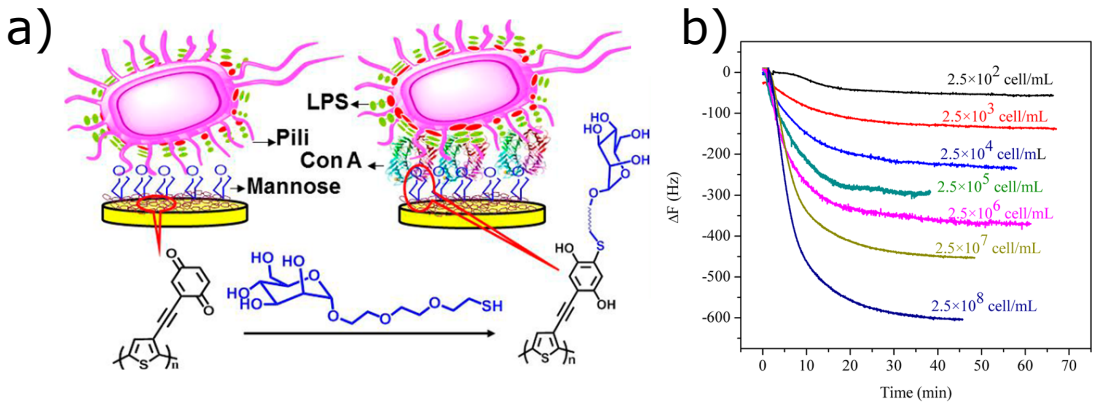

Figure 1.42: a) Electrochemical quartz crystal microbalance (EQCM) based sensor for *E. coli* bacteria developed by *Zeng et al.*[288] In the absence of **Con A**, cell binding is only possible through direct interaction of the bacterial pili with mannose units. **Con A** addition mediates a second orthogonal binding mechanism, interaction with the lipopolysaccharides (LPS) on the cell surface. b) Frequency response of the QCM for different concentrations of *E. coli* cells. Adapted with permission from [288], © 2015, American Chemical Society.

2 Objectives

The overarching concept of this work was the functionalization of linear polythiophene backbones to influence the structure formation or the optoelectronic properties and to develop complex functional materials with added benefits for specialized applications. Furthermore, the thermal and optical properties as well as the electronic properties of the materials upon electrochemical and chemical doping or in transistor devices (OFETs or EGOFETs) should be studied.

P3HT-*b*-PDMS Rod-Coil Block Copolymers

The influence of a coil-like poly(dimethylsiloxane) block on the film structure formation as well as the transistor performance of rod-like regioregular **P3HT** should be explored. Few examples of such materials have been developed in recent years and were mainly studied in solution self-assembly experiments as well as for their performance in organic photovoltaics.[3, 158, 164, 166] Blends of the two homopolymers have shown high hole mobilities in OFET devices recently, posing the question if superior results may be possible with chemically defined block copolymers.[162] The **PDMS** blocks can be expected to induce microphase separation in thin film and provide mechanical flexibility to the films, which might make such block copolymers possible materials for bendable transistors or even electromechanical devices like actuators.[2, 163] A **P3HT-*b*-PDMS** material should thus be synthesized and evaluated for its film structure formation and transistor performance.

Side-chain π-extended Polythiophenes

Utilizing a synthetic procedure developed in our group, an existing family of branched alkylthiophene-substituted polythiophenes (**P3TCxCy** derivatives) should be extended to shorter side chains (2-ethylhexyl) in the form of the polymer **P3TC6C2**.[4–7] The earlier **P3TCxCy** derivatives, ranging from **P3TC12C8** to **P3TC8C4**, had shown altered structure formation and favorable frontier orbital energies compared to simple **P3AT**s and better processability in comparison to similar π-extended materials with linear alkyl chains. Since electronic performance increased with decreasing side chain lengths, it was interesting to further test the limits of this approach concerning thermal properties, solubility, film properties and field effect mobilities in OFET devices and compare the material to the longer side-chain analogues.

Smart Materials through Alkyl Side-chain Modifications

Side-chain terminal modification allows to functionalize the polythiophene backbone with complex functionalities. Conjugated polyelectrolytes (CPEs) combine ionic and electronic conductivity mechanisms in single materials. In a joint project with *Dr. Rotraut Merkle* from *Max Planck Institute for Solid State Research*, Stuttgart, our group was interested in decoupling these mechanisms in regioregular polythiophene-based CPE materials. The cationic CPE **PTIm-Br** should be synthesized and compared with the anionic derivative **PTS-TBA** synthesized by *Dr. Roman Tkachov*. Subsequently, the aggregation-related optical properties in solutions and thin films, as well as the optical properties and conductivity values upon chemical doping of the two CPEs should be compared.

A copolymer platform which allows the versatile functionalization with adjustable densities of complex molecules through CuAAC should furthermore be developed. The applicability of this platform as a basis for smart materials with added functionality should subsequently be demonstrated. Two applications were chosen for this task: crosslinking of conjugated redox polymers (CRPs) and the development of sensor materials.

Crosslinking approaches for conjugated polymer films have been shown to allow the preservation of film structures upon ageing and even in contact with many solvents or electrolytes.[289–291] This is especially important for applications like energy storage devices, where polymer films are in contact with liquid electrolytes for many years. Building on earlier work of our group on triphenylamine (**TPA**) and carbazole redox polymers as well as **P3AT**s, the objective was to develop hybrid CRP materials which were designed to be crosslinkable by electrochemical or chemical oxidation and in the same process should be able to reach high conductivities through doping of both the polythiophene backbone and the crosslinks.[233, 249]

The versatile copolymer platform should be further utilized for developing regioregular polythiophenes bearing α-D-mannose units as pendant groups. In cooperation with the group of *Prof. Dr. Benoît Piro* at *Laboratoire ITODYS*, Paris, these materials should be tested as a model system for the applicability of the EGOFET geometry in a sensor device for the protein Concanavalin A (**Con A**).[75] This protein is well-investigated for its high affinity to α-D-mannose and has been detected with conjugated polymer sensor materials in fluorescence-based assays and EQCM-based sensor systems.[14, 282–284, 287] Before employing the materials in EGOFET devices, they should first be evaluated in standard bottom-gate/bottom-contact OFET geometry.

3 P3HT-*b*-PDMS Rod-Coil Block Copolymers

As discussed in the Introduction, studies on blends of **PT** and **PDMS** materials in organic electronics applications yielded promising results. Very few examples of a combination of these rod-type and coil-type polymeric materials in the form of block copolymers have been reported.[3, 158, 164, 166] Especially the influence of the flexible PDMS block concerning film formation and microphase separation has not been thoroughly investigated. Since block copolymers can be expected to exhibit formation of individual block domains on much smaller length scales than simple blends, they might be even more viable candidates for (flexible) devices in organic electronics. In the following, investigations on the film formation and charge carrier mobilites of a **P3HT-*b*-PDMS** block copolymer system will be presented.

3.1 Synthesis of Homopolymers and Block Copolymer

A copper(I) catalyzed alkyne-azide cycloaddition click chemistry (CuAAC) approach according to *Manners et al.*, in which the two end-functionalized homopolymers were linked post-polymerization was used for the synthesis of the **P3HT-*b*-PDMS** block copolymers (Scheme 3.1).[3, 165] CuAAC offers the advantage of often quantitative yields and can be performed under mild reaction conditions.[115] Additionally, the involved azide and alkyne end groups are reasonably stable under environmental conditions, compared to species typically involved as end groups in siloxane chemistry, like Si-Cl or Si-O^- groups.[158]

Initially, the published method was exactly followed, using an azidomethyl spacer (x = 1) on the **PDMS** chain end. However, this led to very unsatisfactory results of the click reaction, which will be further investigated in this chapter. When exchanging the methyl spacer by a butyl spacer (x = 4), block copolymer yields were greatly improved.

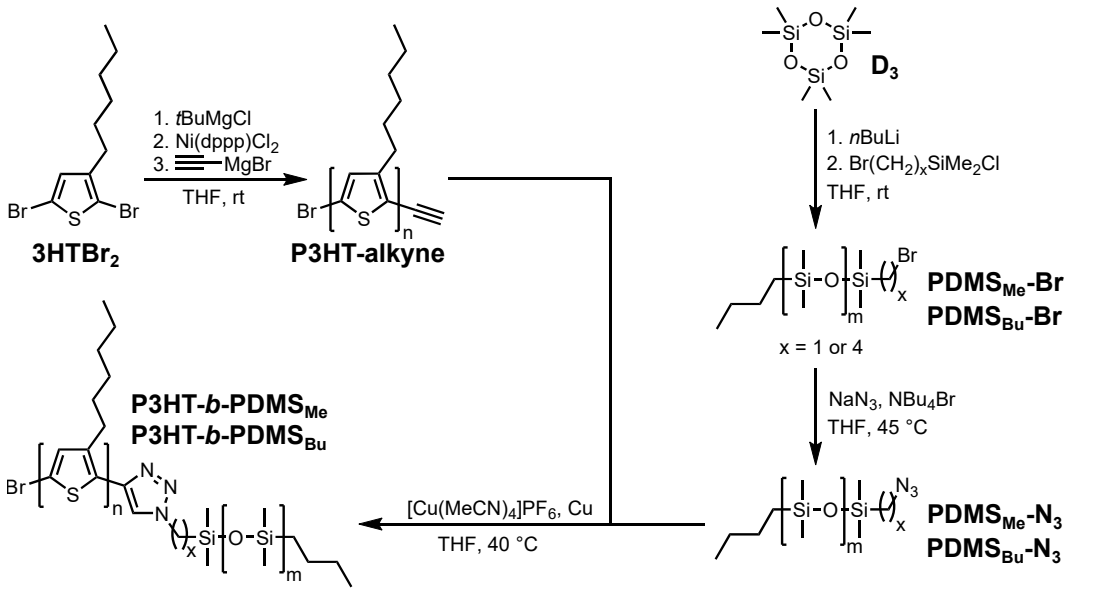

Scheme 3.1: Synthesis of end-functionalized **P3HT** and **PDMS** homopolymers and CuAAC approach to synthesize **P3HT-*b*-PDMS** copolymers.

3.1.1 Alkyne-functionalized Poly(3-hexylthiophene)

The alkyne functionalized polythiophene block was synthesized *via* GRIM polymerization in THF starting from the monomer 2,5-dibromo-3-hexylthiophene (**3HTBr$_2$**) followed by endcapping with the *Grignard* reagent ethynylmagnesium bromide. Two batches (**P3HT-alkyne-1** and **P3HT-alkyne-2**) with molecular weights ($\overline{M_n}$) of 8.0 and 7.5 kg/mol (SEC) and polydispersities of 1.1 and 1.3, respectively, were obtained (Table 3.1). MALDI-TOF measurements yielded lower molecular weights (Figure 3.5 c, black spectrum) with a maximum of the distribution around 4.6 kg/mol. SEC measurements calibrated against polystyrene standards are known to overestimate polythiophene molecular weights.[103] MALDI measurements additionally allowed to investigate the end groups present on the individual chains. The functionalization was found to be essentially quantitative, the main part of the chains bearing Br/alkyne end groups. However, negligible amounts of H/alkyne and a small fraction of alkyne/alkyne-terminated chains were also detected, which is in line with literature findings for this reaction.[132] Assuming quantitative functionalization (Br/alkyne) of **P3HT-alkyne-1**, the molecular weight average calculated from the integral ratio of the signals for thiophene β-protons (6.90 ppm) and alkyne-H (3.53 ppm) was 4595 g/mol, corresponding to 27 repeating units (Figure 3.1). For **P3HT-alkyne-2**, this method yields a degree of polymerization of 31 repeating units.

NMR spectroscopy also confirmed high regioregularity of the polythiophenes (>95%). IR spectroscopy additionally proved the successful functionalization with alkyne end

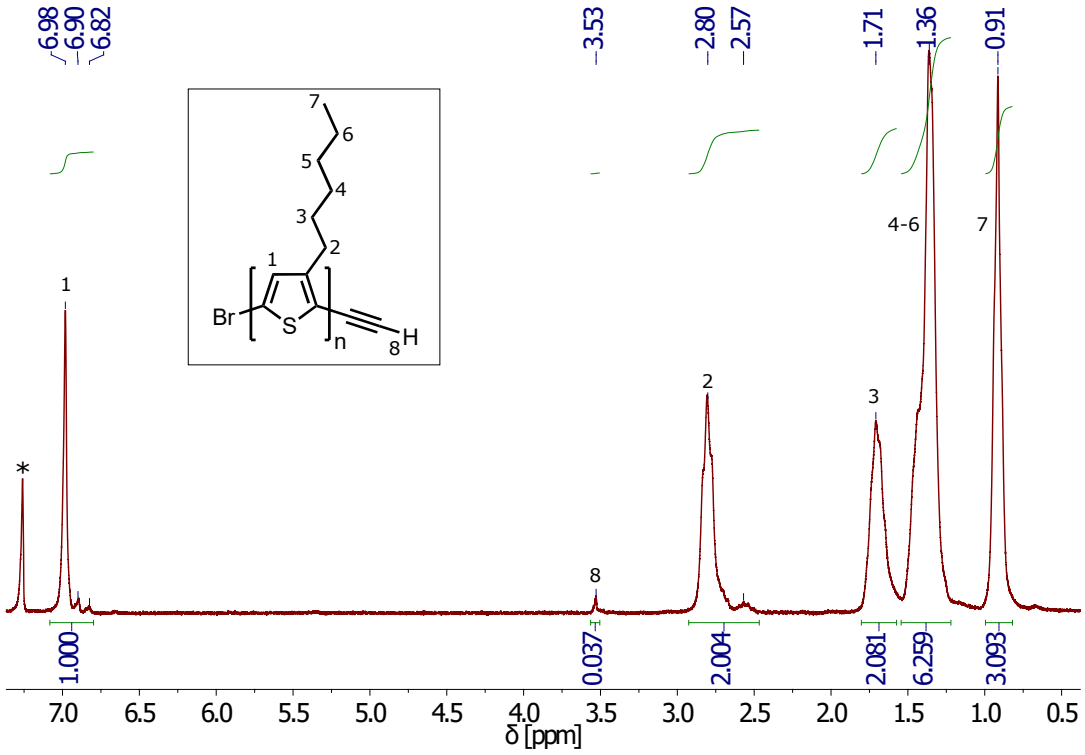

Figure 3.1: ^{1}H-NMR spectrum of purified **P3HT-alkyne-1** (room temperature, $CDCl_3$).

groups, with bands corresponding to the alkyne-H and triple bond at 3309 and 2094 cm^{-1}, respectively. In accordance with literature findings, the **P3HT-alkyne** batches showed slow dimerization under environmental conditions at room temperature, resulting in a small shoulder in the SEC measurements at doubled molecular weight (Figure 3.5 b). This can be ascribed to a *Glaser*-like coupling of the alkyne moieties which is probably enabled by the effect of the conjugation with the backbone π-system, since such a reaction is not found in terminal alkynes attached to alkyl spacers at room temperature.[130, 132] To suppress this unwanted side reaction as much as possible, both polymer batches were isolated by precipitation in cold methanol without attempting *Soxhlet* purification requiring elevated temperatures, collected by centrifugation and dried *in vacuo*. The products were stored at -24 °C. SEC measurements recorded after ten months showed that the batches did not dimerize further under these conditions (Figure 3.2).

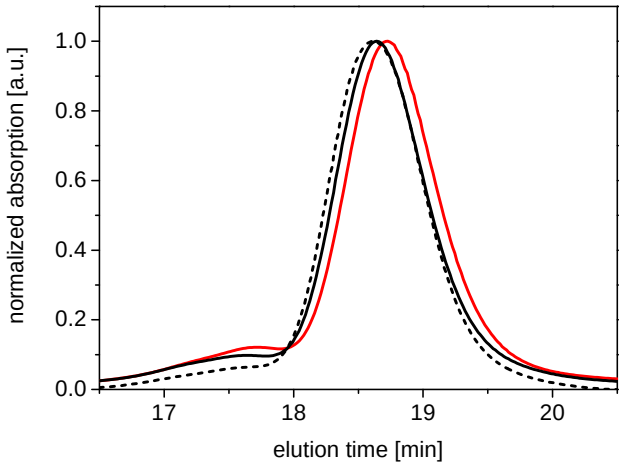

Figure 3.2: SEC chromatograms of **P3HT-alkyne-1** (black) directly after purification (solid line) and after 10 months of storage at -24 °C (dashed line), as well as **P3HT-alkyne-2** (red).

Table 3.1: Molecular properties of the **P3HT-alkyne** batches.

Polymer batch	$\overline{M}_n$[a)]	$\overline{M}_w$[a)]	PDI[a)]	$\overline{DP}_n$[b)]	Alkyne functionalization[c)]
P3HT-alkyne-1	8.0	9.0	1.1	27	>95%
P3HT-alkyne-2	7.5	9.5	1.3	31	>95%

a) Molecular weight averages (in kg/mol) and polydispersity indices were determined by SEC (THF solution, rt), calibrated against polystyrene standards. b) Degree of polymerization calculated from NMR integral ratios of thiophene β-H and alkyne-H signals, assuming quantitative endcapping. c) Percentage of successfully end-functionalized polymer chains, approximated from MALDI-TOF measurements.

3.1.2 Azide-functionalized Poly(dimethylsiloxane)

Initially, a **PDMS$_{Me}$-N$_3$** batch with a CH_2 spacer between the last Si atom and the azide group was synthesized, following the protocol of *Manners et al.*[3, 165] Anionic polymerization of the cyclic monomer hexamethylcyclotrisiloxane (**D$_3$**) in THF was initiated at room temperature with *n*BuLi. After depletion of the monomers, addition of (bromomethyl)chlorodimethylsilane terminated the reaction, introducing a halide end group. Successful, near-quantitative endcapping could be confirmed by comparison of the integral ratios of NMR signals corresponding to the CH_3 end of the butyl residue introduced through the initiator (0.88 ppm) and the CH_2 group next to the bromide (2.43 ppm). Molecular weights determined from NMR end group analysis (integral of

PDMS methyl protons at 0.07 ppm, referenced to terminal initiator protons at 0.88 ppm: ~11.6 kg/mol, corresponding to 156 repeating units) closely matched those found by polystyrene-calibrated SEC measurements ($\overline{M_n}$ = 12.5 kg/mol, PDI = 1.1). Halide-azide exchange was subsequently performed in THF at 45 °C, using tetrabutylammonium bromide as a phase transfer catalyst to improve the solubility of sodium azide. Successful reaction to azide end groups could again be followed by NMR spectroscopy (Figure 3.3), with the signal corresponding to the adjacent CH_2 group switching quantitatively from 2.43 to 2.74 ppm. In addition, azide IR bands at 2098 cm^{-1} were found.

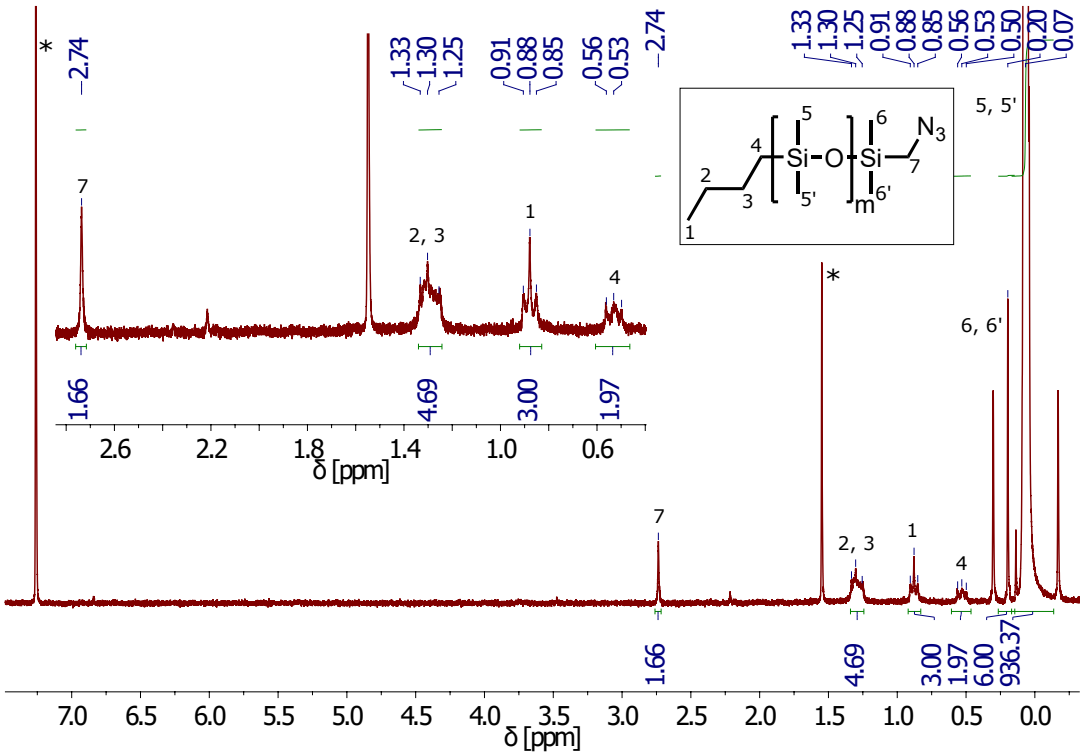

Figure 3.3: ^{1}H-NMR spectrum of purified **$PDMS_{Me}$-N_3** with methyl spacer (room temperature, $CDCl_3$).

Later, three batches of **$PDMS_{Bu}$-N_3** blocks bearing butyl spacers instead of a methyl spacer were synthesized by *Kai Mundsinger* during the course of his research internship. The corresponding capping reagent (4-bromobutyl)chlorodimethylsilane (**4-Br-BDMCS**) was not commercially available and was thus synthesized by a chloroplatinic acid catalyzed hydrosilylation reaction (Scheme 3.2). All three batches of **$PDMS_{Bu}$-N_3** showed comparable molecular weights (9.5 to 10.0 kg/mol, $\overline{M_n}$) and PDI values of 1.1 (Table 3.3).

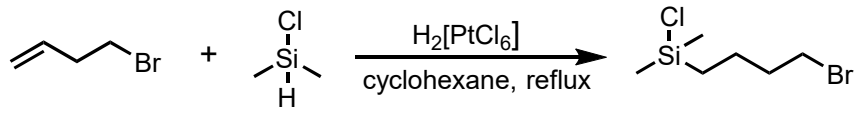

4-Br-Butene **DMCS** **4-Br-BDMCS**

Scheme 3.2: Synthesis of capping reagent (4-bromobutyl)chlorodimethylsilane (**4-Br-BDMCS**) by hydrosilylation.

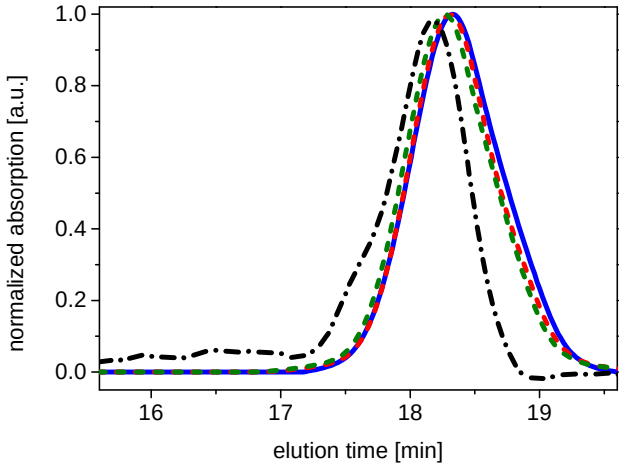

Figure 3.4: SEC chromatograms of $\mathbf{PDMS_{Me}\text{-}N_3}$ (black) and three $\mathbf{PDMS_{Bu}\text{-}N_3}$ batches (blue, red, green).

Table 3.2: Molecular properties of the $\mathbf{PDMS\text{-}N_3}$ batches.

Polymer batch	$\overline{M}_n$ [a)]	$\overline{M}_w$ [a)]	PDI [a)]	$\overline{DP}_n$ [b)]	Azide functionalization [c)]
$\mathbf{PDMS_{Me}\text{-}N_3}$	12.5	13.5	1.1	156	83%
$\mathbf{PDMS_{Bu}\text{-}N_3\text{-}1}$	10.0	11.0	1.1	111	77%
$\mathbf{PDMS_{Bu}\text{-}N_3\text{-}2}$	10.0	10.5	1.1	114	73%
$\mathbf{PDMS_{Bu}\text{-}N_3\text{-}3}$	9.5	10.5	1.1	94	77%

a) Molecular weight averages (in kg/mol) and polydispersity indices were determined by SEC (THF solution, rt), calibrated against polystyrene standards. b) Degree of polymerization calculated from NMR integral ratios of **PDMS** repeating unit methyl protons and initiator terminal butyl proton signals. c) Percentage of successfully end-functionalized polymer chains, approximated from NMR integral ratios of initiator terminal proton and end group methyl or butyl spacer protons.

3.1.3 Block Copolymer Synthesis *via* Click Chemistry

Connection of the individual homopolymer blocks by the CuAAC reaction was first attempted using **P3HT-alkyne-1** and the azidomethyl-terminated $\mathbf{PDMS_{Me}\text{-}N_3}$. Figure 3.5 b shows representative examples of SEC elugrams. Both following the exact conditions of the synthesis protocol of the *Manners* group and using our own catalyst and solvent systems, only very little development of a block copolymer SEC signal was detected. Examining the corresponding NMR spectra of purified products of such reactions (Figure 3.5 a) it was however surprising to find that the signal corresponding to the alkyne-H in **P3HT-alkyne-1** at 3.53 ppm had completely vanished and a new signal at 7.61 ppm, most probably corresponding to a triazole proton with a very similar integral, had formed. In addition, the CH_2 group adjacent to the azide group in $\mathbf{PDMS_{Me}\text{-}N_3}$ had switched from 2.74 to 4.17 ppm. However, instead of an integral ratio of 2/1 to the triazole proton, as would be expected for a block copolymer, a ratio of exactly 3/1 was found, indicating a CH_3 moiety. In addition, the quite significant downfield shift to 4.17 ppm hinted that the corresponding protons were not anymore neighbouring an Si atom. The singlet at 0.07 ppm, corresponding to the **PDMS** CH_3 groups only had an integral of 2.1, referenced to the thiophene β-protons, instead of the expected value of ~34 (calculated from the repeating unit ratios of the blocks). In combination with the absence of a block copolymer signal in SEC, this led to the hypothesis that the near-quantitative formation of triazole rings by the CuAAC reaction had been indeed successful, however, cleavage of Si-C bonds must have occured (Scheme 3.3). Such a mechanism might be enabled by stabilization of the intermediate carbanion formed on the methyl group due to the effect of the neighbouring triazole ring and might thus be suppressable by using a longer alkyl spacer between the **PDMS** chain and the azide end group.

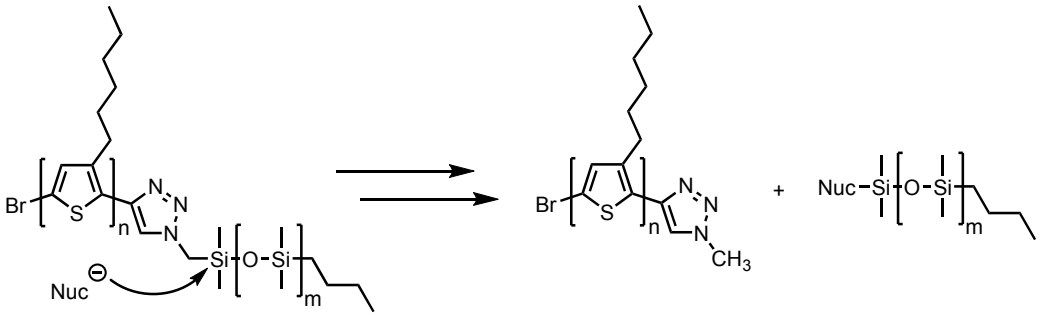

Scheme 3.3: Postulated mechanism of block copolymer cleavage in the case of a triazole-CH_2 linker unit.

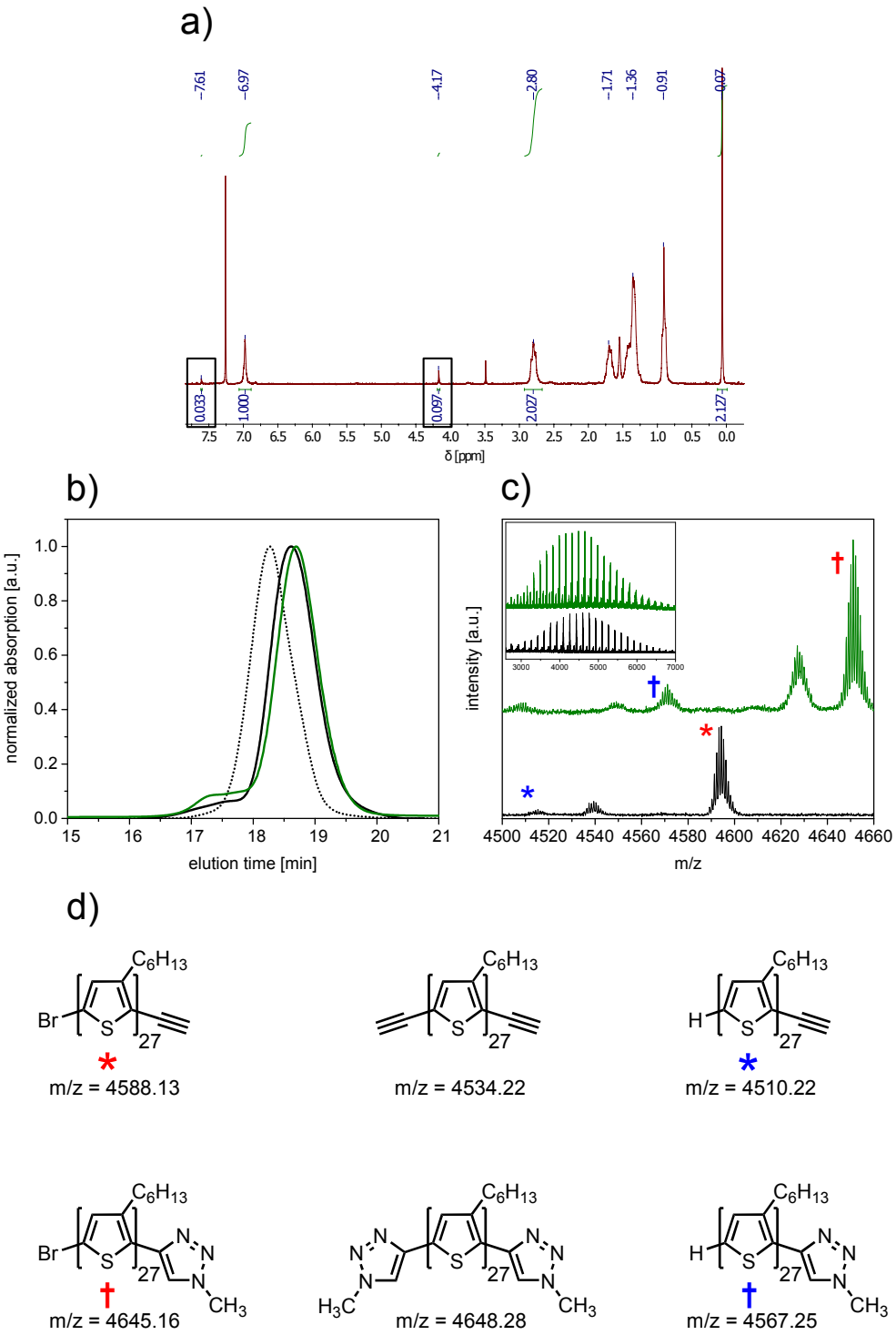

Figure 3.5: a) ^{1}H-NMR spectrum of the click reaction product formed from **P3HT-alkyne-1** and $\mathbf{PDMS_{Me}\text{-}N_3}$ (room temperature, $CDCl_3$). Triazole protons (7.61 ppm) and neighbouring methyl protons (4.17 ppm) are highlighted. b) SEC chromatograms of **P3HT-alkyne-1** homopolymer (black), $\mathbf{PDMS_{Me}\text{-}N_3}$ homopolymer (dotted) and click reaction product (green). c) MALDI-TOF mass spectra of **P3HT-alkyne-1** homopolymer (black) and click reaction product (green). d) Differently end-substituted **P3HT** species identified by mass spectrometry.

Further MALDI-TOF studies on the reaction products confirmed this hypothesis (Figure 3.5 c, green spectrum). All Br/alkyne-, H/alkyne- and alkyne/alkyne-functionalized **P3HT** chains had completely vanished and instead, chains with Br/triazole-CH_3 and H/triazole-CH_3 end groups could be detected. Triazole-CH_3/triazole-CH_3-functionalized chains were also expected to have formed, however, the corresponding signals in the MALDI spectrum coincidentally are superimposed with the Br/triazole-CH_3 signals. Indeed, when a **PDMS$_{Bu}$-N$_3$-1** batch with a butyl spacer was used, a significant **P3HT-*b*-PDMS** fraction was visible in the SEC elugram (Figure 3.6, blue plot).

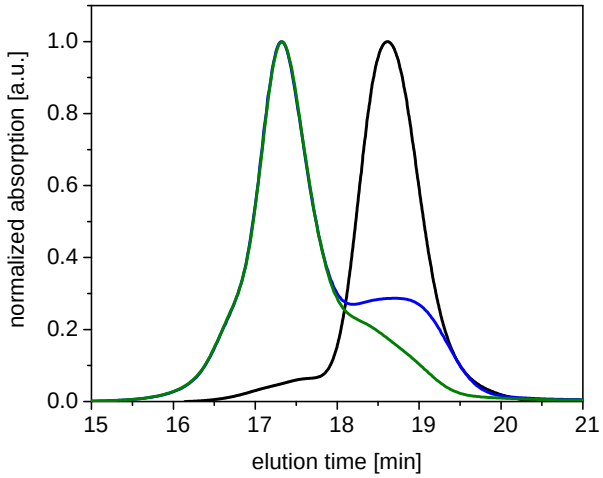

Figure 3.6: SEC chromatograms of **P3HT-alkyne-1** homopolymer (black), crude click reaction product (blue) and block copolymer **P3HT-*b*-PDMS$_{Bu}$** after purification *via* preparative SEC (green).

Table 3.3: Molecular properties of the precursor polymers **P3HT-alkyne-1** and **PDMS$_{Bu}$-N$_3$-1** and the block copolymer before and after SEC purification.

Polymer batch	$\overline{M}_n$[a)]	$\overline{M}_w$[a)]	PDI[a)]
P3HT-alkyne-1	8.0	9.0	1.1
PDMS$_{Bu}$-N$_3$-1	10.0	11.0	1.1
P3HT-*b*-PDMS$_{Bu}$ crude	12.5	20.0	1.6
P3HT-*b*-PDMS$_{Bu}$ purified	17.0	22.0	1.3

a) Molecular weight averages (in kg/mol) and polydispersity indices were determined by SEC (THF solution, rt), calibrated against polystyrene standards.

The ^{1}H-NMR signal at 4.17 ppm was not registered in the block copolymer, thus confirming a successful click reaction without subsequent C-Si bond cleavage (Figure 3.7). Residual

$PDMS_{Bu}$-N_3-1 homopolymer could be successfully removed from the soft, rubbery product by controlled precipitation through dropwise addition of methanol.

Table 3.4: Repeating unit, weight and volume fractions of the **P3HT** and **PDMS** blocks in **P3HT-*b*-$PDMS_{Bu}$**.

	rep. unit fraction [%][a)]	weight fraction [w%][b)]	vol. fraction [v%][c)]
P3HT	18.7	34.0	36.9
PDMS	81.3	66.0	63.1

a) Calculated from respective NMR signals of **P3HT** β-protons and **PDMS** methyl protons. b) Calculated using molecular weights of the repeating units of 166.30 and 74.15 g/mol, respectively. c) Calculated using densities of **P3HT** and **PDMS** of 1.10 and 0.97 g/cm^3, respectively.[71, 292]

However, some unreacted **P3HT-alkyne-1** homopolymer was still detected. This might be either a result of a small amount of non-functionalized **P3HT** chains which were not able to react to block copolymers at all, or of an incomplete click reaction. Thus, purification of the crude product mixture *via* preparative size exclusion chromatography was attempted. The *Manners* group also mentioned the necessity of several runs of preparative SEC to obtain a sufficiently pure block copolymer, hinting at a similarly non-quantitative click reaction.[3]

The green plot in Figure 3.6 shows the respective SEC elugram of the purified block copolymer batch. A yield of 9 mg of block copolymer still containing a small fraction of **P3HT** homopolymer was obtained. It has to be noted that the signal of the homopolymer fraction appears greatly amplified due to the effect of the non-absorbing **PDMS** block present in the copolymer fraction. This purified product was further investigated in preliminary studies to get a general idea (within the limitations of the small amounts of material available and the slight impurities present) on temperature-dependent optical properties in thin films as well as performance in OFET devices.

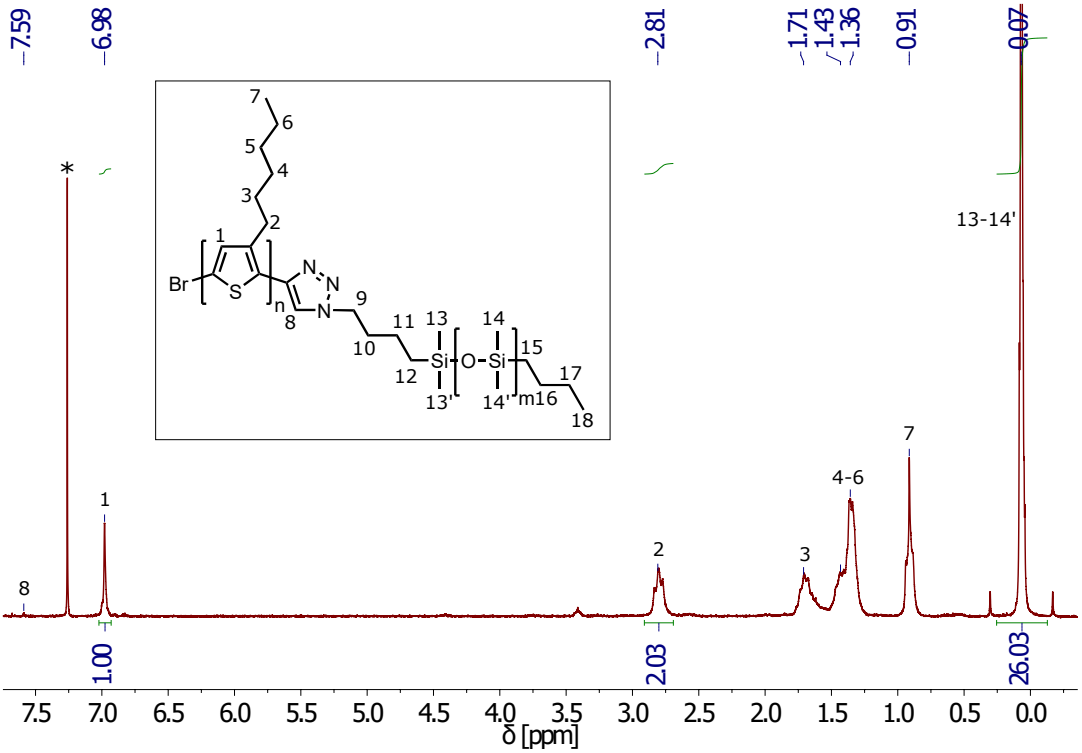

Figure 3.7: ^{1}H-NMR spectrum of purified **P3HT-*b*-PDMS$_{Bu}$** (room temperature, $CDCl_3$).

3.2 Characterization of the Block Copolymer

3.2.1 Temperature Dependency of Optical Properties in Thin Films

The temperature-dependent UV/Vis absorption behavior of thin films of **P3HT-*b*-PDMS$_{Bu}$**, deposited by spin coating from 5 mg/mL chloroform solutions, was investigated (Figure 3.8). The **P3HT-alkyne-1** homopolymer was measured as a reference. Both thin films were heated from room temperature to 200 °C at a heating rate of 5 K/min and then slowly cooled down to room temperature at 2 K/min. In the initial spectra at rt, already a more significant fine structure of the polythiophene backbone band with maxima at 520, 546 and 597 nm is seen for the block copolymer compared to the homopolymer. Such a fine structure has been shown to be a sign of intra- and intermolecular π-π stacking interactions of the backbone.[62] Since the **P3HT** species present in both thin films are identical except for the end group, the differences are hinting at a film structure allowing a higher degree of conformational freedom in the case of the block copolymer films. This is likely to be a consequence of the flexible PDMS content of the material and allows for a higher degree of order during the comparably fast evaporation of the chloroform

solvent during spin coating. In the homopolymer films, fast drying causes the disordered structure from solution to "freeze", leading to less planarized and aligned polymer chains and thus less tendency for π-π stacking. Such phenomena are often encountered when fast-drying solvents are used for film deposition.[57] In the block copolymer films however, chains might still be able to move to a certain degree during and even after drying of the film, thus leading to a high degree of aggregation resulting in the significant fine structure.

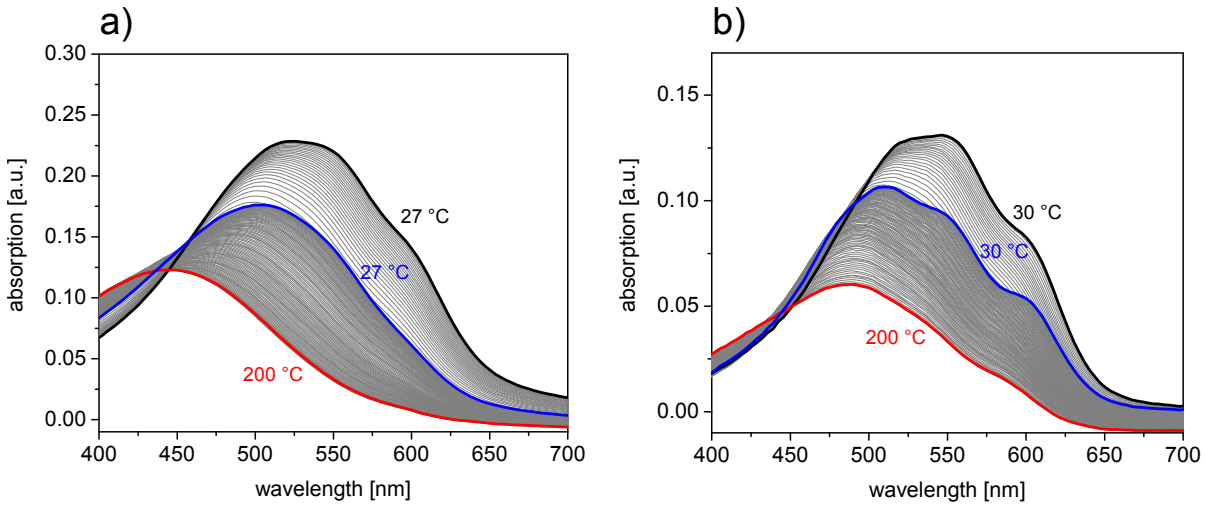

Figure 3.8: Temperature-dependent thin film absorption measurements of a) **P3HT-alkyne-1** homopolymer and b) **P3HT-*b*-PDMS$_{Bu}$**. Films were spin coated on glass substrates from 5 mg/mL $CHCl_3$ solutions, heated from rt (black spectra) to 200 °C (red spectra) at 5 K/min and then cooled to rt (blue spectra) at 2 K/min.

The differences become even more apparent when the spectra recorded during heating and cooling scans are considered. In the **P3HT-alkyne-1** homopolymer film, heating to 200 °C causes the fine structure to vanish completely and the backbone band maximum is significantly blue-shifted to 446 nm. Such spectra are indicative of free chains which are encountered in polythiophene solutions in good solvents or in melts of the bulk polymer. In the block copolymer spectra at the same temperature, the blue-shift is much less significant and the shoulder at 583 nm still persists to a certain degree. This might be an indication of residual aggregates still being present even at these high temperatures. When slowly cooling down to room temperature, the fine structure is only very weakly recovered for the **P3HT-alkyne-1** homopolymer film, however, for **P3HT-*b*-PDMS$_{Bu}$** the individual shoulders get even more pronounced. These findings further point to a higher degree of conformational freedom of the **P3HT** blocks in the block copolymer films during cooling, which is likely enabled by the **PDMS** domains surrounding the polythiophene. Similar results were obtained by *Ogino et al.* when comparing UV/Vis

spectra of blend films of **P3HT/PCBM** and **P3HT-*b*-PDMS/PCBM** before and after thermal annealing.[166] The incorporation of the **PDMS** block led to increased recovery of the fine structure of the **P3HT** spectrum related to aggregation and improved phase separation of the **P3HT-b-PDMS/PCBM** blend. An interplay of both effects was attributed to be the cause of the improvements found in organic solar cell performance.

3.2.2 Bottom-gate/Bottom-contact Transistors

P-type charge carrier (hole) mobilities were determined by organic field effect transistor (OFET) measurements in the bottom-gate/bottom-contact geometry. Polymer films of both the **P3HT-alkyne-1** homopolymer and the **P3HT-*b*-PDMS$_{\mathbf{Bu}}$** block copolymer were deposited on the transistor substrates by spin coating from 5 mg/mL solutions in chloroform. Every substrate was composed of 16 individual transistors, four each with 20, 10, 5 and 2.5 µm channel lengths, respectively. The gate consisted of n-doped silicon which was contacted directly *via* the probe station table. A 230 nm thick silicon oxide layer was employed as the gate dielectric and the source and drain electrodes were arranged as an interdigitated structure of gold combs contacted *via* needle contacts which were pierced through the polymer thin films. To determine the output characteristics of the transistors (Figure 3.9 a and c), the gate voltage (V_g) was held constant and the source-drain voltage (V_{sd}) was varied from 0 to -80 V. This process was repeated for gate voltages between 0 and -80 V in steps of 20 V. To determine the transfer characteristics (Figure 3.9 b and d), V_{sd} was kept constant at -60 V and V_g was varied from 20 to -80 V. From the slope of a linear fit of the square root plots (dashed lines) of the resulting transfer curves (solid lines) the field effect mobilities could be determined. The x-axis intercepts of these linear fits corresponded to the threshold voltages (V_{th}). All measurements were averaged over at least four individual transistors. 20 µm channels were used since they tended to yield the most reliable results. However, mobility values obtained with shorter channel lengths were found to be very comparable.

Both **P3HT-alkyne-1** and **P3HT-*b*-PDMS$_{\mathbf{Bu}}$** as-cast films exhibited behavior typical for semiconducting polymers. In the output curves, for a V_g of 0 V (off-state), no significant flow of current through the channel was detected ($I_{sd}<10^{-7}$ A). When sweeping V_{sd} at higher gate voltages, the source-drain current initially increases nearly linearly (linear regime) and subsequently approaches a limit (saturation regime) when all charge carriers present at the respective gate voltage are fully utilized.

Both polymers show field effect mobilites in the order of 10^{-4} $cm^2V^{-1}s^{-1}$, values in the lower expectation range for regioregular **P3HT** (10^{-4} to 10^{-1} $cm^2V^{-1}s^{-1}$, depending on the exact

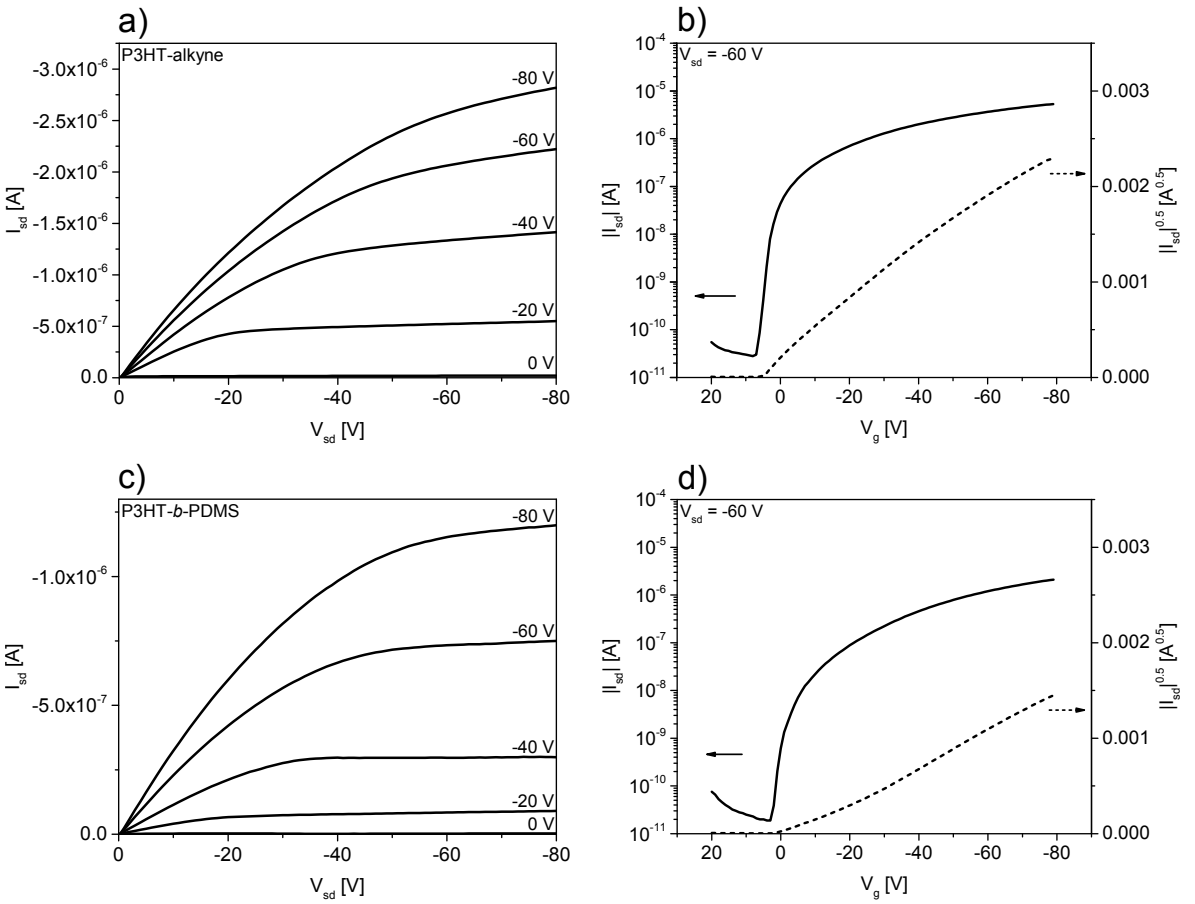

Figure 3.9: Output and transfer characteristics of a), b) **P3HT-alkyne-1** and c), d) **P3HT-*b*-PDMS$_{\mathbf{Bu}}$** (as-cast) organic field effect transistors.

degree of regioregularity and the device manufacturing conditions).[57, 67, 68] This might be at least partly explained by the low molecular weight of the **P3HT** block, which often leads to inferior electronic properties, and the influence of the alkyne end groups for the homopolymer films. However, values obtained for the block copolymer and homopolymer transistors are surprisingly close, despite the high amount (volume fraction of 63.1%) of electronically inactive **PDMS** material present in **P3HT-*b*-PDMS$_{\mathbf{Bu}}$**.

Relating these results to the thin film absorption spectra, a possible explanation lies in the proposedly more efficient packing of the polythiophene blocks in the block copolymer which might lead to better charge transfer between polymer chains. The effect of thermal annealing on the transistor properties was also probed. Temperatures of 100 °C for 3 h were chosen since these conditions should allow for efficient reorganisation of the film structure through softening of the **PDMS** matrix while the occurence of any unwanted thermally initiated side reactions can be mostly excluded. *Ogino et al.* used temperatures of 150°C for 10 min for annealing their solar cells. Unfortunately, after annealing, **P3HT-**

***b*-PDMS$_{\mathbf{Bu}}$** performance dropped by around one order of magnitude while values for the homopolymer remained virtually unchanged. It has to be noted that interchain packing efficiency is not the only factor influencing the current flow through the channel at a given gate potential, especially for complex block copolymer systems. The size and shape of individual **P3HT** and **PDMS** domains might have been influenced by heating the polymer films, possibly leading to a higher degree of insulation of electroactive material, *i.e.* less pathways for charge carriers to pass through the channels.

Table 3.5: Bottom-gate/bottom-contact OFET characteristics of **P3HT-alkyne-1** and **P3HT-*b*-PDMS$_{\mathbf{Bu}}$**.

	μ [cm^{2}V^{-1}s^{-1}][a)]	V_{th} [V][b)]	I_{on}/I_{off}[c)]
P3HT[57, 67, 68]			
70% rr, $\overline{M_w}$ = 126 kg/mol	$2{\cdot}10^{-5}$	-	-
81% rr, $\overline{M_w}$ = 175 kg/mol	$2{\cdot}10^{-4}$	-	-
91% rr, $\overline{M_w}$ = 11 kg/mol	$1{\cdot}10^{-2}$	-	-
95% rr, $\overline{M_w}$ = 28 kg/mol	$5{\cdot}10^{-2}$	-	-
98% rr, $\overline{M_w}$ = 20 kg/mol	$1{\cdot}10^{-2}$	-	10^4
P3HT-alkyne-1			
as-cast film	$2.5{\cdot}10^{-4}\pm2.0{\cdot}10^{-5}$	7±1	$2.0{\cdot}10^5$
annealed (100 °C, 3 h)	$2.1{\cdot}10^{-4}\pm8.3{\cdot}10^{-6}$	-12±5	$4.3{\cdot}10^4$
P3HT-*b*-PDMS$_{\mathbf{Bu}}$			
as-cast film	$1.2{\cdot}10^{-4}\pm4.7{\cdot}10^{-5}$	-8±3	$1.1{\cdot}10^5$
annealed (100 °C, 3 h)	$3.0{\cdot}10^{-5}\pm1.4{\cdot}10^{-6}$	11±1	$8.8{\cdot}10^3$

a) Field effect mobilities determined from slope of linear fit $\frac{\partial\sqrt{|I_{sd}|}}{\partial V_g}$ at V_{sd} = -60 V. Values are averaged over four independent transistors. b) Threshold voltages determined from x-axis intercept of the same fit. c) On/off current ratios determined between minimum and maximum source-drain current values of a representative transistor.

In order to elucidate this factor further, the OSC layer surfaces of the transistors were probed by atomic force microscopy (AFM) to obtain insights into the film structure on the nanometer scale. It has to be noted that in a bottom-gate/bottom-contact configuration, current flows through the channel close to the interface between gate dielectric and the semiconductor layer and investigations of the film surface can only provide a first rough estimate of the situation in this part of the film.

As-cast films of the **P3HT-alkyne-1** homopolymer (Figure 3.10 a) showed a very smooth film surface with small inhomogeneities. Locally ordered, lamellar-like textures were found, surrounded by regions showing no obvious texture in AFM. For **P3AT**s, the

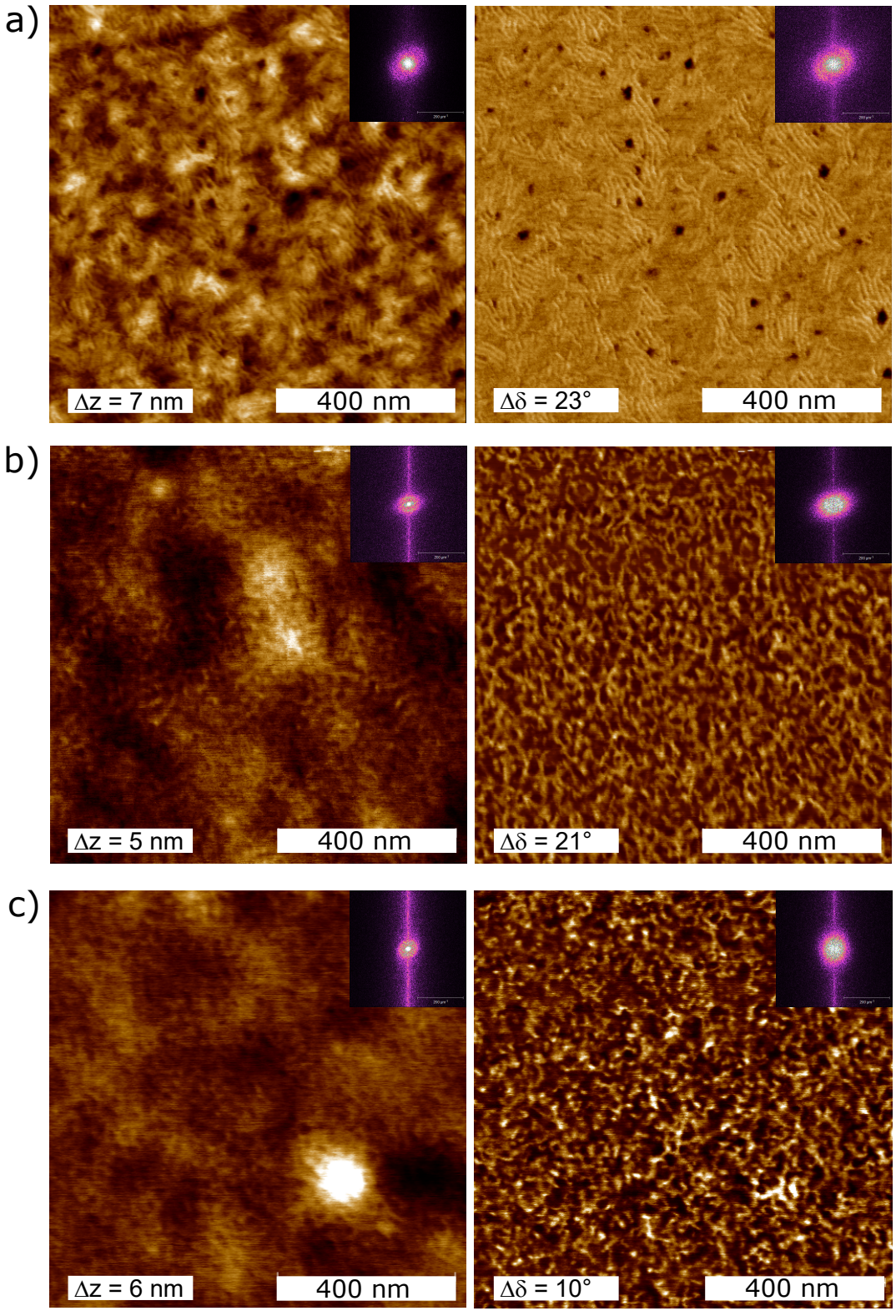

Figure 3.10: AFM height (left) and phase (right) images of thin films on transistor substrates: a) as-cast film of **P3HT-alkyne-1** homopolymer, b) as-cast film of **P3HT-*b*-PDMS$_{Bu}$** and c) thermally annealed film of **P3HT-*b*-PDMS$_{Bu}$** (100 °C, 3 h). Insets show the *Fourier* transformations (2D-FFT) of the images.

lamellar structures are believed to consist of crystalline edge-on-oriented segments of chains, which are π-stacked perpendicular to the lamellae direction and separated by amorphous interlamellar zones.[57, 293] For very low molecular weight regioregular **P3HT**, this has been shown to lead to the formation of nanorods in as-cast films deposited by spin coating.[294] The non-textured domains in the **P3HT-alkyne-1** films likely consist of chains lying "flat-on" on the substrate, a kinetically trapped morphology which is often associated with less regioregular polymers or occurs upon fast solvent evaporation.[57] Since charge transport in transistor devices occurs mainly in chain direction and in π-stacking direction, the face-on morphology is detrimental for transistor performance which likely contributes to the comparably low hole mobility values observed for **P3HT-alkyne-1**.
The influence of the soft **PDMS** blocks in the **P3HT-*b*-PDMS$_{\mathbf{Bu}}$** copolymer films was immediately apparent already during measurements. Images with satisfactory resolution could only be obtained at low scan rates below 0.1 Hz, presumably due to the softer structure of the films. Figure 3.10 b and c show as-cast and thermally annealed **P3HT-*b*-PDMS$_{\mathbf{Bu}}$** films. The surfaces are rather smooth and clear indications for microphase separation between the blocks are found. Abundant circular features obtained upon close inspection of the height images point to a morphology of standing cylinders, however with rather low long-range order. The absence of significant features in *Fourier*-transformed (2D-FFT, insets) height and phase images further confirmed the lack of long-range-ordered periodical structures. In the 2D-FFT of the height image of Figure 3.10 b, a very weak circle is seen, corresponding to a periodicity of ~33 nm, which fits to the individually measured diameters of the standing cylinder features in the height image (32-36 nm). In order to assign the **P3HT** and **PDMS** blocks to specific regions of the images, the phase image of the as-cast block copolymer film (Figure 3.10 b, right side) was further analyzed by masking all points below a threshold of 10.4° and calculting the percentage of the masked area compared to the total area of the image. The obtained value of 39.5% corresponds well with the calculated volume fraction of the **P3HT** blocks (36.9%), which led to the assumption that the areas with low phase angles (dark portions of the image) correspond to the **P3HT** blocks. Performing a similar analysis on the annealed film phase image (Figure 3.10 c, right side) yielded a value of 40.5% for the proposed area covered by **P3HT**. In total, the results obtained from AFM studies point to a morphology of rather unordered standing cylinders with diameters of approximately 32-36 nm, in which the minority phase **P3HT** is enclosed by a **PDMS** matrix. Only small changes in film morphology can be seen after annealing, with the height image showing a slightly higher amount of cylindrical structures. Concerning the influence of annealing, more detailed studies will be necessary to unambiguously link morphological changes to

electronic performance of **P3HT-*b*-PDMS** and to optimize annealing conditions in order to improve transistor performance.

3.3 Summary

In this chapter experiments on block copolymer systems consisting of rod-like regioregular **P3HT** and flexible **PDMS** coil blocks with narrow molecular weight distributions were presented. Synthesis of these materials was carried out adapting a protocol originally introduced by the *Manners* group.[3, 165] The individual blocks with a repeating unit ratio of ~4.3/1 were produced by GRIM and living anionic polymerization procedures, respectively and the alkyne and azide functionalities were introduced by endcapping methods. Initial attempts to connect the two blocks in a grafting-to approach were however unsuccessful. NMR spectroscopy and SEC measurement results led to the hypothesis of cleavage of an Si-C bond after triazole formation to be the cause. The associated proposed mechanism could be unambiguously proven by MALDI-TOF measurements. The cleavage reaction was shown to be facilitated by the stabilizing effect of the triazole ring formed during the click reaction, neighbouring the Si-C bond if an azidomethyl-terminated **PDMS** block was employed. Consequently, block copolymer formation could be greatly improved by using a **PDMS** derivative bearing an azidobutyl spacer. Unfortunately, while all excess **PDMS** homopolymer could be removed, small amounts of **P3HT** homopolymer were reproducibly detected. Purification by preparative SEC resulted in the removal of most of this impurity, however, yields were greatly diminished through this process.

Room temperature UV/Vis spectra of thin films exhibited a more significant fine structure related to π-π interactions of the **P3HT** blocks in case of the **P3HT-*b*-PDMS$_{\mathbf{Bu}}$** materials compared to the **P3HT-alkyne-1** homopolymer. Upon heating to 200 °C and subsequent slow cooling back to rt, the differences got even more pronounced. In a simplified picture, these phenomena can be attributed to a block copolymer film structure in which the conjugated blocks are able to move more freely in a matrix of **PDMS** and thus reorganisation for efficient π-π stacking is facilitated.

Comparison of field effect mobilities through bottom-gate/bottom-contact transistor measurements of **P3HT-alkyne-1** and **P3HT-*b*-PDMS$_{\mathbf{Bu}}$** showed very comparable values despite the lower relative amount of electroactive material present in the block copolymer films. It is thus reasonable to assume that pathways of conjugated domains are formed in the films over which charge transport can occur. Thermal annealing of the transistors at 100 °C for 3 h had a negligible effect on the performance of **P3HT-alkyne-1**,

however, for the block copolymer the mobilities decreased by almost an order of magnitude. Results from AFM studies of the semiconductor film surfaces of the transistors show clear indications for phase separation of the **P3HT** and **PDMS** blocks in the block copolymer as compared to the **P3HT-alkyne-1** homopolymer films. A morphology of standing cylinders with very weak long-range order was obtained, in which the minority phase **P3HT** is enclosed by **PDMS**. The diameters of the individual cylinders lay in the range of ~32-36 nm.

4 Side-chain π-extended Polythiophenes

The incorporation of conjugated aromatic or vinylene extensions in the β-position of linear polythiophenes has been found to induce interesting changes to the optical and electronic properties of these materials.[172–174] Such systems largely retain the pecularities of fully branched polythiophenes, especially the lowered frontier orbitals, which has been shown to lead to improved open circuit voltages in organic solar cells (OSCs) and to higher stability against oxidation under atmospheric conditions. However, due to typically lower steric hindrance, their backbones are able to assume a more planar conformation, which can be expected to improve charge carrier mobilities substantially.

Even the shortest side-chain derivative, **P3TC8C4**, could still be fully dissolved in chlorinated benzene derivatives, albeit with a significant degree of aggregation at room temperature. Since the performances of the materials have been shown to greatly improve with decreases in side chain lengths, we set out to further explore the limits of this approach by investigating the next logical analogue in this regard, **P3TC6C2**.

4.1 Monomer and Polymer Synthesis

The side-chain π-extended polythiophene derivative **P3TC6C2** was synthesized according to the convergent reaction pathway originally developed by *Dr. Martin Scheuble* (Scheme 4.1).[6, 7] Compared to the original strategy used by *Dr. Thomas Richter*, this route offers the advantage of employing a common intermediate (3-bromo-2,2'-bithiophene, **3-BrT$_2$**) as the backbone building block of the monomers for all differently side-chain substituted derivatives.[4, 5]

3-BrT$_2$ was synthesized by a *Suzuki* coupling approach starting from 2,3-dibromothiophene (**2,3-BrT**), which had been shown to be much more feasible than a bromination/debromination approach.[7] In parallel, the side-chain building block 2-(2-ethylhexyl)-5-pinacolatoborylthiophene (**TC6C2-B**) was synthesized in a two-step reaction sequence including the attachment of the side chain to the thiophene *via* reaction of the lithiate with 2-ethylhexyl bromide followed by the generation of the boronate ester. *Suzuki* coupling of the two building blocks yielded the monomer precursor **3TC6C2** which was purified by column chromatography. Separation from side-products was found to be highly improved in comparison to the derivatives with longer side chains, leading to a yield of 94% (**3TC12C8**: 45%, **3TC10C6**: 68%, **3TC8C4**: 26%).[7] Bromination with NBS yielded the monomer **3TC6C2Br** (for NMR spectrum see Figure 4.1).

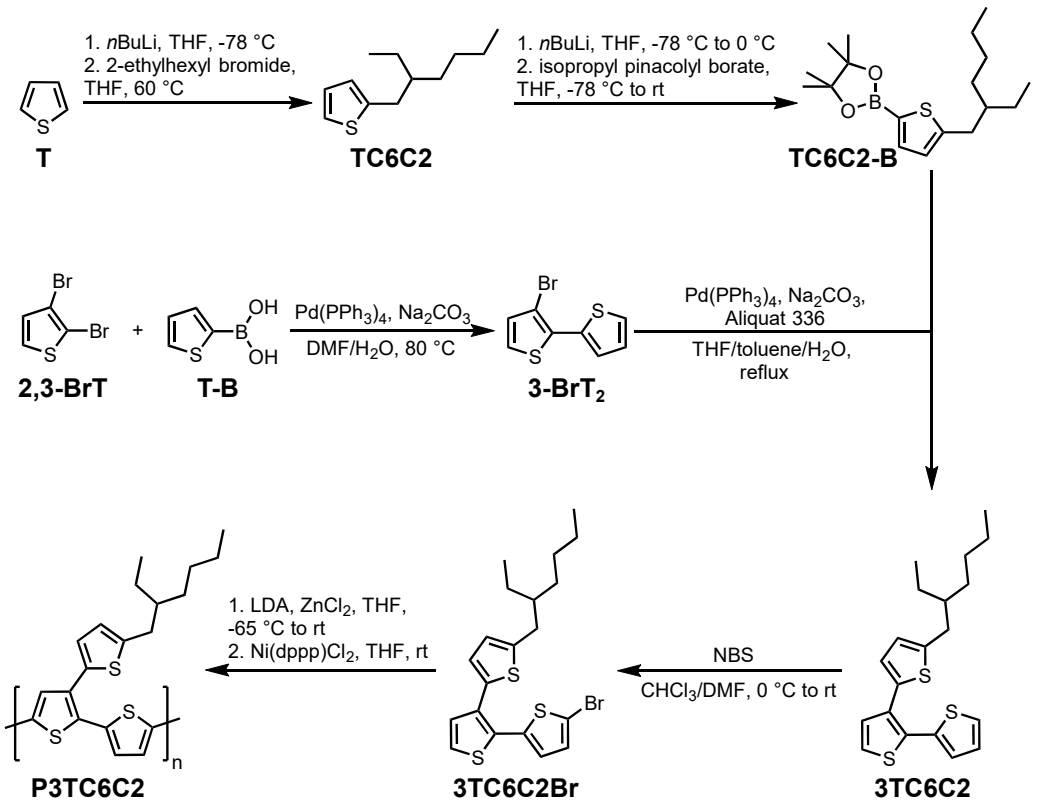

Scheme 4.1: Synthesis pathway to monomer **3TC6C2Br** and polymerization procedure yielding side-chain π-extended polythiophene **P3TC6C2**, following the protocol of *Dr. Martin Scheuble*.[7]

This monomer was subsequently lithiated with LDA at -65 °C in THF, reacted with $ZnCl_2$ to produce the *Negishi* intermediate and polymerized by addition of the catalyst Ni(dppp)Cl_2. After quenching with aqueous HCl and precipitation, *Soxhlet* fractionation with acetone (washing fraction, neglected), chloroform and chlorobenzene was performed. Compared to all **P3TCxCy** derivatives with longer side chains, solubility was greatly diminished, with only ~20% of the crude product soluble in the two solvents at reflux temperatures. The $CHCl_3$ and CB fractions (termed $\mathbf{P3TC6C2_{CHCl_3}}$ and $\mathbf{P3TC6C2_{CB}}$ in the following) were collected and subjected to further investigations.

High-temperature size exclusion chromatography measurements (HT-SEC, Figure 4.2) showed monomodal molecular weight distributions of both polymer batches, with $\mathbf{P3TC6C2_{CHCl_3}}$ expectedly exhibiting a slightly lower molecular weight and similar polydispersity index (Table 4.1).

Although the same monomer-to-catalyst ratio and reaction conditions as for the longer side-chain derivatives synthesized by *Dr. Martin Scheuble* were used, the obtained molecular weights of **P3TC6C2** were slightly lower. However, polydispersities showed similar values.

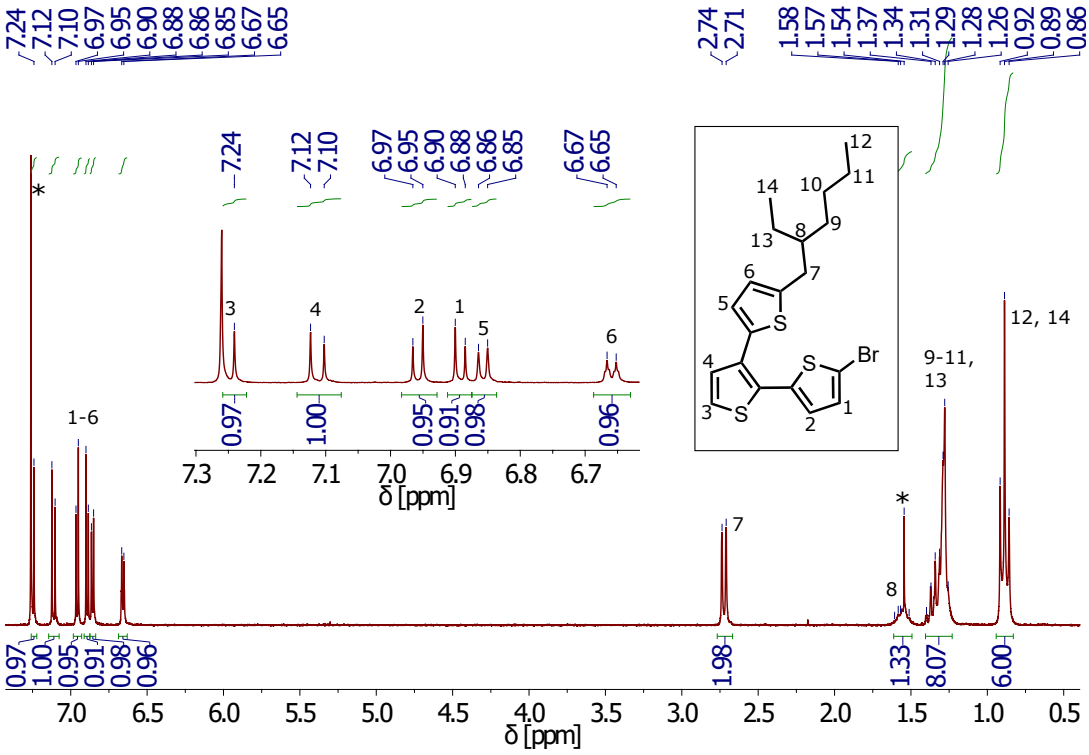

Figure 4.1: ^{1}H-NMR spectrum of purified monomer **3TC6C2Br** (room temperature, $CDCl_3$).

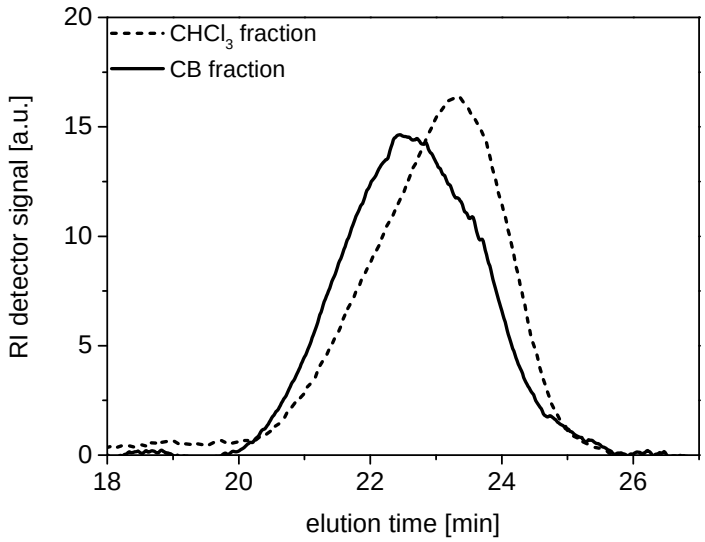

Figure 4.2: High-temperature size exclusion chromatography (HT-SEC) measurements of the chloroform and chlorobenzene *Soxhlet* fractions of **P3TC6C2** performed at 160 °C in 1,2,4-trichlorobenzene.

Table 4.1: Molecular properties of side-chain π-extended polymer batches **P3TC6C2$_{CHCl_3}$** and **P3TC6C2$_{CB}$**.

Polymer batch	$\overline{M}_n$[a)]	$\overline{M}_w$[a)]	PDI[a)]
P3TC6C2$_{CHCl_3}$	7.5	14.0	1.9
P3TC6C2$_{CB}$	10.0	20.0	2.0

a) Molecular weight averages (in kg/mol) and polydispersity indices were determined by SEC (THF solution, rt), calibrated against polystyrene standards.

This can most probably be ascribed to the greatly diminished solubility of these polymers leading to earlier precipitation of shorter chains during polymerization.

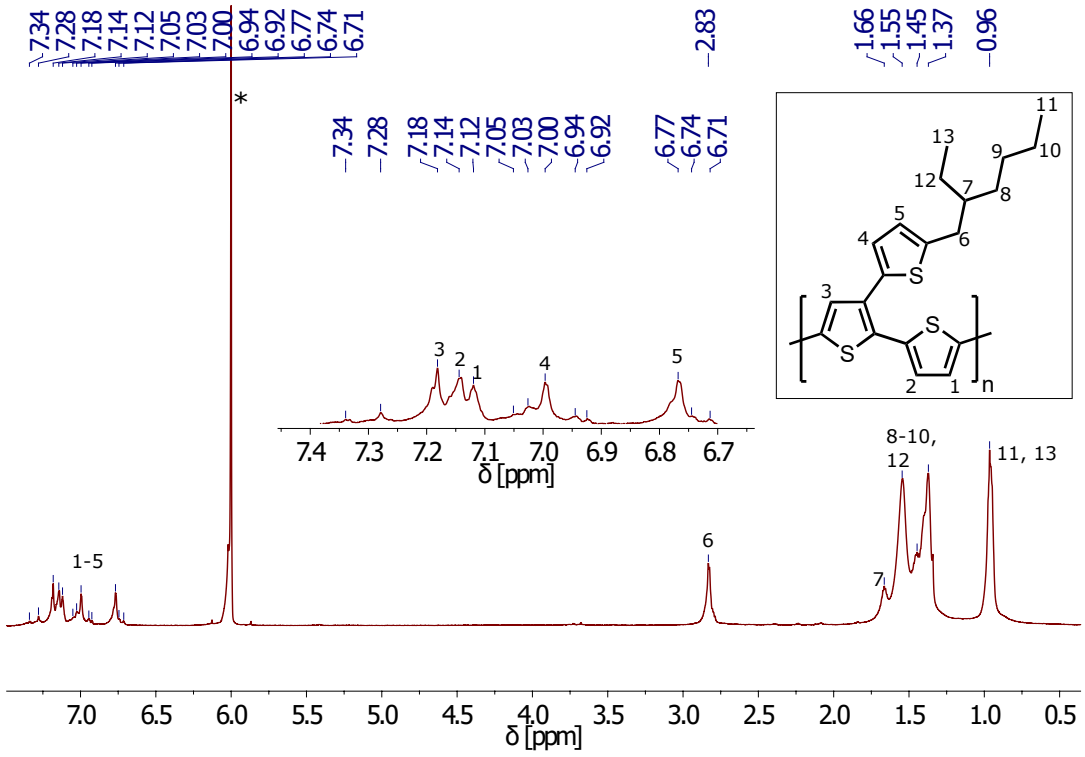

Figure 4.3: ^{1}H-NMR spectrum of **P3TC6C2$_{CHCl_3}$** recorded in $C_2D_2Cl_4$ at 100 °C.

Figure 4.3 shows high-temperature ^{1}H-NMR spectra of **P3TC6C2$_{CHCl_3}$**, recorded at 100 °C in $C_2D_2Cl_4$. This method allowed to determine regioregularities of the longer side-chain analogues by analysis of the signals in the aromatic region. Especially small signals upfield of proton 5 can be used as a measure for the degree of regioregularity. However, for both **P3TC6C2** batches the spectra are significantly less resolved, especially for the aromatic signals, and the peaks for the backbone protons are shifted closer together, hinting at a much higher tendency for aggregation of the backbone. Unfortunately, due

to the bad resolution of the individual signals, it was not possible to exactly determine the regioregularity of the polymers. However, since all other **P3TCxCy** derivatives were shown to feature >95% regioregularity and the same reaction conditions incorporating an AB-type monomer were used, a similar degree of regioregularity can be expected.

4.2 Thermal Behavior

4.2.1 Measurements in Bulk Polymer Powder

Thermogravimetric Analysis and Differential Scanning Calorimetry

The temperature stability and phase transition temperatures of **P3TC6C2** were probed by a combination of thermogravimetric analysis (TGA) and differential scanning calorimetry (DSC) measurements (see Figure 4.4 a). The polymers showed thermal stability under an argon atmosphere up to ~422 °C (determined at a mass loss of 3%), values very comparable to **P3HT** (~440 °C).[295] In DSC experiments (at rates of 10 K/min for heating and 5 K/min for cooling), no phase transitions below 50 °C, which could be ascribed to alkyl chain motion, were found.[61]

Table 4.2: Melting points of **P3TC6C2** compared to its analogues and **P3HT**.

Polymer	Melting point [°C]
P3HT[296]	216
P3TC16[4]	270
P3TC12C8[6]	182
P3TC10C6[6]	188
P3TC8C4[6]	210
P3TC6C2$_{CHCl_3}$	291
P3TC6C2$_{CB}$	300

This is in line with results for other **P3TCxCy** derivatives, where a significant transition was only found for **P3TC12C8** and not for the shorter alkyl chains.[6, 7] Melting transitions were found at 300 and 291 °C for the CB and $CHCl_3$ fractions of **P3TC6C2**, respectively. T_m values were estimated from the respective maxima of endothermic peaks in 2nd cycle heating scans to exclude the thermal history of the samples. These temperatures are remarkably high when compared to the other **P3TCxCy**s, where T_m values of 182, 188 and 210 °C were found in decreasing order of alkyl side chain lengths, and also compared

to **P3HT** and other linear **P3AT**s which usually possess T_m values below 240 °C.[61, 296] Melting temperatures seem to follow an exponential trend when side chains are shortened (Figure 4.4 b), however, the slightly different molecular weights of the **P3TC6C2** batches compared to the other derivatives might also play a role.

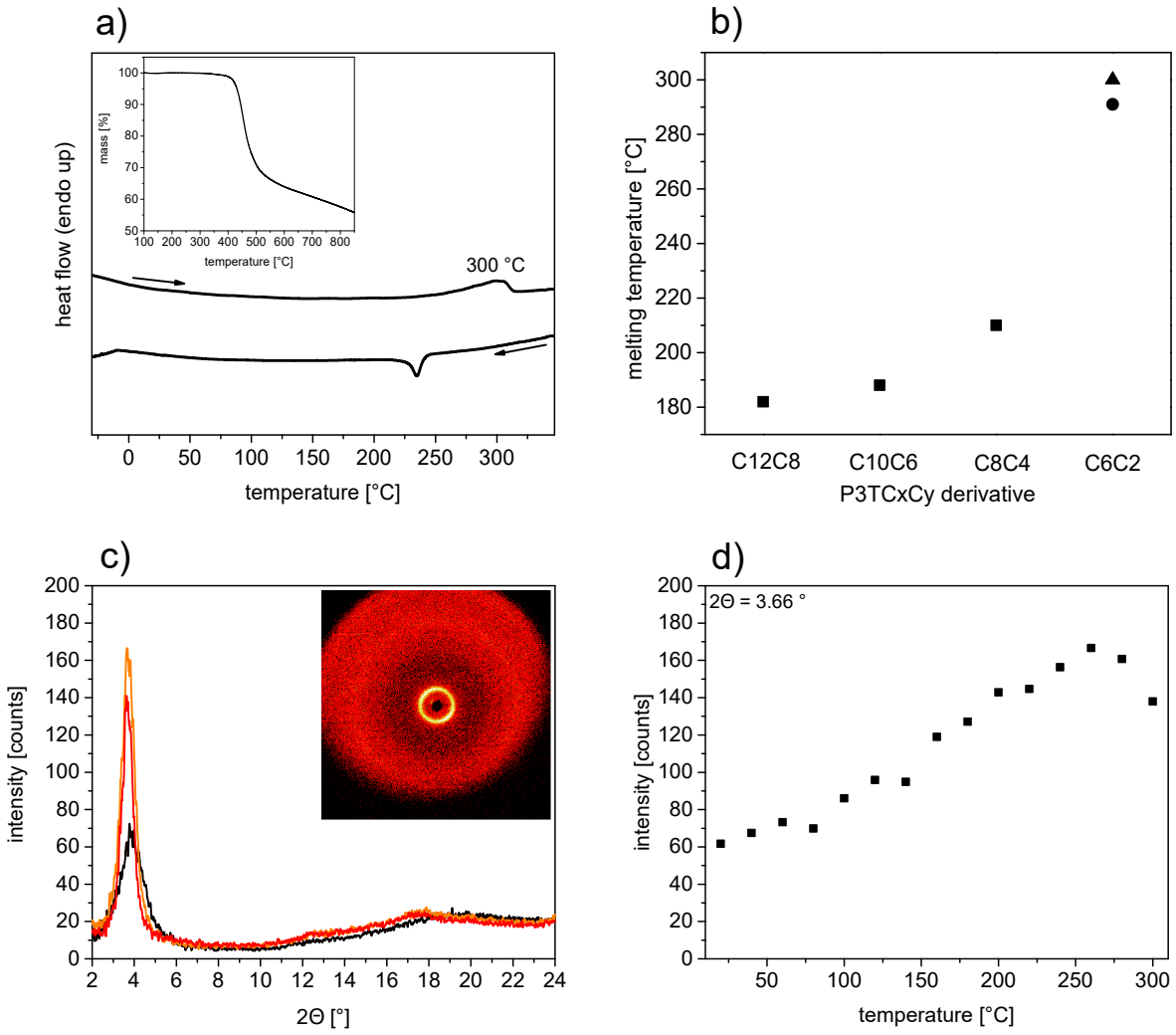

Figure 4.4: a) DSC heating and cooling scans of $\mathbf{P3TC6C2_{CB}}$ recorded at a heating rate of 10 K/min and a cooling rate of 5 K/min. Inset shows TGA run for the same polymer. b) Exponential trend of increasing melting points for decreasing **P3TCxCy** side chain lengths. The triangle and dot correspond to the T_m of $\mathbf{P3TC6C2_{CB}}$ and $\mathbf{P3TC6C2_{CHCl_3}}$, respectively. c) WAXS powder diffraction patterns at 20 °C (black), 260 °C (orange) and 300 °C (red). Inset shows diffraction pattern at 260 °C. d) Peaktrend of scattering intensities at $2\Theta = 3.66°$ from room temperature to 300 °C.

Wide Angle X-ray Scattering

The molecular structure of **P3TC6C2$_{CB}$** in bulk powder was further studied by temperature-dependent wide angle X-ray scattering (WAXS) experiments (Figure 4.4 c and d). A powder sample of the chlorobenzene fraction of the polymer was irradiated with copper K_α irradiation ($\lambda = 0.154$ nm) and diffractograms were recorded between 20 and 300 °C (the limit of the temperature range of the used *Bruker Nanostar* device). The diffractograms resembled the results of earlier measurements on longer side-chain **P3TCxCy** derivatives. A sharp reflex in the 2Θ region between 3°and 4°, which has been assigned to d_{100}, the interchain distance in the direction of the alkyl chains, and a broad reflection between 2Θ = 16-20°, corresponding to the π-π stacking distance between chains, were found.[297] At room temperature, the reflexes lay at 3.89° (22.7 Å) and ~19.0° (4.7 Å), very close to the values found for **P3TC8C4** (22 and 4.6 Å). Considering the trend in d_{100} values found for the other **P3TCxCy**s, the transition from **P3TC8C4** to **P3TC6C2** seems to mark the point where interchain distances in the direction of the alkyl chains are not anymore mainly determined by alkyl chain lengths and the (identical) side-chain thiophene structures seem to play a larger role. Compared to linear **P3AT**s, the d_{100} distances are comparable to poly(3-decylthiophene) (**P3DT**) with 23.2 Å and significantly higher than **P3HT** with 16.4 Å.[297, 298] Upon increasing the temperature, both reflexes get sharper and more defined while simultaneously shifting to lower 2Θ values, corresponding to higher distances on the molecular scale. The intensity of the d_{100} reflex also increases steadily (Figure 4.4 shows a trend of this intensity with temperature, taken at 2Θ = 3.66°). At 260 °C, maximum intensity is reached and the two reflexes are found at 3.66 and ~17.5°, corresponding to interchain distances of 24.1 and 5.1 Å in alkyl chain and π-π stacking directions, respectively. At even higher temperatures up till the measurement limit of 300 °C, the d_{100} reflex intensity starts to rapidly decrease while still shifting to smaller 2Θ values (3.64°, 24.2 Å at 300 °C), indicating a loss in intermolecular order. In accordance with DSC measurements, in which the endothermal transition starts at ~250 °C, this can clearly be attributed to melting of the material and is in line with measurements which had been performed on **P3TC12C8**.

Table 4.3: Room temperature interchain distances in direction of the alkyl chains (d_{100}) and in π-π stacking direction ($d_{020}/2$) of **P3TC6C2** compared to its analogues and **P3HT**.

Polymer	d_{100} [Å]	$d_{020}/2$ [Å]
P3HT[297]	16.4	3.8
P3TC12C8[6]	24.9	4.6
P3TC10C6[6]	23.5	4.6
P3TC8C4[6]	22.3	4.6
$\mathbf{P3TC6C2_{CHCl_3}}$	22.6	4.7
$\mathbf{P3TC6C2_{CB}}$	22.7	4.7

4.2.2 Solution and Thin Film Optical Absorption

Both the **P3TC6C2** chloroform and chlorobenzene *Soxhlet* fractions were found to be at least partly insoluble in low-boiling solvents like THF and $CHCl_3$ at room temperature. The weakest tested solvent in the order of increasing solvation strength ($CHCl_3$ ≈ THF < CB < *o*DCB < TCB ≈ 1-CN) which was able to fully dissolve both polymer batches in concentrations of 3 mg/mL was chlorobenzene. Even for this solvent, thermal energy by means of a heat gun had to be applied to fully dissolve all polymer particles. However, after cooling to rt and standing for at least 12 h, no visible precipitation occured in CB. Compared to the other **P3TCxCy** derivatives with longer branched alkyl chains, this means a drastically lower solubility.

Temperature-dependent solution absorption measurements were first attempted for *o*DCB solutions (3 mg/mL). $\mathbf{P3TC6C2_{CHCl_3}}$ and $\mathbf{P3TC6C2_{CB}}$ were fully dissolved under heating and the solutions left to stand overnight at rt to reach an equilibrium of aggregation. The black spectra in Figure 4.5 a and b represent the absorption properties of both batches at rt. A very defined fine structure is seen, with superimposed absorption bands with maxima at approximately 510, 547 and 583 nm for $\mathbf{P3TC6C2_{CB}}$ and 506, 536 and 583 nm for $\mathbf{P3TC6C2_{CHCl_3}}$ fraction. The band at the lowest wavelength corresponds to freely dissolved chains, which exhibit a low degree of planarization and thus shorter average conjugation lengths. The ~540 nm and ~580 nm bands can be ascribed to the 0-0 and 0-1 transitions starting to appear in more planarized, aggregated polymer species, respectively.[62, 63] The ratio of the three bands is very different for the two **P3TC6C2** fractions, with $\mathbf{P3TC6C2_{CB}}$ exhibiting much more prominent aggregation-related maxima compared to $\mathbf{P3TC6C2_{CHCl_3}}$, for which the band corresponding to free

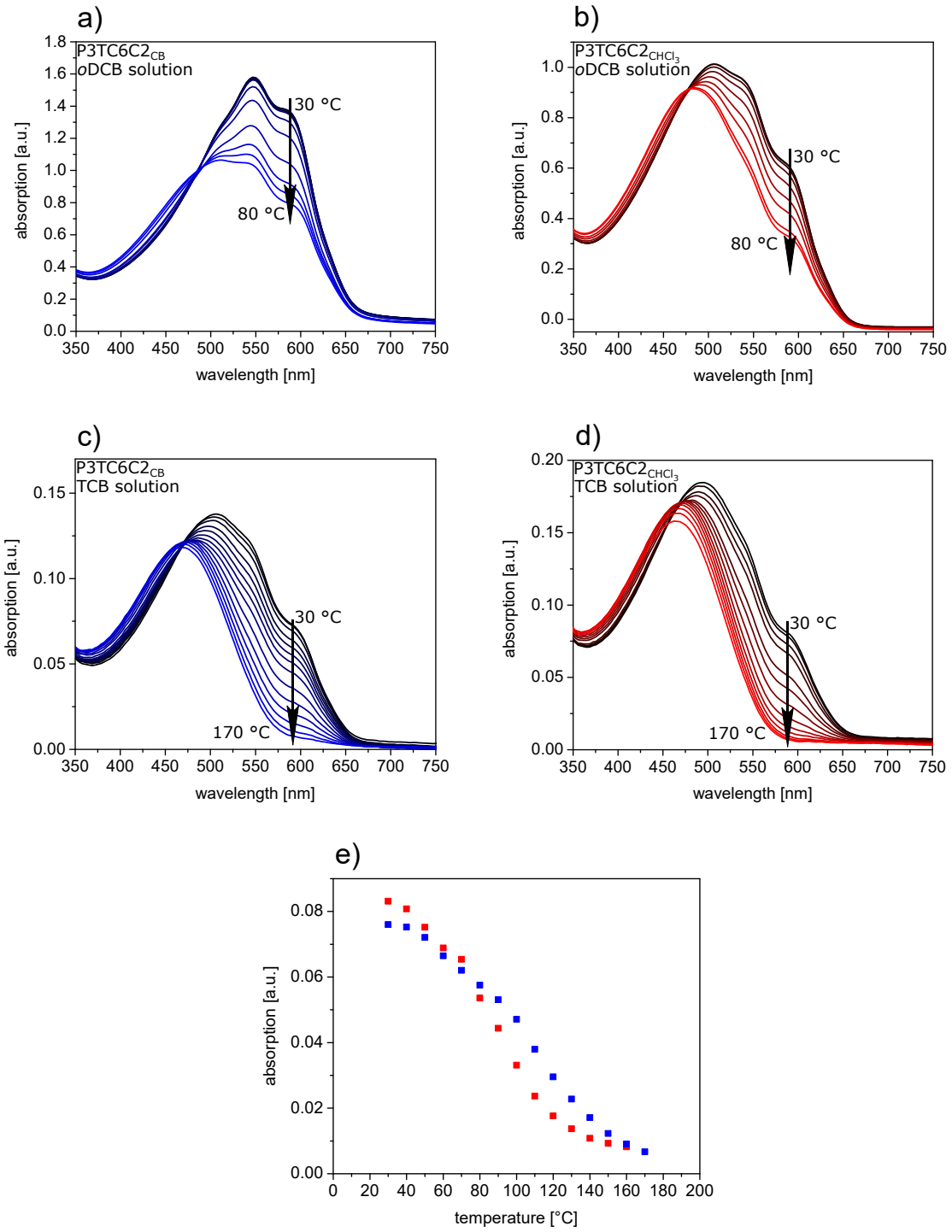

Figure 4.5: Temperature-dependent absorption spectroscopy measurements of **P3TC6C2$_{CB}$** (blue) and **P3TC6C2$_{CHCl_3}$** (red) in 3 mg/mL *o*DCB (a, b) and TCB (c, d) solutions. *o*DCB solutions were heated from rt to 80 °C and 1,2,4-trichlorobenzene solutions were heated to 170 °C. e) Peak trends corresponding to wavelengths of 583 nm in measurements c and d. This band, which corresponds to the 0-1 interchain vibrational transition, provides the best measure for the vanishing of the aggregation-related fine structure with rising solution temperature.

chains was more significant. A higher aggregation tendency can thus be assumed for the sample with higher molecular weight.

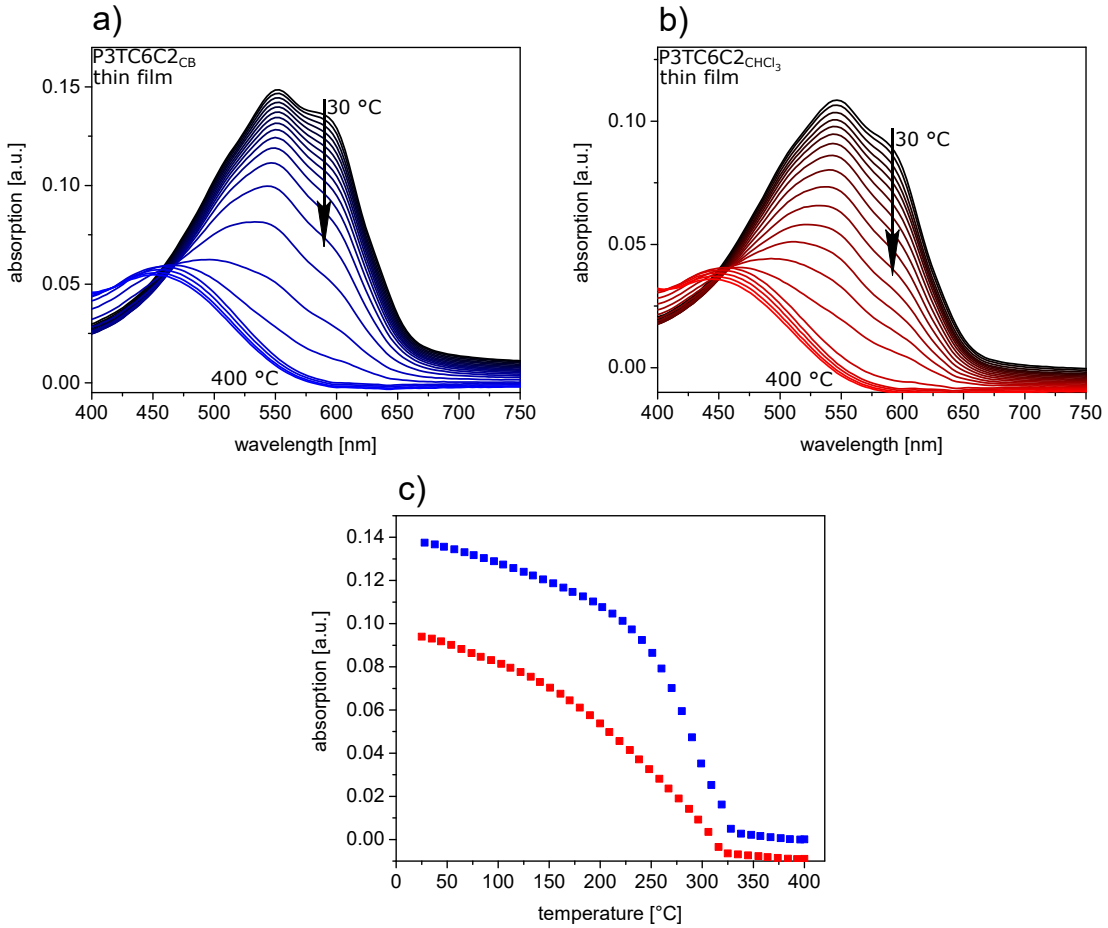

Figure 4.6: a), b) Temperature-dependent absorption spectroscopy measurements of thin films spin coated from 3 mg/mL *o*DCB solution of **P3TC6C2$_{CB}$** (blue) and **P3TC6C2$_{CHCl_3}$** (red) from rt to 400 °C. e) Peak trends corresponding to wavelengths of 580 nm.

Overall, the spectrum of **P3TC6C2$_{CB}$** closely resembles the room temperature *o*DCB solution spectrum of **P3TC8C4**, while the two aggregation-related shoulders are even more pronounced. However, when the solubilities at elevated temperatures are compared, differences become very obvious.[7] The solutions of both batches were slowly heated (1 K/min) from rt to 80 °C, to ensure aggregation equilibrium at all times (blue and red spectra in Figure 4.5 a and b). While it had been possible to dissolve **P3TC8C4** as fully free polymer chains, despite the higher molecular weight of the batch, in *o*DCB at 80 °C, both **P3TC6C2** fractions still show significant aggregation at this temperature. Again, this is more readily apparent for **P3TC6C2$_{CB}$** than for **P3TC6C2$_{CHCl_3}$**, which already exhibits a main band at $\lambda_{max} = 483$ nm with very weak aggregation shoulders.

When switching the solvent from *o*DCB to 1,2,4-trichlorobenzene (TCB), the higher solvation strength of this solvent is immediately visible. The corresponding room temperature spectra (black graphs in Figure 4.5 c and d) closely resemble the *o*DCB spectra at 80 °C. In addition, TCB exhibits a higher boiling point, allowing to heat the solutions up to the temperature limit of the setup at ~170 °C. It was found that even at such high temperatures, in one of the best solvents available for polythiophenes, a small residual aggregation shoulder at ~590 nm was visible for **P3TC6C2$_{\mathbf{CB}}$**. However, for both *Soxhlet* fractions, the dominant band around 480 nm indicated freely dissolved polymer chains. Figure 4.5 e shows a peak trend of the aggregation shoulder at 583 nm for the TCB solution measurements.

In temperature-dependent thin film absorption measurements (Figure 4.6), both batches behaved very similarly. Polymer films were deposited on glass substrates by spin coating from 3 mg/mL *o*DCB solutions, dried *in vacuo* and heated to 400 °C at a rate of 1 K/min. Again, the spectra showed a distinct fine structure at room temperature, with maxima of the superimposed bands at 512, 552 and 580 nm, very slightly red-shifted compared to the solution spectra. Upon heating, the high-wavelength bands start to decrease slowly between rt and ~150 °C for **P3TC6C2$_{\mathbf{CHCl_3}}$** and ~220 °C for **P3TC6C2$_{\mathbf{CB}}$**, at even higher temperatures this process accelerates even more. Around 325 °C the vibronic fine structure fully vanishes for both polymers. The accelerated decrease of the aggregation bands at higher temperatures coincides with the loss of intermolecular order found in WAXS measurements and the endothermic transition present in DSC in the same temperature range and can thus be likely ascribed to melting of the polymer films as well. At the highest measured temperatures, film spectra for both batches are highly blue-shifted compared to room temperature, showing a broad band with a maximum around 460 nm and without any fine structure, again corresponding to freely moving chains.

4.3 Electrochemical and Chemical Doping

The effect of β-conjugation on the backbone π-systems in branched or linear π-extended polythiophenes has been shown to lead to an often significant lowering of the frontier orbital levels compared to the parent linear **P3AT**s.[172–174] For our **3T**-based materials, HOMO and LUMO values of -5.4/3.1 eV, -5.6/-3.1 eV and -5.6/-3.0 eV were found for (electro)chemically synthesized hyberbranched systems, **P3TC16** and the **P3TCxCy**s, respectively, using the value of -5.1 eV for the internal standard redox couple Fc/Fc$^+$ on

the *Fermi* scale.[5, 7, 171] A possible benefit can be found in the potentially higher stability against oxidation by atmospheric oxygen, which is a key aspect when applicability of the materials in organic electronics devices under real-world conditions is the goal. As far as electrochemical or chemical p-type doping is concerned, higher oxidation potentials or stronger oxidation agents are thus needed to generate polaronic or even bipolaronic charge carrier species.

Table 4.4: Frontier orbital levels of **P3TC6C2**, its analogues, chemically and electrochemically synthesized hyberbranched **P3T** and **P3HT**, determined from electrochemical cyclic voltammetry measurements against the reference Fc/Fc^+, assuming a value of -5.1 eV on the *Fermi* scale. Band gap values E_g are calculated as the difference between HOMO and LUMO levels.

Polymer	E_{ox}[V]	HOMO [eV]	E_{red}[V]	LUMO [eV]	E_g [eV]
P3HT[57]	0.02	-5.12	-2.26	-2.84	2.28
$\mathbf{P3T_{ch}}$[171]	0.28	-5.40	-2.02	-3.08	2.32
$\mathbf{P3T_{ec}}$[171]	0.31	-5.43	-2.04	-3.06	2.37
P3TC16[5]	0.46	-5.56	-2.04	-3.06	2.50
P3TC12C8[6]	0.5	-5.6	-2.1	-3.0	2.6
P3TC10C6[6]	0.5	-5.6	-2.1	-3.0	2.6
P3TC8C4[6]	0.5	-5.6	-2.1	-3.0	2.6
$\mathbf{P3TC6C2_{CHCl_3}}$	0.4	-5.5	n/d	n/d	n/d
$\mathbf{P3TC6C2_{CB}}$	0.4	-5.5	n/d	n/d	n/d

To study the oxidative doping behavior, **P3TC6C2** was subjected to spectroelectrochemical measurements as well as chemical doping under spectroscopic control.
For spectroelectrochemistry, films of $\mathbf{P3TC6C2_{CHCl_3}}$ were deposited on indium tin oxide (ITO) electrodes from 5 mg/mL solutions in *o*DCB, dried and employed as the working electrode in a three-electrode electrochemical cell. The films were oxidized by cyclic voltammetry in 0.1 M NBu_4PF_6 solution in acetonitrile as the supporting electrolyte at a scan rate of 20 mV/s. Optical absorption spectra of the films were recorded at each potential step (Figure 4.7 a). The spectral behavior upon oxidation closely resembles the one typically found for **P3AT**s, however, the onset is shifted to higher potentials (**P3TC6C2**: 0.4 V vs. Fc/Fc^+, **P3HT**: 0.02 V).[57] Around the onset of the oxidation wave (0.4 V vs. Fc/Fc^+), the neutral **P3TC6C2** band (543 nm) starts to decrease, accompanied by an increase in absorption of a very broad band with a maximum of approximately 830 nm which is typically attributed to radical cation (polaron) species in polythiophenes.[52] The clearly visible isosbestic point at 630 nm further confirms the interconversion of the neutral

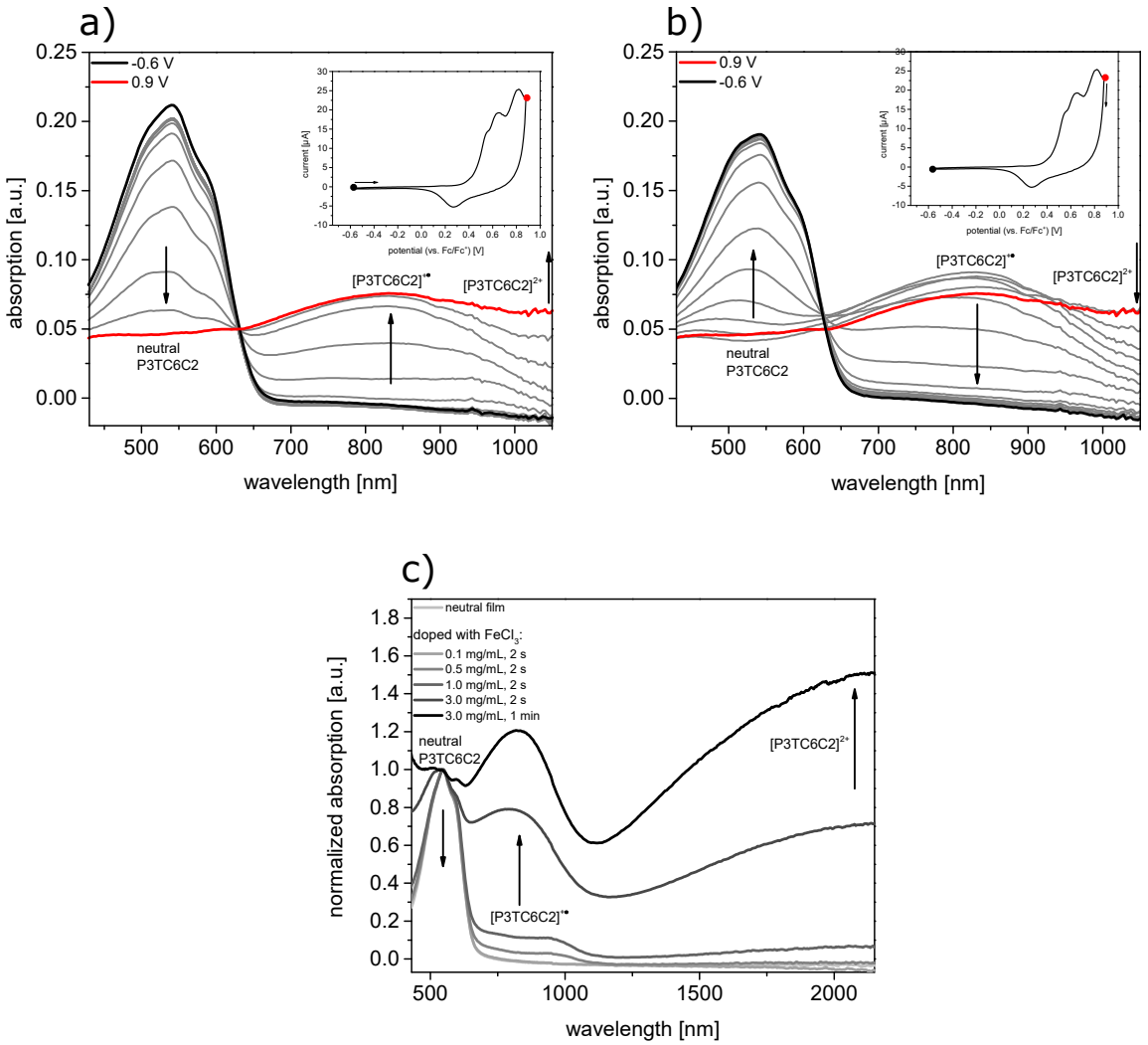

Figure 4.7: Optical absorption properties of $\mathbf{P3TC6C2_{CHCl_3}}$ thin films upon electrochemical doping *via* cyclic voltammetry and chemical doping with iron(III) chloride. a) Charge and b) discharge scan of a CV measurement coupled with *in-situ* UV/Vis spectroscopy. The insets show the corresponding voltammogram. b) Thin film absorption spectra of $\mathbf{P3TC6C2_{CHCl_3}}$, recorded immediately after chemical doping with different concentrations of iron(III) chloride in acetonitrile solution.

into a charged species. As potentials approach the limit of 0.9 V vs. Fc/Fc^+, a broadening of the band accompanied by an increase in absorption around 1050 nm provides indication for beginning formation of bipolaronic species. Notably, the potentials required for this process are at least 300 mV higher than for **P3HT** and even at 0.9 V, the polaron band has not yet started to decrease. Since especially bipolaronic species are associated with irreversible film degradation due to side reactions ("overoxidation"), this provides another indication for higher stability under atmospheric conditions.[37]

For p-type polymers, strong oxidants are typical chemical dopants. Reasonably long-term stable, high conductivities have especially been achieved with 2,3,5,6-tetrafluoro-7,7,8,8-tetracyanoquinodimethane (**F_4TCNQ**), one of the strongest small molecule acceptors known to date. **F_4TCNQ** has a LUMO level at -5.24 eV, as measured *via* UPS and IPES, enabling facile electron transfer from **P3HT** (HOMO ~ 5.0 eV).[40–42] In contrast to **P3HT** however, chemical doping experiments on **P3TC6C2** films on glass substrates with **F_4TCNQ** were unsuccessful. Even for concentrations as high as 5 mg/mL in acetonitrile, polymer films immersed for several minutes did not show any signs of oxidation. When the stronger oxidant **$FeCl_3$** was employed with immersion times between two seconds and one minute, the development of polaronic species for the lower concentrations until 0.5 mg/mL and of bipolaronic species for the higher concentrations was clearly visible (Figure 4.7 b).[53] Conductivities could not be determined using our four-point-probe setup, which is limited to values higher than approximately 10^{-6} S/cm. Since spectroscopic evidence for high doping levels upon **$FeCl_3$** oxidation was found, the low conductivity values are likely connected to structural phenomena, *e.g.* bottlenecks in interchain transport.

4.4 Transistor Measurements

In order to compare the p-type charge carrier mobilities of the **P3TC6C2** batches to the other **P3TCxCy** analogues, bottom-gate/bottom-contact OFET measurements were carried out. Mobilities for the longer side-chain derivatives ranged from $1.2{\cdot}10^{-7}$ to $1.2{\cdot}10^{-5}$ $cm^2V^{-1}s^{-1}$, values at least three orders of magnitude below the reference material **P3HT** which has been shown to be capable of reaching mobilities in the order of 10^{-2} $cm^2V^{-1}s^{-1}$, and in the range of **P3AT**s with longer side chains like **P3DT** ($\sim 7{\cdot}10^{-5}$ $cm^2V^{-1}s^{-1}$).[68] This has been ascribed mainly to the branched side-chains which hinder efficient packing to a certrain degree, as well as the face-on orientation of the polymer chains in **P3TCxCy** films.[6, 7] However, a clear trend of increasing mobilities with decreasing length of the branched side chains had been found. In the previous chapters, a higher temperature-stability of **P3TC6C2** aggregates in solution and thin films has been shown. Compared to the differences between melting temperatures of the other **P3TCxCy**s also a much higher increase in temperatures needed to break up ordered structures in bulk polymer between **P3TC8C4** and **P3TC6C2** has been shown by WAXS and DSC expimeriments (6 °C between **P3TC12C8** and **P3TC10C6**, 90 °C between **P3TC8C4** and **P3TC6C2$_{CB}$**). Since these phenomena greatly correlate with interchain stacking and steric hindrance due to the side chains present for the individual

polymers, it was interesting to study if a similarly high jump in charge carrier mobilities could be observed.

Polymer films of both **P3TC6C2** batches were deposited from 5 mg/mL *o*DCB solutions, either directly on the precleaned transistor substrates or on substrates which had been treated with octadecyltrichlorosilane (**ODTS**) vapors for the formation of a self-assembled monolayer (SAM) on the SiO_x surface.[6, 299] Such SAMs have been shown to be very beneficial to increase crystallization and order in conjugated polymer films, since they decrease the hydrophilicity of the SiO_x surface and lead to a more suitable interaction with the highly hydrophobic polymers during film formation. This is especially important in bottom-gate transistors, where charge carriers travel through the channel directly at the substrate-polymer interface.

Output curves were recorded at source-drain voltages between 0 and -80 V and gate potential steps of 20 V between 0 and -80 V. Transfer characteristics were determined between V_g of 20 and -80 V at V_{sd} = -80 V. As can be seen in Figure 4.8, the quality of the obtained output curves greatly improved when **ODTS** treated substrates were used. Similar observations had also been made for the other **P3TCxCy** derivatives.

Charge carrier mobilities for the **P3TC6C2** batches ranged from $2.0 \cdot 10^{-5}$ to $6.3 \cdot 10^{-5}$ $cm^2V^{-1}s^{-1}$ with the CB batch showing overall marginally higher values (Table 4.5). This corresponds to an increase in mobilities of almost one order of magnitude compared to **P3TC8C4**. Threshold voltages significantly increased when transistors of $\mathbf{P3TC6C2_{CHCl_3}}$ were annealed at 100 °C, which might be explained by the generation of trap states within the polymer films.

Transistors of the $\mathbf{P3TC6C2_{CHCl_3}}$ were further investigated by atomic force microscopy (AFM) to gain insights into the structure of the films on the nanometer scale (Figure 4.9). The film structure found is most comparable to the one obtained for as-cast films of **P3TC8C4** deposited on glass substrates from the same solvent. Compared to the longer side-chain analogues **P3TC12C8** and **P3TC10C6**, both show less smooth surfaces which can be mainly attributed to the higher degree of aggregation in room temperature solutions. Upon closer inspection of the phase image, a slight texture of the film is visible, pointing at the presence of small, unordered aggregates in the film. These can be related to the fine structure present in the thin film absorption spectra shown earlier. However, no indications for long-range order, a preferred orientation or lamellar-like structures were obtained. This finding corresponded with the absence of birefringence in polarized optical microscopy (POM). Attempted solvent-vapor annealing with chloroform and CS_2 vapors was unsuccessful, presumably due to the low solubility of **P3TC6C2**.

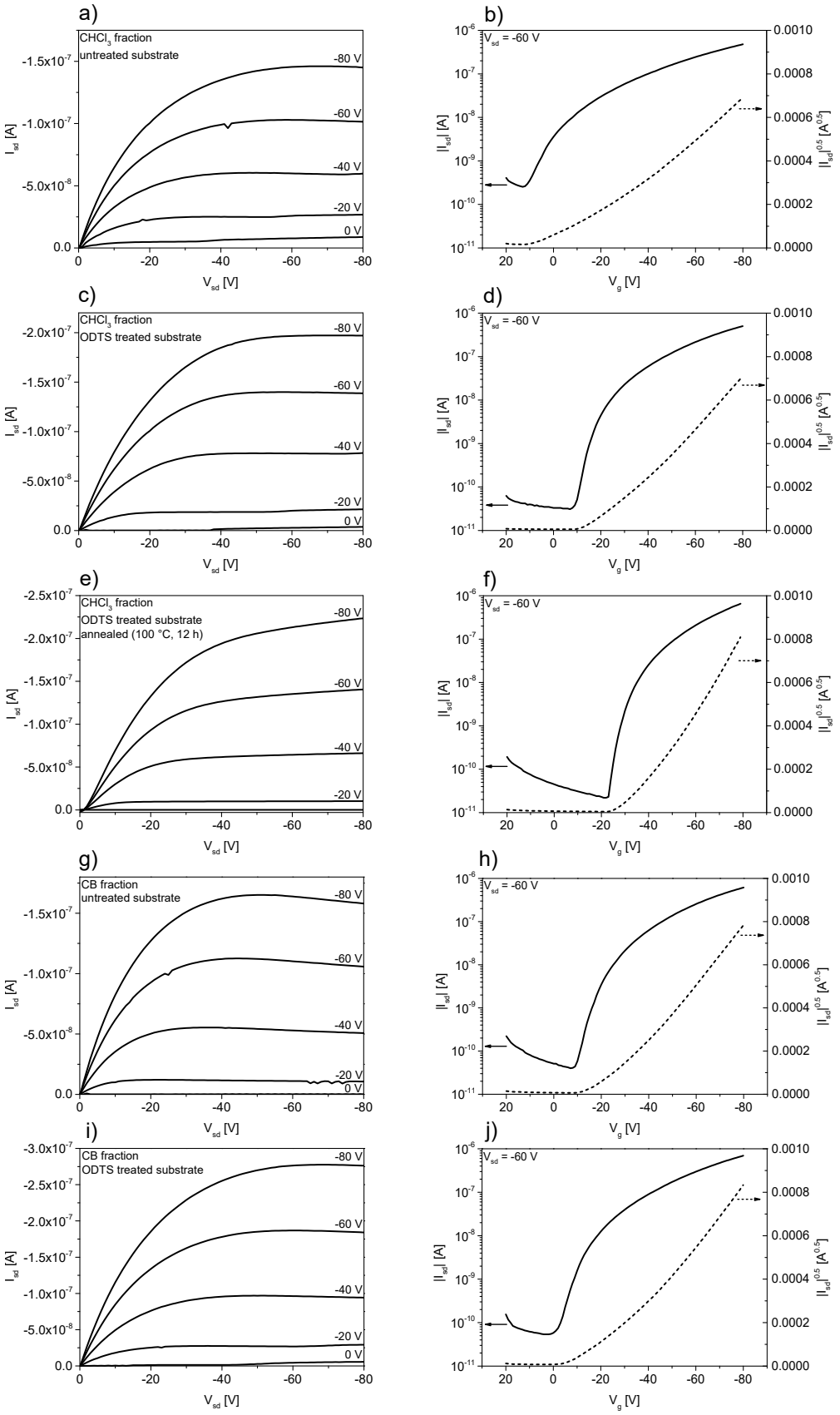

Figure 4.8: Output (left) and transfer (right) characteristics of a)-f) **P3TC6C2$_{\mathbf{CHCl_3}}$** and g)-j) **P3TC6C2$_{\mathbf{CB}}$** bottom-gate/bottom-contact organic field effect transistors.

Table 4.5: Bottom-gate/bottom-contact OFET characteristics of **P3TC6C2$_{CHCl_3}$** and **P3TC6C2$_{CB}$** on pristine and **ODTS** treated transistor substrates, compared to the respective analogues and **P3HT**.

	μ [cm^{2}V^{-1}s^{-1}][a]	V_{th} [V][b]	I_{on}/I_{off}[c]
P3HT[68]	$1\cdot10^{-2}$	-	10^4
P3TC16[4]			
untreated substrate	$4.5\cdot10^{-4}$	9	10^5
ODTS treated substrate	$2.3\cdot10^{-3}$	7	10^5
ODTS treated substrate, annealed (140 °C, 2 h)	$1.4\cdot10^{-2}$	-	-
P3TC12C8[6]			
untreated substrate	$1.2\cdot10^{-7}$	-	14[d]
ODTS treated substrate	$7.6\cdot10^{-7}$	-4	4603[d]
ODTS treated substrate, annealed (120 °C, 1 h)	$1.1\cdot10^{-6}$	-17	973[d]
P3TC10C6[6]			
untreated substrate	$4.4\cdot10^{-6}$	-47	1531[d]
ODTS treated substrate	$2.9\cdot10^{-6}$	-17	1913[d]
ODTS treated substrate, annealed (120 °C, 1 h)	$1.2\cdot10^{-6}$	-18	780[d]
P3TC8C4[6]			
untreated substrate	$7.4\cdot10^{-6}$	-42	1987[d]
ODTS treated substrate	$1.6\cdot10^{-6}$	-3	762[d]
ODTS treated substrate, annealed (120 °C, 1 h)	$3.8\cdot10^{-6}$	-2	1851[d]
P3TC6C2$_{CHCl_3}$			
untreated substrate	$2.0\cdot10^{-5}\pm2.7\cdot10^{-6}$	-2±1	$1.9\cdot10^3$
ODTS treated substrate	$2.8\cdot10^{-5}\pm5.3\cdot10^{-6}$	-18±5	$1.6\cdot10^4$
ODTS treated substrate, annealed (100 °C, 12 h)	$6.3\cdot10^{-5}\pm2.9\cdot10^{-6}$	-26±3	$1.2\cdot10^5$
P3TC6C2$_{CB}$			
untreated substrate	$4.1\cdot10^{-5}\pm8.6\cdot10^{-7}$	-12±5	$1.5\cdot10^4$
ODTS treated substrate	$3.7\cdot10^{-5}\pm1.2\cdot10^{-5}$	-12±3	$1.3\cdot10^4$

a) Field effect mobilities determined from slope of linear fit $\frac{\partial\sqrt{|I_{sd}|}}{\partial V_g}$ at V_{sd} = -80 V. b) Threshold voltages determined from x-axis intercept of the same fit. c) On/off current ratios determined between minimum and maximum source-drain current values of a representative transistor. d) Values determined from the ratio between maximum source-drain current and the respective current values at $V_g = 0$ V.

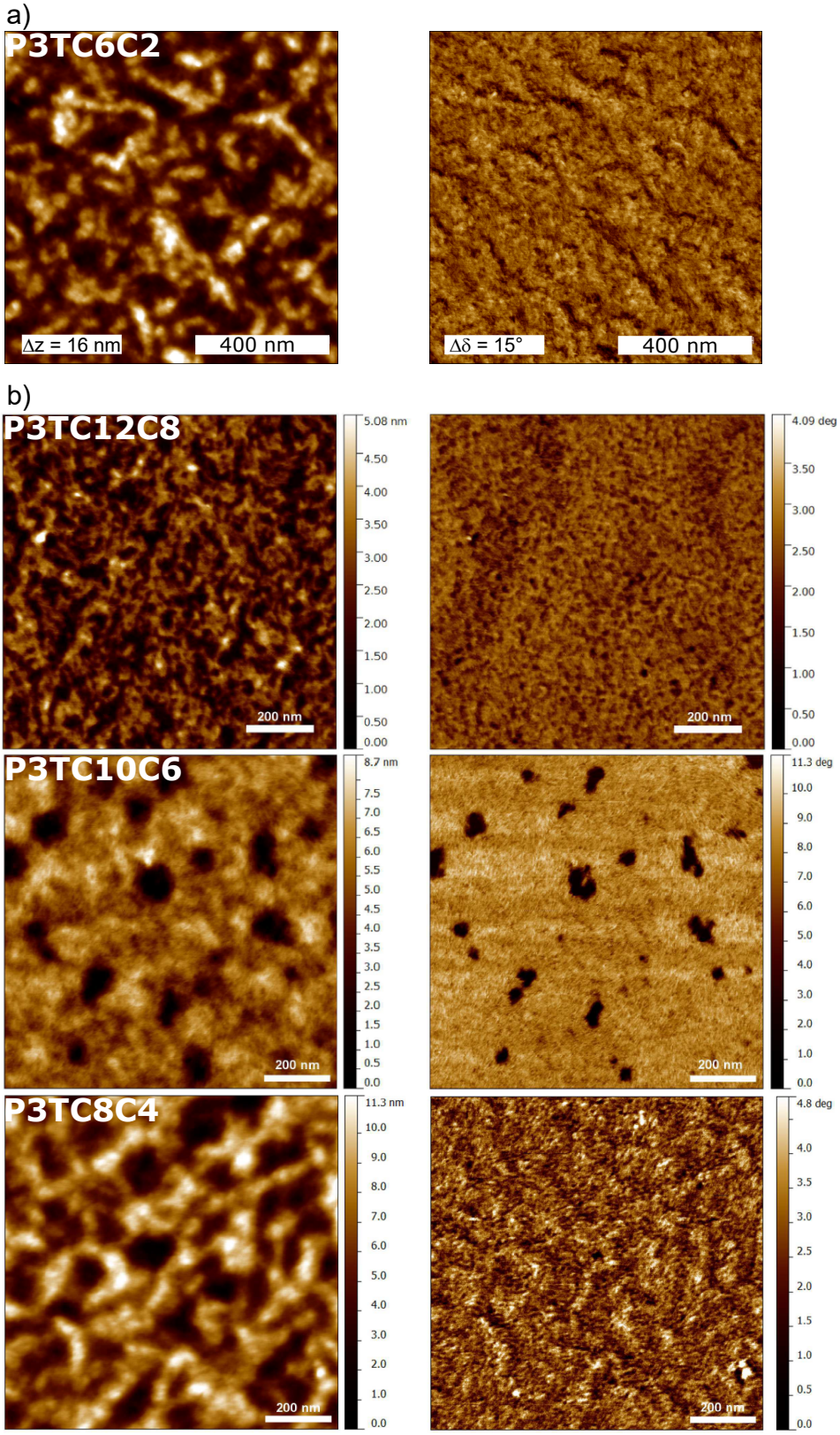

Figure 4.9: AFM height (left) and phase (right) images of a) **P3TC6C2$_{CHCl_3}$** thin films cast on an OFET substrate from *o*DCB (5 mg/mL). b) AFM images of **P3TC12C8**, **P3TC10C6** and **P3TC8C4** as-cast thin films on glass substrates for comparison. Data measured by *Dr. Martin Scheuble*.[6] Adapted with permission from [6].

4.5 Summary

As presented in this chapter, it was possible to synthesize the side-chain π-extended analogue **P3TC6C2** by the same convergent method applied for the other **P3TCxCy** derivatives.[7] During monomer synthesis, the shorter side chains even slightly facilitated purification of the intermediates by column chromatography. Upon polymerization, already a significantly decreased solubility of the material was found, resulting in low yields of soluble polymer after *Soxhlet* purification, the need for the high-boiling solvent chlorobenzene and slightly lower molecular weights despite the identical reaction conditions. The chloroform and chlorobenzene fractions with $\overline{M_n} = 7.5$ and 10 kg/mol, respectively, were investigated further.

Evaluation of the thermal properties of bulk polymer powders by DSC and TGA measurements revealed melting points at 291 (**P3TC6C2$_{\mathbf{CHCl_3}}$**) and 300 °C (**P3TC6C2$_{\mathbf{CB}}$**), values significantly higher than for **P3TC8C4**. A roughly exponential trend of T_m values with decreasing side chain lengths could be observed. The polymers were stable up to ~422 °C under inert conditions. In accordance with experiments performed on **P3TC12C8**, temperature-dependent WAXS measurements showed a slight widening of interchain distances in the direction of the alkyl chains, accompanied by a sharpening and increase of intensity of the associated d_{100} reflex up to 260 °C. At even higher temperatures, the intensity decreased, indicating loss of order which could be ascribed to the beginning melting transition found in this temperature range. Like for the other **P3TCxCy**s, this process seems to mainly involve the side chain direction.

The significantly higher temperatures needed for breaking up intermolecular order are registered in solution and thin film optical absorption measurements as well. Compared to the other **P3TCxCy** derivatives, for which heating of CB solutions to 80 °C was sufficient to produce fully dissolved chains in all cases, for **P3TC6C2**, this point could only be reached in 1,2,4-trichlorobenzene at 170 °C. Similar trends were observed for film measurements, in which a complete loss of fine structure in the spectra could only be reached at temperatures higher than 325 °C, as compared to ~255 °C for **P3TC8C4**.

Attempts to electrochemically and chemically dope the thin films of the material under spectroscopic control yielded optical properties very comparable to other polythiophenes like **P3HT**, albeit with higher potentials and stronger chemical oxidation agents necessary to reach the same effects.[52, 53] This was best visible in the complete inability of the acceptor molecule **F$_4$TCNQ**, which can easily oxidize **P3HT**, to dope **P3TC6C2**.[40, 47] Similar experiments with iron(III) chloride were successful and judging from spectroscopic results, high doping levels could be reached. However, it was not possible to measure

conductivity values using four-point-probe equipment, *i.e.* the values most likely lie below 10^{-6} S/cm. This is 6-7 orders of magnitude lower than for doped **P3HT**, suggesting that charge transport must be impeded by factors other than doping levels, *e.g.* bottlenecks in interchain charge transport.
The obtained charge carrier mobility values from **P3TC6C2** OFET measurements (up to $6.3 \cdot 10^{-5} \pm 2.9 \cdot 10^{-6}$ $cm^2V^{-1}s^{-1}$) were still not competitive with reference materials like **P3HT**.[68] However, they represented an improvement of about one order of magnitude over the mobilities of **P3TC8C4**, confirming again that a decrease in side chain lengths in these systems has a generally favorable effect. Attachment of **ODTS** self-assembled monolayers to the transistor substrate surface improved output and transfer characteristics in terms of threshold voltages and on/off ratios. However, the effect on measured mobilities was rather minor. AFM investigations of the transistors showed film surfaces comparable to **P3TC8C4** thin films on glass.

5 Smart Materials through Alkyl Side-chain Modifications

5.1 Electronic Conductivity of Conjugated Polyelectrolytes

Parts of this chapter have been published:

Mixed conductivity of polythiophene-based ionic polymers under controlled conditions
R. Merkle, P. Gutbrod, P. Reinold, M. Katzmaier, R. Tkachov, J. Maier, S. Ludwigs
Polymer **2017**, *132*, 216.

Conjugated polyelectrolyte materials are, under suitable conditions, able to exhibit simultaneous electronic and ionic conductivity, opening potential applications for example in charge storage devices or electrochemical transistors.[207, 300] There, CPEs compete with state-of-the-art mixed-conductor blend materials like **PEDOT/PSS**, which are essentially combinations of doped conjugated polymers and separate polyelectrolyte materials stabilizing the CP in its doped state.[301] Although conjugated polyelectrolytes have not yet reached the performances of these blends in many applications, they are interesting alternatives, mainly due to synthetic flexibility allowing for virtually unlimited combinations of backbones and pendant groups and the ability to tailor their properties over a wide range. For non-auto-doped CPEs, the two conductivity regimes exist mostly independently in the same material, *i.e.* electronic charge transport takes place mainly along the (doped) backbone π-systems and by charge carrier hopping from chain to chain, while the ionic pendant groups are exclusively involved in ionic conductivity.
Decoupling and independently studying electronic and ionic conductivities in CPE systems is not a trivial task, since most measurement methods are only able to determine combined conductivity values. In addition, both processes are highly dependent on external factors, like solvent content in the case of ionic conductivity and dopant concentrations for electronic conductivity. Depending on the conditions, both conductivities can vary over several orders of magnitude and ionic conductivity can be largely dominated by electronic processes or *vice versa*. Auto-doping phenomena obviously further complicate matters. In collaboration with *Prof. Dr. Joachim Maier* and *Dr. Rotraut Merkle* from *Max Planck Institute for Solid State Research*, Stuttgart, our group started a project to study ionic and electronic conductivity of two regioregular polythiophene-based CPE model systems,

one anionic and one cationic, under controlled conditions. My contribution to this project was the synthesis and basic characterization of one of the materials (**PTIm-Br**), the evaluation of solubility and aggregation phenomena by optical absorption spectroscopy, as well as the determination of electronic conductivities upon external chemical doping of the polymers. These results will be presented in this chapter. For investigations on ionic conductivities under atmospheres of controlled humidity, using a combination of thermogravimetry, impedance spectroscopy and DC measurements, the reader is referred to the joint publication on this project.[11]

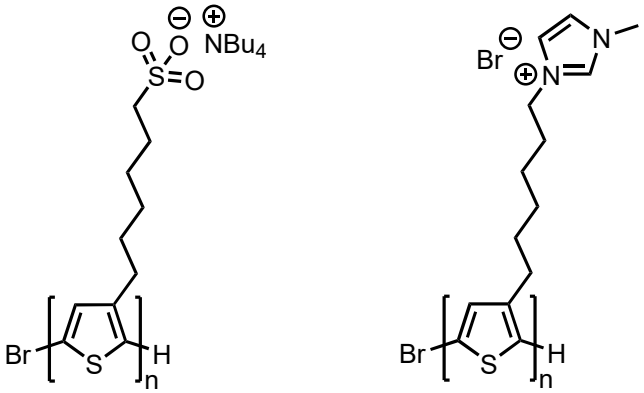

Figure 5.1: Structures of anionic and cationic conjugated polyelectrolytes **PTS-TBA** and **PTIm-Br** studied in this project.

The CPEs consisted of highly regioregular polythiophene backbones bearing tetrabutylammonium sulfonate (termed **PTS-TBA**) or imidazolium bromide (**PTIm-Br**) pendant groups and were specifically chosen since they showed no signs of auto-doping.

5.1.1 Monomer and Polymer Synthesis

The conjugated polyelectrolytes **PTS-TBA** and **PTIm-Br** were synthesized using polymer analogous functionalization reactions based on polythiophene precursor polymers bearing terminal bromide substituents attached to their hexyl side chains (**P3BrHT**). Displacement of these bromide substituents was used for attaching the ionic groups, either by quaternization reaction with 1-methylimidazole (**PTIm-Br**) or substitution with tetrabutylammonium sulfite for **PTS-TBA**. Both batches of **PTS-TBA** including the respective precursor polymers $\mathbf{P3BrHT_{15}}$ and $\mathbf{P3BrHT_{23}}$ were synthesized by *Dr. Roman Tkachov*. The synthesis protocols for these polymers are given in the Experimental Part of this thesis (chapter 7) for reference.

Synthesis of Precursor Polymers

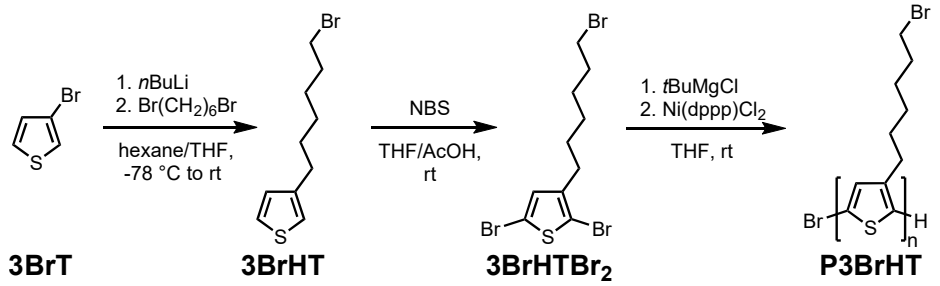

Scheme 5.1: Synthesis of monomers and polymerization procedure for precursor polymer **P3BrHT**$_8$.

Three batches of the precursor polymers **P3BrHT** were synthesized adapting literature protocols (Scheme 5.1), starting from 3-bromothiophene (**3BrT**), which was first reacted with *n*BuLi, the lithiate precipitated at -78 °C and the supernatant containing all impurities removed under protective atmosphere *via* cannula.[302]

Table 5.1: Molecular properties of precursor polymers **P3BrHT$_8$**, **P3BrHT$_{15}$** and **P3BrHT$_{23}$**.

Polymer batch	$\overline{M_n}$[a)]	$\overline{M_w}$[a)]	PDI[a)]
P3BrHT$_8$	8.0	13.0	1.6
P3BrHT$_{15}$	15.0	18.0	1.2
P3BrHT$_{23}$	23.0	31.0	1.3

a) Molecular weight averages (in kg/mol) and polydispersity indices were determined by SEC (THF solution, rt), calibrated against polystyrene standards.

Clean solvents were added and a ten-fold excess of 1,6-dibromohexane was used, into which the precipitate was allowed to slowly melt to suppress the formation of twice thiophene-substituted derivatives. These would later lead to crosslinked chains during the course of the polymerization reaction. The product was then dibrominated using NBS. GRIM polymerization was then carried out by generation of the *Grignard* reagent followed by addition of the catalyst Ni(dppp)Cl_2, yielding the precursor polymers **P3BrHT**. SEC yielded the molecular properties of **P3BrHT$_8$** ($\overline{M_n}$ = 8 kg/mol, PDI = 1.6). The two batches **P3BrHT$_{15}$** ($\overline{M_n}$ = 15 kg/mol, PDI = 1.2) and **P3BrHT$_{23}$** ($\overline{M_n}$ = 23 kg/mol, PDI = 1.3) were synthesized by Dr. Roman Tkachov using a slightly different procedure (see chapter 7).

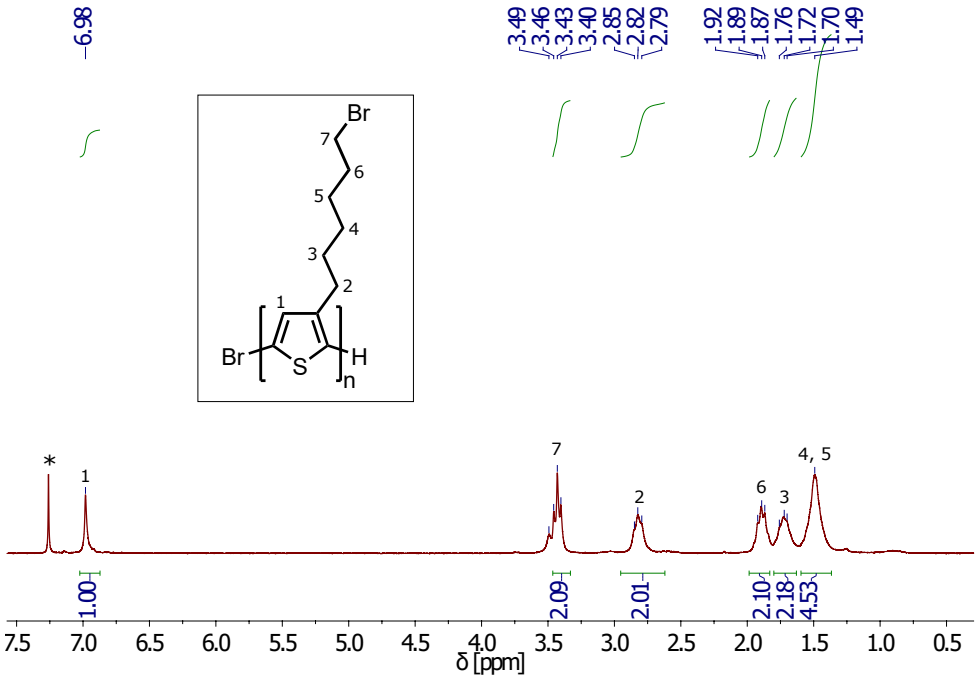

Figure 5.2: ^{1}H-NMR spectrum of purified precursor polymers **P3BrHT$_8$** (room temperature, $CDCl_3$).

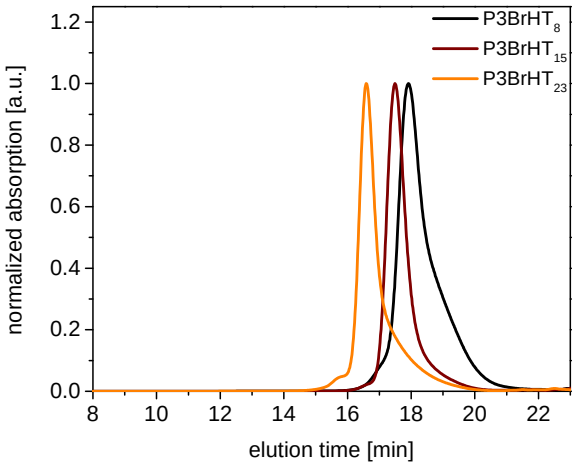

Figure 5.3: SEC chromatograms of precursor polymers **P3BrHT$_8$**, **P3BrHT$_{15}$** and **P3BrHT$_{23}$**.

Polymer Analogous Functionalizations

The CPEs **PTIm-Br** and **PTS-TBA** were synthesized from their respective precursor polymers by post-polymerization reactions (see Scheme 5.2).

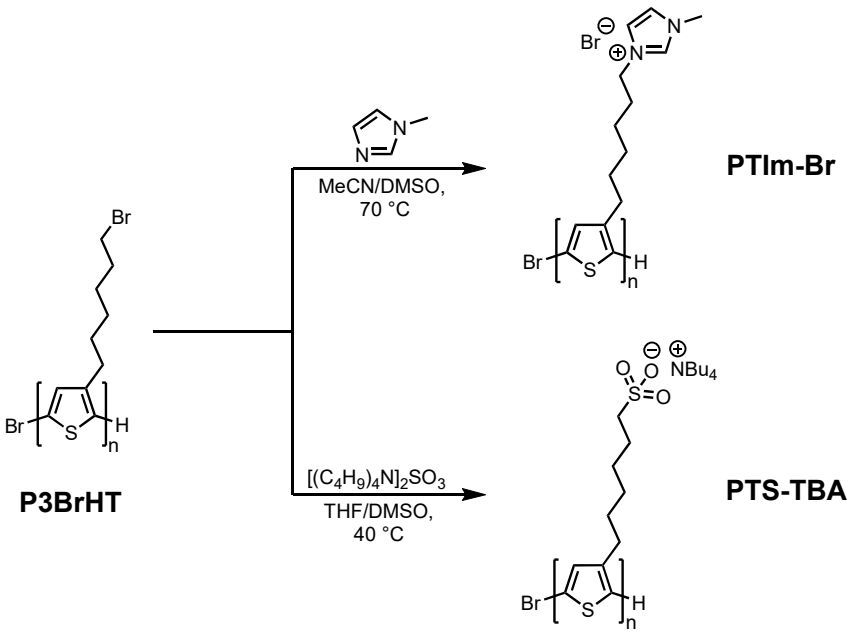

Scheme 5.2: Polymer analogous functionalizations of **P3BrHT** yielding conjugated polyelectrolytes **PTIm-Br** and **PTS-TBA**.

Quaternization reaction of $\mathbf{P3BrHT_8}$ with 1-methylimidazole in an acetonitrile/DMSO mixture at 70 °C yielded **PTIm-Br**.[10] The progressing reaction could be conveniently followed by slow dissolution of the previously fully insoluble polymer powder of **P3BrHT** upon successive development of ionic imidazolium bromide moieties. The pure conjugated polyelectrolyte could be isolated by simple precipitation in THF. Successful introduction of imidazolium groups could be proven by ^{1}H-NMR (Figure 5.4) and IR spectroscopy (Figure 5.6), which corresponded to literature results. Especially the appearance of imidazolium-related signals at 7.86, 7.75, 7.20 and 3.87 ppm, as well as the shift of the alkyl proton adjacent to the pendant group to 4.21 ppm gave clear indications for a quantitative functionalization.

Two batches of **PTS-TBA** were previously synthesized by *Dr. Roman Tkachov* by reacting $\mathbf{P3BrHT_{15}}$ and $\mathbf{P3BrHT_{23}}$ with tetrabutylammonium sulfite at 40 °C in a mixture of THF and DMSO.[9] Purification was performed by dialysis against ultrapure water followed by lyophilization, yielding **PTS-TBA-1** and **PTS-TBA-2**, respectively. ^{1}H-NMR spectra corresponded with literature results. (Figure 5.5). Presumably due to strong aggregation of the backbone, the signal of the thiophene proton is suppressed. Signals get increasingly well-resolved upon increasing distance from the backbone, which is especially significant for the counterion alkyl signals. Comparison of the integrals of the tetrabutylammonium CH_3 proton signal at 0.90 ppm and the multiplet at 2.71 ppm

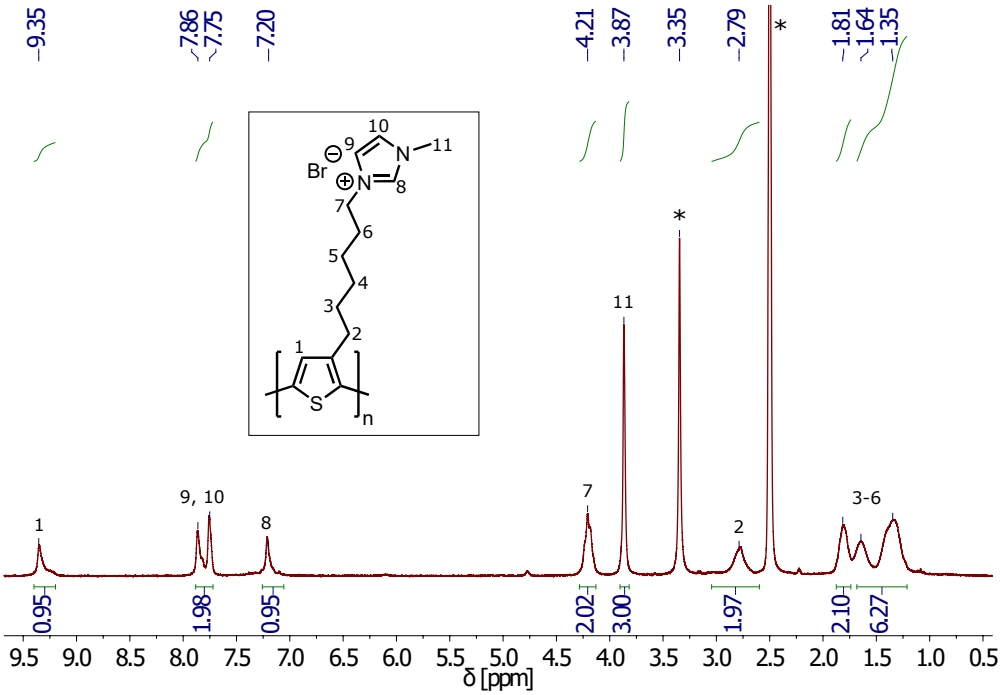

Figure 5.4: ^{1}H-NMR spectrum of purified CPE **PTIm-Br** (room temperature, DMSO-d6).

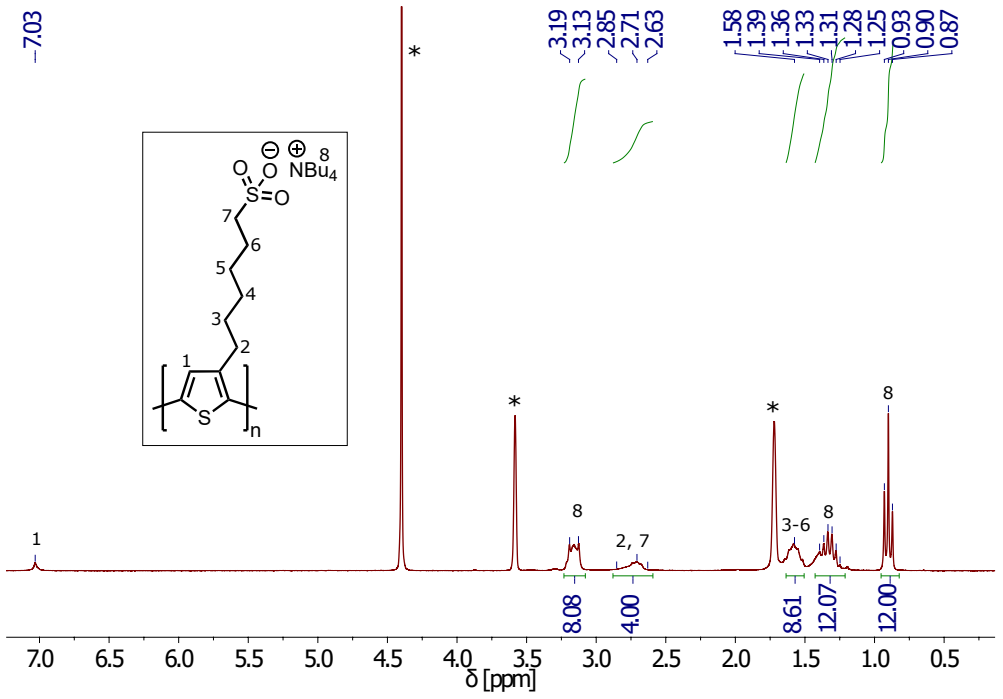

Figure 5.5: ^{1}H-NMR spectrum of purified CPE **PTS-TBA** (room temperature, THF-d8:D_2O = 2:1).

corresponding to two of the side-chain CH_2-groups allowed to confirm a quantitative polymer analogous functionalization.

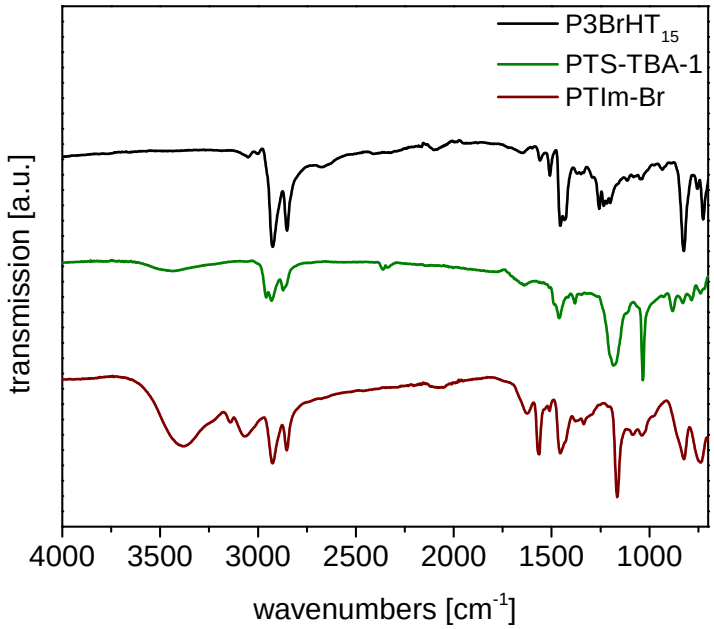

Figure 5.6: Comparison of IR spectra of the precursor polymer **P3BrHT$_{15}$**, as well as functionalized CPEs **PTS-TBA-1** and **PTIm-Br**.

5.1.2 Solution and Thin Film Absorption Properties

Figure 5.7 shows optical absorption spectra of **PTS-TBA-1** and **PTIm-Br** both in solution and in thin films. Methanol and water were used as solvents to compare the tendency of aggregation of the polymers. Solution measurements suggest that methanol is a rather good solvent for both polymers. The spectra exhibit featureless absorption bands with maxima at 444 and 436 nm for **PTS-TBA** and **PTIm-Br**, corresponding to bright orange solutions. In analogy to **P3HT** such spectra can be attributed to ideally dissolved, free polymer chains in solution.[57] The fact that both CPEs can be fully dissolved in methanol, without any signs of aggregation, already highlights the strong influence of the ionic pendant groups. The complex interplay of electrostatic attractive and repulsive interactions, along with the steric bulk of the pendant groups, seems to overpower the backbone π-π stacking interactions which would lead to precipitation in methanol for most non-ionic conjugated polymers like **P3HT**. However, these ion-related

electrostatic interactions can in contrast also lead to polymer aggregation themselves, even if π-π stacking is not present.[213] Such ion aggregation interactions have been shown to cause self-assembly of micellar-like aggregates for some CPEs.[214]

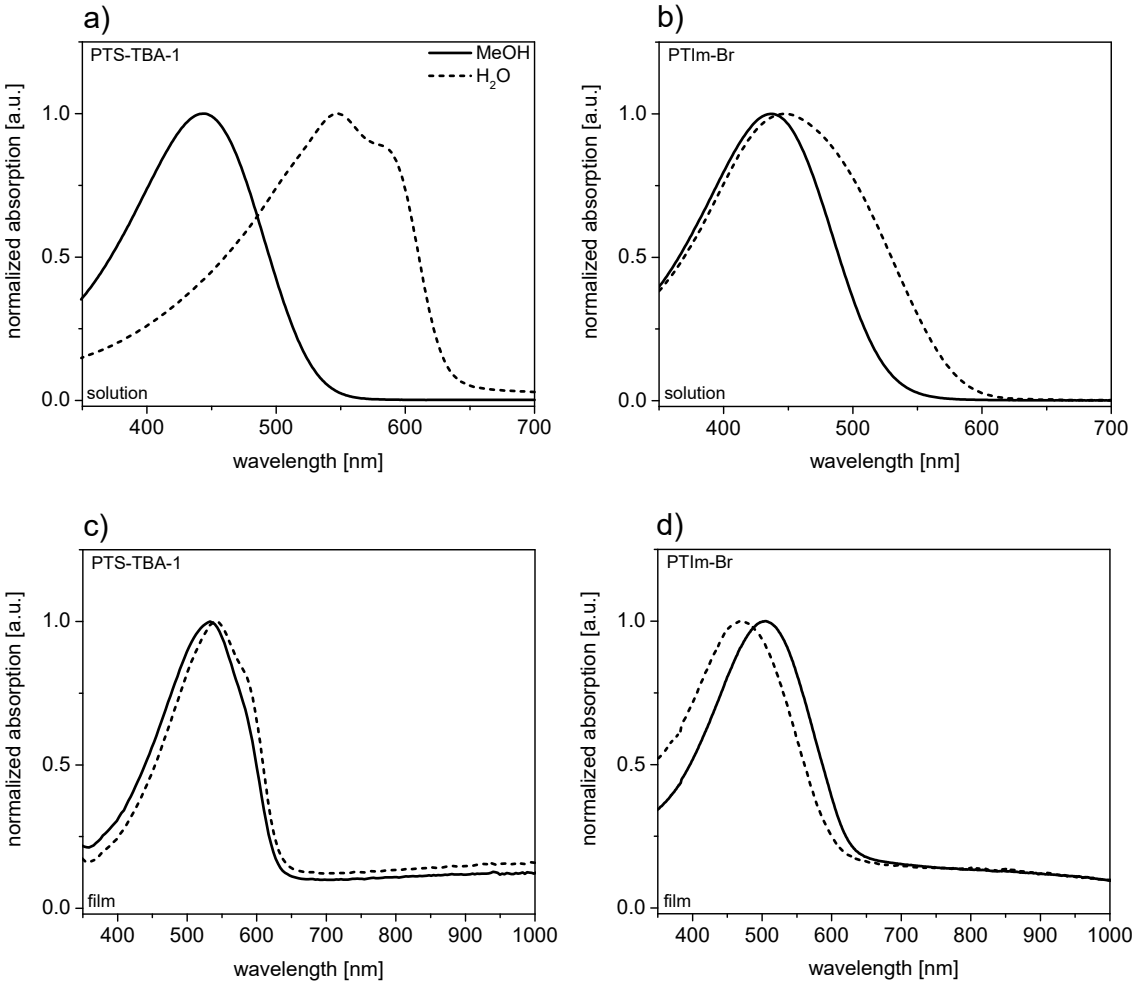

Figure 5.7: a), b) Optical absorption measurements of **PTS-TBA-1** and **PTIm-Br** in 3 mg/mL methanol (solid line) or water (dashed) solutions. c), d) Spectra of thin films spin coated from these solutions.

In aqueous solutions more significant differences between the CPEs were found. **PTS-TBA** exhibits a strongly red-shifted spectrum with a clearly visible fine structure. In addition to the band maximum at 548 nm a shoulder at ~585 nm is found. Such spectra correspond to deep-red to violet colored solutions and are typical for strongly aggregated polythiophene chains.[63] *Thelakkat et al.* found that the aggregation behavior of **PTS-TBA** is strongly dependent on the solvent or mixture of solvents used.[9] **PTIm-Br** spectra however only exhibit a broadening of the main band to higher wavelengths with

the band maximum only shifting very slightly to 448 nm, suggesting a significantly lower degree of planarization through aggregation in water compared to **PTS-TBA**.
Spectra of **PTS-TBA** thin films spin coated from methanol and water solutions show only very minor differences. No signs of the development of bands of charged species in the 600-1000 nm region were found, giving no indication for any auto-doping effects.[193] Both film spectra show a fine structure with band maxima of 533 and 543 nm for MeOH and H_2O films and shoulders around ~590 nm which can be attributed to stacking interactions of the backbones.[57]
PTIm-Br thin films show rather peculiar absorption behavior. Films spin coated from both solvents exhibit fully featureless spectra which are only slightly red-shifted compared to solution measurements, with band maxima at 471 and 505 nm for water and methanol, respectively. The low tendency for aggregation of this CPE has been ascribed to the sterically demanding imidazolium bromide pendant groups in literature.[206] Interestingly, for this polymer the films spin coated from water show an even more "solution-like" absorption behavior which might be related to the rather strong tendency of this polymer to retain water molecules in its periphery. The strongly hydrophilic nature of the polymer is in line with its good water solubility. We even observed strongly hygroscopic behavior leading to the formation of aqueous polymer solution droplets when powders of **PTIm-Br** were left under ambient conditions for several hours. This theory is further supported by literature DSC measurements in which a T_g at 72 °C and endothermic behavior after this T_g in the first heating cycle was found, most probably corresponding to water evaporation from the polymer.[206] Conjugated polyelectrolytes with bromide counterions have been shown to retain water particularly strongly by *Nguyen* and *Bazan*.[303] In addition, IR spectra gave indication for the presence of residual water in both CPEs, but especially in **PTIm-Br** (broad band around 3300 cm^{-1}, Figure 5.6).

5.1.3 Electronic Conductivity of Chemically Doped CPEs

Since experiments on chemical doping of **P3HT** with 2,3,5,6-tetrafluoro-7,7,8,8-tetracyanoquinodimethane (**F_4TCNQ**) had shown promising results, this acceptor molecule was also employed for oxidative doping of the CPEs. **F_4TCNQ** has a LUMO level at -5.24 eV, as measured *via* UPS and IPES, enabling facile electron transfer from **P3HT** (HOMO ~ 5.0 eV).[40–42] Its reduced form, the radical anion **$F_4TCNQ^{-\bullet}$**, has been shown to form a stable charge-transfer complex with polythiophenes both in solution and in thin films.[41, 43–46] This, in conjunction with being a bulky counterion, leads to a relatively even distribution inside the polymer films and reduced diffusion of the counterion

through the film, making these doped films stable even under ambient conditions for several days with minimal decreases in conductivity. The measured values of conductivity of polythiophenes doped with this dopant are among the highest reported, with **P3HT** films reaching conductivities up to ~10 S/cm.[40, 47] Thus, this dopant is investigated intensely for applications in thermoelectric generators.[89, 304, 305] Furthermore, slight **F_4TCNQ** doping has been applied *e.g.* to OSCs and OFETs.[306, 307] The improvements in characteristics of the respective devices have been attributed to an interplay of increases in hole mobilities, improved charge carrier injection from the electrodes and, most importantly, the filling of trap states through the charges additionally created *via* the doping reaction.
The electronic conductivity values of the CPEs chemically doped with **F_4TCNQ** were measured using the four-point-probe method which excludes influences of resistances between the polymer film and the metal contacts.[308] Absorption properties of the doped thin films on glass substrates were investigated simultaneously. Measurements on **PTS-TBA** were performed by *Moritz Katzmaier* during the course of his research internships, partly under supervision by *Philipp Gutbrod* and myself.
A recently reported sequential doping method according to *Moulé et al.* and *Schwartz et al.* was adapted.[40, 47] CPE films were first deposited on glass substrates by spin coating and dried *in vacuo*. Subsequently, the substrates were fixed on a spin coater chuck, covered with a solution of the dopant in the orthogonal solvent THF of varying concentration (0.1-4 mg/mL) and any excess solution was removed by spinning off after a waiting time of 5 seconds. Absorption spectroscopy and conductivity measurements were performed immediately to exclude dedoping or film degradation.
At the lowest **F_4TCNQ** concentrations conductivity values around $4 \cdot 10^{-6}$ S/cm for the **PTS-TBA-2** batch and $2 \cdot 10^{-5}$ S/cm for **PTS-TBA-1** were measured (Figure 5.8). At higher dopant concentrations conductivities reached saturation around 0.5 mg/mL, with the highest measured values at 2.3±0.8 S/cm (**PTS-TBA-2**) and 0.6±0.1 S/cm (**PTS-TBA-1**). These values are remarkably high, considering the sterically demanding side chains bearing ionic groups including the respective counterions, which also lead to complex electrostatic attraction and repulsion interactions. The non-ionic reference material **P3HT** has been shown to be capable of reaching saturation conductivity values around 5-8 S/cm when doped with **F_4TCNQ**.[40, 47]
UV/Vis absorption properties (Figure 5.9) recorded immediately after the four-point-probe measurements showed trends corresponding well to the conductivity values.[309] The optical behavior found upon chemical doping is very similar to pure polythiophenes like **P3HT**. In the neutral state a distinct band around 510 nm is present. Upon increasing the dopant concentrations, this band decreases and a very broad band appears between

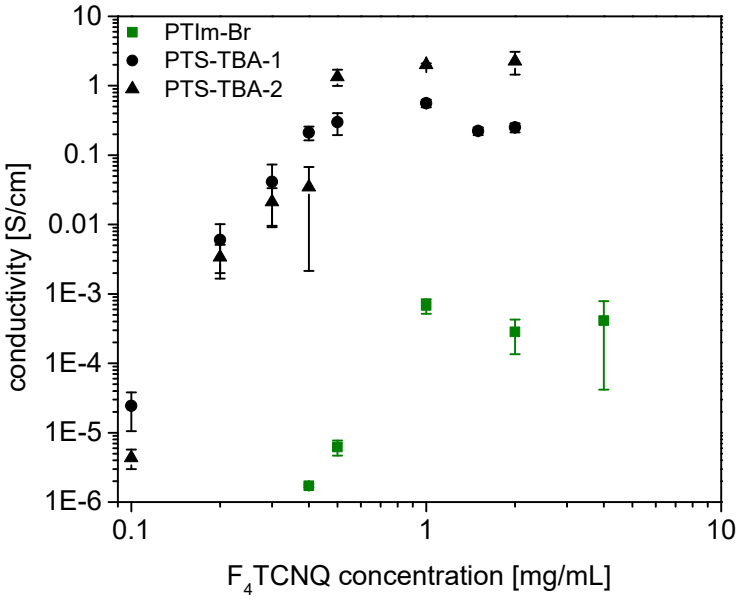

Figure 5.8: Four-point-probe conductivity measurements of conjugated polyelectrolytes **PTS-TBA** and **PTIm-Br**.

~600 and 1000 nm which can be attributed to the radical cation (polaron) species of the polythiophene backbone. Concerning electronic conductivity, these polaron species can be assumed to represent the dominant type of charge carriers in the CPE films. A slight increase in absorption around 1050 nm in the films doped with higher **F_4TCNQ** concentrations hints at the appearance of dication (bipolaron) species which are often found when polythiophene backbones are doped to high doping levels.[53] The polaron band is superimposed by two bands with maxima at approximately 760 and 870 nm, which can be assigned to the radical anion form of **F_4TCNQ**.[41, 43, 44] At dopant concentrations higher than ~0.5 mg/mL excess neutral **F_4TCNQ** is deposited on the film surface, leading to the development of a very distinct band with a maximum at 398 nm. The appearance of neutral dopant species and the saturation of the radical cation band absorption and conductivity values indicated that the highest possible doping level under the given conditions was reached.

PTIm-Br films showed lower conductivities at the same dopant solution concentrations compared to **PTS-TBA**. At the lowest concentrations, values around ~10^{-6} S/cm were found. These values corresponded well with measurements performed by *Vohlídal et al.*, who found conductivities between 10^{-10} and 10^{-6} S/cm for the neutral, undoped polymer.[10] With increasing dopant concentration, conductivities could be increased to $6.8 \cdot 10^{-4} \pm 1.6 \cdot 10^{-4}$ S/cm. UV/Vis absorption spectra of **PTIm-Br** point to an overall lower doping efficiency compared to both **PTS-TBA** batches. For all **F_4TCNQ** concentrations,

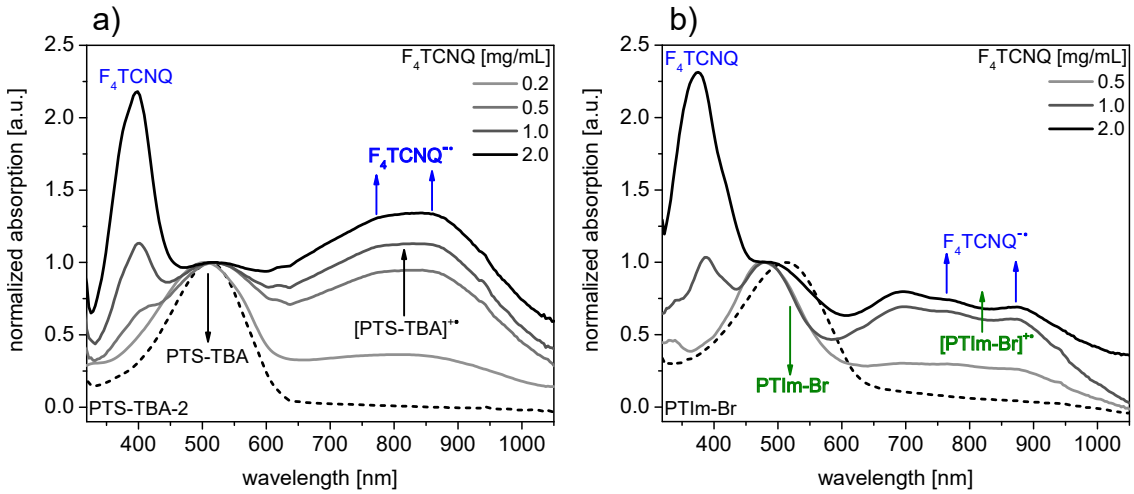

Figure 5.9: Optical absorption spectra of thin films of anionic and cationic conjugated polyelectrolytes **PTS-TBA-2** (a) and **PTIm-Br** (b) doped with varying solution concentrations of **F_4TCNQ**.

the ratio of the neutral and polaron backbone bands suggests a significantly lower charge carrier concentration which is likely to be the main reason for the lower measured conductivities. A possible explanation for this behavior can be found in comparison with literature examples of self-doped CPEs which almost always bear a negatively charged ion attached to the side chain in the case of a p-type backbone like polythiophene.[37, 193] It is likely that these negative charges in close proximity to the backbone, which can not diffuse freely through the polymer film due to the covalent tethering, lead to electrostatic stabilization of the radical cation charge carriers generated on the polymer backbone.[310] This might also be the case for our sulfonate-bearing polymer **PTS-TBA**. The NBu_4^+ counterions might be leaving the proximity of the backbone and even form electroneutral species together with the reduced dopant radical anions. *Chabinyc* and *Bazan* found higher conductivities with decreasing counterion size in self-doped narrow-bandgap CPEs, further supporting this theory.[311] If the tethered ionic group is however positive, like in the **PTIm-Br** system, the repulsive electrostatic interactions with the backbone polaron species would lead to destabilization of charge carriers. This would explain both the lower doping levels observed in optical absorption measurements as well as the lower measured conductivites. Further supporting this theory is the fact that covalently bound cations have been shown to be beneficial for n-type self-doping, in which negatively charged species are generated on the polymer backbone.[193, 312] Due to the complex interplay of different species in the polymer systems, other factors like the water content of the films or

species formed from the respective polyelectrolyte and dopant counterions might however also play a role.

5.1.4 Summary

In this chapter the synthesis and spectroscopic characterization of cationic and anionic conjugated polyelectrolytes as well as an evaluation of the electronic conductivities of these materials upon external chemical doping was presented. The CPEs **PTS-TBA** (bearing tetrabutylammonium sulfonate pendant groups) and **PTIm-Br** (containing imidazolium bromide units) were synthesized by polymer-analogous functionalizations starting from three batches of the precursor polymer **P3BrHT**.[9, 10]

Both polymers were well soluble in methanol without any spectroscopic evidence for the formation of aggregates. In water, only a slight broadening of the absorption band was seen for **PTIm-Br**, while **PTS-TBA** exhibited a significant red-shift, accompanied by the development of a fine structure which, analogous to the parent polymer **P3HT**, is indicative of aggregation of the chains in solution.[62] The role of the ionic pendant groups in aggregate formation of this polymer remains to be elucidated. In thin films spin coated from methanol or water solutions, both polymers showed very similar spectra with only minimal fine structure. Comparison of **PTIm-Br** film spectra revealed a high tendency for water retention of this polymer, which is in line with literature results on other CPEs with bromide counterions.[303]

Upon sequential "spin-doping" of CPE thin films with different concentrations of the strong acceptor dopant $\mathbf{F_4TCNQ}$ in the orthogonal solvent THF, optical absorption spectroscopy as well as four-point-probe conductivity measurements revealed significant differences between the cationic and anionic derivatives. Both **PTS-TBA** batches exhibited spectral evidence for exceptionally high doping levels, which manifested in conductivities of up to $2.3\pm0.8\,\mathrm{S/cm}$ and $0.6\pm0.1\,\mathrm{S/cm}$, values even comparable to regioregular **P3HT** doped with $\mathbf{F_4TCNQ}$.[40] **PTIm-Br** showed both drastically lower obtainable doping levels as well as conductivities, with values already saturating at $6.8\cdot10^{-4}\pm1.6\cdot10^{-4}\,\mathrm{S/cm}$. These significant differences in doping efficiencies for the two CPEs were attributed to a stabilizing effect of the negative charge tethered to the backbone in **PTS-TBA** which can be expected to stabilize positive polaronic charge carriers generated on the backbone upon oxidative doping.[310] According to this theory **PTIm-Br** would show the opposite effect, with coulombic repulsion between the radical cations and the positively charged imidazolium moieties leading to lower maximum doping levels.

5.2 Development of an Alkyne-functionalized Copolymer Platform

Polymer analogous copper(I) catalyzed alkyne-azide cycloaddition click chemistry (CuAAC) was identified as the most promising method for extending beyond the bromine-based functionalization used for creating the conjugated polyelectrolytes in the previous chapter and attaching more complex organic molecules to polythiophene backbones. CuAAC typically offers quantitative yields and high versatility and has been used for the functionalization of (bio)polymers in a plethora of cases in literature.[114–116] A convergent synthesis route, in which the functional groups are grafted onto the backbone after polymerization furthermore allows to conveniently synthesize differently functionalized polymers from the same prepolymer, as compared to polymerizing monomers already containing the functional group. Additionally, bulky side chains attached to monomer units have been shown to severely influence or even hinder controlled polymerization methods for conjugated polymers based on cross-coupling reactions, a drawback which can be elegantly avoided by polymer analogous functionalization. Two principal types of polythiophenes can be employed as precursor polymers in such an approach: either the azide or the alkyne moieties can be attached as pendant functionalities to the polymer backbone. Here a synthesis protocol based on the monomer unit (4-(thiophen-3-yl)-but-1-inyl)-triisopropylsilane (**3TBT**), originally introduced by *Venkataraman et al.* in 2008 was modified, in which the precursor polymer bears **TIPS**-protected alkyne units which are then functionalized with the respective organic azide after deprotection.[12] The *Venkataraman* group polymerized preformed dimers of this alkyne-functionalized monomer and 3-hexylthiophene (**3HT**), which consequently always leads to alternating copolymers with a 50/50 ratio. Here, the approach is extended to random copolymers of the two monomer units, which allows to produce tailor-made precursor polymers with controlled contents of alkyne groups, allowing to adjust the amount of any functional molecule introduced through the CuAAC modification exactly.

5.2.1 Synthesis of Copolymers with Adjustable Alkyne Contents

First, the two monomers 2,5-dibromo-3-hexylthiophene (**3HTBr$_2$**) and (4-(2,5-dibromothiophen-3-yl)-but-1-inyl)-triisopropylsilane (**3TBTBr$_2$**) were synthesized in straightforward reaction sequences from commercially available starting materials (see Scheme 5.3). The **TIPS**-protected alkynes were introduced *via* the reaction of the respec-

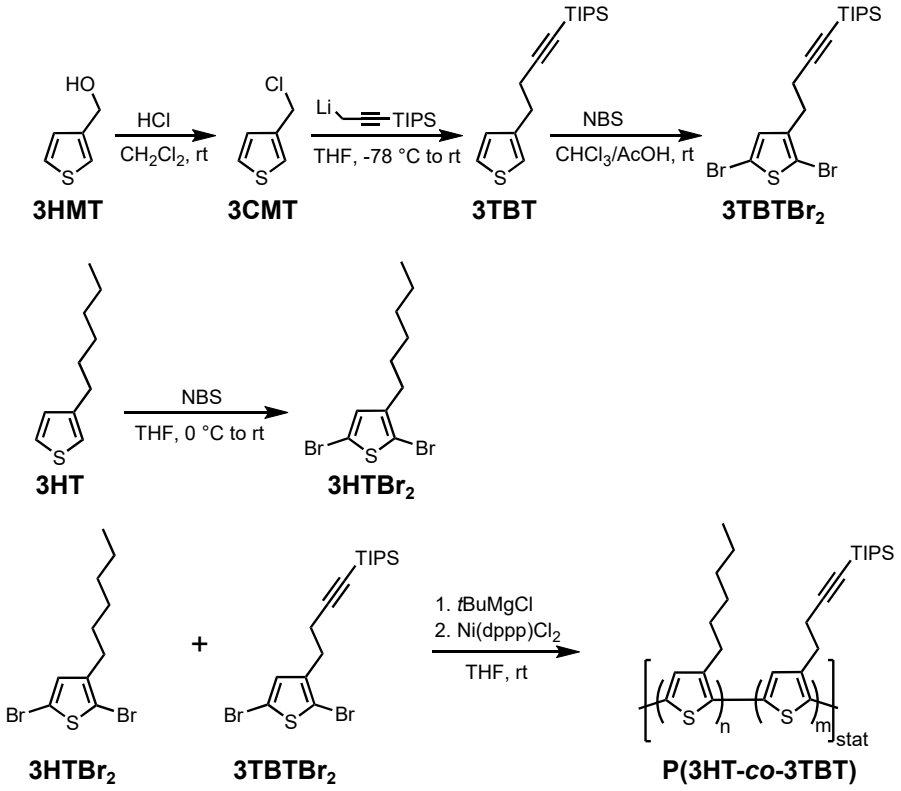

Scheme 5.3: Synthesis of monomers **3HTBr$_2$** and **3TBTBr$_2$** and GRIM polymerization procedure to **P(3HT-*co*-3TBT)**.

tive lithiate with a halogen-substituted thiophene derivative.[313] **3CMT** degraded under ambient conditions so it was used in the next step as fast as possible. Dibromination of both monomers was carried out with NBS.

The precursor polymers **P(3HT-*co*-3TBT)** were synthesized *via Grignard* Metathesis Polymerization (GRIM). This method is well known for producing highly regioregular polythiophenes from halogenated monomers *via* a pseudo-living chain growth mechanism.[30] Six precursor polymers with different feed ratios of the monomers were synthesized (Table 5.2). NMR spectroscopy revealed good agreement between monomer feed ratio and polymer repeating unit ratio within the error of NMR integration and high regioregularity of the polymers (Figure 5.11).

The signal for the β-protons of the **3HT** repeating units at 6.98 ppm showed slight splitting caused by different chemical environments (neighboring repeating units) in ratios according to the polymer composition which indicated a fully statistic copolymer. Size exclusion chromatography revealed narrow polydispersities in most cases. However, the copolymerization of **3HTBr$_2$** with **3TBTBr$_2$** seems to lead to a slightly lower degree of control over the GRIM polymerization compared to the synthesis of pure 3-alkylthiophene

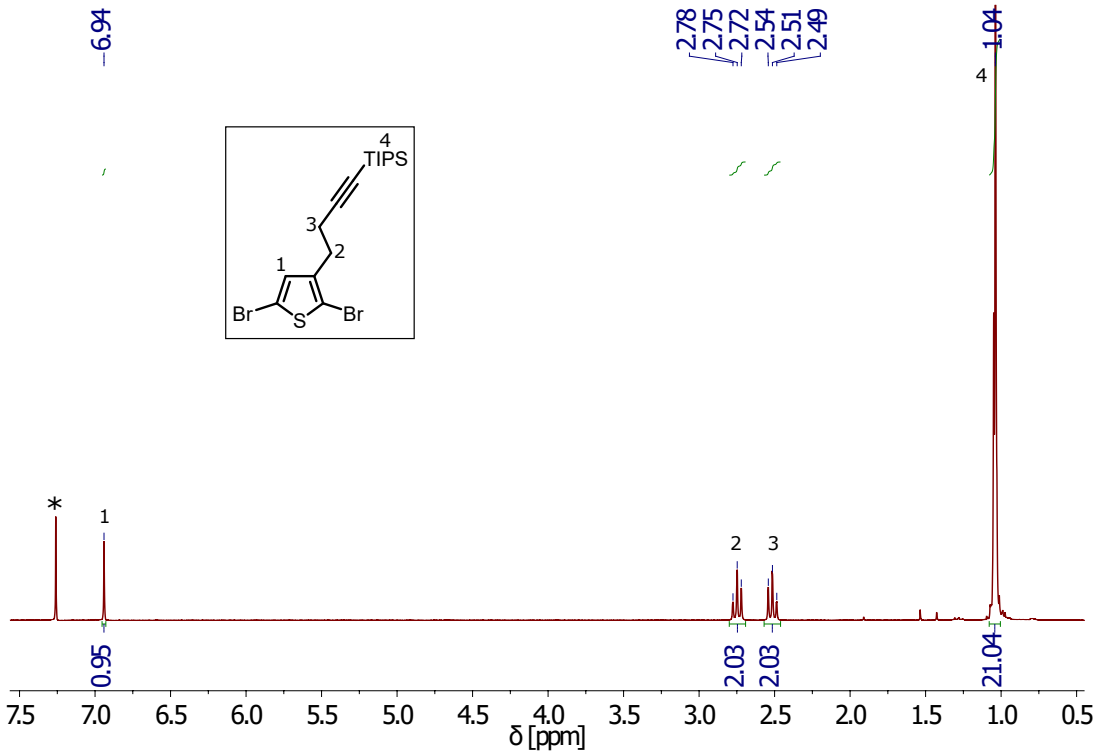

Figure 5.10: ^{1}H-NMR spectrum of purified **3TBTBr$_2$** (room temperature, $CDCl_3$).

Table 5.2: Molecular properties of precursor polymers **P(3HT-*co*-3TBT)** with varying repeating unit ratios.

	P(3HT-*co*-3TBT)					
feed ratio[a)]	0/100	40/60	50/50	70/30	70/30	90/10
rep. unit ratio[a)]	0/100	41/59	55/45	67/33	73/27	91/9
$\overline{M_n}$[b)]	9.5	18	9	18.5	18	21
$\overline{M_w}$[b)]	18	29	13	29	23	40.5
PDI[b)]	1.9	1.6	1.4	1.6	1.3	1.9

a) Monomer feed ratios **3HTBr$_2$/3TBTBr$_2$** and repeating unit ratios **3HT/3TBT** (determined by NMR spectroscopy) are given in mol%/mol%. b) Molecular weight averages (in kg/mol) and polydispersity indices were determined by SEC (THF solution, rt), calibrated against polystyrene standards.

polymers which typically show polydispersities below 1.3 after simple precipitation in methanol. This can be explained by a possible coordinative interaction of the nickel catalyst with the alkynyl groups and by the bulky protecting groups which might influence chain growth. Small shoulders at doubled molecular weight were found for all polymers (Figure 5.12).

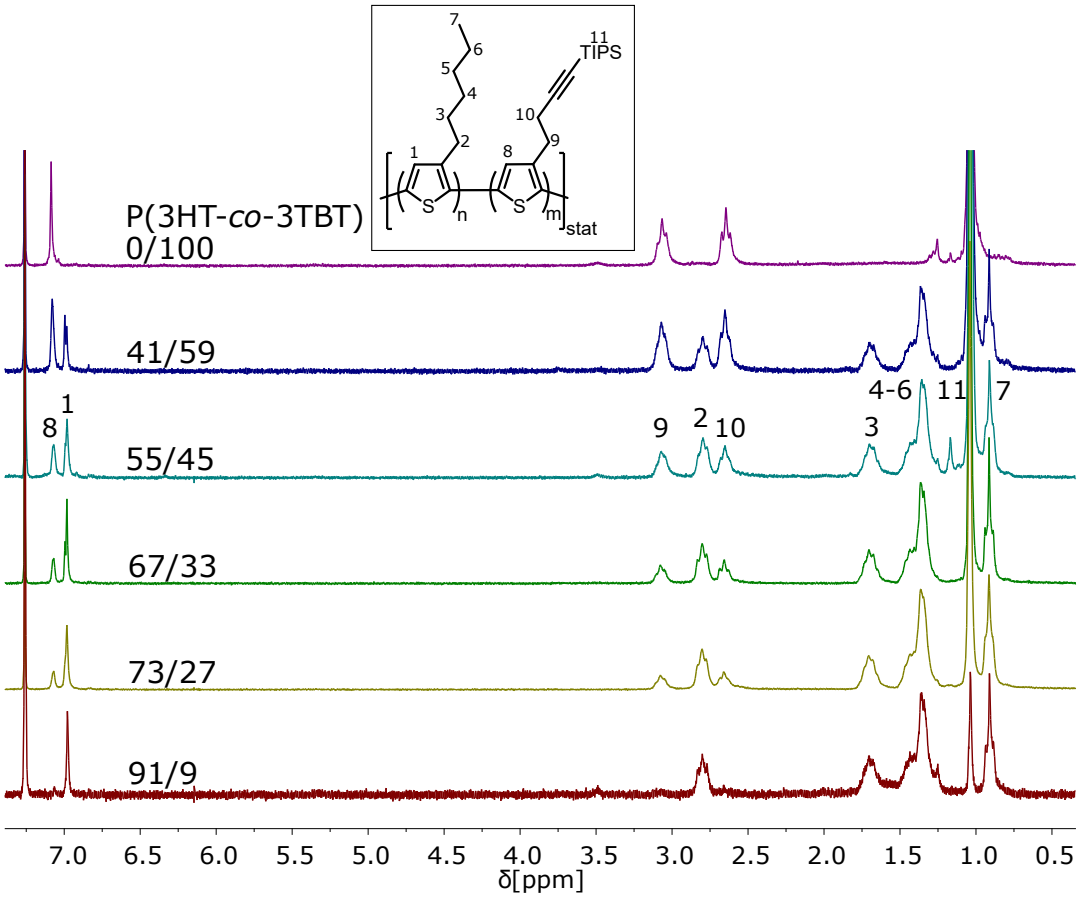

Figure 5.11: Comparison of ^{1}H-NMR spectra of precursor polymers **P(3HT-*co*-3TBT)** with different repeating unit ratios (room temperature, $CDCl_3$).

These stem from dimerization of polymer chains *via* disproportionation of the active Ni species on the chain ends when using methanol as a quenching agent, as has been shown by *Thelakkat et al.*[103] While this side reaction can be often suppressed by performing a more rapid quenching using hydrochloric acid, acidic conditions were also expected to lead to a (partial) deprotection of the alkynes by cleavage of the silyl protecting groups. HCl addition to the triple bond followed by several side reactions has been shown for chain-end alkynyl functionalized polythiophenes and was expected to occur as a side reaction after deprotection.[132]

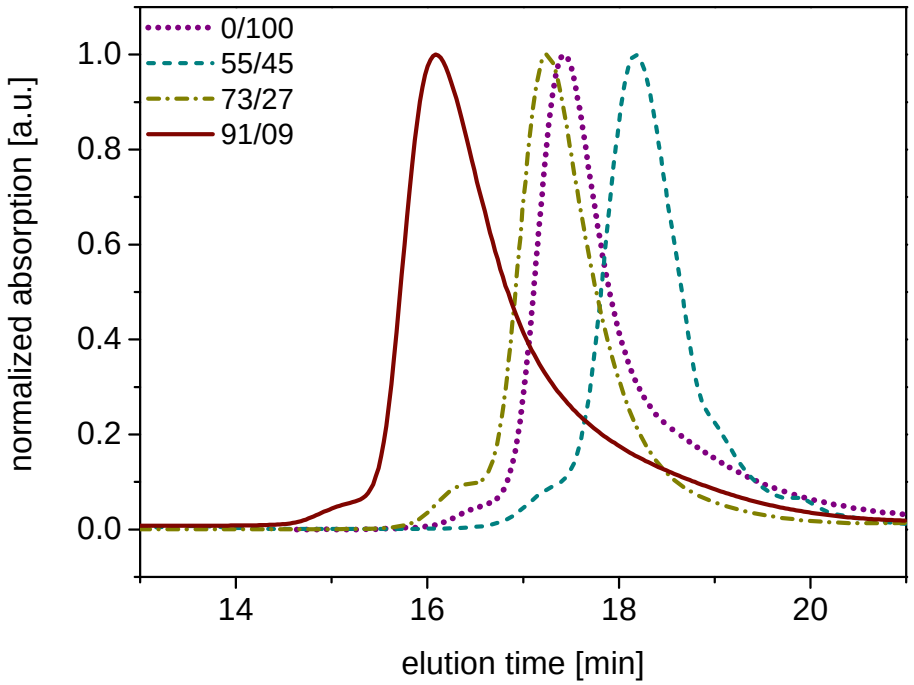

Figure 5.12: SEC traces of four representative polymer batches of **P(3HT-*co*-3TBT)** with different repeating unit ratios.

5.2.2 Summary

Based on the repeating units **3TBT** and **3HT**, a functionalizable alkyne-bearing polythiophene copolymer platform with easily controllable contents of alkyne groups has been developed in this chapter. GRIM polymerization of the dibrominated monomers was possible in any ratio and allowed to produce highly regioregular polymers with decent molecular weights and relatively narrow molecular weight distributions. The sterically demanding **TIPS** protecting groups as well as the effect of the alkyne moieties seemed to lead to a slightly lower degree of control over the polymerization compared to simple **3HT** homopolymers. The protecting groups were effective in protecting the alkyne groups against the conditions of GRIM polymerization and allowed the use of *Grignard* reagents by prohibiting deprotonation of the terminal alkyne-H. Building on the alkyne-based copolymer platform discussed in this chapter, triphenylamine-functionalized crosslinkable polythiophenes as well as protein sensor materials bearing α-D-mannose units were created. The syntheses and applications of these materials will be shown in the following.

5.3 Polythiophenes with Redox-active Crosslinks

Parts of this chapter have been published:

Simultaneous doping and crosslinking of polythiophene films
P. Reinold, K. Bruchlos, S. Ludwigs
Polym. Chem. **2017**, *8*, 7351.

A key property of both conjugated and redox polymers is their ability to form homogeneous thin films upon deposition on various (flexible) substrates from suitable solvents using methods like large scale roll-to-roll printing, spin coating or blade coating.[23] Compared to their small molecule counterparts, these films are much less prone to dissolution, which is especially important for applications in which the polymers are in direct contact with organic solvents.

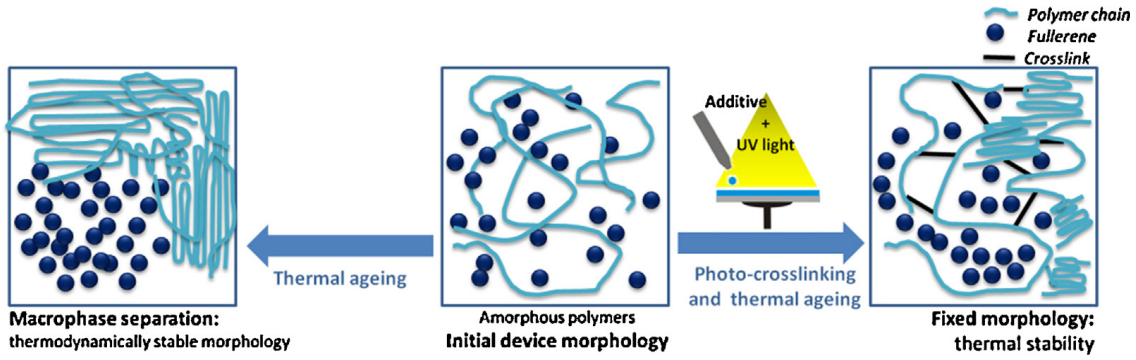

Figure 5.13: Crosslinking allows the preservation of controlled film morphologies upon ageing of devices or upon contact with solvents which would otherwise slowly dissolve the films. The principle is shown here exemplarily for blend films of conjugated polymers and fullerene in organic photovoltaics, in which crosslinking prohibits the phase separation of the blend.[290] Adapted with permission from [290], © 2015, Elsevier Ltd.

Crosslinking techniques allow to further improve the stability of the films while preserving the controlled film structure and to broaden the range of available electrolytes.[289] Such techniques typically employ either the reactions of functional groups present on the polymer chains or small crosslinker molecules which are added to the polymer solution prior to deposition or deposited onto the polymer film from an orthogonal solvent and then react with the polymer chains.[290] These crosslinking reactions are often triggered by UV irradiation or heat. Typical reactions include the displacement of halogen substituents, ring opening of oxetanes, oligomerization of vinyl groups, thiol-ene chemistry or coupling

of nitrenes generated *in situ* from azides.[314–317] Disulfide bond formation even allows reversible crosslinking.[318] Crosslinking of conjugated polymers has been reported for a multitude of applications, including organic photovoltaics, organic light emitting diodes, organic field effect transistors and battery materials.[291, 319–324]

An alternative method is oxidative crosslinking, based on dimerization of radical cation species on charged aromatic groups.[325, 326] In contrast to most chemical approaches the resulting crosslinks are electroactive themselves. Especially (oligo)thiophene, carbazole and triarylamine derivatives are often used for such reactions, owing to their reliable coupling chemistry.[327–330] In this chapter the synthesis and characterization of crosslinkable conjugated redox polymers (CRPs) containing triphenylamine **TPA** units covalently attached to a regioregular polythiophene backbone as pendant groups will be shown. Based on previous experience with both **P3AT**s and **TPA** derivatives, these two classes of materials were expected to be redox matched, *i.e.* coupling of **TPA** units and later charging and discharging of **TPB** dimers should occur in the potential window of highest conductance of the polythiophene (**PT**) backbone in which it is found in its charged (polaron) state ($\mathbf{PT}^{+\bullet}$). *Li et al.* synthesized polymers with a closely related structure for photovoltaic applications, however, the **TPA** donor units were able to electronically communicate with the backbone π-system *via* a conjugated bridge, thus these systems would not allow for independent redox chemistry of the pendant groups.[331]

5.3.1 Polymer Synthesis in Solution and Basic Characterization

Starting from the versatile alkyne-functionalized copolymer platform introduced in the previous chapter, two different linking approaches for were investigated, in which the **TPA** group was either placed in conjugation to the triazole ring formed during the click reaction (**PT-TPA**) or separated further from the backbone by an alkyl spacer (**PT-spTPA**).

Synthesis of Triphenylamine Azides

The triphenylamine azide compounds $\mathbf{TPA\text{-}N_3}$ and $\mathbf{spTPA\text{-}N_3}$ were synthesized from 4-aminotriphenylamine ($\mathbf{TPA\text{-}NH_2}$) (accessible *via* nucleophilic aromatic substitution and reduction of the NO_2 group from diphenylamine, **DPA** and 4-fluoronitrobenzene, **NFB**), either by diazotation and subsequent azide transfer reaction using sodium azide or by attachment of a 6-bromohexanamide linker followed by bromine-azide exchange (Scheme 5.4).[332–334] In addition to NMR spectroscopy and high resolution mass spectrometry the intense azide IR absorption bands around 2100 cm^{-1} further confirmed successful conversion

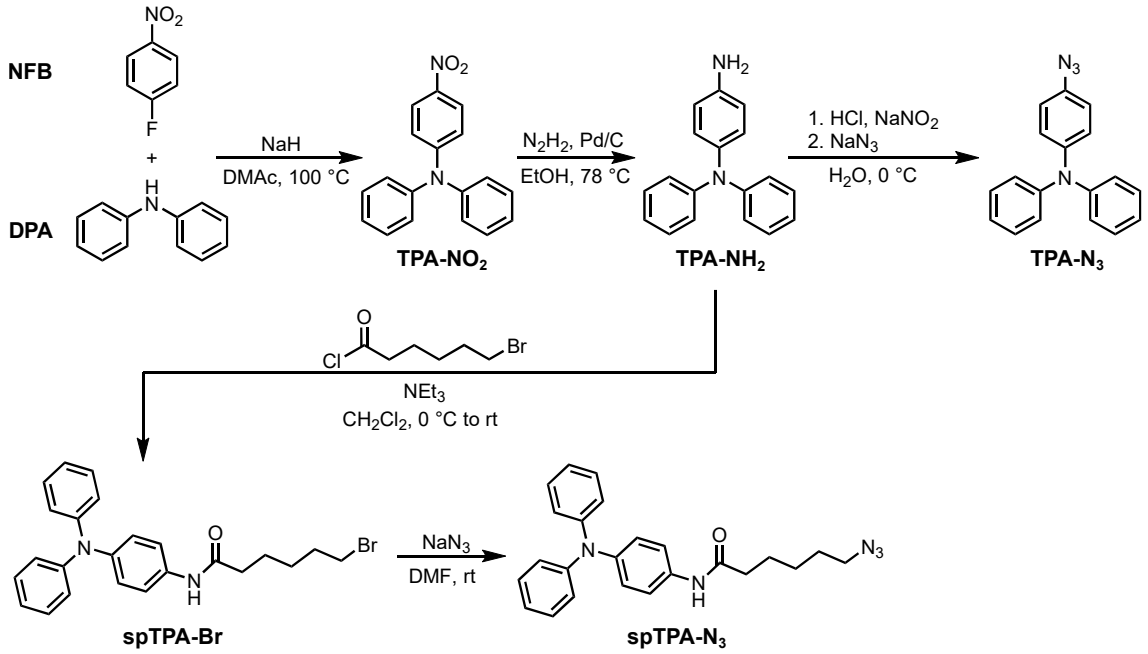

Scheme 5.4: Reaction paths for the synthesis of triphenylamine azides **TPA-N_3** and **spTPA-N_3**.

to the respective azide compounds. **TPA-N_3** was found to be highly light-sensitive, as irradiation with UV light caused reactions to a number of colored compounds, presumably due to generation of nitrenes and subsequent azo coupling.

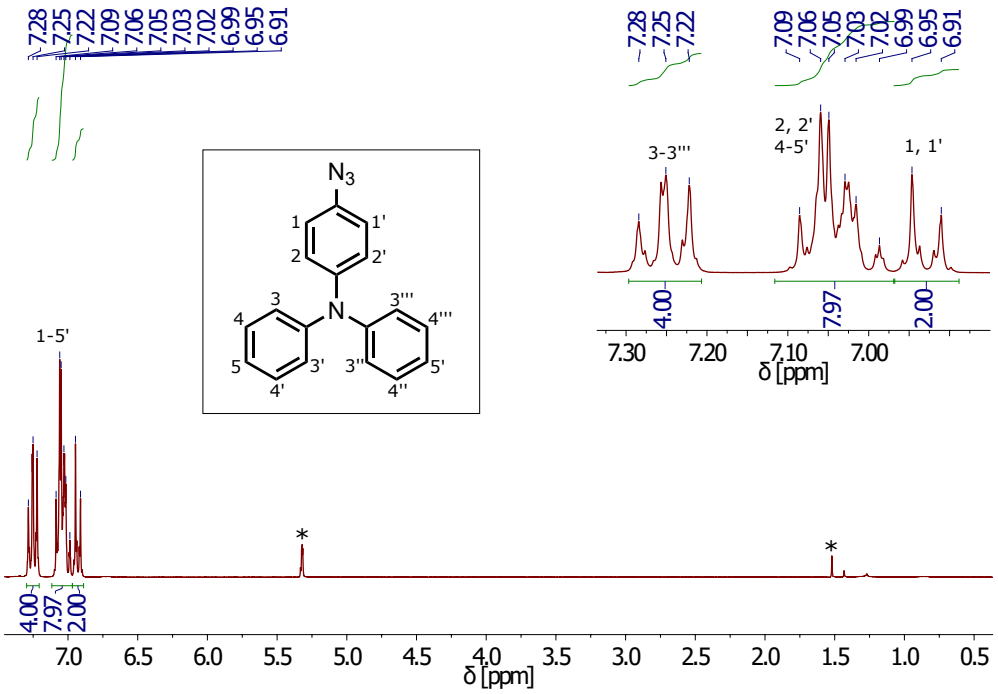

Figure 5.14: ^{1}H-NMR spectrum of purified triphenylamine azide compound **TPA-N$_3$** (room temperature, CD_2Cl_2).

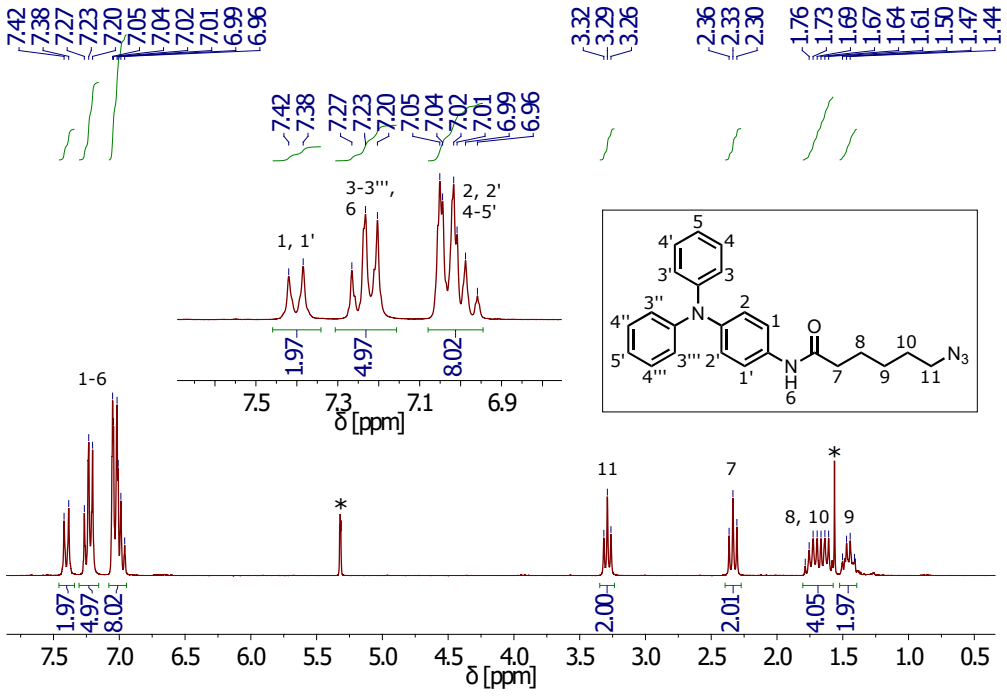

Figure 5.15: ^{1}H-NMR spectrum of purified triphenylamine azide compound **spTPA-N$_3$** (room temperature, CD_2Cl_2).

Polymer Analogous Functionalizations

Postfunctionalization by CuAAC with both **TPA** azides was performed starting from the same precursor polymer, **P(3HT-*co*-3TBT)** with a ratio of 73/27 repeating units. This ensured ideal comparability of the properties of the two different **TPA** linking approaches by eliminating influences from differences in the polymer backbone composition, molecular weight and polydispersity (Scheme 5.5).[12]

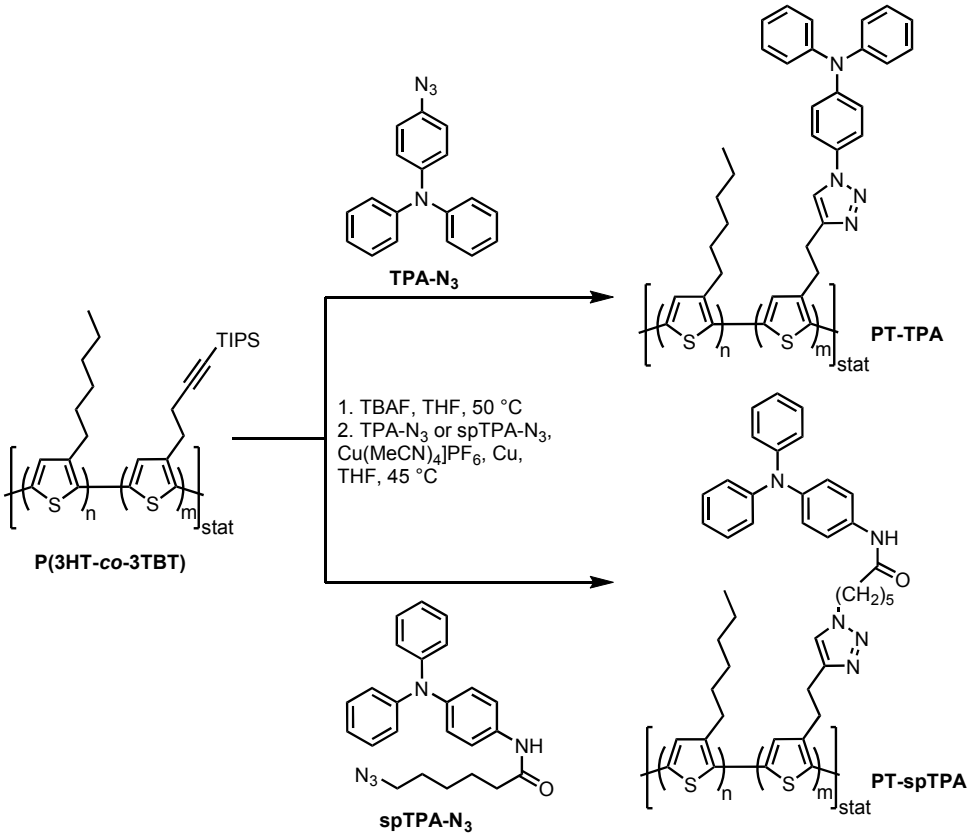

Scheme 5.5: Polymer analogous functionalizations to CRPs **PT-TPA** and **PT-spTPA**.

The precursor polymer was first deprotected using tetrabutylammonium fluoride (TBAF) solution in THF at 50 °C. The deprotected backbone was then reacted with an excess of the respective azide compound in degassed THF in the presence of the catalyst $[Cu(MeCN)_4]PF_6$ and copper powder for several days at 45 °C. Unreacted small molecules and catalyst traces were removed by passing the polymer solution over aluminium oxide, *Soxhlet* purification with MeOH and EtOAc and subsequent preparative SEC. Quantitative conversion of the alkynyl side chains and azide moieties to triazole rings could be proven by disappearance of the ^{1}H-NMR signal associated to the terminal alkyne proton at 2.05 ppm and by a shift of the side chain CH_2 protons adjacent to the alkyne groups

from 2.59 ppm to 3.22 and 3.14 ppm for **PT-TPA** and **PT-spTPA**, respectively (Figure 5.16 a, highlighted part of the spectra).

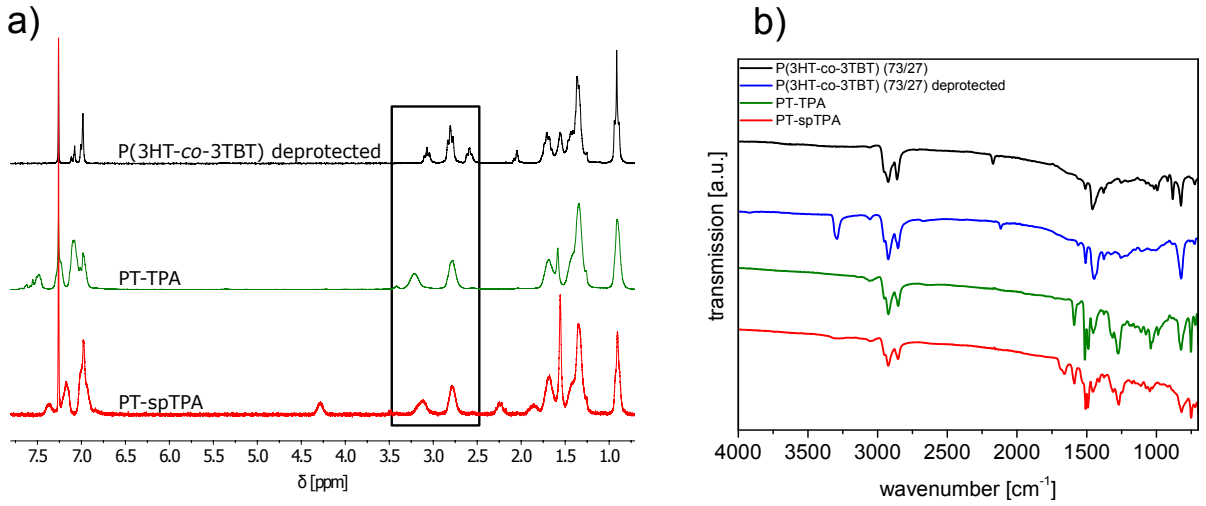

Figure 5.16: Comparison of a) ^{1}H-NMR and b) ATR-IR spectra of protected and deprotected precursor polymer **P(3HT-*co*-3TBT)** (73/27) and functionalized conjugated redox polymers **PT-TPA** and **PT-spTPA**.

A multiplet with an integral of 4H also containing the CH_2 protons next to the backbone thiophene was formed. In addition, new signals appeared in the region from 7.3 to 7.7 ppm in which triazole protons are typically found. Finally, the CH_2 protons adjacent to the azide group in **spTPA-N$_3$** were shifted quantitatively from 3.29 to 4.28 ppm in **PT-spTPA**. The signal assignments for **PT-TPA** were additionally proven by synthesizing the model compound **T-TPA** for which **TPA-N$_3$** was "clicked" to the deprotected monomer **3TBTBr$_2$** (see Scheme 5.6 and Figure 5.17).

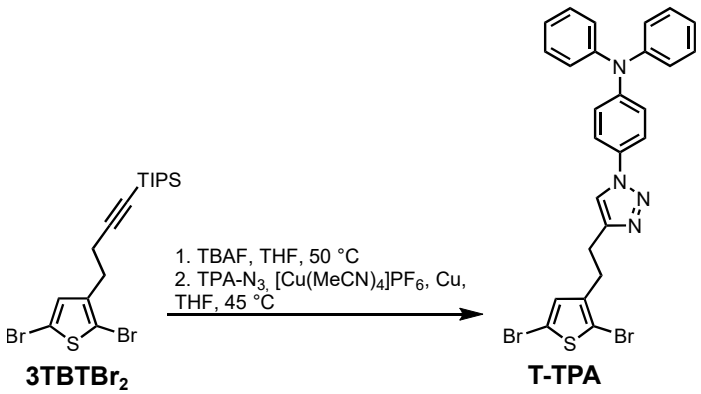

Scheme 5.6: Synthesis of model compound **T-TPA** through CuAAC between **3TBTBr$_2$** and **TPA-N$_3$**.

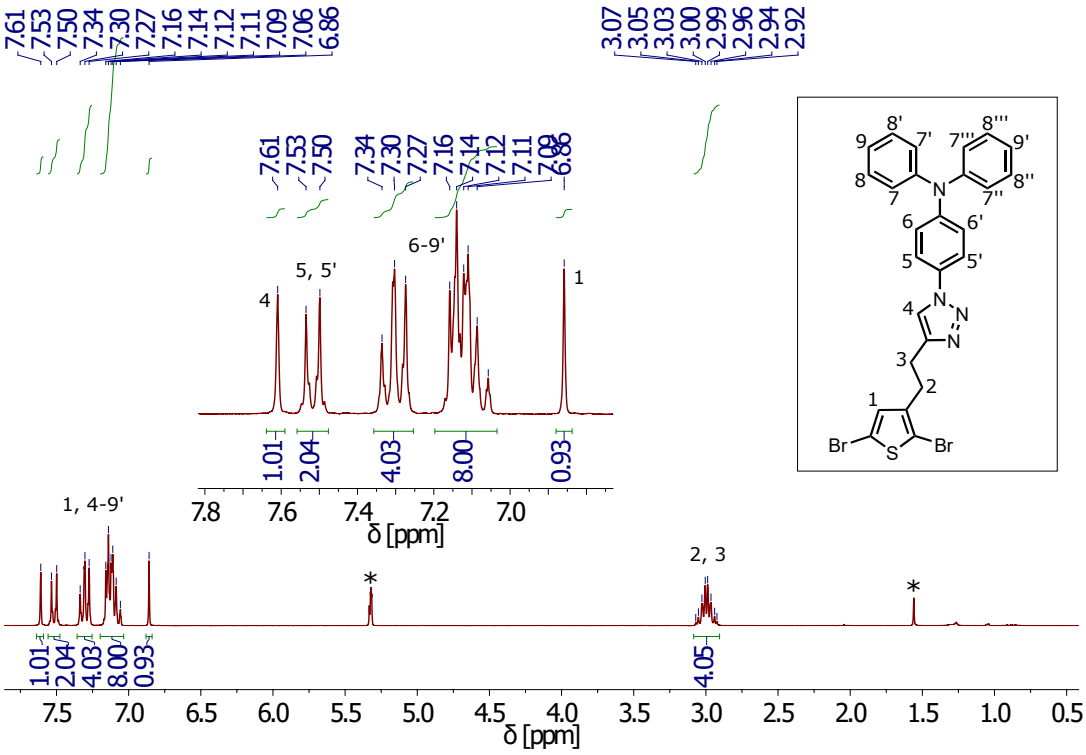

Figure 5.17: ^{1}H-NMR spectrum of purified model compound **T-TPA** (room temperature, CD_2Cl_2).

In addition, IR spectroscopy confirmed the quantitative functionalization of the polymers (Figure 5.16 b). In the spectrum of the protected precursor polymer only the band around 2170 cm^{-1} corresponding to the triple bond is seen. After deprotection a band at ~3290 cm^{-1} appears, which can be assigned to the alkyne-H bond. Both bands vanish quantitatively after the CuAAC reaction and no traces of residual azide around 2100 cm^{-1} are found.

SEC measurements revealed a small decrease in molecular weight upon deprotection of the precursor polymer. Compared to the precursor polymer, **PT-spTPA** showed a higher increase in apparent molecular weight than **PT-TPA**, corresponding to a higher hydrodynamic radius due to the alkyl spacer linkage (Table 5.3). Slightly narrower molecular weight distributions were found for both functionalized polymers which can be explained by the preferred dissolution of smaller oligomers during *Soxhlet* purification with EtOAc. For comparison reasons a **P(3HT-*co*-3TBT)** batch with a repeating unit ratio of 91/9 was furthermore functionalized with **spTPA-N_3**. Spectroscopic data was found to match the expected **TPA** substitution content, thus suggesting universal applicability of this approach to synthesize products with varying content of pendant groups limited only by solubility issues of deprotected precursor polymers with alkyne substitution contents

higher than ~50%. Attempts to polymerize **T-TPA** were unsuccessful due to instability of the *Grignard* intermediate.

Table 5.3: Molecular properties of CRPs **PT-TPA** and **PT-spTPA**.

	PT-TPA	**PT-spTPA**	
rep. unit ratio	73/27	73/27	91/9
$\overline{M_{\mathbf{n}}}$	21	24.5	29
$\overline{M_{\mathbf{w}}}$	26	30.5	48.5
PDI	1.2	1.2	1.7

Optical Absorption Properties

UV/Vis spectroscopy yielded valuable information about the aggregation behavior of the polymers in solution and thin films (Figure 5.18).
In the solution spectra (Figure 5.18 a and b), compared to **P(3HT-*co*-3TBT)** (λ_{max} = 445 nm) the backbone absorption bands at 438 and 446 nm for **PT-TPA** and **PT-spTPA** are not significantly influenced by the functionalization indicating little distortion of the backbone due to steric hindrance and the absence of aggregation phenomena which could be caused by stacking of the pendant **TPA** groups. Planarization of the backbone, *e.g.* due to aggregation would lead to elongation of the effective conjugation length and typically causes a strong red-shift and often the development of a vibronic fine structure.[63] The backbone absorption spectrum in both CRPs is superimposed by the absorption of the neutral **TPA** units around 310 and 330 nm (**PT-TPA**) and at 308 nm (**PT-spTPA**). Compared to **TPA-N_3** both the model compound **T-TPA** and **PT-TPA** exhibit a broadened neutral **TPA** band. This feature can presumably be attributed to the extension of the π-system due to formation of the triazole ring. Similar absorption characteristics were found by *Tian et al.* for a **TPA**-containing OLED emitter molecule in which four **TPA** units were linked with conjugated triazole rings.[333] When comparing solution and thin films both the backbone absorption bands of **PT-spTPA** and **PT-TPA** are red-shifted and broadened compared to the solution spectra (Figure 5.18 c and d). No significant development of a fine structure is seen in the film spectra of both functionalized polymers giving no indication for π-π stacking. Thin films of regioregular **P3HT** films typically exhibit shoulders at ~550 nm and ~610 nm. In the film spectrum of **PT-TPA** the fine structure of the neutral **TPA** band (335 nm) vanishes while the band itself is still found to be significantly broader than the corresponding one for **PT-spTPA** (327 nm). The absorption properties of the **PT-spTPA** batch with a functionalization of 9% are

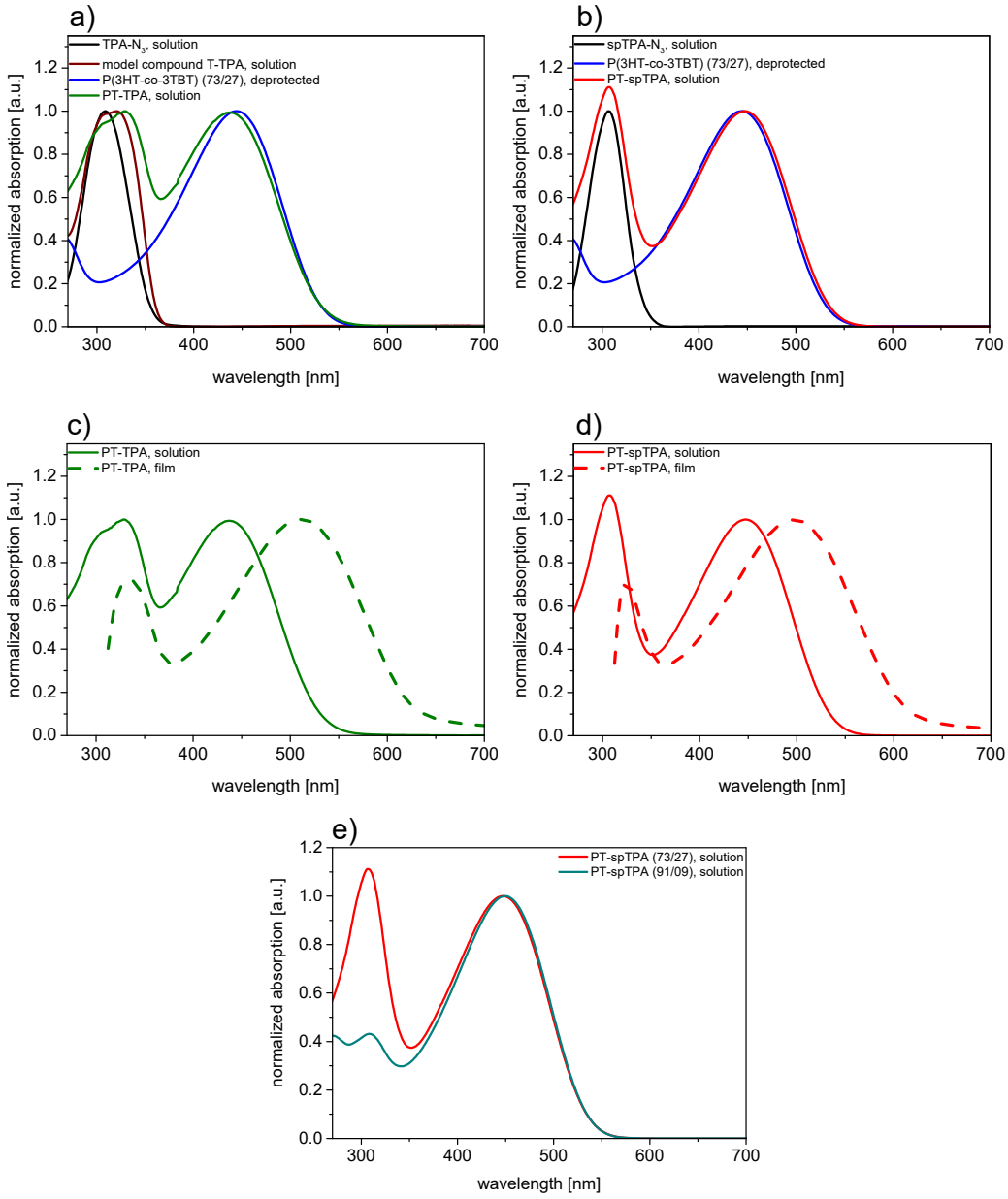

Figure 5.18: a), b) Optical absorption properties of **PT-TPA** and **PT-spTPA** compared to their respective starting materials and the model compound **T-TPA** in solution. c), d) Comparison of solution (THF, 0.1 mg/mL) and thin film (spin coated from 5 mg/mL $CHCl_3$ solution) spectra of the CRPs. e) Solution spectra of **PT-spTPA** with side chain functionalization of 27 and 9%.

essentially identical to the 27% batch except for the much less prominent neutral **TPA** band (Figure 5.18 e).

Thermal Properties

Thermogravimetric analysis (TGA) coupled with *in-situ* differential scanning calorimetry (DSC) measurements was used to assess the thermal stability of the precursor polymer and both CRPs (Figure 5.19) All polymers remained intact until at least 260 °C with **PT-spTPA** being stable at temperatures as high as 346 °C. Decomposition was found to take place in two separate steps for all polymers, likely corresponding to pendant group (**TIPS** or **TPA**) and backbone decomposition. No melting transition could be detected before polymer decomposition. However, endothermic steps were found for both CRPs in a similar temperature range (~160-200 °C) but not for the precursor polymer, pointing at a thermal transition involving the **TPA** pendant groups.

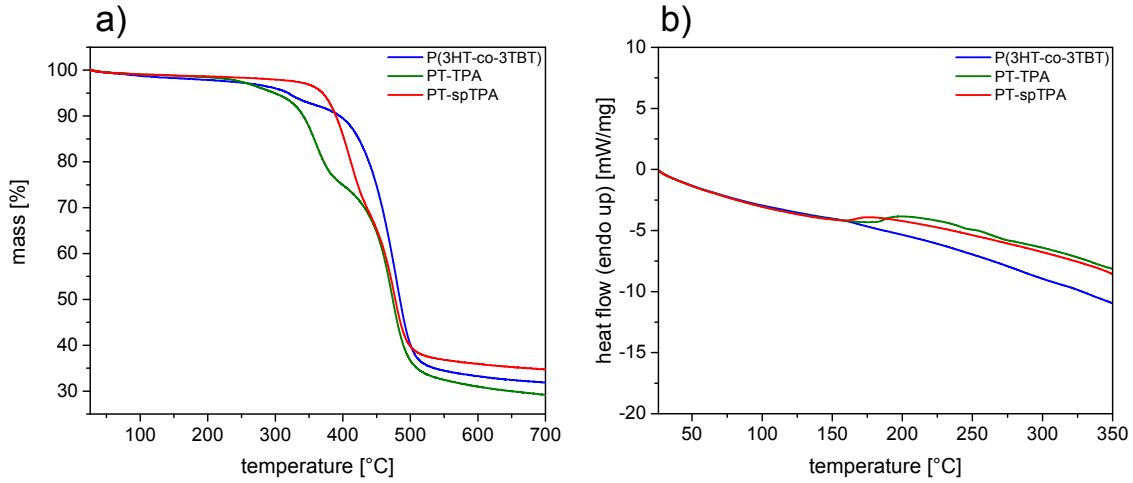

Figure 5.19: a) TGA and b) *in-situ* DSC analysis of precursor polymer **P(3HT-*co*-3TBT)**, **PT-TPA** and **PT-spTPA**.

5.3.2 Functionalization of Thin Films

CuAAC represents a powerful method to not only connect highly complex molecules in homogeneous solutions but also to functionalize the surfaces of metals (*via* self-assembled monolayers), various (nano)particles and polymer films, to name a few, under heterogeneous reaction conditions. Such approaches are especially useful on the interface of materials science, polymer chemistry and biochemistry, where, due to solvent incompatibility issues, reactions on solid-liquid interfaces are very common.[119–123] If a heterogeneous reaction proceeds quantitatively with high selectivity (which is usually the case for CuAAC) and contaminants from the reaction solution can be fully rinsed off, such approaches may

even represent a good alternative to solution-functionalization, since workup times can be greatly reduced.

The combination of deprotected **P(3HT-*co*-3TBT)** films and **TPA** azides is interesting as a model system in this regard since both species show significant absorption in the UV/Vis regime which allows for optical detection of **TPA** in the film and an approximation of the degree of functionalization by comparison with spectra of films with known substitution content.

As mentioned before, **P(3HT-*co*-3TBT)** batches with a **3TBT** content higher than ~50% showed solubility issues in their deprotected state in the solvents typically applied for CuAAC, in our case THF. Thus, these would be ideally functionalized by an efficient heterogeneous film-functionalization approach. A batch of the polymer with a repeating unit ratio of 41/59 was deprotected using the standard procedure, purified by repeated *Soxhlet* extraction and thin films were spin coated on precleaned glass substrates from *o*DCB solutions as a basis for all further experiments, which were mainly performed by *Tim Hierlemann* during the course of his research internship.

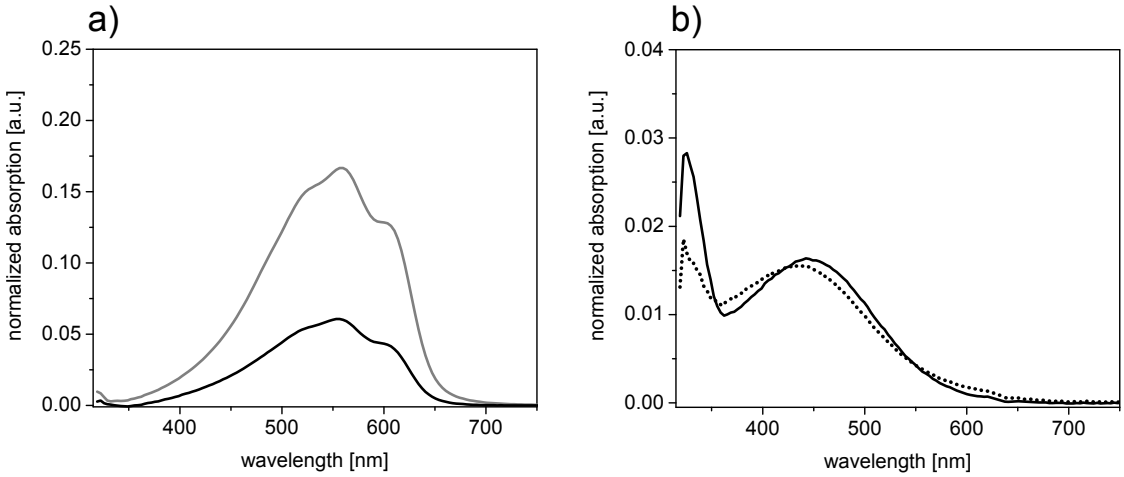

Figure 5.20: a) Absorption spectra of reference **P3HT** (grey) and deprotected **P(3HT-*co*-3TBT)** (black) films after immersion into **spTPA-N$_3$** solutions in DMSO for 3 d at 40 °C and subsequent washing procedure. b) Spectra of **P(3HT-*co*-3TBT)** films reacted under similar conditions at rt (dotted) and 40 °C (solid line) in the presence of Cu(0) powder.

Since it is not possible to differentiate between covalently bound and physically adsorbed **TPA** molecules in the films using optical absorption spectroscopy, establishing an efficient washing procedure which quantitatively removes all contaminants from the films is highly important. Thus, films of deprotected **P(3HT-*co*-3TBT)** and a reference **P3HT** batch (*Merck*, $\overline{M_n}$ = 30.9 kg/mol, PDI = 1.9) were first subjected to 5 mM **spTPA-N$_3$** solutions

in DMSO or MeCN at 40 °C for 3 d without stirring. Subsequently, the films were rinsed four times with MeCN at rt and then subjected two times to fresh p.a. grade methanol at 40 °C for 20 min. The films were then dried *in vacuo* at 40 °C overnight. Figure 5.20 a shows the film spectra of a **P3HT** film (grey) and a deprotected **P(3HT-*co*-3TBT)** film (black) after this washing procedure. For better comparability, all spectra in the following experiments were baseline-corrected between 800 and 1000 nm. Both films showed spectra typical for polythiophene backbones and no signs of a **TPA** band in the UV region confirming the successful removal of adsorbed **TPA** species.
When the same experiment was repeated in the presence of copper powder but without a Cu(I) catalyst (Figure 5.20 b), somewhat surprisingly, **TPA** bands at 326 nm were found for the **P(3HT-*co*-3TBT)** films and the backbone absorption band lost its fine structure along with a shift to lower wavelengths. These findings are very strong hints for covalently bound **spTPA** species. Since no dedicated Cu(I) catalyst was added, the catalytically active species must stem from comproportionation reactions on the surface of the copper powder particles, which has been shown for example for CuAAC-based adhesive systems in literature.[335]

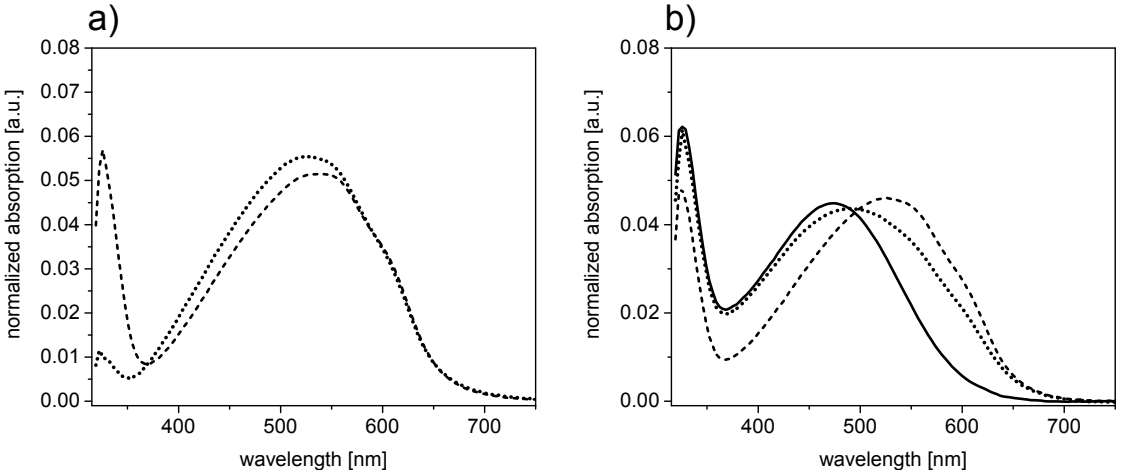

Figure 5.21: Absorption spectra of films functionalized with **spTPA-N$_3$** in a) acetonitrile at rt (dotted) and 40 °C (dashed line) and b) DMSO at rt (dotted), 40 °C (dashed) and 60 °C (solid line). Concentrations of dissolved species were 5 mM **spTPA-N$_3$** and 0.5 mM $[Cu(MeCN)_4]PF_6$.

Subsequently, polymer films were subjected to several typical CuAAC conditions (MeCN or DMSO solvent; 5 mM **spTPA-N$_3$**, 0.5 mM $[Cu(MeCN)_4]PF_6$, Cu powder; rt to 60 °C for 3 d) to study the effect of temperature and solvent type on the reaction (Figure 5.21). When acetonitrile at rt was used, only a very weak **TPA** band was observed. Presumably, under these conditions, the solvent was not able to fully penetrate the film and thus,

only a small fraction of the film was functionalized. Indeed, for the reaction at 40 °C in the same solvent, a much more significant **TPA** band was found. When the solvent was changed to DMSO, even at room temperature the solvent seemed to be able to deeply penetrate the polymer film, resulting in a clearly visible **TPA** absorption. Differences in the spectra measured after carrying out the CuAAC reaction at different temperatures were rather minor. The spectrum at the highest temperature of 60 °C exhibited the highest influence of the reaction on the film structure, resulting in a fully vanishing fine structure of the backbone band and a significant blue-shift. Since the spectra were very similar for all three temperatures, one can already assume that functionalization took place nearly quantitatively.

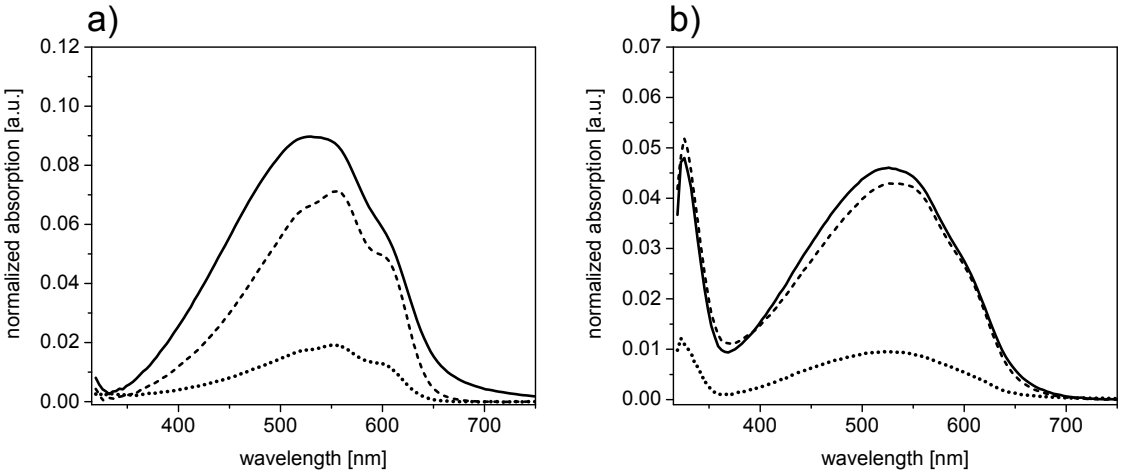

Figure 5.22: Dependency of functionalization efficiency on film thickness: UV/Vis absorption spectra of a) as-cast thin films of deprotected **P(3HT-*co*-3TBT)** spin coated from 5 (solid line), 3 (dashed) and 1 mg/mL (dotted) solutions in *o*DCB and b) the same films heterogeneously functionalized with **spTPA-N$_3$** in DMSO at 40 °C.

The CuAAC reaction was further carried out (DMSO, 40 °C) for films spin coated from solutions of different concentrations. As shown in Figure 5.22 a, the different thicknesses of these as-cast films are apparent in the absorption intensities of the backbone bands. However, when these films were subjected to the same CuAAC conditions (Figure 5.22 b), the ratios of maximum **TPA** and backbone absorptions and the overall shapes of the spectra were almost identical. This finding confirmed the independence of the functionalization efficiency on film thickness (at least in the range of ~20-80 nm which was studied here) and thus further hints at full penetration of the solution and near-quantitative functionalization.

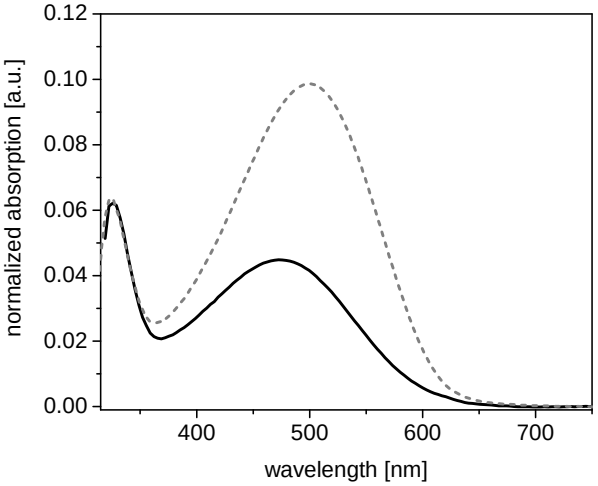

Figure 5.23: Comparison of absorption spectra of deprotected **P(3HT-*co*-3TBT)** (41/59) thin films functionalized with **spTPA-N$_3$** in DMSO at 60 °C (solid line) and solution-functionalized **PT-spTPA** (73/27) (dashed grey line).

Lastly, the spectrum of a **P(3HT-*co*-3TBT)** (41/59) thin film heterogeneously functionalized with **spTPA-N$_3$** in DMSO at 60 °C was compared to solution-functionalized **PT-spTPA** (73/27) spin coated from *o*DCB. The much more prominent **TPA** band of the 41/59 film is immediately visible while the shapes of the backbone bands are very similar.

In conclusion, the film functionalization approach seems to be an efficient alternative to solution functionalization. If suitable reaction conditions (solvent, temperature) are chosen, near-quantitative functionalization of the films with any organic azide compound should be feasible.

5.3.3 Electrochemical Doping and Crosslinking

Cyclic Voltammetry and Spectroelectrochemistry

The precursor polymer **P(3HT-*co*-3TBT)** (73/27) as well as both CRPs **PT-TPA** and **PT-spTPA** were studied with cyclic voltammetry coupled with *in-situ* optical absorption spectroscopy. These experiments have been shown in the past to be valuable tools to elucidate intermediate species both for the doping mechanism of polythiophenes as well as the dimerization of triarylamine and carbazole units.[52, 54, 249, 336] The polymers were spin coated on gold and ITO electrodes, dried and then electrochemically cycled in 0.1 M NBu_4PF_6 solution with a typical scan rate of 20 mV/s. The precursor polymer (Figure

5.24) exhibits typical behavior for polythiophene backbones with rather weak π-π stacking. At the onset of backbone oxidation (0.14 V against Fc/Fc^+, corresponding to a HOMO level of -5.24 eV) the neutral **PT** band at 536 nm starts to decrease in intensity while the backbone polaron band ($\mathbf{PT^{+\bullet}}$) slowly increases. In the peaktrend plots (Figure 5.24 a and c) this can be easily followed. In addition, an isosbestic point is clearly seen at 627 nm. At potentials higher than ~0.58 V the $\mathbf{PT^{+\bullet}}$ band starts to broaden and decrease in intensity while the increasing absorption around 1050 nm provides indication for the formation of backbone bipolaron species ($\mathbf{PT^{2+}}$) which exhibit an extremely broad absorption band with a maximum in the NIR region.[53] In the backward scan (Figure 5.24 c and d) the reverse process is taking place until the neutral **PT** band is fully recovered. The weak shoulder at ~610 nm is mostly recovered after discharging the polymer film and the 2nd cycle CV is very similar to the the first, indicating only little changes in film structure due the uptake and release of counterions during the electrochemical experiment. In the spectroelectrochemical measurements of **PT-TPA** (Figure 5.25), the situation gets more complex. In the fully discharged state at -0.54 V, neutral **TPA** (329 nm) and **PT** (520 nm) are present. When increasing the potential first the backbone oxidation starts to take place starting from its onset potential of 0.08 V. At ~0.5 V a steep increase in current is seen in the cyclic voltammogram which is caused by the four electrons released per dimer (two for oxidation of two **TPA** monomers and two for **TPB** reoxidation). The wave exhibits a pronounced maximum at $E_p = 0.65$ V. At the onset of this wave the neutral **TPA** band starts to decrease and a new band corresponding to the dication $\mathbf{TPB^{2+}}$ appears with a maximum around 724 nm which steadily increases. The intermediate radical cation band ($\mathbf{TPA^{+\bullet}}$) could not be registered suggesting fast and essentially quantitative dimerization of the **TPA** pendant groups. At high potentials again an increase in absorption around 1050 nm is observed which can be mainly attributed to $\mathbf{PT^{2+}}$. However, NIR absorption has also been found for **TPA**/**TPB** species, thus complicating the assignment of this increase in absorption.[336] In the backward scan (Figure 5.25 c and d), discharge of the $\mathbf{TPB^{2+}}$ units over the $\mathbf{TPB^{+\bullet}}$ radical cation species (482 nm) to the neutral **TPB** species (359 nm) can be observed. The band corresponding to the intermediate $\mathbf{TPB^{+\bullet}}$ species is hardly visible due to superposition with the neutral **PT** band. In the cyclic voltammogram the two-electron discharge process of the $\mathbf{TPB^{2+}}$ groups is seen as two highly overlapping waves. It has to be noted the backbone discharge is also taking place simultaneously. In the 2nd and all following cycles (compare Figure 5.25 e) charging and discharging of the polythiophene backbone accompanied by the two-electron charging and discharging process of **TPB** is seen. The shape of the **PT** oxidation wave changes between the first and all following cycles while its onset potential remains unchanged, indicating

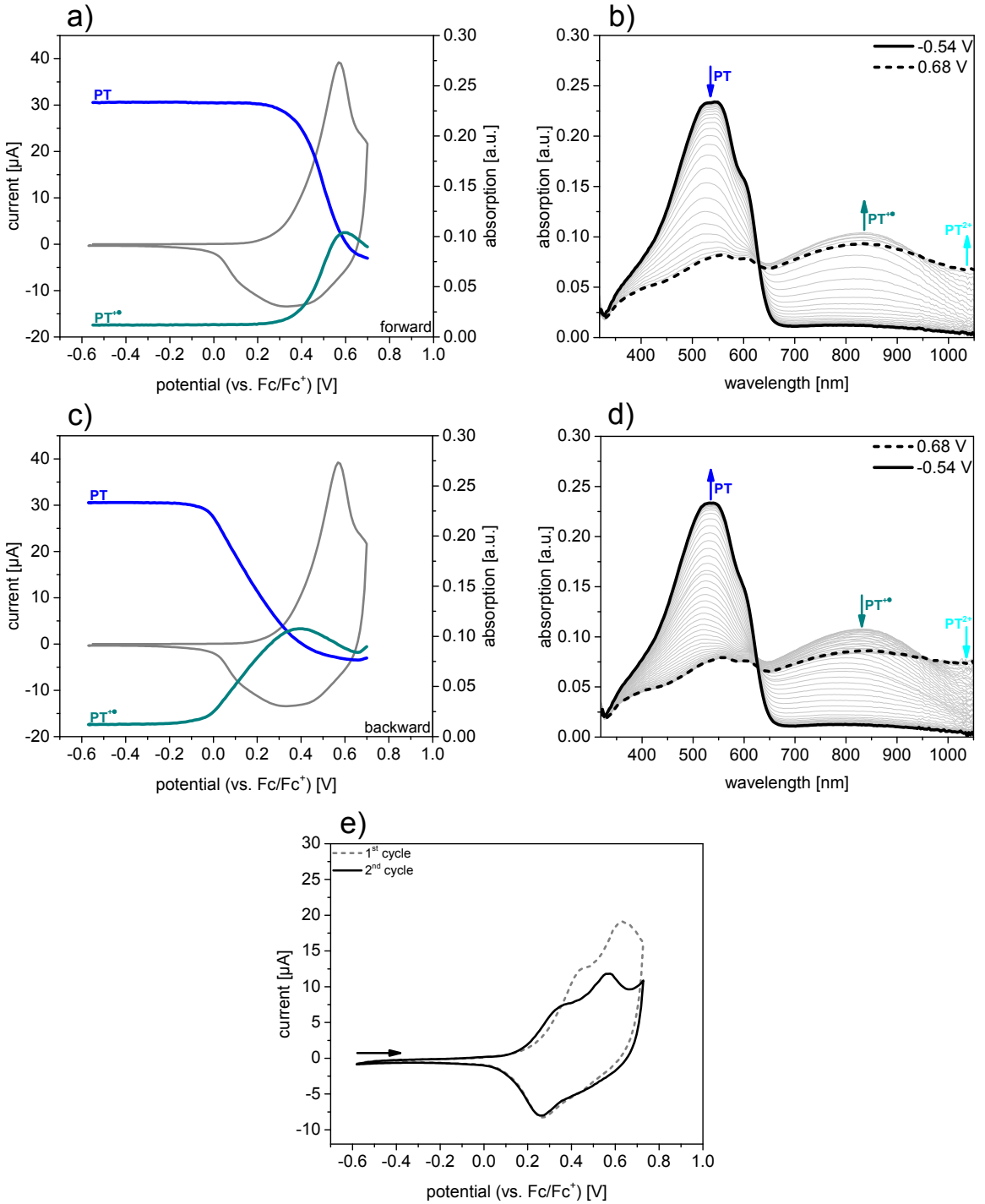

Figure 5.24: a), b) Forward and c), d) backward scans of spectroelectrochemical measurements of **P(3HT-*co*-3TBT)** thin films. e) Comparison of 1st and 2nd cycle CV measurements on gold electrode.

an influence of the crosslinking reaction on film morphology. From the oxidation and reduction waves in the 2nd cycle the half-wave potentials $E_{1/2}$(**TPB/TPB$^{+\bullet}$**) ~ 0.53 V and $E_{1/2}$(**TPB$^{+\bullet}$**/*TPB^{2+}*) ~ 0.62 V were approximated.

Because the optical absorption bands of the different **TPA**/**TPB** and **PT** species appearing during the oxidation of the CRPs are highly superimposed in many cases, the assignments for **PT-TPA** were further verified by solution spectroelectrochemical measurements of the model compound **T-TPA** (Figure 5.26) in a custom-built quartz cell under thin-layer conditions. The same electrolyte and measurement conditions as for thin film measurements were used and the concentration of the analyte in the electrolyte solution was 1 mg/mL. In the forward scan (Figure 5.26 a and b) the interconversion of neutral **TPA** into **TPB^{2+}** dimers can easily be followed at potentials higher than ~0.5 V. Due to the absence of **PT** backbone absorption it was possible to detect the intermediate **TPA$^{+\bullet}$** species at λ_{max} = 356 nm. The band maxima of neutral **TPA** (328 nm) and **TPB^{2+}** (714 nm) fit very well to the assignments for **PT-TPA** thin films, considering the slight shift of band maxima due to superposition with the backbone bands. In the backward scan (Figure 5.26 c and d) the two-electron reduction of **TPB^{2+}** to neutral **TPB** is seen and the appearance and disappearance of the intermediate **TPB$^{+\bullet}$** radical cation can easily be followed in the peaktrend plot. **TPB** and **TPB$^{+\bullet}$** exhibited band maxima of 359 and 489 nm, respectively, again confirming the assignments made for **PT-TPA**.

In **PT-spTPA** thin films (Figure 5.27) the dimerization potential was found to be lower compared to **PT-TPA** with a peak potential of the dimerization wave at E_p = 0.50 V. This can be attributed to the smaller pendant group π-system (triazole ring not conjugated with **TPA**) and the influence of the amide linkage on the **TPA** system. The backbone oxidation onset remains almost unchanged (0.05 V). The dimer oxidation and reduction waves are shifted towards lower potentials as well ($E_{1/2}$(**TPB/TPB$^{+\bullet}$**) ~ 0.40 V and $E_{1/2}$(**TPB$^{+\bullet}$/TPB^{2+}**) ~ 0.52 V).

Notably, the separate waves for the two-electron charging and discharging process are found to be much better resolved than in **PT-TPA** films which presumably can be mainly attributed to the higher spatial separation of the pendant groups from the backbone and the associated higher degree of conformational freedom. While the **TPA** and **PT**/**PT$^{+\bullet}$** absorption band maxima as well as the **TPB** and **TPB$^{+\bullet}$** bands stay roughly the same at 326 (**TPA**), 365 (**TPB**), 513 (**PT**), 479 (**TPB$^{+\bullet}$**) and 850 nm (**PT$^{+\bullet}$**), the **TPB^{2+}** band is shifted significantly to higher wavelengths (~858 nm) which can be attributed to the different substitution of the **TPA** unit as well. Due to superposition with the **PT$^{+\bullet}$** band this band can only be definitely assigned with the help of the peaktrend

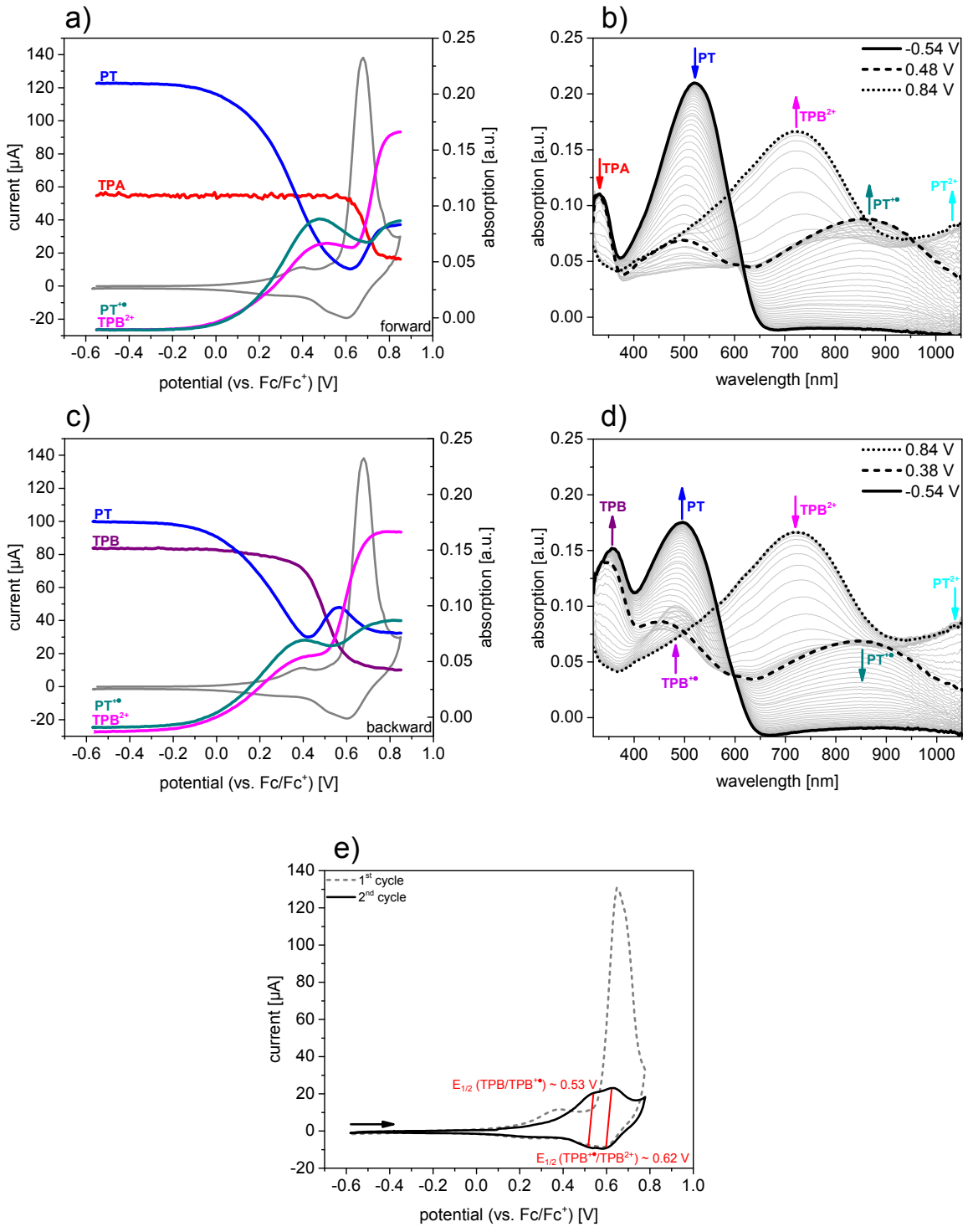

Figure 5.25: a), b) Forward and c), d) backward scans of spectroelectrochemical measurements of **PT-TPA** thin films. e) Comparison of 1st and 2nd cycle CV measurements on gold electrode.

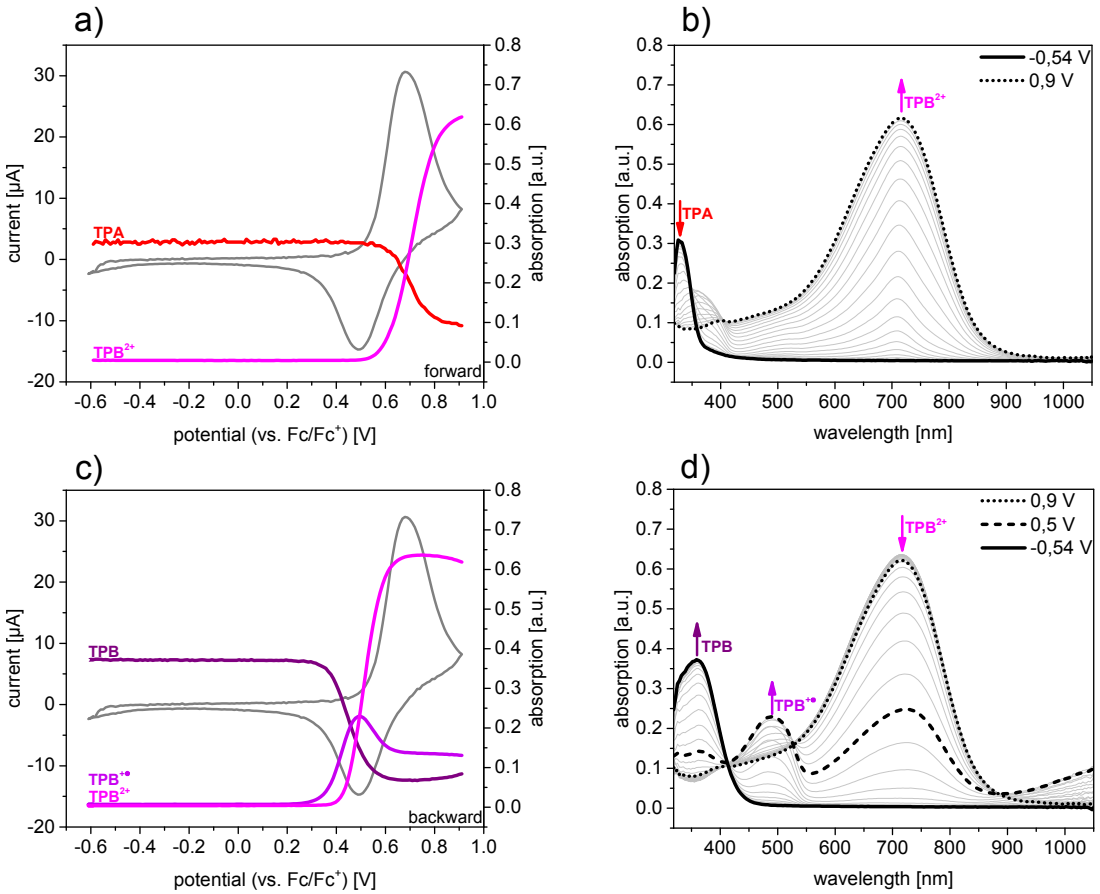

Figure 5.26: a), b) Forward and c), d) backward scans of spectroelectrochemical measurements of model compound **T-TPA** in solution.

plots (Figure 5.27 a and c) in which a plateauing of the absorption is found around 0.4 V in the forward scan, corresponding to a fully developed $\mathbf{PT^{+\bullet}}$ band (compare spectrum at 0.42 V in Figure 5.27 b). At potentials higher than ~0.5 V the absorption starts to increase again corresponding to the development of the $\mathbf{TPB^{2+}}$ band. In contrast to **PT-TPA** the increase of an additional band at 744 nm was reproducibly registered at potentials higher than 0.4 V and during the course of $\mathbf{TPB^{2+}}$ generation which was attributed to $\mathbf{TPA^{+\bullet}}$ radical cations. Additionally, a very weak, barely visible band emerges around 385 nm. The band at 744 nm persists as a shoulder in the backward scan and also in the 2nd cycle suggesting that some **TPA** units were not able to dimerize in these experiments. The reappearance of a neutral **TPA** band next to the neutral **TPB** band in the fully discharged crosslinked polymer spectrum (Figure 5.27 d), spectrum at -0.54 V) further supports this finding. As an additional proof for the origin of this shoulder, spectroelectrochemical measurements of highly dilute (0.1 mg/mL) solutions of $\mathbf{spTPA\text{-}N_3}$ were performed (Figure 5.28).

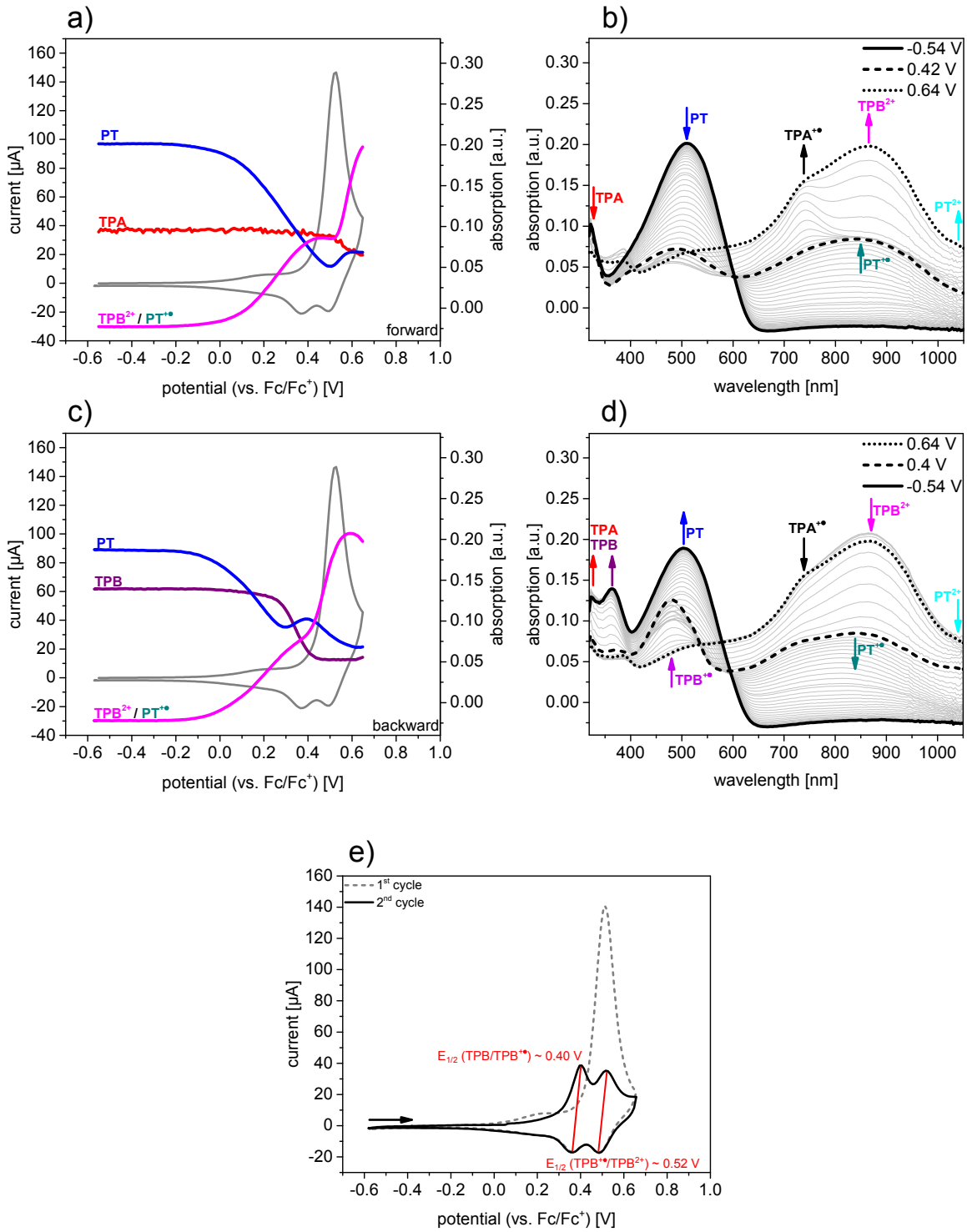

Figure 5.27: a), b) Forward and c), d) backward scans of spectroelectrochemical measurements of **PT-spTPA** thin films. e) Comparison of 1st and 2nd cycle CV measurements on gold electrode.

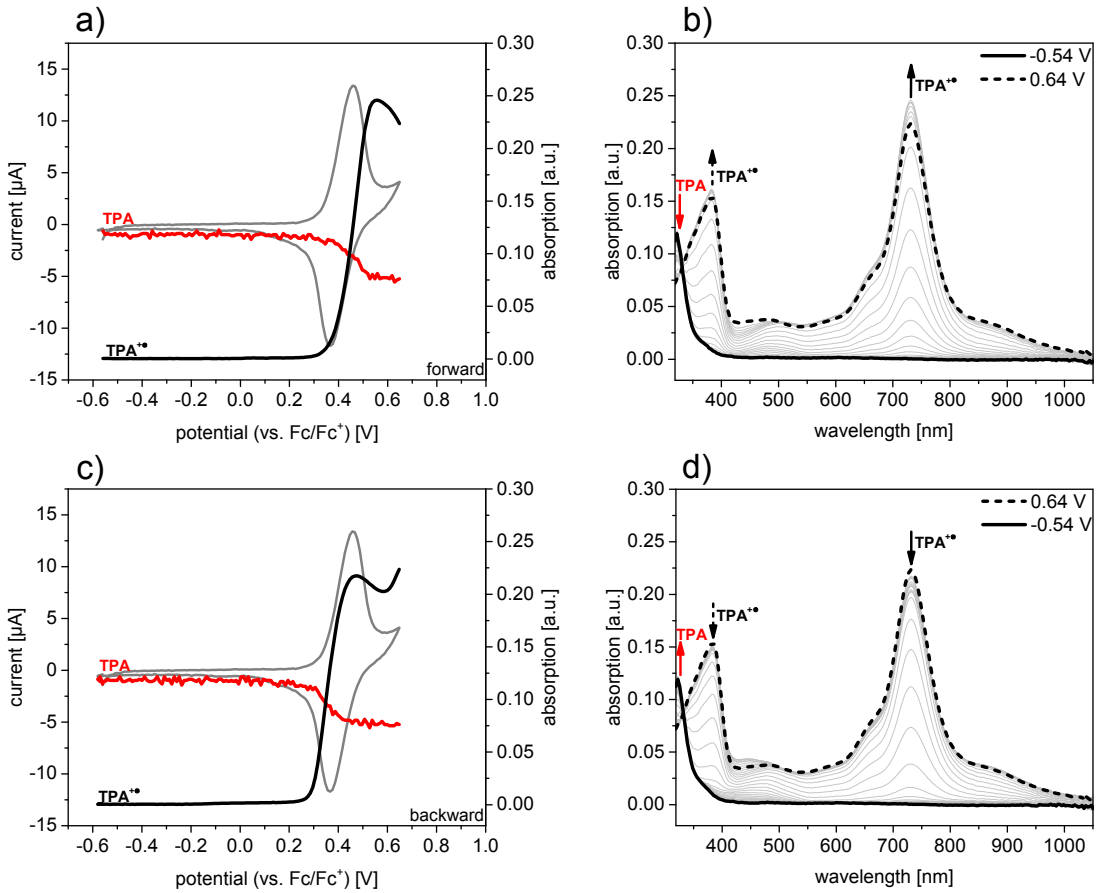

Figure 5.28: a), b) Forward and c), d) backward scans of spectroelectrochemical measurements of model compound **spTPA-N$_3$** in highly dilute solution (0.1 mg/mL).

It was found that it was possible to almost fully suppress the dimerization reaction and only charge and discharge the **TPA** units in a one-electron process at such low concentrations which gave us the opportunity to unambiguously assign the bands at 382 and 731 nm in the solution measurements to **TPA$^{+\bullet}$** which correspond to the bands at 385 and 744 nm in the thin film measurements.

Conductance Profiles and Conductivity Approximations

After investigating the processes and chemical species occurring in the CRPs during oxidative dimerization on the molecular level, we focused our attention on the potential-dependent conductance profiles of the polymers (Figure 5.29). *In-situ* measurements utilizing a setup similar to an electrolyte-gated transistor were performed. As mentioned earlier, redox polymers containing **TPA** pendant groups attached to an insulating, nonconjugated backbone have been found to exhibit mixed-valence conductance.[232, 233]

The associated conductance profiles typically show very narrow potential windows of conductance with two significant maxima corresponding to exactly half-filled states of the radical cation and dication oxidation states, respectively. The fully discharged and fully charged states possess minimum conductance. Both **PT-TPA** and **PT-spTPA** were however found to exhibit onsets of conductance corresponding to the onsets of the backbone oxidation waves in the cyclic voltammogram followed by broad plateaus of high conductance values without a significant maximum. Such profiles are typical for polythiophenes and other conjugated polymers, suggesting charge delocalization along the conjugated backbone as the dominant pathway of charge transport.[37, 39, 49, 337–339] When comparing the precursor polymer **P(3HT-*co*-3TBT)** and the functionalized CRPs, the onset of the increase in conductance is found to correspond very well to the onset of backbone doping in all cases. In the first cycle, the dimerization reaction caused a small drop in conductance which was immediately recovered after crosslinking. The decrease in conductance during the backward scan in the first cycle as well as the conductance increase and decrease in further cycles were shifted to slightly higher potentials. In the 2nd cycles, approximately the same values of maximum conductance as in the first cycles were reached for all polymers. The **TPB** oxidation and reduction potentials lie within the plateau of maximum conductance for both CRPs, thus confirming the assumption of a redox matched polymer system.[247] When oxidizing the polymer films to potentials higher than ~1.0 V vs. Fc/Fc$^+$ a drop in conductance values was registered and in the following cycles the previous values were not reached anymore. This can be attributed to overoxidation phenomena which are well-known for various conjugated polymers and lead to irreversible degradation of the polymer films due to side reactions.[37]

Since the calculation of material-specific conductivity values from *in-situ* conductance profiles tends to produce biased results mainly due to effects of the potential applied during the simultaneous CV measurement, *ex-situ* two-point-probe (2PP) measurements of the crosslinked films (Figure 5.30) were performed. A commercially available **P3HT** batch (*Merck*, $\overline{M_n}$ = 30.9 kg/mol, PDI = 1.9) was used as a reference material. The polymers were deposited on interdigitated Pt electrodes (100 µm channels), crosslinked *via* cyclic voltammetry and afterwards charged to a potential of 0.65 V vs. Fc/Fc$^+$ and held at this potential. For crosslinking and charging both interdigitated electrode combs were set as the working electrode. The electrode was then removed from the electrolyte and the two-point-probe measurement setup was immediately connected to the two combs and a current applied between the electrodes. The conductivity values were approximated from the measured film resistance and the physical dimensions of the electrode, neglecting contact resistances. To obtain reliable results the homogeneity and thickness of the films

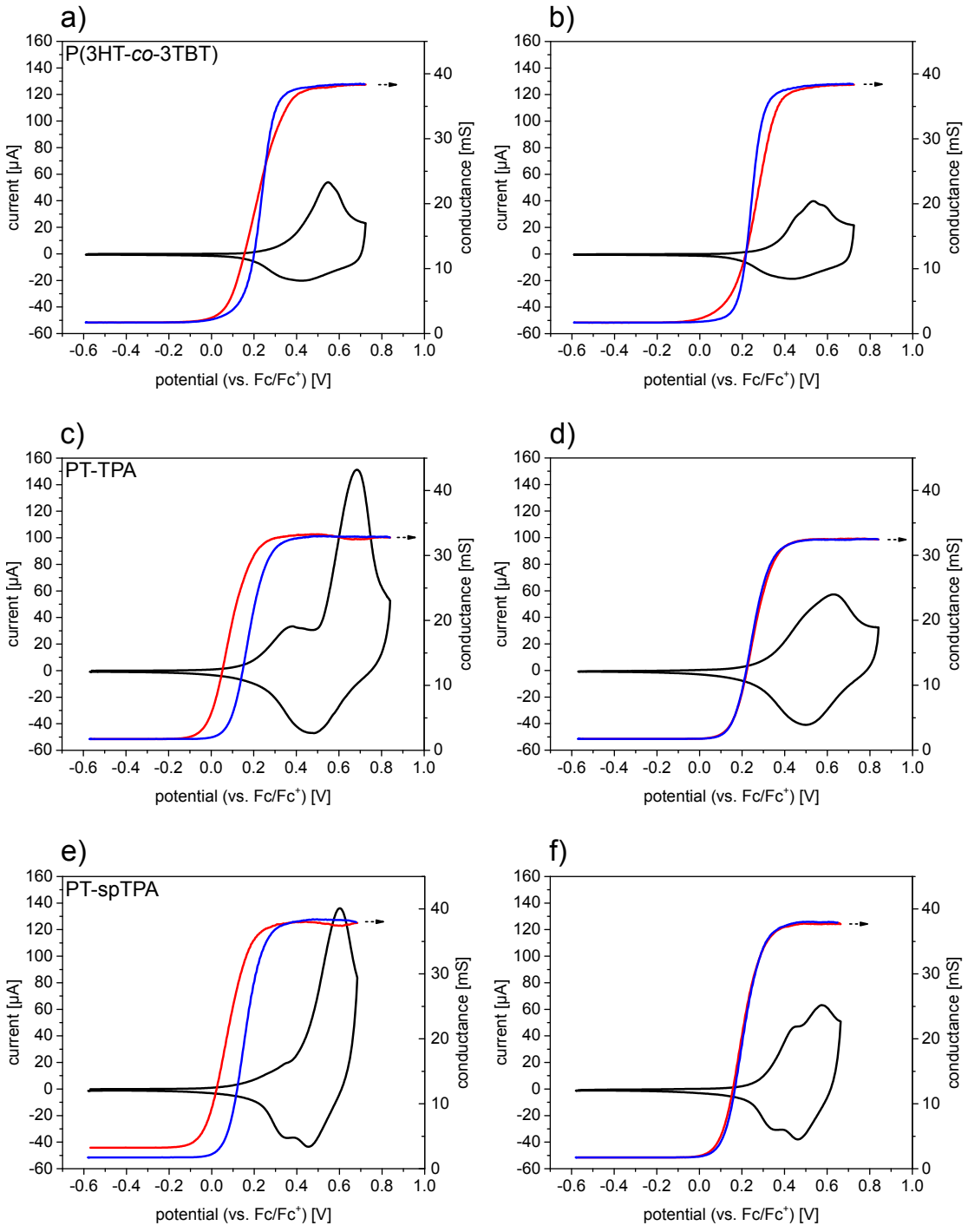

Figure 5.29: a), c), e) 1st cycle and b), d), f) 2nd cycle CV measurements of polymer thin films on interdigitated Pt electrodes coupled with *in-situ* conductance measurements. Forward scan conductance profiles are shown in red, backward scan values in blue.

on the interdigitated area of the electrodes had to be carefully controlled by profilometry. A representative measurement can be seen in the inset of Figure 5.30 b. The bare glass area of the substrates was used as the baseline for the measurements. For **P3HT**, **PT-TPA** and **PT-spTPA** conductivity values of 1.12, 0.04 and 0.15 S/cm in the charged state were obtained by this method, compared to $2.25 \cdot 10^{-4}$, $4.04 \cdot 10^{-5}$ and $5.79 \cdot 10^{-5}$ S/cm for the neutral films. Neutral as well as charged films were measured immediately after removal from the electrolyte. It has to be noted that, due to contact resistances, 2PP measurements are generally less accurate than four-point-probe (4PP) measurements which were not feasible in this case due to the underlying conducting substrates which would falsify the results. However, contact resistances in the system add to the polymer film resistance and thus lower the apparent film conductivity. The results are thus likely to slightly underestimate the real conductivity values. On both **PT-TPA** and **PT-spTPA** conductivities were measured over 10 h under ambient conditions to test the long-term stability of the electrochemically charged crosslinked films (Figure 5.30 b). During the course of the first hour a slight drop in conductivity values occured, likely related to the drying of residual electrolyte from the electrochemical charging process. During the remaining time of the measurement the conductivity values remained almost constant for both polymers.

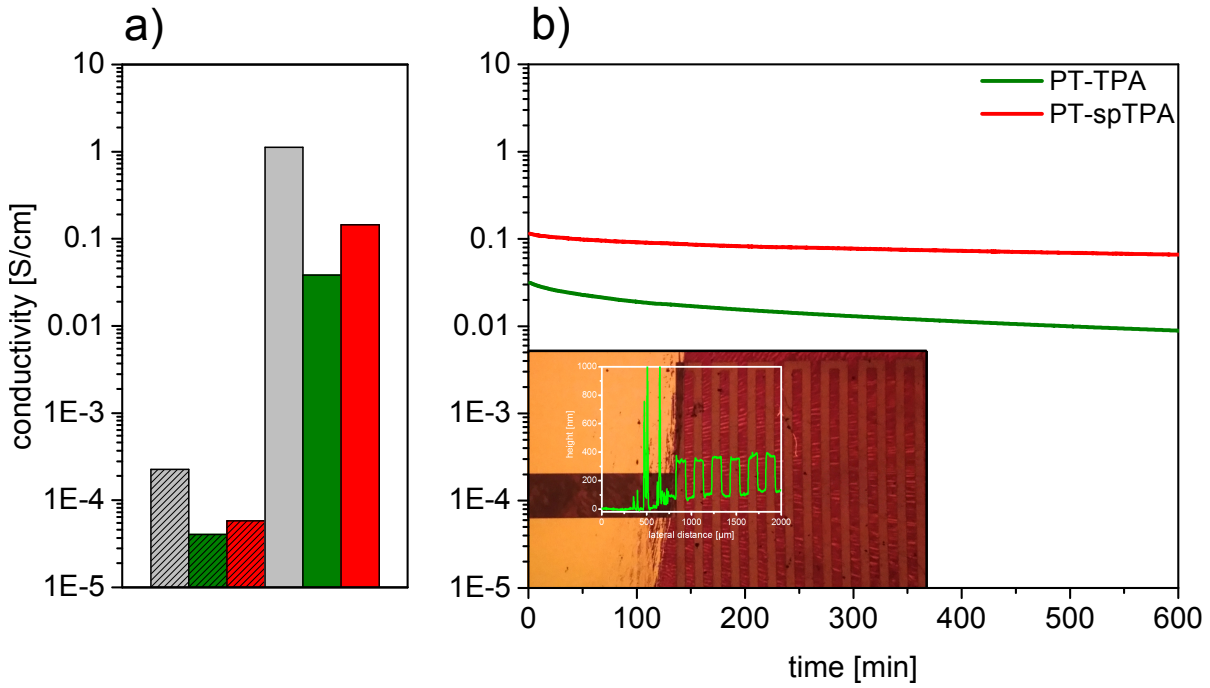

Figure 5.30: a) Two-point-probe conductivity approximations of as-cast (hatched) and electrochemically oxidized (0.65 V vs. Fc/Fc^+) films of **P3HT** (grey), **PT-TPA** (green) and **PT-spTPA** (red). b) Conductivity behavior of CRP films measured under ambient conditions for 10 h. Inset: Representative height profile of CRP film on interdigitated Pt electrode. The bare glass area was set as the baseline for profilometry.

Stability Investigations of Crosslinked Films

Macroscopically, the dimerization reaction caused a color change of the thin films of **PT-TPA** and **PT-spTPA** from dark red to bright orange and the films became insoluble in all tested solvents including chloroform, THF and halogenated benzene derivatives, which previously rapidly dissolved the as-cast films. In Figure 5.31 a, light miscroscopic photographs of a film of **PT-TPA** on a gold electrode before and after crosslinking are seen. The film was spin coated on the electrode from a homogeneous solution in chloroform and only a part of the film was electrochemically crosslinked by controlling the immersion depth in the electrolyte solution. After crosslinking, both the crosslinked and the non-crosslinked parts of the film were partially immersed into chloroform for one hour resulting in quantitative dissolution of the as-cast part of the film. It was possible to perform cyclic voltammetry experiments of the crosslinked films in THF-based electrolytes which would quickly dissolve the as-cast films. The first 50 cycles of such an experiment are displayed in Figure 5.31 b. Since no coloring of the electrolyte solution was observed

during the course of the experiment, the decrease in measured currents is most likely caused by some detachment of solid polymer film from the electrode.

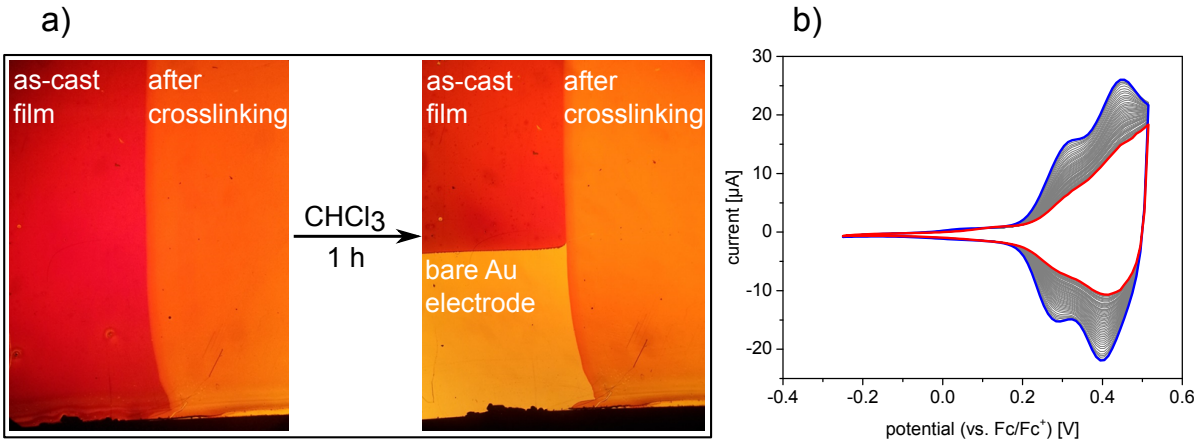

Figure 5.31: a) Partially crosslinked thin film of **PT-TPA** on a gold electrode before and after immersion into chloroform for 1 h. The solvent only dissolves the non-crosslinked part of the film. b) Cycles 2 (blue) to 50 (red) of a crosslinked **PT-spTPA** film on gold in a THF-based electrolyte.

5.3.4 Chemical Doping and Crosslinking

We first tested $\mathbf{F_4TCNQ}$ as a dopant for **PT-TPA** (Figure 5.33 a and b). $\mathbf{F_4TCNQ}$ doping can be achieved either by combining the dopant and polymer solutions prior to film deposition ("solution mixing") or by spin coating the dopant solution onto the dried polymer film from an orthogonal solvent or dipping the film into the dopant solution ("sequential doping").[40, 47, 340] The latter method was chosen due to reported problems with aggregation of the doped polymer in mixed solutions and because sequential doping seems to often lead to higher conductivites.

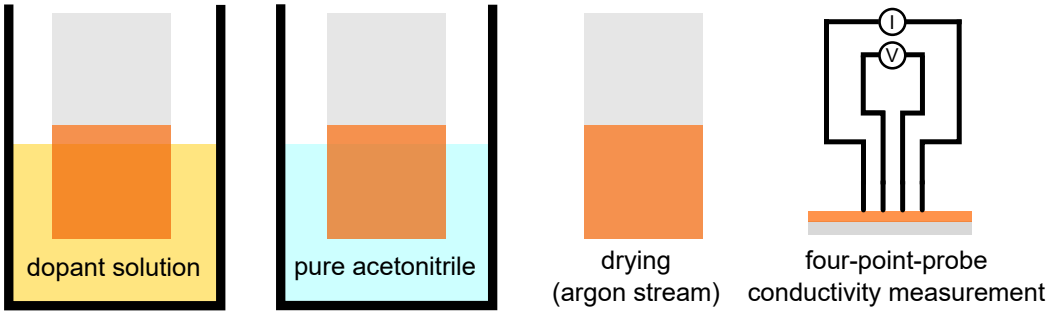

Figure 5.32: Sequential method used for chemical doping of thin films of **PT-TPA** and **PT-spTPA**, followed by conductivity measurements.

The polymer was spin coated on cleaned glass substrates from a 5 mg/mL solution in toluene, dried and the film immersed into **F_4TCNQ** solutions in acetonitrile with concentrations varying from 0.01 to 3 mg/mL for one minute (Figure 5.32). The films were then shortly dipped into pure acetonitrile to remove excess unreacted **F_4TCNQ** and blown dry under a stream of argon. Optical absorption spectra (Figure 5.33 a) and four-point-probe conductivity values (Figure 5.33 b) were measured immediately to exclude degradation of the doped films. From the absorption spectra, normalized to the maximum of the neutral **TPA** band at 335 nm, the doping of the conjugated polythiophene backbone is clearly visible.[309] The neutral **PT** band (516 nm) decreases with increasing concentration of the dopant and the radical cation **$PT^{+\bullet}$** band (~720-920 nm) increases. The **$PT^{+\bullet}$** band is additionally superimposed with bands corresponding to the radical anion **$F_4TCNQ^{-\bullet}$** with maxima at 774 and 880 nm.[41, 43, 44] However, **F_4TCNQ** was clearly not able to oxidize a significant amount of **TPA** units, since the corresponding neutral **TPA** band is not influenced and no additional bands corresponding to charged **TPA** or **TPB** moieties emerged. From electrochemical peak potentials E_p of the **TPA** oxidation waves of **PT-TPA** (0.65 V vs. Fc/Fc^+) and **PT-spTPA** (0.50 V), the respective HOMO levels at -5.75 and -5.62 eV could be approximated.[48] **TPB**/**$TPB^{+\bullet}$** half-wave potentials lie at 0.53 V and 0.40 V for the two polymers, corresponding to HOMO levels of -5.63 and -5.50 eV. In studies on alkyl-substituted **TPB** units our group found slightly lower values of $E_{1/2}$(**TPB**/**$TPB^{+\bullet}$**) = 0.29 V (-5.39 eV).[233] A similar **TPB** derivative with an ionization energy of -5.40 eV was reported to be only partially charged by **F_4TCNQ**.[341] These findings suggest that **F_4TCNQ** is not capable of oxidizing the **TPA** units in our polymers and initiate the dimerization. For comparison, as shown in chapter 4, **F_4TCNQ** was also not able to dope **P3TC6C2** thin films which exhibited an oxidation onset at 0.4 V, corresponding to a HOMO level at -5.5 eV.

PT-TPA films doped at **F_4TCNQ** concentrations of 0.01 mg/mL did not exhibit conductivities measurable with our four-point-probe setup which is limited to values higher than approximately 10^{-6} S/cm. However, at concentrations of 0.05 mg/mL and higher, the conductivity values increased steeply, reaching saturation above 1 mg/mL with the highest obtained value at 0.5±0.2 S/cm for a concentration of 3 mg/mL.

Iron(III) chloride was additionally employed as a dopant since this *Lewis* acid has been used for both synthesizing and doping polythiophenes and dimerizing carbazoles and triphenylamines in literature.[53, 224, 256, 259, 342–344] Monomer oxidation and dimerization follows a similar mechanism to electrochemical oxidative coupling.[92, 171] Vapor phase doping of **P3HT** with **$FeCl_3$** has been shown to lead to conductivities up to 63 S/cm.[53] In solution-doping experiments, ~40 S/cm could be reached.[345] Such strong oxidation agents

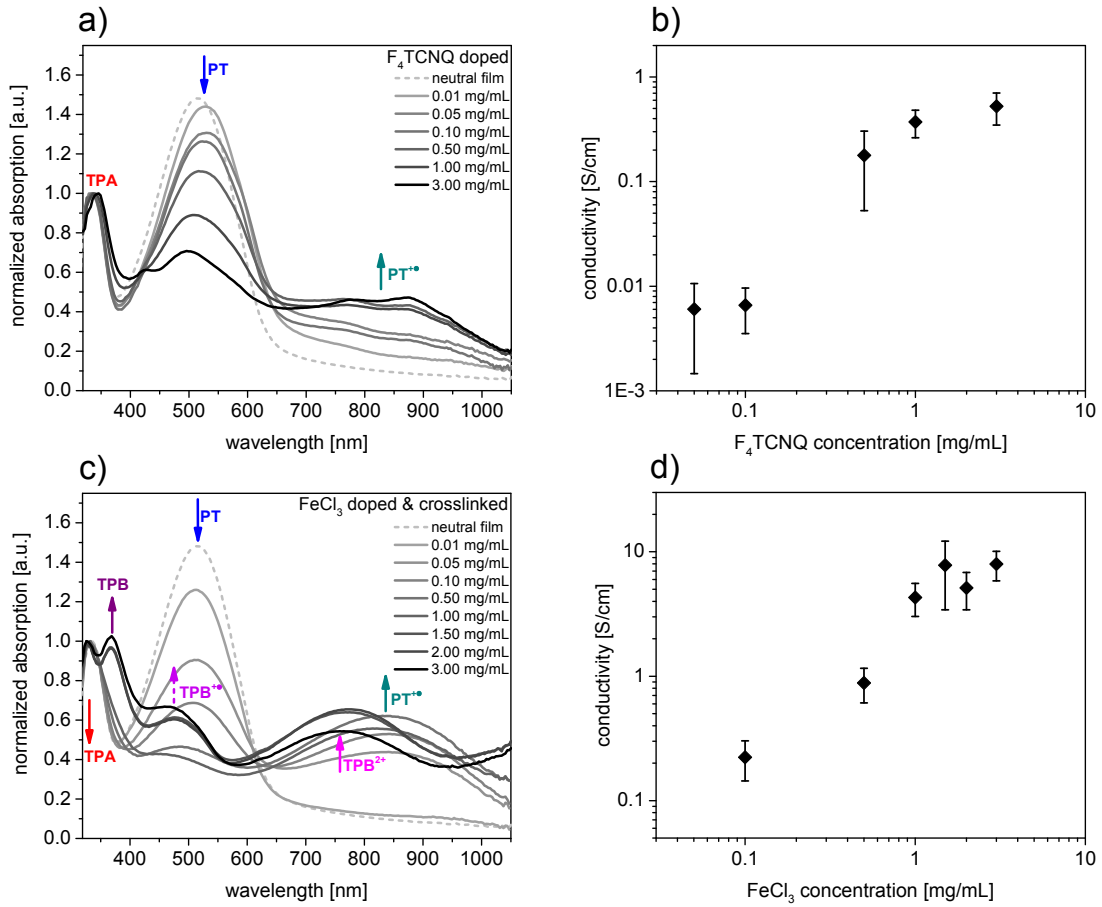

Figure 5.33: Optical absorption spectra of thin films of **PT-TPA** doped with a) **F_4TCNQ** and c) **$FeCl_3$**. b), d) Corresponding bulk conductivities measured *via* four-point-probe.

are however able to overoxidize and irreversibly degrade the polymer films if the doping conditions are not carefully controlled. The long-term stability of the conductivities of these doped films, especially under ambient conditions, remains unsatisfactory, presumably due to diffusion phenomena of the small counterions.[345]

A similar doping protocol as for **F_4TCNQ** was used, however, the immersion times were shortened to only two seconds since **$FeCl_3$** solutions of the same concentrations were found to react much quicker with the polymer films. In some cases, longer immersion times even led to a partial degradation of the films, accompanied by detachment of polymer flakes from the glass substrates. The absorption spectra (Figure 5.33 c) again clearly show backbone doping (**PT** at 516 nm, **$PT^{+\bullet}$** around 837 nm). In addition, at **$FeCl_3$** concentrations higher than 1.5 mg/mL, bands for all neutral and charged **TPA** and **TPB** species found during the electrochemical experiments appear simultaneously (**TPA** at 335 nm; **TPB** at 368 nm; **$TPB^{+\bullet}$** at ~465 nm; **TPB^{2+}** at ~757 nm). This clearly suggests

crosslinking due to oxidation by **$FeCl_3$** and a mechanism similar to electrochemical crosslinking. The spectra of the highest dopant solution concentrations are very similar to the spectra of electrochemically doped **PT-TPA** films, suggesting at least comparable doping levels. The neutral **TPA** species was however not fully consumed, showing that a fraction of the pendant groups was not dimerized.

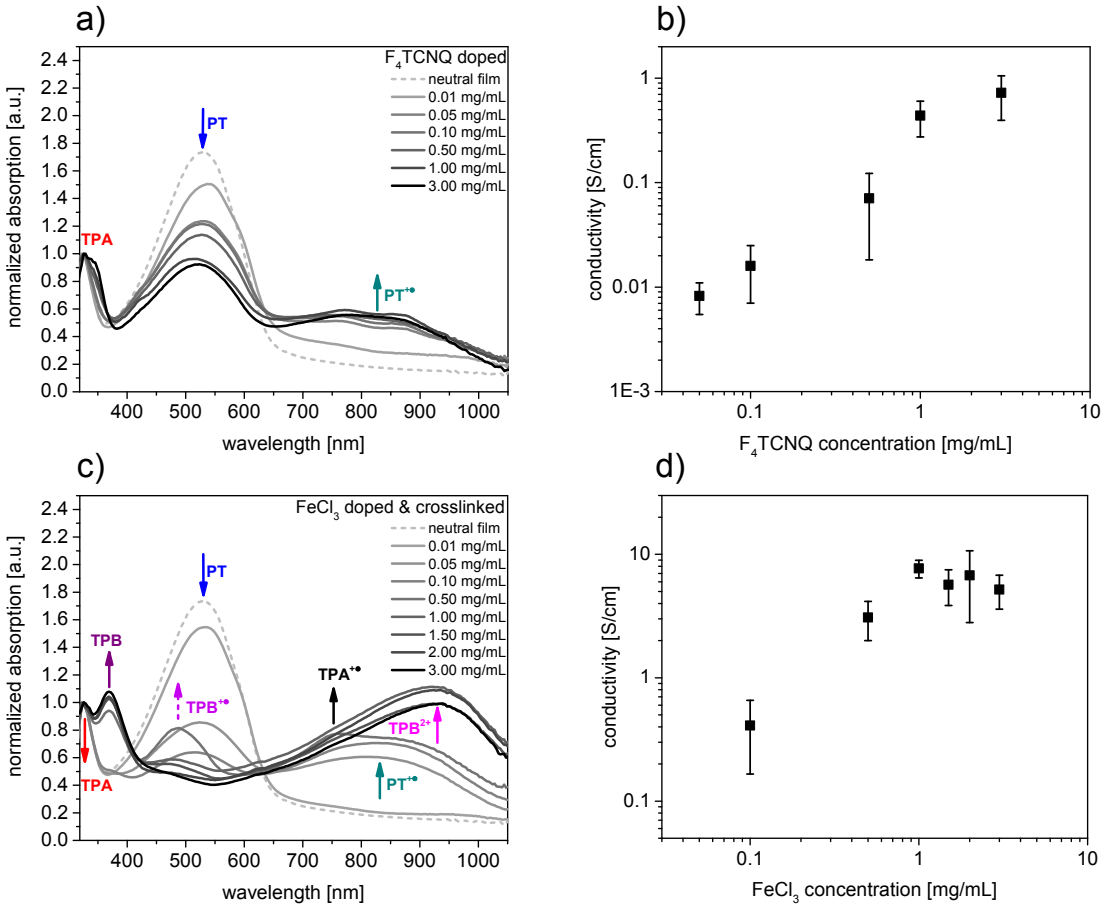

Figure 5.34: Optical absorption spectra of thin films of **PT-spTPA** doped with a) **F_4TCNQ** and c) **$FeCl_3$**. b), d) Corresponding bulk conductivities measured *via* four-point-probe.

Conductivity measurements for **$FeCl_3$**-doped films (Figure 5.33 d) show the same trend as has been found for **F_4TCNQ** doping, however, the obtained values are generally about one order of magnitude higher. This can be presumably mainly attributed to the higher obtainable doping levels due to the stronger oxidant and to the incorporation of additional charged **TPA** and **TPB** species which can contribute to the overall conductivity. For **PT-TPA**, saturation was reached at values as high as 8.0±2.1 S/cm. This is in line with literature findings which reported maximum values up to 63 S/cm in vapor doping experiments. With oxidants as strong as **$FeCl_3$** it is however easily possible to overoxidize

the polymers, leading to a decrease in conductivity and possible damage to the film. Exact control of the doping conditions is thus highly important. We experienced such phenomena when the immersion time was chosen too high. In the absorption spectra of the highest concentrations (>1.5 mg/mL) the increase in absorption around 1050 nm indicates significant development of bipolaron species which was not present in the **F_4TCNQ** doped films. Compared to films doped with **F_4TCNQ** the high conductivity values decayed significantly faster, suggesting lower stability of the doped films, possibly due to diffusion of the smaller counterions through the film.

For **PT-spTPA**, doping with both dopants yielded very similar results in terms of absorption properties and conductivity values (see Figure 5.34), compared to **PT-TPA**. Again, **F_4TCNQ** was not able to dimerize the pendant groups and crosslink the polymer. Conductivity values reached up to 0.7±0.3 S/cm. In the absorption spectra for **$FeCl_3$** doping (Figure 5.34 c) a very similar picture as in the electrochemical experiments is seen. Even the shoulder representing the intermediate **TPA** radical cation species **$TPA^{+\bullet}$** at ~757 nm was registered in one spectrum at a dopant solution concentration of 0.5 mg/mL. As expected from the lower oxidation potentials of the **TPA** and **TPB** units measured in electrochemical experiments, the dimerization reaction is found already at lower dopant solution concentrations of 0.1 mg/mL for **PT-spTPA** compared to **PT-TPA** (1.5 mg/mL). Table 5.4 summarizes all band maxima for the various **PT**, **TPA** and **TPB** species encountered during electrochemical and chemical doping. Saturation of conductivity values was found in the range of 7.7±1.3 S/cm for **PT-spTPA**.

Table 5.4: Maximum wavelengths of characteristic optical absorption bands corresponding to species involved in electrochemical and chemical doping and crosslinking.

	Maximum wavelengths λ_{max} [nm]						
	PT	**PT$^{+\bullet}$**	**TPA**	**TPA$^{+\bullet}$**	**TPB**	**TPB$^{+\bullet}$**	**TPB^{2+}**
	Electrochemical Doping[a]						
P(3HT-*co*-3TBT)	536	~834	-	-	-	-	-
PT-TPA	520	~864	329	-	359	~482	~724
T-TPA	-	-	328	356	359	489	714
PT-spTPA	513	~850	326	385, 744	365	~479	~858
spTPA-N$_3$	-	-	322	382, 731	-	-	-
	Chemical Doping with F$_4$TCNQ[b]						
PT-TPA	516	~720-920	335	-	-	-	-
PT-spTPA	529	~720-920	325	-	-	-	-
	Chemical Doping with FeCl$_3$[c]						
PT-TPA	516	~837	335	-	368	~465	~757
PT-spTPA	529	~847	325	-	372	~485	~933

a) Absorption spectra of polymers **P(3HT-*co*-3TBT)**, **PT-TPA** and **PT-spTPA** measured *in situ* during cyclic voltammetry of polymer thin films on ITO electrodes. Model compounds **T-TPA** and **spTPA-N$_3$** measured in solution at concentrations of 1 and 0.1 mg/mL, respectively. b) Thin film absorption spectra of polymer films on glass substrates measured immediately after doping.

5.3.5 Summary

In this chapter the synthesis and basic characterization of the conjugated redox polymers **PT-TPA** and **PT-spTPA** as well as electrochemical and chemical doping of these materials was presented. A typical conjugated polymer backbone (polythiophene) was combined with pendant triphenylamine (**TPA**) redox units which can be electrochemically and chemically dimerized to tetraphenylbenzidine (**TPB**) units which crosslink the polymer films.[233, 249]

The polymers were synthesized by a "click chemistry" postfunctionalization approach starting from the same alkyne-functionalized, regioregular polythiophene precursor copolymer **P(3HT-*co*-3TBT)** with a molar repeating unit ratio of 73/27.[12] This method allowed to ideally compare the properties of the two CRPs, excluding influences from differences in the polymer backbone composition, molecular weight and polydispersity. The successful functionalization and purity of the polymers was proven by a combination of NMR, IR and UV/Vis spectroscopy as well as size exclusion chromatography. The materials were

found to be soluble without any optically measurable aggregation phenomena in solvents like chloroform or THF, enabling facile deposition on substrates by standard methods like spin coating, blade coating or printing. All polymers showed good thermal stability with **PT-spTPA** being stable at temperatures as high as 346 °C.

Both CRPs as well as the precursor polymer were studied in electrochemical doping experiments consisting of cyclic voltammetry of thin films coupled with *in-situ* absorption spectroscopy as well as conductance measurements. While the precursor polymer showed spectroelectrochemical behavior typical for polythiophene backbones, in **PT-TPA** and **PT-spTPA** the electrochemical doping was accompanied by crosslinking of the pendant **TPA** groups to **TPB** dimers. Spectral evidence of all species (Table 5.4) involved in both the doping and dimerization processes was found. Some absorption bands could be unambiguously assigned by comparison with solution spectroelectrochemical experiments of model compounds. The conductance profiles of all three polymers showed typical behavior for polythiophene backbones, pointing at delocalization of charge carriers along the conjugated backbone as the dominant pathway of charge transport.[37, 49] In the crosslinked polymer films, both **TPB** dimer oxidation and reduction potentials lay within the plateau of maximum conductance, thus confirming the assumption of a redox matched polymer system. The material specific bulk conductivities of the thin films were further approximated by *ex-situ* two-point-probe measurements, yielding values in the range of 10^{-1} S/cm, compared to approximately 1 S/cm for the reference regioregular **P3HT**. The crosslinking reaction rendered the polymer films fully insoluble in all tested solvents and even extended electrochemical cycling of a crosslinked film in a THF-based electrolyte was possible.

Chemical doping of the polymers was performed with both the strong acceptor molecule $\mathbf{F_4TCNQ}$ and the *Lewis* acid $\mathbf{FeCl_3}$.[40, 53] UV/Vis spectroscopy of the doped films and four-point-probe conductivity measurements were performed. While in the case of $\mathbf{F_4TCNQ}$ doping only the polythiophene backbone could be charged, leading to decent conductivities of 0.5±0.2 and 0.7±0.3 S/cm for **PT-TPA** and **PT-spTPA**, respectively, doping with $\mathbf{FeCl_3}$ led to simultaneous crosslinking of the polymer chains by **TPB** dimers. Optical absorption spectra showed clear evidence of the same species which are involved in electrochemical oxidative dimerization, confirming a similar mechanism. Four-point-probe measurements yielded high conductivities up to 8 S/cm, close to the highest literature values for regioregular **P3HT** doped with $\mathbf{FeCl_3}$.

5.4 Mannose-functionalized Polythiophenes as Sensor Materials

Extending possible applications for the highly versatile alkyne-functionalized copolymer platform further, the precursor polymer system was tested as a basis for sensor materials. The strong interaction between the protein Concanavalin A (**Con A**) and α-D-mannose was chosen as a model system. In cooperation with the group of *Prof. Dr. Benoît Piro* at *Laboratoire ITODYS*, Paris, we planned to employ a polythiophene backbone functionalized with pendant α-D-mannose units as a model system for a **Con A** sensor based on the electrolyte-gated organic field effect transistor (EGOFET).[15, 75, 76] EGOFETs offer compatibility to aqueous buffer solutions and potentially extremely sensitive detection capabilities, especially for net negatively charged proteins like **Con A**. Its working principle is based on analyte binding on the interface between the organic semiconductor layer and the electrolyte. The analyte influences the electrochemical capacitance at this interface which in turn alters the transistor characteristics at a given gate potential. To the best of my knowledge, this is the first attempt to adapt the EGOFET principle for **Con A** sensing.

5.4.1 Polymer Synthesis in Solution

Motivated by the essentially quantitative polymer analogous functionalization of the **P(3HT-*co*-3TBT)** precursor polymers with two structurally different triphenylamine azides described in the previous chapter, similar conditions were chosen for synthesizing the mannose functionalized polythiophenes, which were termed **PT-Man**. Initially, the mannose azide **Man-PrN$_3$** bearing an azidopropyl linker was synthesized and used to functionalize the precursor polymer, which led to solubility issues. A second mannose azide derivative with an oligo(ethylene glycol) spacer (**Man-OEGN$_3$**) was later synthesized by *Marc Schnierle* during the course of his research internship, leading to highly improved solubility of the respective **PT-Man** derivative.

Synthesis of Mannose Azides

Both mannose azides were synthesized *via* modified literature procedures, starting from the commercially available, pure anomer α-D-mannose in its pentaacetylated form (**Man-OAc$_5$**).[279, 282]

The respective bromo- or iodo-terminated spacers were attached in the anomeric position by activation with BF_3. The blocking effect of the neighbouring acetyl protecting group and the anomeric effect led to retention of the α-configuration of the product. Halide-azide

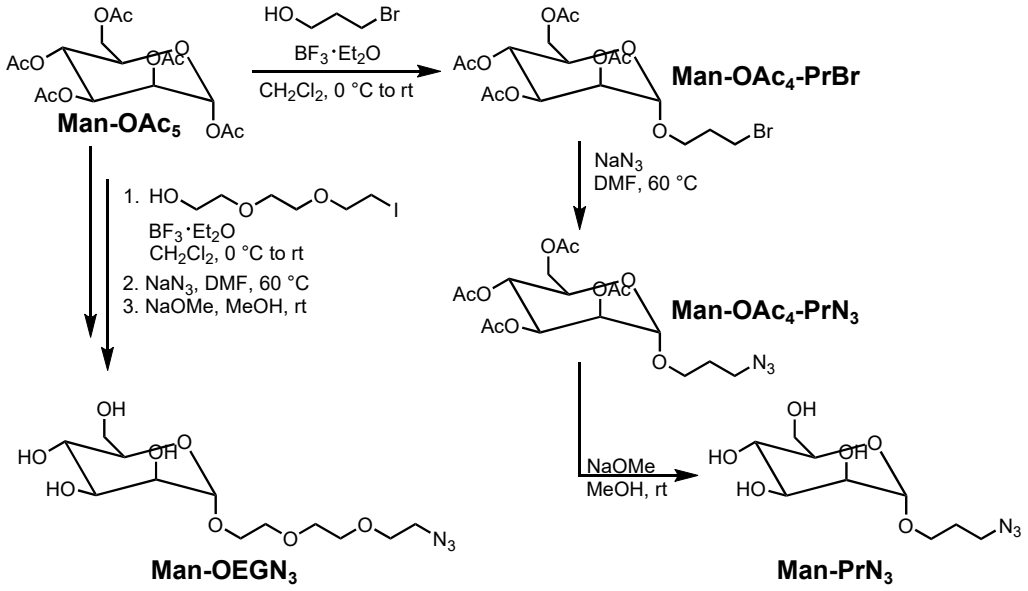

Scheme 5.7: Synthesis pathway to mannose azides **Man-PrN$_3$** and **Man-OEGN$_3$**, starting from the pentaacetylated pure anomer α-D-mannose **Man-OAc$_5$**.

exchange was subsequently performed in DMF at 60 °C, yielding the protected mannose azides **Man-PrN$_3$** and **Man-OEGN$_3$**. Deprotection of the alcohol groups was then performed using *Zemplén* transesterification conditions.[346] Quantitative azide exchange as well as deprotection reactions could be confirmed by a combination of NMR and IR spectroscopy as well as mass spectrometry.

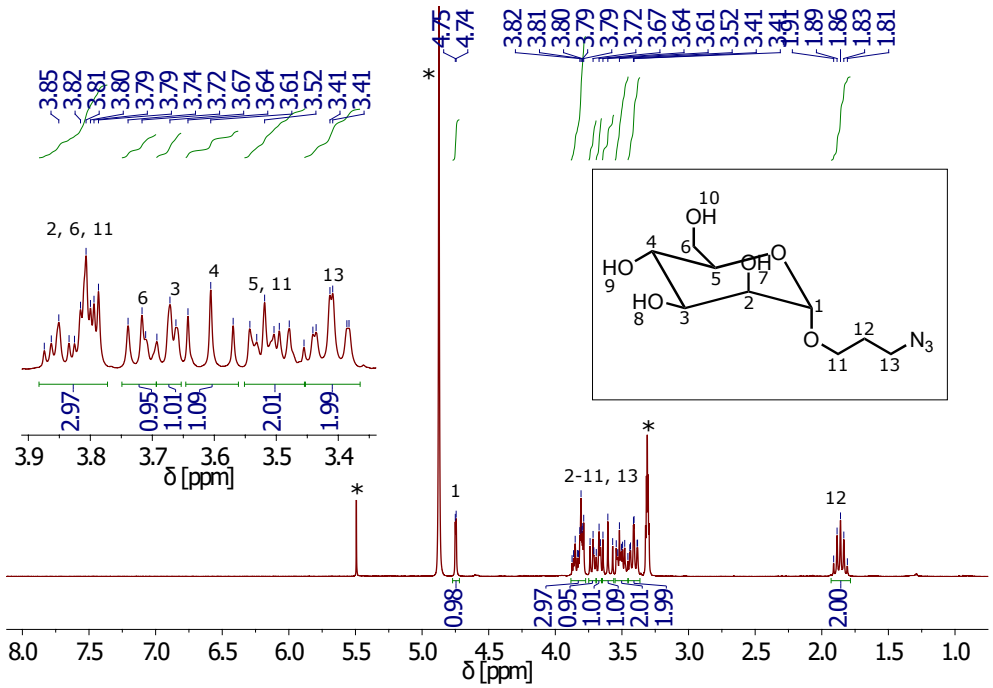

Figure 5.35: ^{1}H-NMR spectrum of purified mannose azide **Man-PrN$_3$** (room temperature, MeOD).

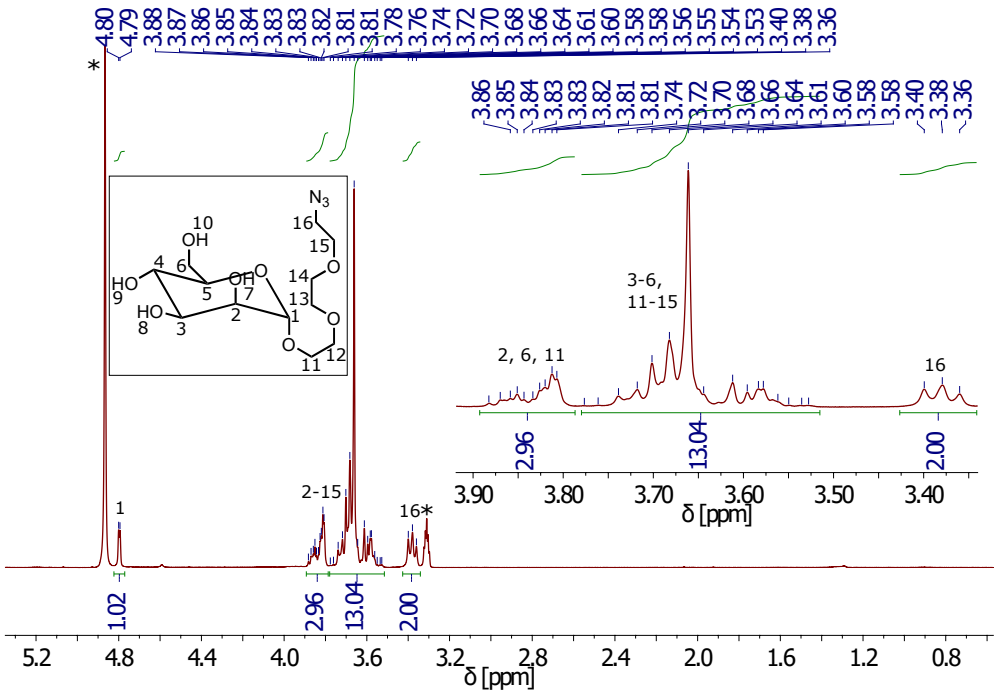

Figure 5.36: ^{1}H-NMR spectrum of purified mannose azide **Man-OEGN$_3$** (room temperature, MeOD).

Polymer Analogous Functionalizations

For the synthesis of the **PT-Man** polymers, CuAAC conditions similar to the synthesis of **PT-TPA** and **PT-spTPA** (chapter 5.3) were chosen (see Scheme 5.8). A **P(3HT-*co*-3TBT)** batch with a molar repeating unit ratio of 67/33, $\overline{M_n}$ = 18.5 kg/mol and a PDI of 1.6 was used.

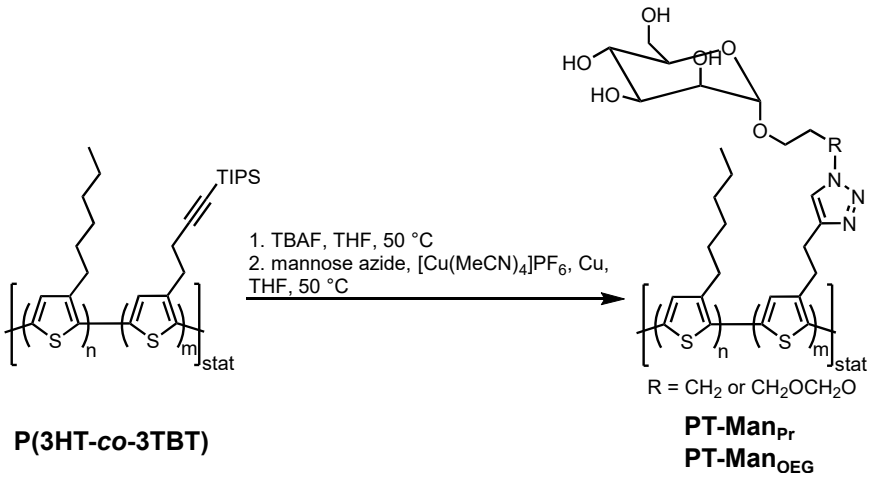

Scheme 5.8: Polymer analogous functionalization procedure yielding **PT-Man** polymers with propyl (**PT-Man$_{Pr}$**) and oligo(ethylene glycol) spacers (**PT-Man$_{OEG}$**).

Initially, postfunctionalization of the deprotected **P(3HT-*co*-3TBT)** precursor with the acetyl-protected mannose azide was attempted, since this would exclude possible side reactions of the sugar moieties during the CuAAC process. However, although presumably successful, this reaction led to products which were not compatible to the *Zemplén* conditions due to solubility reasons. Postfunctionalization was thus attempted with the deprotected mannose azides. For both polymers this led to interesting solubility behavior. The products were completely insoluble in all tested pure solvents like water, methanol, DMF, DMSO, acetone, THF, chloroform and *o*DCB, even at the respective reflux temperatures. However, in mixtures of *o*DCB and DMSO (2/1 to 5/1) the solubility increased significantly. In the case of the shorter propyl spacer derivative **PT-Man$_{Pr}$**, ultrasonication at 100 °C was needed to dissolve most of the polymer and some insoluble material still had to be removed by syringe filtration before film deposition. Successful functionalization could only be assumed for this polymer from the comparison of IR spectra which clearly showed the presence of OH groups (Figure 5.37). **PT-Man$_{OEG}$** with the longer oligo(ethylene oxide) spacer was however fully soluble in 5/1 mixtures of

*o*DCB and DMSO after slight heating. Only for this derivative it was possible to confirm the functionalization by NMR spectroscopy (Figure 5.38).

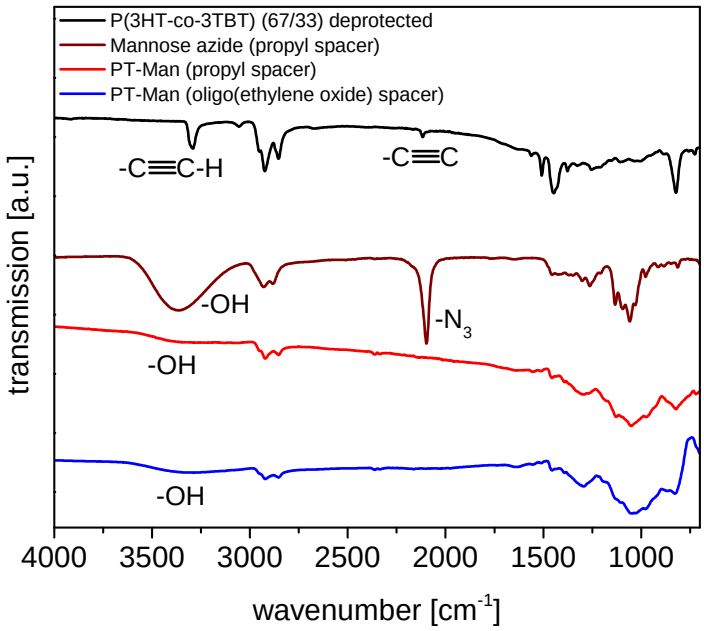

Figure 5.37: Comparison of IR spectra of the deprotected precursor polymer **P(3HT-*co*-3TBT)**, **Man-PrN$_3$** and both **PT-Man** derivatives.

A broad signal is seen in the region between 3.0 and 5.5 ppm, corresponding to the mannose and spacer protons. The quantitative shift of the polythiophene side chain protons at position 9 and 10 to 3.56 ppm was registered (compare chapter 5.3). The peculiar solubility behavior can be ascribed to the amphiphilic nature of the polymers: while polythiophene backbones are highly hydrophobic and exhibit strong π-π stacking interactions between the chains, the free alcohol groups of the mannose pendants tend to form inter- and intramolecular hydrogen bonds. In pure polar solvents like methanol or DMSO, the backbone stacking leads to low solubility while in chlorinated solvents like $CHCl_3$ or *o*DCB, which are among the best solvents for pristine polythiophenes, hydrogen bond formation hinders the separation of the chains. In mixtures of a good solvent for the backbone and a hydrogen bond acceptor like DMSO, hydrogen bonds can not only form between the sugar moieties but also between alcohol groups and solvent molecules, thus significantly lowering chain-chain interactions and enabling dissolution of the polymeric materials.

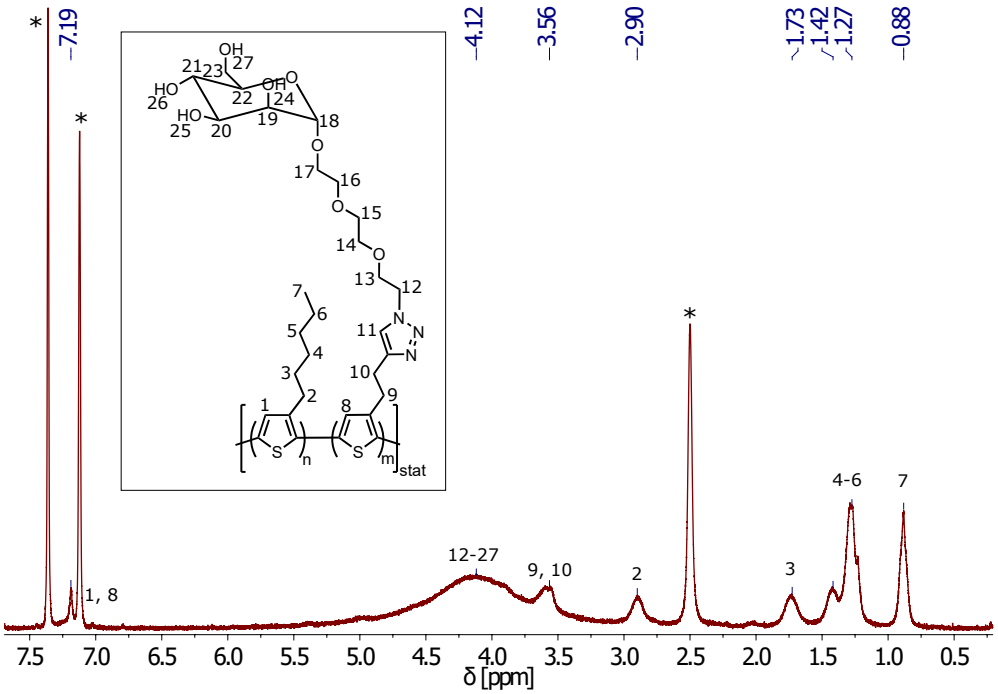

Figure 5.38: ^{1}H-NMR spectrum of **PT-Man$_{OEG}$** (room temperature, *o*DCB-d4:DMSO-d6 = 5:1).

5.4.2 Thin Film Functionalizations

The abovementioned solubility issues greatly complicated film deposition by spin coating, which was a prerequisite for any further tests in transistor devices. Even for **PT-Man$_{OEG}$**, small amounts of the co-solvent DMSO were still necessary to break up hydrogen bonds and fully dissolve the polymer. The differences in drying times of the individual solvents in the *o*DCB/DMSO mixture were found to lead to very inhomogeneous films. Furthermore, residual DMSO in the film greatly impacted transistor characteristics and quantitative removal of this solvent from the film was a very time-consuming process, requiring high vacuum and elevated temperatures of up to 120 °C, under which some degradation of the sugar moieties could not be fully excluded.

Since for **PT-TPA** and **PT-spTPA**, a heterogeneous film functionalization approach with a triphenylamine azide compound had yielded promising results, a similar protocol was adapted to the **PT-Man** system as an alternative. Considering the working principle of an EGOFET-based sensor device, full functionalization of the organic semiconductor bulk is not necessary, in fact, exclusive functionalization of the OSC surface would be optimal.[15, 76] Analyte binding should occur only near the film surface and an unfunctionalized underlying polymer film can be expected to possess superior transistor performance. Additionally, such a system containing no hydrophilic units in the polymer bulk can be

expected to be less prone to the intrusion of electrolyte into the OSC layer which would further degrade transistor performance.

The **P(3HT-*co*-3TBT)** batch was thus deprotected and purified by repeated *Soxhlet* extraction, spin coated on the respective transistor substrate from 5 mg/mL *o*DCB solutions and left to dry *in vacuo* at 40 °C overnight. After control measurements of the transistor characteristics of these unfunctionalized films the substrates were immersed in degassed CuAAC solutions in the solvents methanol, DMSO or acetonitrile containing the respective mannose azide and $[Cu(MeCN)_4]PF_6$ in 2.5 mM concentrations each, as well as small amounts of copper powder. The films were allowed to react either at room temperature for three days or at 45 °C for one day, dried and the transistor characteristics measured to find optimal conditions with the least impact on transistor performance. The results of this optimization process as well as measurements on solution-functionalized **PT-Man** derivatives will be discussed in the following.

5.4.3 Transistor Measurements

Bottom-Gate/Bottom-Contact Transistors

Since EGOFETs are highly complex devices in which several possible sources of error have to be considered, a bottom-gate/bottom-contact geometry was used as a starting point to test transistor performance and stability of all polymer systems. Figure 5.39 shows a representative comparison of the output and transfer characteristics of the deprotected precursor polymer (a, b), as well as solution-functionalized **PT-Man$_{Pr}$** (c, d) **PT-Man$_{OEG}$** (e, f). Films were spin coated from 5 mg/mL solutions in pure *o*DCB for **P(3HT-*co*-3TBT)**, *o*DCB/DMSO = 5/1 for **PT-Man** with short spacer and *o*DCB/DMSO = 2/1 for the oligo(ethylene oxide) spacer derivative. All films were dried *in vacuo* at 80-120 °C for at least 12 h prior to the measurements, since lower temperatures or shorter drying times were found to highly impact transistor characteristics, presumably due to residual solvent present in the film. An overview of the measured transistor performances is given in Table 5.5.

The deprotected precursor polymer reached high field effect mobilities at $1.2{\cdot}10^{-3}{\pm}2.1{\cdot}10^{-4}\,cm^2V^{-1}s^{-1}$, values comparable to other structurally similar poly(3-alkylthiophene)s like **P3HT**.[68] In addition, both the output and transfer curves showed almost ideal behavior, with clearly saturating I_{sd} upon increasing V_{sd} and V_g. For both **PT-Man** derivatives, the incorporation of the sugar derivatives into the bulk of the polymer film led to significant decreases in mobility values to $1.9{\cdot}10^{-6}{\pm}3.3{\cdot}10^{-7}$ and

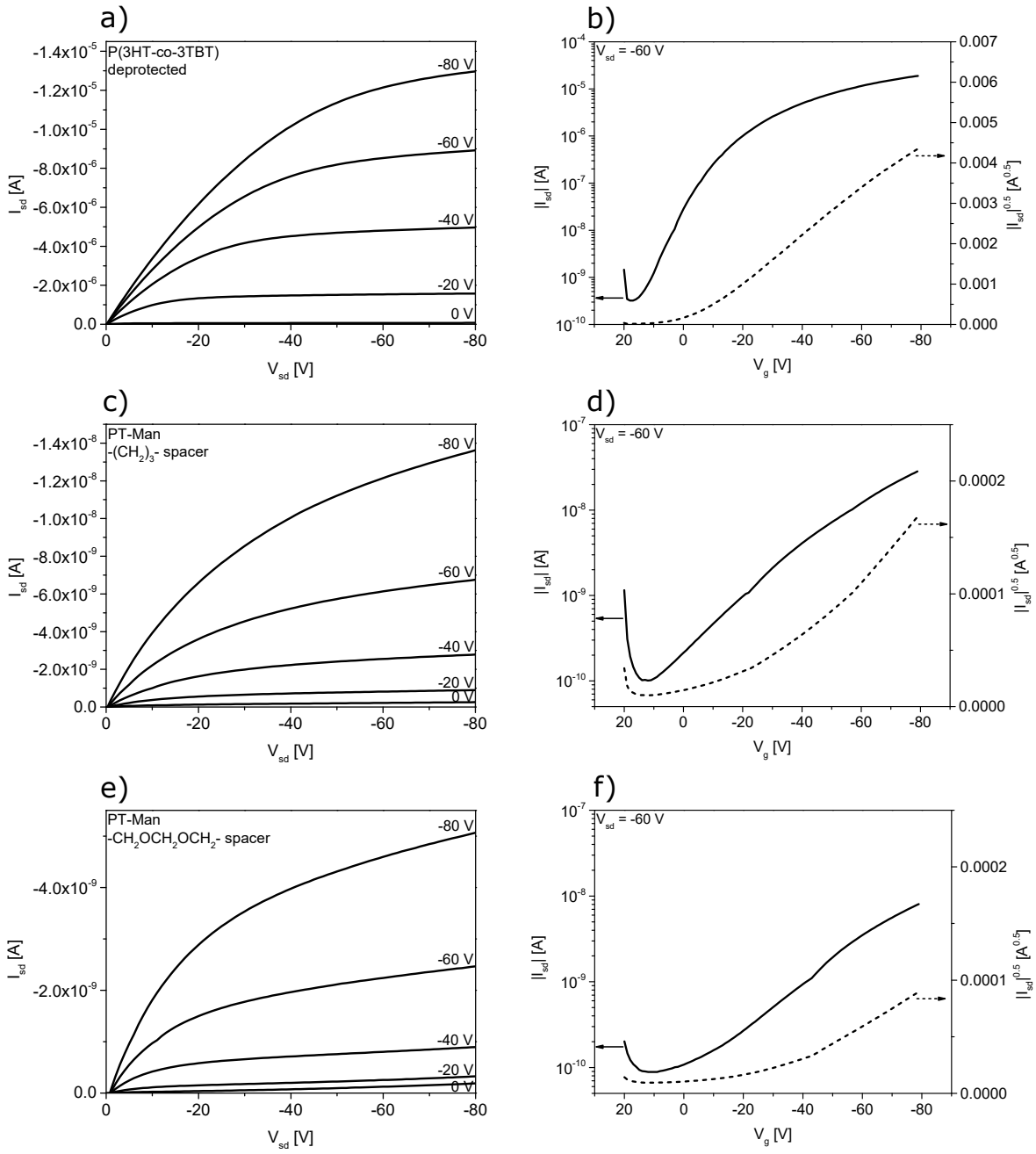

Figure 5.39: Output (a, c, e) and transfer (b, d, f) characteristics of deprotected **P(3HT-*co*-3TBT)** and **PT-Man** bottom-gate/bottom-contact organic field effect transistors.

$5.1 \cdot 10^{-7} \pm 2.7 \cdot 10^{-7}$ $cm^2V^{-1}s^{-1}$, respectively, accompanied by higher threshold voltages. These findings can most likely be mainly attributed to hindered charge transport from chain to chain due to the bulky mannose substituents. In direct comparison to the precursor

polymer, also the source-drain current saturation was much less pronounced, especially at high gate potentials.

To circumvent these issues, as mentioned before, a heterogeneous film functionalization approach was attempted as an alternative. Ideally, only the polymer chains in close proximity to the film surface would be functionalized, while the bulk of the film would not be influenced. Since in a bottom-gate/bottom-contact transistor, charges travel through the channel close to the substrate/OSC interface, measurements of the performance of such devices before and after functionalization can yield valuable information about the degree of influence on the bulk of the film.

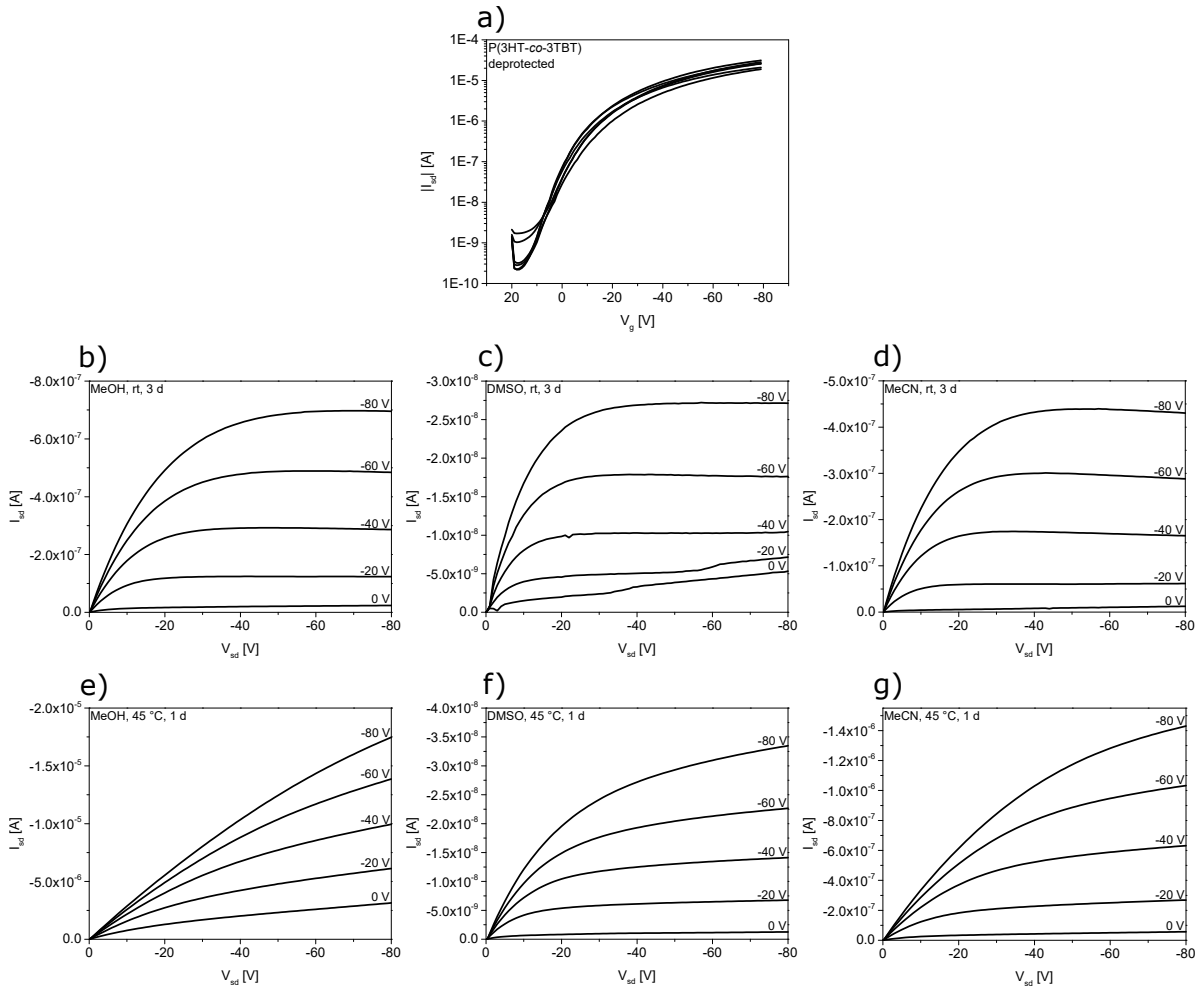

Figure 5.40: a) Comparison of transfer characteristics of the six deprotected **P(3HT-*co*-3TBT)** films on separate transistor substrates used for the optimization of thin film functionalization. b)-g) Output characteristics of the same transistors after functionalization with mannose azide under the denoted conditions.

First, films of deprotected precursor polymer were deposited on six transistor substrates by spin coating from 5 mg/mL *o*DCB solutions under identical conditions. After drying, the transfer characteristics of the six films were compared to ensure low deviations between the individual substrates (Figure 5.40 a). After exposing the films to the different functionalization conditions and drying, the transistors were compared (Figure 5.40 b-g and Table 5.5). In relation to the unfunctionalized films, all transistors showed a decrease in field effect mobilities. Two films, which were functionalized at 45 °C for 1 d in MeOH and at rt for 3 d in DMSO, respectively, exhibited output characteristics which were strongly superimposed by an ohmic behavior of the current with increasing source-drain potential. This can be interpreted as a clear sign for intrusion of the solutions into the polymer film and thus, these conditions were deemed unsuitable for film functionalization in EGOFET devices. All other transistors showed decent characteristics with varying performance. Overall, the film functionalization in acetonitrile solutions seemed to have the least impact on the transistors with field effect mobilities only decreasing by about one order of magnitude. Thus, all following EGOFET functionalizations were carried out in acetonitrile either for three days at room temperature or for one day at 45 °C.
Summarizing these preliminary bottom-gate/bottom-contact transistor experiments with mannose-substituted polythiophenes, all of the polymer films clearly behaved as expected for semiconducting materials. Thus, the materials should be in principle suitable for use in a transistor-based sensor device. The introduction of the mannose units caused drops in transistor performance in all cases. However, for the planned application in EGOFET devices, while certainly helpful, high field effect mobilities are not the most important factor. Stability of the OSC layer in contact with the electrolyte solution under an applied current is crucial, and such behavior can not be adequatly tested with a bottom-gate/bottom-contact OFET geometry alone.

Table 5.5: Transistor characteristics of deprotected precursor polymer **P(3HT-*co*-3TBT)** and solution-functionalized **PT-Man** derivatives. Optimization of heterogeneous thin film functionalization under different conditions for CuAAC reaction.

	μ [$cm^2V^{-1}s^{-1}$][a]	V_{th} [V][b]	I_{on}/I_{off}[c]
P(3HT-*co*-3TBT), deprotected	$1.2\cdot10^{-3}\pm2.1\cdot10^{-4}$	0±2	$5.9\cdot10^{4}$
PT-Man			
-$(CH_2)_3$- spacer	$1.9\cdot10^{-6}\pm3.3\cdot10^{-7}$	-18±3	$2.8\cdot10^{2}$
-$CH_2OCH_2OCH_2$- spacer	$5.1\cdot10^{-7}\pm2.7\cdot10^{-7}$	-19±9	$9.1\cdot10^{1}$
thin film functionalization[d]			
MeOH, rt, 3 d	$8.6\cdot10^{-5}$	0	$9.1\cdot10^{2}$
MeOH, 45 °C, 1 d		failed	
DMSO, rt, 3 d		failed	
DMSO, 45,°C, 1 d	$6.0\cdot10^{-6}$	-1	$6.8\cdot10^{2}$
MeCN, rt, 3 d	$7.4\cdot10^{-5}$	-12	$4.2\cdot10^{2}$
MeCN, 45 °C, 1 d	$1.0\cdot10^{-4}$	6	$5.4\cdot10^{2}$

a) Field effect mobilities determined from slope of linear fit $\frac{\partial\sqrt{|I_{sd}|}}{\partial V_g}$ at V_{sd} = -60 V. b) Threshold voltages determined from x-axis intercept of the same fit. c) On/off current ratios determined between minimum and maximum source-drain current values of a representative transistor. d) Thin films of the deprotected precursor polymer **P(3HT-*co*-3TBT)** on transistor substrates were immersed in degassed solutions of the mannose azide and $[Cu(MeCN)_4]PF_6$ (2.5 mM each) at the respective conditions, together with a small amount of copper powder, dried and the transistor characteristics were immediately measured.

Electrolyte-gated Organic Field Effect Transistors

Motivated by the overall positive results from the experiments on transistor model systems, the **PT-Man** materials were tested in basic EGOFET measurements at *Laboratoire ITODYS*, Paris, under the supervision of *Prof. Dr. Benoît Piro*, *Alexandra Tibaldi* and *Khue Nguyen*. Film preparation and surface functionalization conditions on the EGOFET substrates were similar to the ones used for bottom-gate/bottom-contact transistors. For initial measurements, the source and drain electrodes were first contacted *via* needle contacts and a 20 µL droplet of commercially available PBS buffer (pH = 7.4), containing $CaCl_2$ and $MnCl_2$ in 0.1 mM concentrations, was applied on top of the interdigitated channel area. This electrolyte mixture, in which **Con A** has been shown to possess high activity for mannose binding, can be seen as the "empty" state for all further measurements

and thus, stability under these conditions had to be ensured first.[14] Immediately after immersion of a polished gold wire into the electrolyte droplet as the gate electrode, output characteristics of the devices were measured in potential ranges of 0 to -0.6 V for V_{sd} and 0 to -0.8 V for V_g. The respective backward scans for all output curves were also recorded to check for possible hysteresis of I_{sd}, which would be indicative for instability of the current over time. For the deprotected precursor polymer (Figure 5.41 a), like in the model system measurements, almost ideal output curves could be obtained, with only minimal hysteresis for the highest gate potential step.
The surface-functionalized films (Figure 5.41 b and d) were overall very comparable, with only slightly lower I_{sd} at given potentials compared to the precursor polymer. Unfortunately, for the solution-functionalized **PT-Man** derivatives (Figure 5.41 c and e), all measured EGOFET devices exhibited much worse performance, and, more importantly, a high degree of variation between individual transistors. I_{sd} hysteresis was more significant, pointing at degradation of the performance over time. It is likely that these findings are a consequence of the bulky mannose units inhibiting charge transport to a certain degree, the inhomogeneous film formation due to the necessity for solution mixtures for spin coating as well as a possible intrusion of electrolyte solution into the film, facilitated by the hydrophilic mannose units.

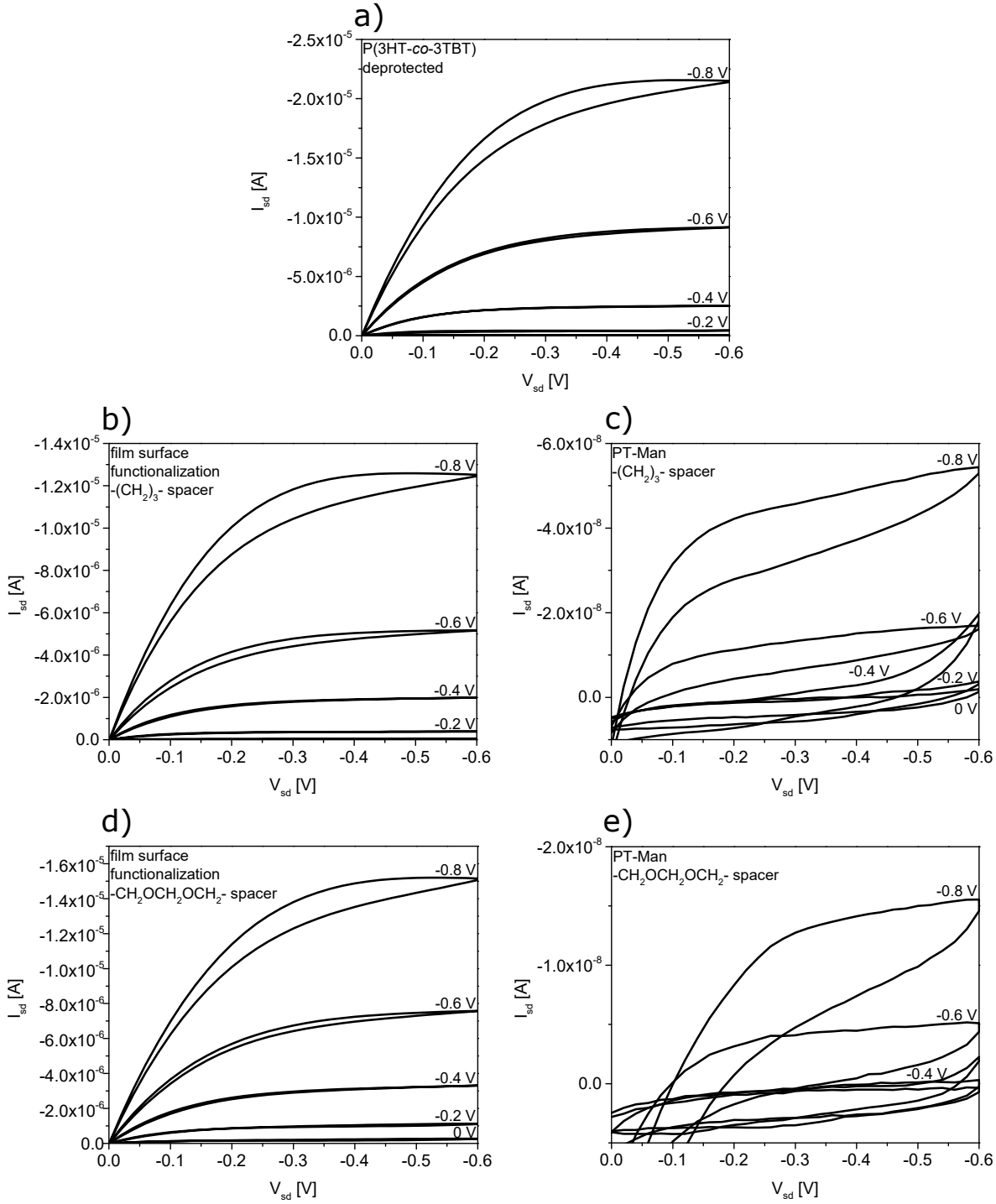

Figure 5.41: Comparison of EGOFET output characteristics of a) deprotected precursor polymer **P(3HT-*co*-3TBT)**, b) and d) films surface-functionalized (MeCN, 45 °C, 1 d) with the two mannose azides **Man-PrN$_3$** and **Man-OEGN$_3$**, c) and e) both **PT-Man** derivatives. The electrolyte droplet consisted of 20 µL of PBS buffer solutions (pH = 7.4) containing additional $CaCl_2$ and $MnCl_2$ in 0.1 mM concentrations.

5.4.4 Concanavalin A Detection

Since the surface-functionalized EGOFET devices exhibited far superior characteristics, further testing of **Con A** detection in the electrolyte solution was mainly focused on these systems. The solution-functionalized **PT-Man** films showed qualitatively similar results, however in a significantly lower current range with much lower reproducibility. In some cases, the transistors with these polymer films failed soon after applying the electrolyte droplet.

Initially, differences in transistor transfer curves between the "empty" state of the electrolyte containing only PBS buffer and $CaCl_2/MnCl_2$ salts and the same system containing additional **Con A** were compared. First, the transfer characteristics were measured using a 20 µL droplet of the aforementioned electrolyte mixture at a source-drain potential of -0.3 V in the range between 0.2 and -0.8 V for V_g. The grey curve in Figure 5.42 shows a representative example. Immediately after completion of the measurement, 10 µL of the same electrolyte solution, additionally containing **Con A** at 150 nM concentration was added to the droplet and the transfer measurement was repeated (black curve).

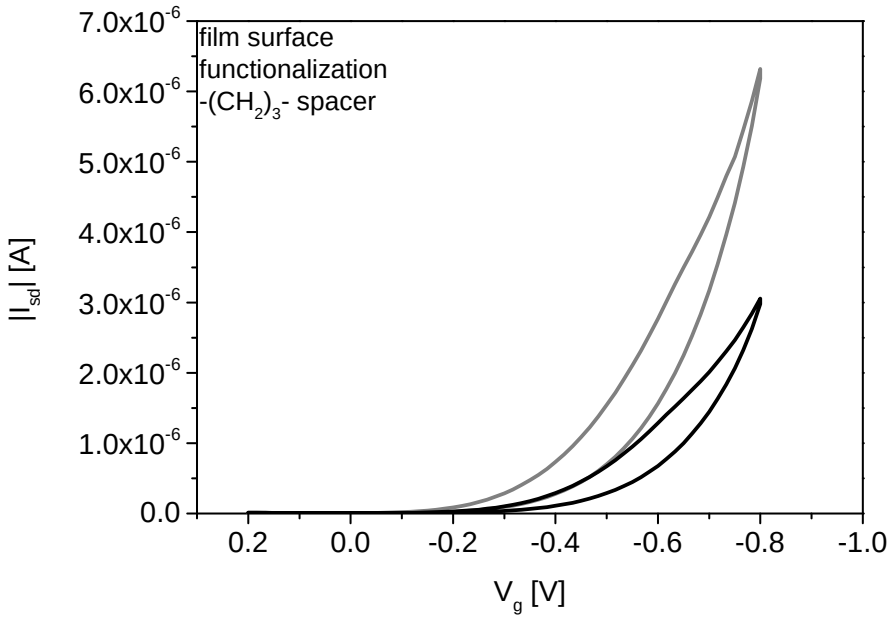

Figure 5.42: Transfer curves (measured at V_{sd} = -0.3 V) of an EGOFET device of deprotected **P(3HT-*co*-3TBT)** surface-functionalized with mannose azide before (grey) and after (black) addition of 10 µL of 150 nM **Con A** in PBS/salt solution to the initial 20 µL PBS/salt droplet.

The transfer curves after addition of the protein were found to reproducibly exhibit lower slopes, *i.e.* measured source-drain currents at a given gate potential were lower compared to the initial measurement. While this might well be an effect of the additional **Con A** concentration in the solution or even of the formation of a protein layer on the film surface due to mannose-protein interactions, mainly two other factors have to be considered. First, the decrease in currents might be caused by degradation of the film over time while in contact with the electrolyte droplet. The clearly visible hysteresis in the transfer measurements might be related. Second, due to the addition of **Con A** solution to the initial droplet, the total droplet volume increased by ~50%. At this stage it could not be excluded that this might play a role as well. However, since both the initial droplet and the additional volume were kept at the same concentrations of PBS buffer and $CaCl_2/MnCl_2$, changes in salt concentrations can be ruled out as a factor.

To obtain a deeper insight into the system, the transistors were monitored *in situ* during addition of the protein. This was achieved by applying both a constant V_{sd} = -0.5 V and a constant V_g = -0.5 V and measuring the changes in source-drain current I_{sd} over time (Figure 5.43). It was found that immediately after applying the potentials, a steep decrease in current could be registered in all cases, which slowly stabilized after approximately one minute. Recording of I_{sd} was thus started after this initial period, usually after between one and two minutes. The measurements were performed for all different polymer film systems, including the unfunctionalized precursor polymer for comparison. In the initial state, again a 20 µL droplet of the electrolyte was applied and the measurement was started. Then, an additional 10 µL of "empty" electrolyte solution were added to the droplet to test for the effect of an increase of electrolyte volume on transistor characteristics. As best visible in Figure 5.43 a, this "disturbance" of the system caused an immediate response of the transistor, manifesting as an increase in I_{sd} which then slowly trended back to stable values. This finding, which was reproducible across all measured transistors, allowed to fully exclude the increase in droplet volume as the reason for changes in transistor characteristics. After currents had stabilized again, 10 µL of 150 nM solutions of Concanavalin A (**Con A**) or human serum albumin (**HSA**) were added to the droplets to test for specificity of the transistor response. For all polymer films, including the deprotected precursor polymers, addition of both proteins to the electrolyte solutions caused clearly visible drops in measured currents. This hints at a significantly negative influence of the presence of the proteins on either the amount or mobility of charge carriers present in the channel. A possible explanation would be the accumulation of protein near the OSC surface, which would influence the capacitance there, leading to decent sensitivity of the tested EGOFET devices for the presence of proteins.

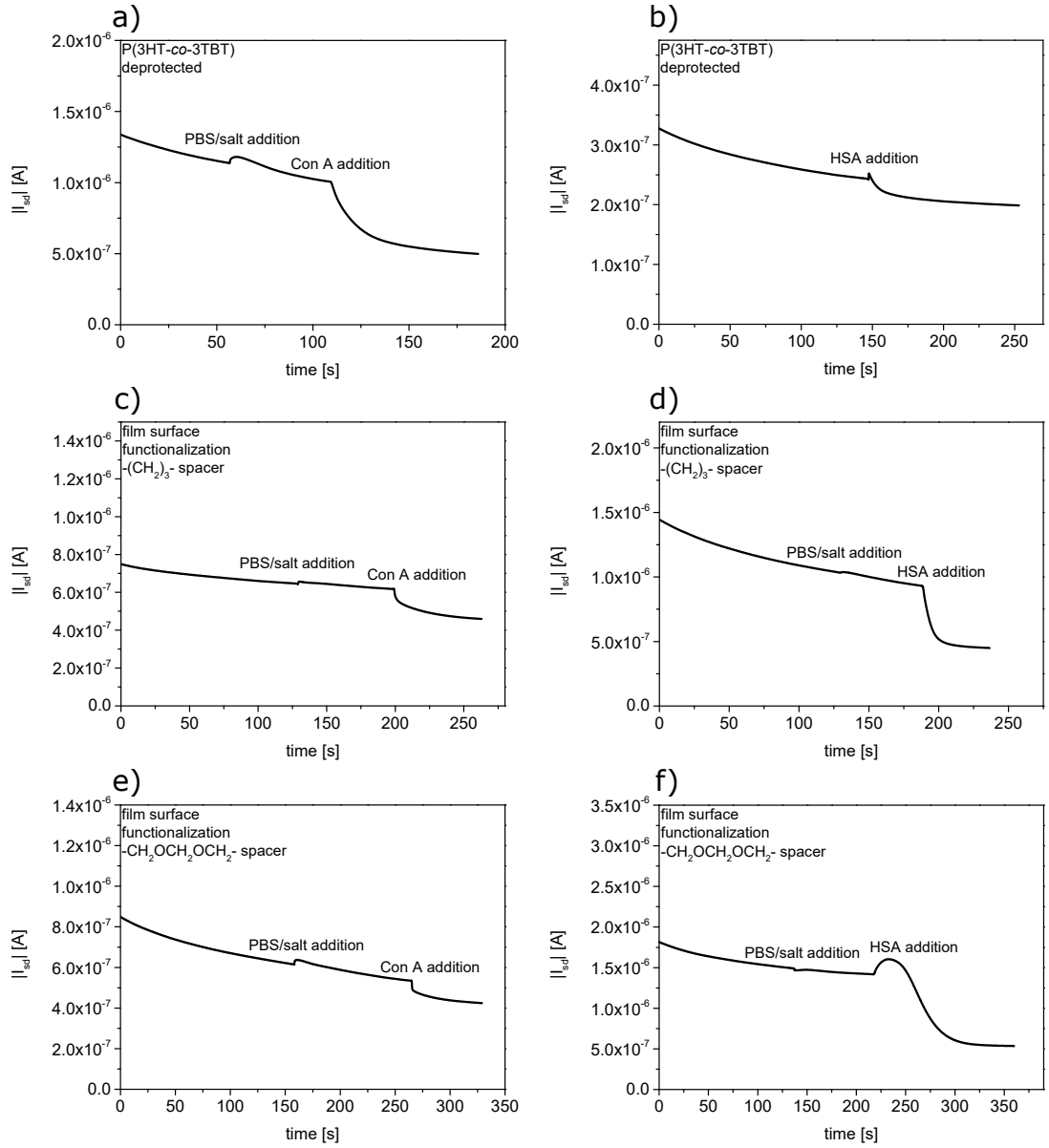

Figure 5.43: Time-dependent measurements of absolute source-drain current at fixed V_{sd} = -0.5 V and V_g = -0.5 V. First, 10 µL of pure PBS/salt solution were added to the initial droplet to check for current stability. Then, 150 nM **Con A** (a, c, e) and **HSA** (b, d, f) in 10 µL of PBS/salt buffer solutions were added.

Control experiments, in which the proteins were replaced by doubled concentrations of $CaCl_2$/$MnCl_2$ in an otherwise identical electrolyte, caused currents to slightly increase instead of decrease. This showed that the presence of freely dissolved, charged species in the electrolyte has an opposite effect compared to protein addition, supporting the theory of protein layer formation on the OSC. Both **Con A** and **HSA** additions led to similar

effects on measured currents, even for the precursor polymer not bearing any mannose units. Since currents dropped in all cases, the type of protein could not be discriminated by a difference in sign of ΔI_{sd}. Also, the current drops relative to the initial currents were not clearly dependent on the type of protein added, with **Con A** addition showing a higher effect than **HSA** for the precursor polymer but a lower effect for the functionalized films. A possible explanation for the quite unspecific response of the EGOFET systems might be found in hydrophobic attractive interactions between the OSC surface and the proteins, which would lead to an accumulation of analyte near the surface even when α-D-mannosyl units are not present. Such phenomena would explain both the current drops upon **HSA** addition, which is not able to interact with the sugar moieties, as well as the positive response found for the unfunctionalized precursor polymers. Similar effects were observed for EGOFET-based biotin/avidin sensor systems by *Piro et al.*, in which functionalization of the OSC surface was chosen as the mode of analyte recognition.[75]

5.4.5 Summary

In this chapter, initial experiments for establishing an EGOFET-based sensor model system utilizing the interaction between Concanavalin A and α-D-mannosyl groups, were presented. A polymer-analogous click chemistry approach was used to attach the sugar derivatives directly to electroactive polythiophene backbones. This allowed to combine both analyte reception and signal transduction properties in a single material. Early solubility issues of the polymers were alleviated by introducing a longer, oligo(ethylene oxide)-based spacer between the backbone and the mannose units. However, small amounts of a hydrogen bond acceptor co-solvent like DMSO were still needed to fully dissolve the polymer, complicating film deposition. For this reason, an alternative film surface functionalization approach was developed, which was expected to lead to improved transistor performance while still allowing for analyte reception on the OSC surface. Initial testing of the materials in the bottom-gate/bottom-contact model geometry was promising, with the films surface-functionalized under optimized conditions exhibiting superior performance compared to the solution-functionalized **PT-Man** derivatives. Similar results were found when the materials were employed in EGOFET devices, using a mixture of PBS buffer and $CaCl_2$/$MnCl_2$ salts as the electrolyte. Since both **PT-Man** materials showed clear signs of electrolyte intrusion into the thin films, resulting in degradation of transistor performances over time, further experiments for protein detection mainly focused on surface-functionalized EGOFETs. Initially, these experiments were carried out by measuring the transistor transfer characteristics at a given source-drain potential

before and after addition of the protein. Subsequently, *in situ* monitoring of the currents over time was used, allowing to exclude several sources of error, like changes in droplet volume or film degradation over time. In both variants, significant drops in I_{sd} were registered which could be unambiguously proven to be effects of the protein addition.

6 Conclusion and Outlook

The work presented in this dissertation was concerned with the chemical modification of linear polythiophenes to alter the structure formation and the electrooptical properties of the materials or to introduce new functionalities through the attachment of more complex moieties. The chosen approaches included modifying the backbone of regioregular poly(alkylthiophene)s through the connection of flexible **PDMS** coil segments to form block copolymers and the introduction of branched alkylthiophene π-extensions to alter the optoelectronic properties of the systems. Further work was concerned with developing smart materials through the introduction of ionic groups, crosslinkable triphenylamine moieties as well as α-D-mannose anchor units for protein sensor applications.

P3HT-*b*-PDMS Rod-Coil Block Copolymers

A combination of rigid **P3HT** and flexible poly(dimethylsiloxane) (**PDMS**) blocks promises improved stability of thin films under mechanical strain, which is highly important for applications like bendable displays and plastic microelectronics.[2] A CuAAC-based grafting-to approach was adapted and substantially improved after a cleavage mechanism was identified.[3] The cleavage mechanism, which was proven by NMR, SEC and MALDI-TOF measurements, only occurs if a methylene spacer (x = 1 in Scheme 6.1) is used. Thus, a longer spacer (x = 4) was introduced, eliminating block cleavage.

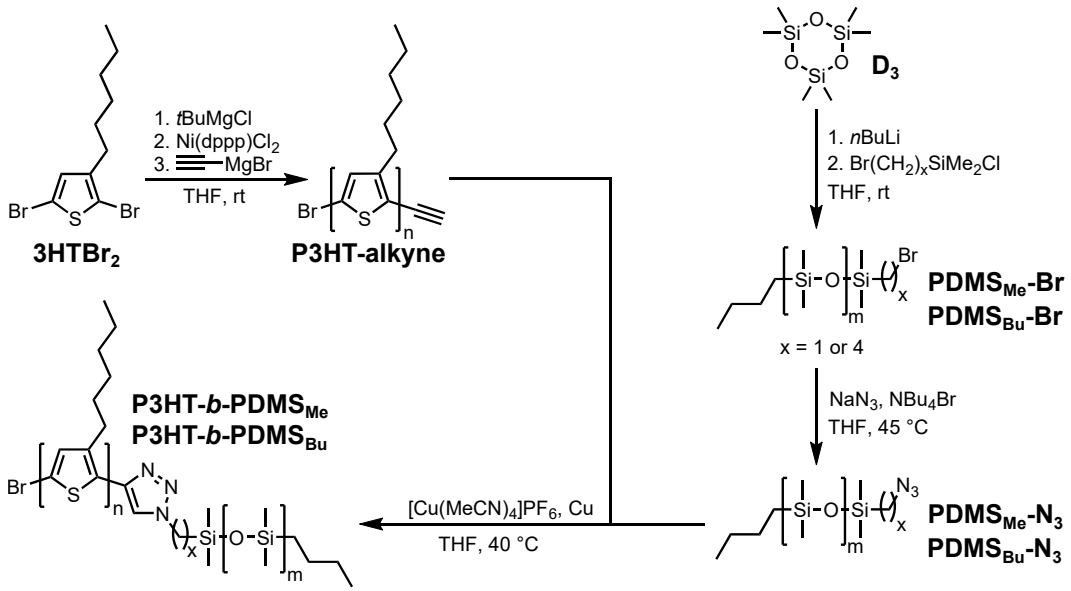

Scheme 6.1: Synthesis of end-functionalized **P3HT** and **PDMS** homopolymers and CuAAC approach to synthesize **P3HT-*b*-PDMS** copolymers.

Spectroscopic evidence for a higher degree of reorientation of the polythiophene blocks in the **PDMS** matrix, which led to improved π-stacking in thin films both at room temperature and in temperature-dependent experiments, was found. The **P3HT-*b*-PDMS** block copolymer already shows a more defined fine structure of the absorption spectra after film deposition compared to the **P3HT-alkyne** precursor. Upon heating to 200°C and cooling to room temperature, the differences become even more significant, which was attributed to the presence of the flexible **PDMS** blocks. Field effect mobilities of the **P3HT** homopolymer and the **P3HT-*b*-PDMS** block copolymer were determined by organic field effect transistor (OFET) measurements and similar values in the range of $10^{-4}\,cm^2V^{-1}s^{-1}$ were found, despite the insulating **PDMS** matrix present in the copolymer films. AFM measurements showed clear signs of microphase separation of the **P3HT** and **PDMS** blocks as unordered standing cylinders in thin films on the transistor substrates. The results on **P3HT-*b*-PDMS** are promising, since already without any optimization, mobility values comparable to the **P3HT-alkyne** homopolymer batch could be obtained. The application of more sophisticated annealing methods might be able to greatly improve the results. Variation of the respective block lengths might also lead to interesting trends. However, the issues associated with nonquantitative block copolymer formation must be first adressed synthetically. Removal of unreacted **P3HT** homopolymer from the crude product mixture is most probably only possible based on size exclusion, for which chromatography setups with higher separating performance would be necessary. Methods like external initiation with a suitably functionalized initiator might secure quantitative functionalization of the **P3HT** block. Additionally, this might have the added benefit of prohibiting dimerization of these chains through *Glaser*-type coupling of alkynes as well as difunctionalization through catalyst detachment, which would further decrease the amount of possible byproducts.

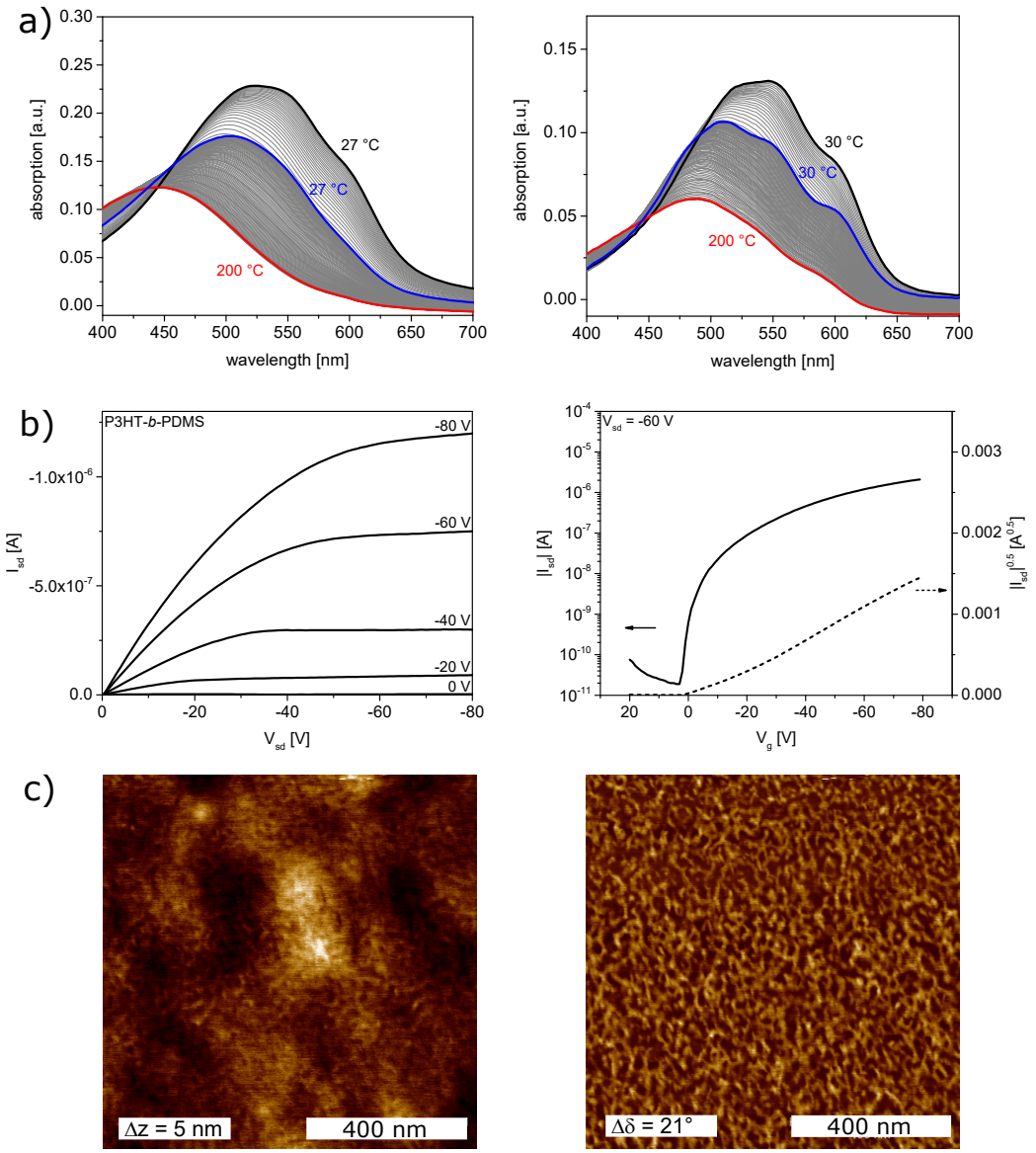

Figure 6.1: a) Temperature-dependent thin film absorption measurements of **P3HT-alkyne** homopolymer (left) and **P3HT-*b*-PDMS** (right). b) Bottom-gate/bottom-contact transistor characteristics of **P3HT-*b*-PDMS**. c) Height (left) and phase (right) AFM images of as-cast **P3HT-*b*-PDMS** thin films on transistor substrates.

Side-chain π-extended Polythiophenes

Extending the π-system of linear polythiophenes by alkylthiophene groups in the side chains was shown to introduce favorable effects on the positions of the frontier orbitals.[4, 5] However, solubility issues occured in earlier attempts, which were mostly alleviated by the introduction of branched instead of linear alkyl side chains.[6, 7] The approach presented

here tested the limits of this method, decreasing side chain length to a 2-ethylhexyl group, leading to the polymer **P3TC6C2**. The material was synthesized and its properties compared to its longer side-chain analogues.

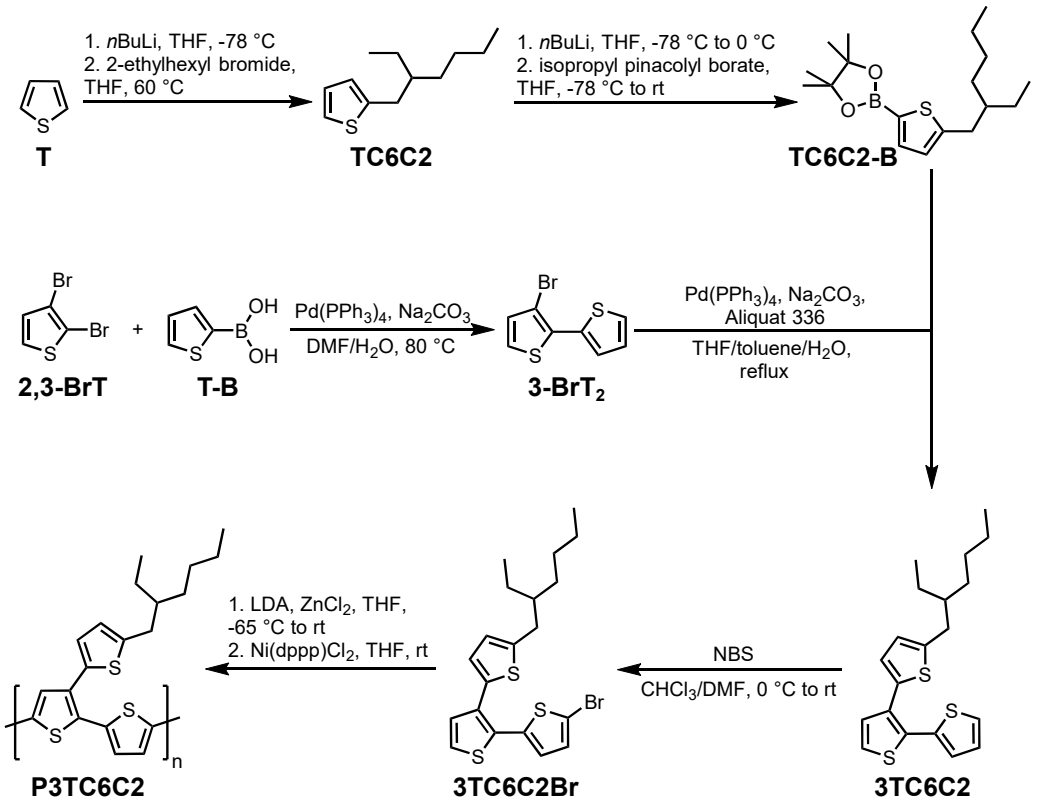

Scheme 6.2: Synthesis pathway to monomer **3TC6C2Br** and polymerization procedure yielding side-chain π-extended polythiophene **P3TC6C2**.[7]

Two *Soxhlet* fractions with 7.5 and 10.0 kg/mol and PDI values of 1.9 and 2.0 were obtained using the established synthesis procedure (Scheme 6.2), which showed significantly diminished solubility compared to the longer side-chain analogues. Thermal properties were evaluated by a combination of DSC, TGA and WAXS measurements, as well as temperature-dependent optical absorption spectroscopy in solutions and thin films and a significantly higher tendency for aggregation and higher melting temperatures up to 300 °C were found. The strong solvent trichlorobenzene and temperatures as high as 170 °C were necessary to fully dissolve the polymers without any spectroscopic evidence of aggregation. It was possible to determine the interchain distances in crystallites in the direction of the alkyl chains and in the π-π stacking direction (22.7 and 4.7 Å, respectively), which were comparable to the values of **P3TC8C4**, hinting that the side-chain thiophene moiety mainly determines the interchain distances for the derivatives with the shortest alkyl chains. Furthermore, electrochemical and chemical doping experiments were conducted.

The optical absorption properties during p-type doping are comparable to other linear polythiophenes like **P3HT**, however, the required potentials lay higher at 0.4 V vs. Fc/Fc^+ corresponding to a lowered HOMO level at -5.5 eV. Similarly, the oxidation agent $FeCl_3$ was necessary to dope **P3TC6C2**, while 2,3,5,6-tetrafluoro-7,7,8,8-tetracyanoquinodimethane (**F_4TCNQ**), which can easily oxidize **P3HT**, showed no effect for **P3TC6C2**.[40] Lastly, OFET measurements were performed to test the transistor performance of **P3TC6C2** and significant improvements (mobilities up to $6.3 \cdot 10^{-5}$ $cm^2V^{-1}s^{-1}$) compared to existing analogues were found. Overall, **P3TC6C2** showed molecular, thermal (aggregation-related) and electronic properties which fit well into the trends already established for the other derivatives.

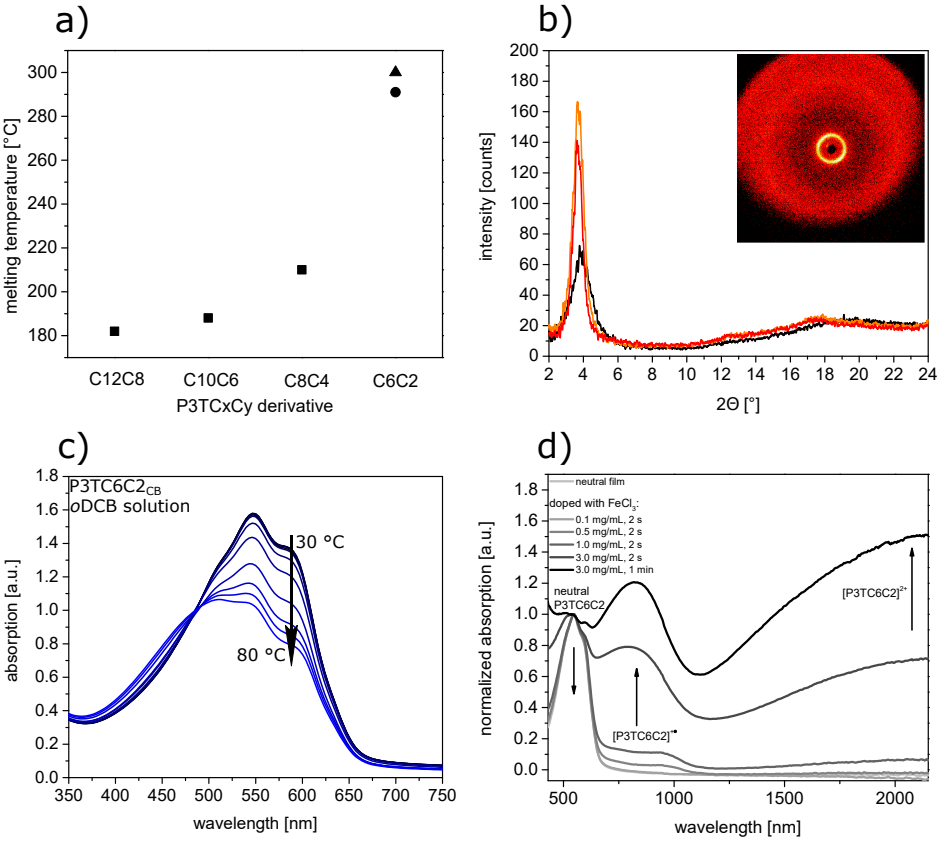

Figure 6.2: a) Melting points of the different **P3TCxCy** derivatives with decreasing side-chain lengths. b) WAXS powder diffraction patterns at 20 °C (black), 260 °C (orange) and 300 °C (red). Inset shows diffraction pattern at 260 °C. c) Temperature-dependent absorption spectroscopy measurement of **P3TC6C2$_{CB}$** in *o*DCB solution. d) Thin film absorption spectra of **P3TC6C2$_{CHCl_3}$** upon chemical doping with different concentrations of iron(III) chloride in acetonitrile solution.

The influence of side chain lengths is clearly nonlinear and generally favorable concerning performances of the materials, however, other factors like the postulated face-on morphology seem to have a more significant, detrimental effect. Judging from the obtained results, **P3TC6C2** certainly marks the limit of this approach with regard to solubility and general handling, as well as polymerizability *via* controlled polymerization methods.

Smart Materials through Alkyl Side-chain Modifications

The concept of side-chain functionalization was employed for the synthesis of conjugated polyelectrolytes (CPEs), which combine electronic and ionic conductivity mechanisms in single materials. The cationic model system **PTIm-Br** was synthesized by polymer analogous functionalization of a precursor polymer and subsequently compared to the anionic CPE **PTS-TBA**.[9, 10] The CPEs were synthesized by polymer analogous functionalizations utilizing the precursor polymer **P3BrHT** (Scheme 6.3).

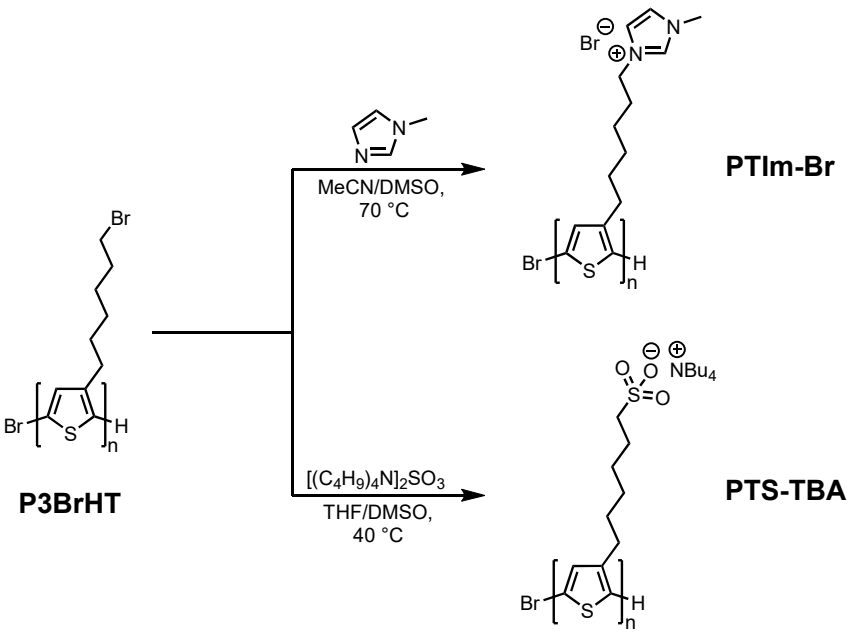

Scheme 6.3: Polymer analogous functionalizations of **P3BrHT** yielding conjugated polyelectrolytes **PTIm-Br** and **PTS-TBA**.

Aggregation phenomena in solution and thin films were evaluated. Both polymers were well soluble in methanol without any spectroscopic evidence for the formation of aggregates. In water, only a slight broadening of the absorption band was seen for **PTIm-Br**, while **PTS-TBA** exhibited a significant red-shift, accompanied by the development of a fine structure. In thin films spin coated from methanol or water solutions, both polymers showed very similar spectra with only minimal fine structure. The electronic conductivities

of CPE films doped with different concentrations of the acceptor dopant **F_4TCNQ** were further investigated and clear differences between the two systems were found, which could be explained by the stabilizing and destabilizing effects of the pendant ionic groups.[11] The **PTS-TBA** batches exhibited conductivities of up to 2.3±0.8 S/cm and 0.6±0.1 S/cm, values comparable to regioregular **P3HT** doped with **F_4TCNQ**. **PTIm-Br** showed drastically lower conductivities, with values already saturating at $6.8 \cdot 10^{-4} \pm 1.6 \cdot 10^{-4}$ S/cm.

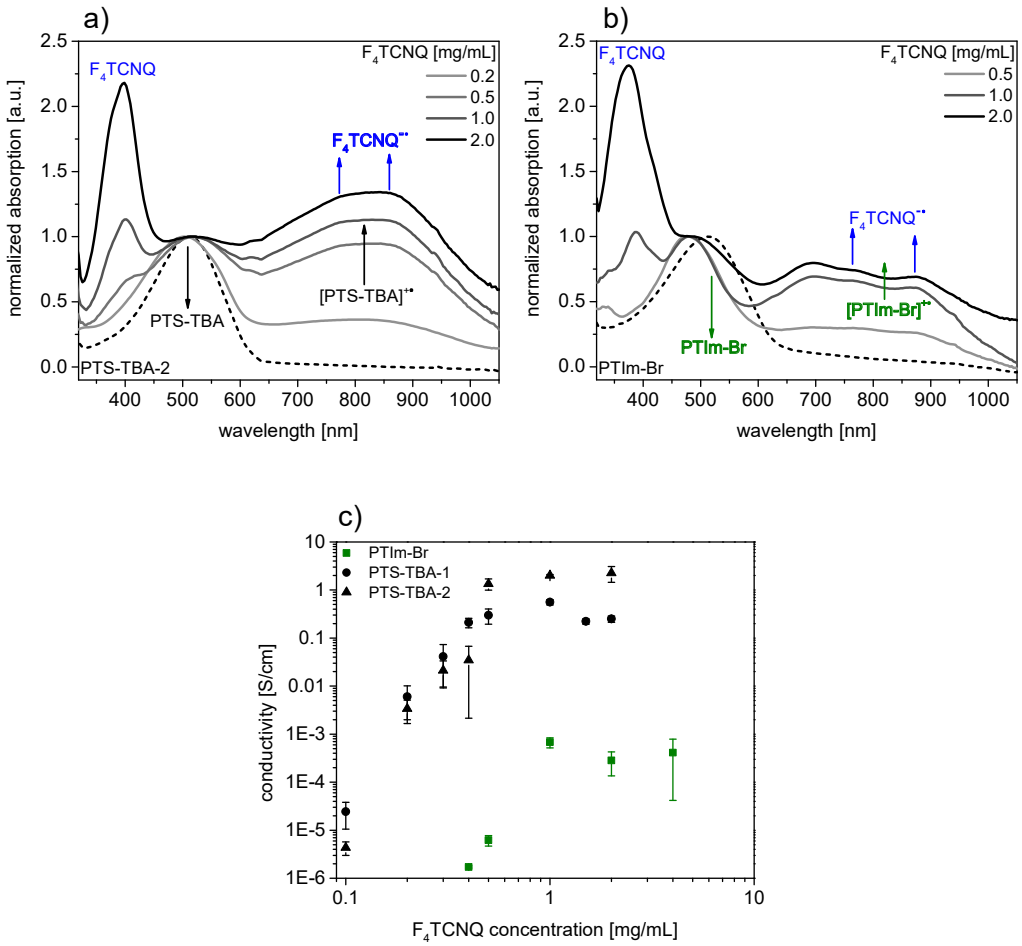

Figure 6.3: Optical absorption spectra of a) **PTS-TBA** and b) **PTIm-Br** thin films after chemical doping with different solution concentrations of **F_4TCNQ** in acetonitrile. c) Corresponding conductivity values of the films measured using the four-point-probe method.

Significant influences of different types of counterions on the physical and electronic properties of CPEs based on the same combination of backbone and tethered ionic species have been reported in literature.[303, 311] Thus, it would be highly interesting to study the effects of varying the counterions in the **PTS-TBA** and **PTIm-Br** systems, employing for example alkali cations or non-coordinating anions like tetrafluoroborate

or hexafluorophosphate, both in terms of ionic and electronic conductivities. Such investigations are currently ongoing in our group. Although more complicated, similar studies might also be extended to polymers showing auto-doping effects. Another variable which can be changed is the amount of ionic groups present on a single polymer chain. Since both of the studied CPEs are based on the same precursor polymer, which is essentially a slightly modified **P3HT** derivative, lowering the ion content in the system is easily possible by GRIM copolymerization with the respective monomer unit bearing an unfunctionalized alkyl chain. Such modifications have been shown to induce interesting effects in terms of solubility behavior and thermal properties, as has been demonstrated by *Maes et al.* for systems derived from **PTIm-Br**, and might have similarly strong impacts on conductivity properties.[206]

Extending the concept of side-chain terminal modification further, an alkyne-substituted copolymer-based platform, providing facile functionalization with different functional molecules *via* CuAAC, was developed.[12] The ratio of the alkyne-containing monomer **3TBT** and the hexyl-substituted **3HT** could be randomly copolymerized in any ratio, allowing to exactly adjust the content of alkyne groups in the finished copolymers. Based on this synthetic platform, conjugated redox polymers (CRPs) bearing redox-active triphenylamine (**TPA**) units, which could be crosslinked in thin films upon chemical or electrochemical oxidation, were developed.[13] The two polymers **PT-TPA** and **PT-spTPA**, which differ in the length and structure of the linker unit between the backbone and the pendant groups, were synthesized by a CuAAC approach (Scheme 6.4). Additionally, anchoring of a triphenylamine azide was also possible in heterogeneous reactions on predeposited thin films, as evidenced by UV/Vis spectroscopy.

The CRPs were studied in electrochemical doping experiments under spectroscopic control. In addition to the species typically associated to the generation of charge carriers on the polythiophene backbones, clear spectroscopic evidence for the dimerization of triphenylamine (**TPA**) to tetraphenylbenzidine (**TPB**) units could be observed.[233, 249] *In-situ* conductance experiments showed that charge transport was largely dominated by the polythiophene backbones and that **TPB** dimer oxidation and reduction occur in the potential window of highest conductance of the films, thus confirming the generation of a redox-matched CRP system. The crosslinking reaction rendered the films completely insoluble in all tested solvents and even extended electrochemical cycling of a crosslinked film in a THF-based electrolyte was possible, which would rapidly dissolve the as-cast films. Chemical doping experiments with $\mathbf{F_4TCNQ}$ led to oxidation of the backbone and conductivity values up to ~0.7 S/cm, however, crosslinking could not be induced with this dopant. With $\mathbf{FeCl_3}$, conductivities reached higher values up to ~8 S/cm and

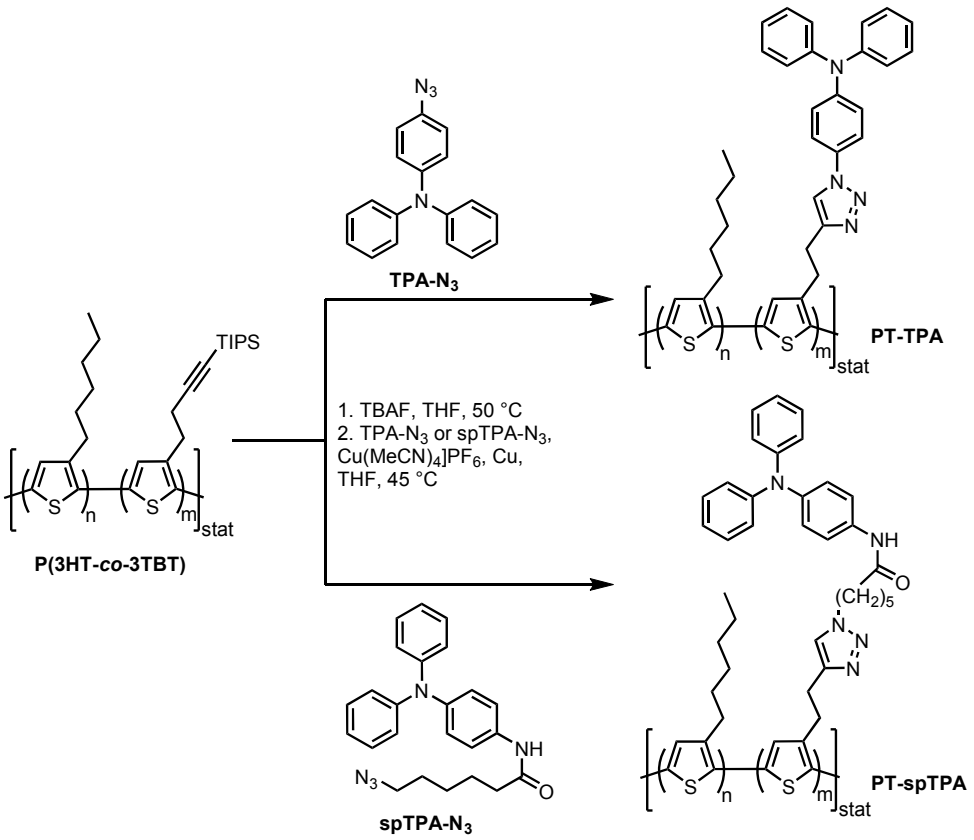

Scheme 6.4: Polymer analogous functionalizations to CRPs **PT-TPA** and **PT-spTPA**.

oxidation of the pendant groups led to crosslinking, for which a similar mechanism as for electrochemical doping could be confirmed.

Further research should be focused on incorporating the materials into devices in which the combination of high conductivity, solvent stability and stable redox chemistry is of high importance, especially for charge storage applications, electrochemical sensors and electrocatalysis.[222, 228] Owing to the highly modular nature of the polymer system, synthesized *via* a convergent postfunctionalization route, the simultaneous functionalization of the same backbone with crosslinker and other functional molecules like catalysts or recognition units should be possible. Other applications of the polymers can be seen in small-scale structuring of polymer films (selective crosslinking on structured electrodes followed by dissolution of the non-crosslinked parts of the film) or multilayer deposition of polymer films without the need for orthogonal solvents.[325, 347] From a synthetic point of view, the effect of exchanging **TPA** for other possible crosslinking units like carbazoles or oligothiophenes could be interesting, since these groups show a similarly reliable coupling chemistry.[327–330]

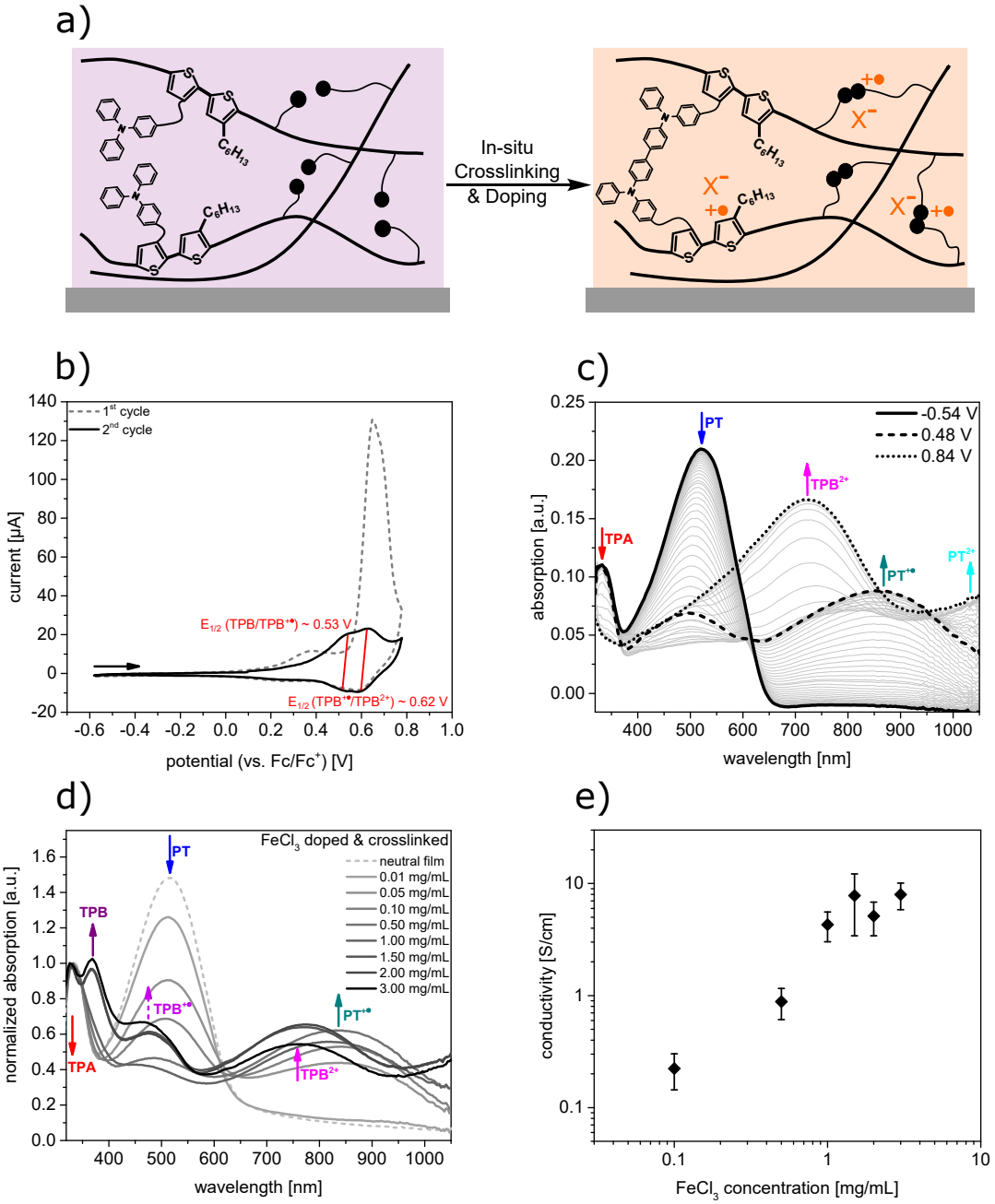

Figure 6.4: a) Sketch detailing the simultaneous doping and crosslinking occuring in **PT-TPA** and **PT-spTPA** thin films upon chemical or electrochemical doping. b) 1st and 2nd cycle CV measurements of **PT-TPA**. c) Evolution of UV/Vis spectra during a forward scan of a spectroelectrochemical measurement of **PT-TPA**. d) Thin film absorption spectra of **PT-TPA** films doped with different concentrations of **$FeCl_3$**. e) Corresponding four-point-probe conductivity values.

The alkyne-substituted copolymer platform was finally utilized for the synthesis of polythiophenes bearing α-D-mannose units (termed **PT-Man**) as protein sensor materials.

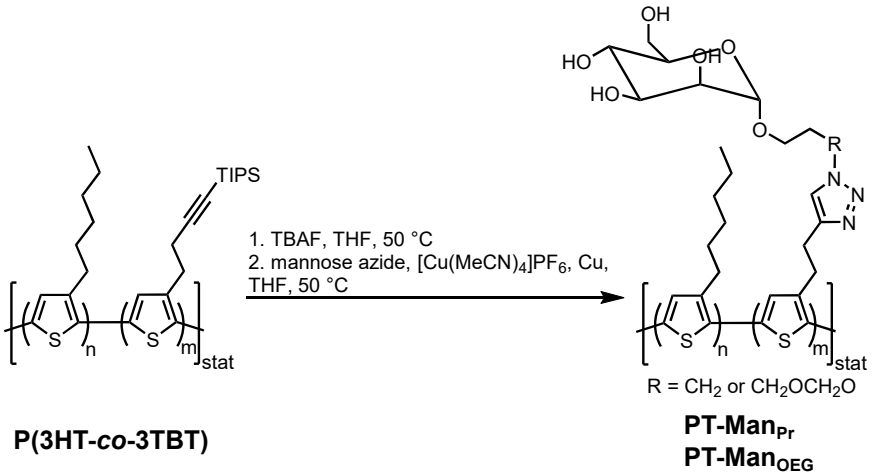

Scheme 6.5: Polymer analogous functionalization procedure yielding **PT-Man** polymers.

The strong interaction between these sugar moieties and the protein Concanavalin A (**Con A**) was employed as a model system to investigate the applicability of such materials in sensor devices based on electrolyte-gated field effect transistors (EGOFETs).[14, 15] Functionalization of the precursor polymers in homogeneous solutions as well as on the surface of predeposited thin films on transistor substrates was performed and the conditions optimized. EGOFET measurements at *Laboratoire ITODYS*, Paris, showed superior stability of the surface-functionalized films. In total, the detection studies showed a high sensitivity but low specificity of the tested EGOFET devices at the present stage. The systems seem to be suitable to discriminate between salts which are freely dissolved in the electrolyte solution and proteins which show affinity to the OSC, resulting in higher local concentrations of the analytes on the surface. Even very low concentrations of analytes (150 nM in the present case) can be reliably detected. However, unspecific hydrophobic interactions between film surface and proteins compete with **Con A** - mannose binding.

If these effects could be mitigated, specificity of the sensor can be expected to greatly increase. Further studies should thus focus on this aspect, for which approaches like the addition of long-chain alcohols to block the surface before analyte addition, have already proven useful in a similar sensor system.[75] An alternative approach would be to wash the protein-containing electrolyte from the surface after the first measurement and to replace it by an "empty" droplet. If the interaction between **Con A** and the sugar moieties on the surface is high enough, the protein should be retained on the OSC and differences

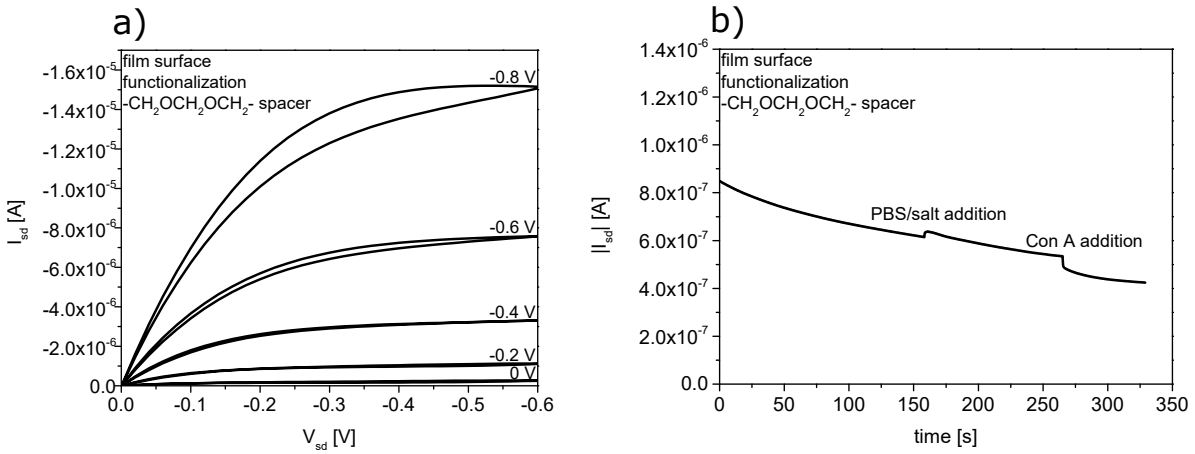

Figure 6.5: a) EGOFET output characteristics of a polythiophene film surface-functionalized with α-D-mannose azide. b) *In-situ* monitoring of the source-drain current of a similar EGOFET device during addition of salt solution and Concanavalin A.

in subsequent measurements might be found. However, such approaches are associated with a large number of uncertainties and it will probably not be trivial to prove that current differences are exclusively effects of the analyte. Mannose units might also be attached to the gate electrode surface by means of electrografting or SAM chemistry.[348] In combination with a stable, high-performance OSC like **PBTTT**, such a system would be potentially less susceptible to solvent intrusion as well as unspecific interactions. Lastly, the applicability of the **PT-Man** materials for **Con A** detection using other types of electrochemical, optical or gravimetric sensor devices should be explored.

7 Experimental Part

Parts of the synthetic work and measurements contained in this dissertation have been contributed by *Moritz Katzmaier*, *Daniel Rose*, *Diana Zelenic*, *Kai Mundsinger*, *Katharina Schmitt*, *Tim Hierlemann* and *Marc Schnierle* during the course of their research internships and Bachelor's Theses. Both batches of **PTS-TBA** were synthesized by *Dr. Roman Tkachov* during his stay at our institute.

7.1 Methods

Synthesis

Reactions were carried out under inert atmosphere in argon-purged, dried glassware. All commercially available chemicals were purchased from *Sigma-Aldrich*, *TCI Chemicals*, *Acros Organics*, *VWR International* or *ABCR* and used without further purification. THF was dried using the solvent purification system *MB-SPS-800* (*MBraun*). All other solvents were dried using established methods.[349] Technical grade solvents were distilled before use. Column chromatography was performed with a stationary phase consisting of silica gel (*Macherey-Nagel Silica 60 M*, 0.04-0.063 mm) unless otherwise stated. Solvent ratios for column chromatography are given as volume fractions (v:v). Preparative size exclusion chromatography was performed using a self-packed column with polystyrene-divinylbenzene copolymer (*Bio-Rad Bio-Beads S-X1*, 1% crosslinkage, bead size 40-80 µm, MW exclusion range 600-14000 g/mol) as the statoniary phase and chloroform as the mobile phase.

Nuclear Magnetic Resonance Spectroscopy (NMR)

^{1}H- and ^{13}C-NMR spectra at room temperature were recorded using a *Bruker Avance DPX 250* spectrometer at 250 MHz and 63 MHz, respectively. High temperature spectra were measured at 100 °C on a *Bruker Ascend 700* spectrometer at 700 MHz and 175 MHz. Chemical shifts δ are given in parts per million (ppm) and the spectra were calibrated based on the solvent residual peaks.[350] Coupling constants J are given in Hz.

UV/Vis Spectroscopy

Room temperature UV/Vis spectra in solution were recorded on a *Perkin Elmer Lambda 35* spectrometer. Film spectra on glass slides were measured using a *Zeiss* device equipped with a *MCS621 Vis II* spectrometer cassette and a *CLH 600 F* lamp on a *THMS600* hot-stage from *LINKAM* connected *via* glass fiber optics (*Ocean Optics*). For *in-situ* measurements (spectroelectrochemistry, chemical doping, temperature-dependent absorption) the same *Zeiss* device was connected to the respective measurement setup. Temperature-dependent measurements were controlled using the hot-stage (thin films) or a separate Peltier element (*5305 TECSource, ArroyoInstruments*) for solution measurements. Background spectra of the respective pure solvents or clean substrates were always subtracted.

Infrared Spectroscopy (IR)

IR spectra were recorded in the Transmission or Attenuated Total Reflection (ATR) mode on a *Bruker IFS 66/S* device.

Size Exclusion Chromatography (SEC)

SEC measurements were performed using an *Agilent 1260 Infinity* system at room temperature with THF (1 mL/min) as the eluent and a column cascade from *Polymer Standards Service* (*PSS*) consisting of a precolumn *SDV 5 µm* (5 cm) and two mixed-bed *SDV linear 5 µm* main columns (30 cm) as the stationary phase. UV ($\lambda = 275$ nm) or refractive index (RI) detectors were used. High temperature size exclusion chromatography (HT-SEC) was performed on a *Varian PL-GPC 220* system in 1,2,4-trichlorobenzene at 160 °C. Eluting species were detected with an RI detector. Narrowly distributed polystyrene standards from *PSS* were used for calibration in all cases.

Mass Spectrometry (MS)

High Resolution Mass Spectra (HRMS) using the Electrospray Ionization (ESI), Electron Impact Ionization (EI) or Chemical Ionization (CI) methods were measured at the *Institute of Organic Chemistry* (*University of Stuttgart*) in the positive or negative mode on *micrOTOF-Q* (*Bruker Daltonics*) or *Finnigan MAT 95* spectrometers. Matrix Assisted Laser Desorption Ionization Time of Flight (MALDI-TOF) spectrometry was performed

at the *Institute of Biochemistry* (*University of Stuttgart*) on a *Bruker Autoflex III* spectrometer. Samples were prepared using the dried-droplet method with DCTB / sodium triflate as the matrix and ionized with Nd:YAG lasers ($\lambda = 355\,\mathrm{nm}$). The spectra were calibrated against separately measured, narrowly distributed PEG standards.

Elemental Analysis (EA)

Elemental Analysis was performed at the *Institute of Organic Chemistry* (*University of Stuttgart*) on an *Elemental Analyzer Model 1106* by *Carlo Erba Strumentazione*.

Differential Scanning Calorimetry (DSC)

DSC measurements were recorded on a *PerkinElmer DSC 4000* system at a heating rate of $10\,\mathrm{K/min}$ and a cooling rate of $5\,\mathrm{K/min}$. One preliminary cycle of heating and cooling was performed before each measurement run to eliminate the thermal history of the sample.

Thermogravimetric Analysis (TGA)

TGA with *in-situ* DSC measurements were carried out at the *Institute of Inorganic Chemistry* (*University of Stuttgart*) using a *Netzsch STA 449 C* instrument under an argon atmosphere with a heating rate of $10\,\mathrm{K/min}$. The decomposition temperature T_d was determined at a mass loss of 3%.

Wide Angle X-ray Scattering (WAXS)

Temperature-dependent WAXS patterns of polymer powders were recorded at the *Institute of Physical Chemistry* (*University of Stuttgart*) on a *Bruker Nanostar* instrument with copper K_α radiation ($\lambda = 0.154\,\mathrm{nm}$). Measurement parameters were $U = 40\,\mathrm{kV}$ and $I = 35\,\mathrm{mA}$. Diffractograms were recorded from $20\,^\circ\mathrm{C}$ to $300\,^\circ\mathrm{C}$ in steps of $10\,^\circ\mathrm{C}$ with a measurement time of $900\,\mathrm{s}$ at each temperature step. Nanoscale distances d were calculated from the diffractograms according to *Bragg's law*

$$n \cdot \lambda = 2 \cdot d \cdot \sin\theta$$

with integer n and scattering angle θ.

Atomic Force Microscopy (AFM)

AFM images were recorded in tapping mode on a *Bruker Dimension Icon* device. For image processing a combination of the software packages *Bruker Nanoscope Analysis* and *Gwyddion* was used.

Electrochemistry

Thin films were prepared by spin coating at room temperature from polymer solutions (5 mg/mL or 10 mg/mL in $CHCl_3$ or *o*DCB unless otherwise stated) onto gold or indium tin oxide (ITO) coated glass slides, as well as interdigitated platinum electrodes from *DropSens* (channel length $l = 5\,\mu m$) or *Freiburger Materialforschungszentrum* ($l = 100\,\mu m$). The substrates were cleaned by ultrasonication in acetone and isopropyl alcohol for 10 min, respectively. All films were prepared and stored under the exclusion of air under vacuum or nitrogen atmosphere. *Autolab PGSTAT101* or *PGSTAT204* potentiostats from *Metrohm* were used for all electrochemical measurements. Scan rates of 20 mV/s (for cyclic voltammetry and spectroelectrochemistry) and 10 mV/s (for *in-situ* conductance measurements) were applied.

Cyclic Voltammetry (CV)

Cyclic voltammetry of thin films was measured at room temperature in a three-electrode cell with a Pt plate counter-electrode and an AgCl-coated silver wire directly immersed into the electrolyte solution as a pseudo-reference electrode. The analyte thin film on gold coated glass was used as the working electrode. Measurements were performed in degassed 0.1 M NBu_4PF_6/MeCN electrolyte (unless otherwise stated) under an argon atmosphere and all values are reported against the ferrocene/ferrocenium (Fc/Fc^+) redox couple. HOMO and LUMO levels are determined from the oxidation and reduction onset potentials (for polymers) or half-wave potentials (for small molecules) according to

$$\begin{aligned} E_{HOMO}[\text{eV}] &= -(E_{ox} + 5.1) \\ E_{LUMO}[\text{eV}] &= -(E_{red} + 5.1) \end{aligned}$$

using -5.1 eV as the formal potential of Fc/Fc^+ in the *Fermi* scale.[48]

Spectroelectrochemistry

For *in-situ* spectroelectrochemistry measurements, ITO coated glass slides ($\leq 20\,\Omega$/sq, *Präzisions Glas & Optik GmbH*) covered with the analyte film were used as working electrodes.[351] A three-electrode setup with a Pt wire as the counter electrode was used in a custom-built quartz cell which was placed inside the spectrometer beam and the working electrode arranged perpendicular to the beam. All spectra were recorded in transmission mode at each potential step of the electrochemical measurement. Solution spectroelectrochemical measurements were performed using the standard electrolyte containing 1 mg/mL (unless otherwise stated) of the respective analyte in another three-electrode custom-built quartz cell. A polished Pt disk electrode with a diameter of 4 mm was employed as the working electrode and as reflection point for the spectrometer beam. Solution spectra were recorded in reflection mode.

In-situ Conductance Measurements

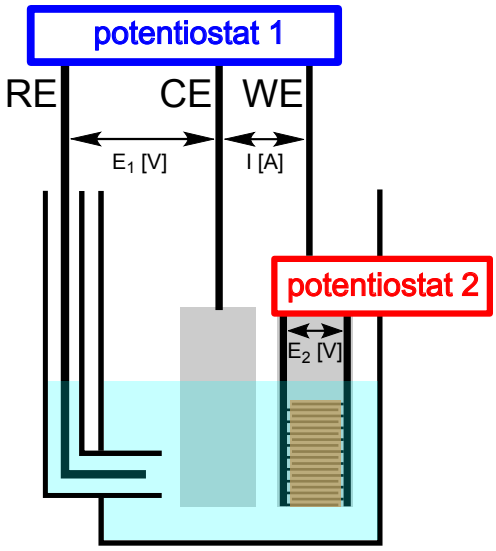

Figure 7.1: Two-potentiostat setup used for measuring potential-dependent conductance profiles of thin films.

Conductance profiles were recorded using a setup similar to an electrolyte-gated electrochemical transistor.[39] Interdigitated Pt electrodes ($l = 5\,\mu$m) were used as the working electrodes. A two-potentiostat setup was used, one applying a constant potential bias V (10 mV) between the electrode combs and the other one controlling the cyclic voltammetry measurement and simultaneously recording the current between working and counter electrode as well as the current between the combs. The conductance values G were

calculated from the measured current I flowing between the combs according to *Ohm's law*:

$$G = \frac{1}{R} = \frac{I}{V}$$

Electrochemical Doping

Films were deposited on interdigitated Pt electrodes ($l = 100\,\mu m$) and charged to a potential of 0.65 V (vs. Fc/Fc^+) with both combs connected as the working electrodes simultaneously. The film was held at this potential and a *Keithley SourceMeter* was connected immediately to the individual combs for conductivity measurements.

Chemical Doping

Thin films were prepared by spin coating the polymers on cleaned glass substrates ($1\,cm^2$) from the respective solutions ($CHCl_3$, toluene, *o*DCB or MeOH, 5 mg/mL or 20 mg/mL unless otherwise stated) at room temperature under an inert atmosphere. For dip-doping the substrates were then immersed into solutions of the dopants iron(III) chloride or 2,3,5,6-tetrafluoro-7,7,8,8-tetracyanoquinodimethane (**F_4TCNQ**) in dry MeCN for two seconds and one minute, respectively, cleaned in pure MeCN and blown dry using a stream of argon.[53] For spin-doping the dry polymer films were covered with 100 µL of a THF solution of **F_4TCNQ** for 5 s on a spin coater chuck and the excess solution was spun off at 2000 rpm for 60 s.[40] Absorption spectra and conductivity values were immediately measured after doping. Film thicknesses t were determined by profilometry using a *Veeco Dektak 150 Surface Profiler* or by AFM.

Conductivity Measurements

Sheet resistivites of the polymer films were measured using the four-point-probe (4PP) technique (*Signatone SP4* probe head, linear arrangement of tips, spacing = 1 mm, *Keithley 2636B SourceMeter*).[308] Linear (ohmic) behavior of the measured resistance values was ensured by scanning different currents within the same order of magnitude. Bulk conductivities σ were then calculated from the measured potentials V and currents I according to the formula:

$$\sigma = \left(\frac{\pi}{\ln 2} t \frac{V}{I}\right)^{-1}$$

For two-point-probe (2PP) approximation of the conductivities of electrochemically doped thin films the combs of the interdigitated Pt electrodes were connected to a *Keithley SourceMeter* immediately after charging the polymer film. I/V characteristics were then measured and the conductivities approximated from these values and the dimensions of the interdigitated array (channel length $l = 100\,\mu m$, combined channel width $w = 100\,\mu m$ and film thicknesses t) using

$$\sigma = \frac{l}{Rwt}$$

neglecting contact resistances.

Transistor Measurements

For bottom-gate/bottom-contact transistors, commercial substrates (*Fraunhofer Institute for Photonic Microsystems*, Dresden) with a gate electrode consisting of n-doped silicon and SiO_x as gate dielectric (thickness = $230 \pm 10\,nm$) were used. Source and drain electrodes consisted of 40 nm thick gold with an ITO adhesion layer. Channel length l was 20, 10, 5 or 2.5 µm and channel width w was 10 mm. The substrates were cleaned by ultrasonication with acetone (twice) and isopropanol for 10 min each and then subjected to oxygen plasma for 10 min. If needed, octadecyltrichlorosilane (**ODTS**) self-assembled monolayers (SAMs) were applied at this point *via* vapor-phase deposition in a self-built chamber consisting of two petri dishes.[352] The substrate was glued to the ceiling of the chamber and 100 µL of **ODTS** were applied to the bottom. The closed chamber was heated to 50 °C for 1 d. The functionalized substrates were cleaned in an ultrasonic bath with isopropanol. The successful functionalization was checked by contact angle measurements. Thin films of the respective polymers were spin coated from $CHCl_3$ or *o*DCB (5 mg/mL, 1000-2000 rpm) under an inert atmosphere. The films were dried *in vacuo* or at 100 °C under nitrogen atmosphere for several hours (for films deposited from *o*DCB). Output and transfer characteristics were then measured with a *Keithley 2636B SourceMeter* on an *EP6* probestation from *Süss MicroTec*. Electrolyte-gated Organic Field Effect Transistor (EGOFET) measurements were performed at *Laboratoire ITODYS*, Paris in the group of *Prof. Dr. Benoît Piro*.[15, 76] The films were prepared on custom-made transistor substrates and a 3D printed array of **PDMS** vessels was placed on the substrate. 50 µL of millipore water or PBS buffer were added to each transistor vessel and a gate electrode made from polished gold wire with a cross sectional area of 1 mm^2 was immersed into the electrolyte as the gate electrode. Output as well as transfer

curves in the saturation regime were recorded. Threshold voltages V_{th} for all transistor measurements were determined by extrapolation of a linear fit of $\sqrt{|I_{sd}|}$ towards zero. Saturation regime charge carrier mobilities μ_{sat} were extracted from the slope of the linear fit according to

$$\mu_{sat} = \frac{2l}{C_{diel}w}\left(\frac{\partial\sqrt{|I_{sd}|}}{\partial V_g}\right)^2$$

with the capacitance of the gate dielectric C_{diel} = 1.5·10^{-4} As/Vm for our bottom-gate/bottom-contact substrates.[65]

7.2 Syntheses

7.2.1 P3HT-*b*-PDMS Copolymers

Ethynyl-terminated P3HT (P3HT-alkyne)

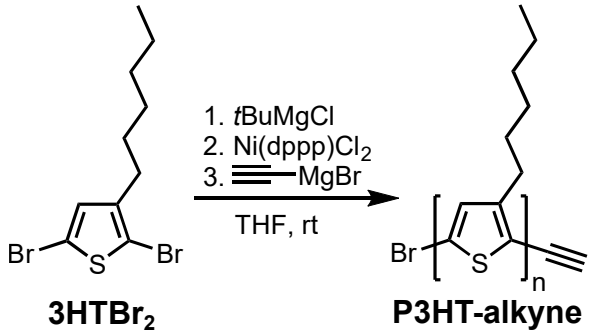

2,5-Dibromo-3-hexylthiophene (**3HTBr$_2$**, 1.63 g, 5.0 mmol, 1 eq) was dissolved in 10 mL of dry THF under argon. *t*BuMgCl solution (2.0 M in Et_2O, 2.5 mL, 5.0 mmol, 1 eq) was added dropwise and the mixture was stirred at rt for 2 h. The solution was diluted to 50 mL with dry THF and Ni(dppp)Cl_2 (45 mg, 0.083 mmol, 0.017 eq) was added quickly. The mixture immediately turned orange-red indicating the formation of polymer chains. After stirring for another 10 min at rt, ethynylmagnesium bromide solution (0.5 M in THF, 4.0 mL, 2.0 mmol, 0.4 eq) was added and the mixture was allowed to react for another 30 min. The polymer **P3HT-alkyne** was precipitated into 100 mL of MeOH, collected by centrifugation, washed with MeOH multiple times and dried under vacuum at rt overnight. Since dimerization of the functionalized chain ends occurs slowly at rt the dry polymer was stored at -25 °C under the exclusion of light and air.

Yield: 336 mg (2.0 mmol, 40%).
^{1}H-NMR (250 MHz, $CDCl_3$): δ [ppm] = 6.98-6.82 (m, 1H), 3.53 (s, 0.04H), 2.80-2.57 (m, 2H), 1.71 (m, 2H), 1.36 (m, 6H), 0.91 (m, 3H).
SEC (THF, PS standards): Batch 1: $\overline{M_n}$ = 8000 g/mol, $\overline{M_w}$ = 9000 g/mol, PDI = 1.1; Batch 2: $\overline{M_n}$ = 7500 g/mol, $\overline{M_w}$ = 9500 g/mol, PDI = 1.3.
IR (ATR): $\tilde{\nu}$[cm^{-1}] = 3309 (alkyne-H), 2094 (alkyne).

(4-Bromobutyl)chlorodimethylsilane (4-Br-BDMCS)

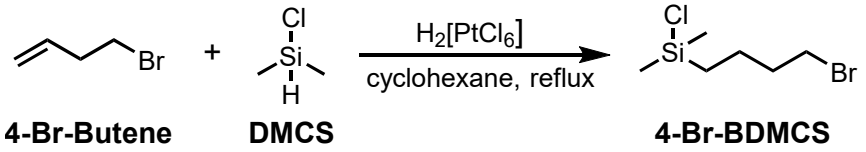

A small grain of chloroplatinic acid (~10 mg) was added to 90 mL of dry cyclohexane under an argon atmosphere. 4-Bromobut-1-ene (10.0 g, 74.1 mmol, 1 eq) and chlorodimethylsilane (**DMCS**, 8.41 g, 88.9 mmol, 1.2 eq) were added and the mixture was refluxed for 20 h. The title compound **4-Br-BDMCS** was obtained by distillation (0.1 mbar, 40 °C) of the crude product mixture as a colorless liquid.
Yield: 11.7 g (51.3 mmol, 69%).
^{1}H-NMR (250 MHz, $CDCl_3$): δ[ppm] = 3.43 (t, J = 6.7 Hz, 2H), 1.92 (m, 2H), 1.64-1.51 (m, 2H), 0.87-0.80 (m, 2H), 0.42 (s, 6H).

Azide-terminated PDMS (PDMS-N_3)

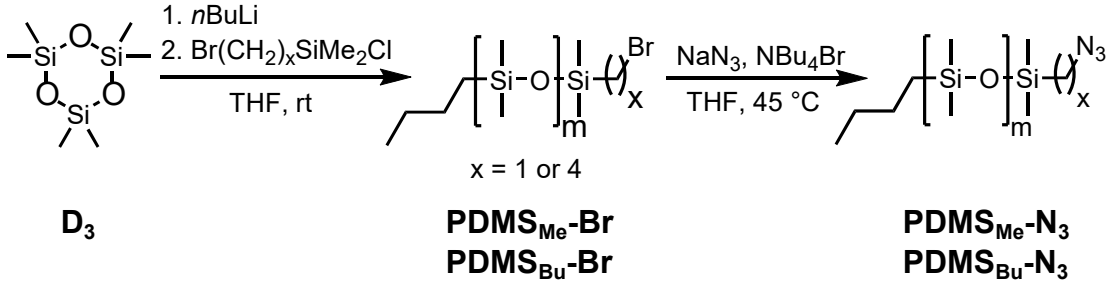

Dry hexamethylcyclotrisiloxane (**D_3**, 2.67 g, 12.0 mmol, 1 eq) was dissolved in 10 mL of dry THF and *n*BuLi (1.6 M in hexane, 0.11 mL, 0.18 mmol, 0.015 eq) was added quickly *via* syringe. After stirring for 3 h at rt (4-bromobutyl)chlorodimethylsilane (**4-Br-BDMCS**, 210 mg, 0.9 mmol, 0.075 eq) or (bromomethyl)chlorodimethylsilane (169 mg, 0.9 mmol, 0.075 eq) was added and the reaction mixture was stirred for 2 h at rt. The reaction was

quenched by dropping the solution into a mixture of 100 mL of methanol and 10 mL of triethylamine causing the polymer to form a separate, colorless liquid phase. The viscous polymer phase was collected by centrifugation, washed three times with methanol and dried *in vacuo*. ^{1}H-NMR analysis of the intermediate bromine-terminated product allowed to approximate the degree of polymerization and end-capping based on comparison of initiator and end-group integrals and was used to assess the degree of azide interconversion in the next step.

Bromomethyl-terminated polymer ($PDMS_{Me}$-Br):

^{1}H-NMR (250 MHz, $CDCl_3$): δ[ppm] = 2.43 (s, 2H), 1.34-1.26 (m, 4H), 0.88 (t, J = 6.7 Hz, 3H), 0.57-0.50 (m, 2H), 0.24 (s, 6H), 0.07 (s, 1059H).

Bromobutyl-terminated polymer ($PDMS_{Bu}$-Br):

^{1}H-NMR (250 MHz, $CDCl_3$): δ[ppm] = 3.41 (t, J = 6.8 Hz, 2H), 1.89 (m, 2H), 1.56-1.46 (m, 2H), 1.35-1.29 (m, 4H), 0.90 (t, J = 6.8 Hz, 3H), 0.59-0.53 (m, 4H), 0.09 (s, 848H).

For bromine-azide exchange, the respective bromine-functionalized **PDMS** (1.50 g, ~0.12 mmol of end groups, 1 eq) was dissolved in 10 mL of dry THF under argon. NaN_3 (28 mg, 0.42 mmol, 3.5 eq) and NBu_4Br (137 mg, 0.42 mmol, 3.5 eq) were added and the solution heated to 45 °C for 24 h (**$PDMS_{Me}$-Br**) or 72 h (**$PDMS_{Bu}$-Br**), respectively. The polymers were then again precipitated and washed with MeOH three times, centrifuged and dried to afford the respective **PDMS-N_3** as colorless liquids.

Yield: 1.39 g (6.2 mmol, 93%).

Azidomethyl-terminated polymer ($PDMS_{Me}$-N_3):

^{1}H-NMR (250 MHz, $CDCl_3$): δ[ppm] = 2.74 (s, 2H), 1.33-1.25 (m, 4H), 0.88 (t, J = 6.8 Hz, 3H), 0.56-0.50 (m, 2H), 0.20 (s, 6H), 0.07 (s, 936H).

SEC (THF, PS standards): $\overline{M_n}$ = 12500 g/mol, $\overline{M_w}$ = 13500 g/mol, PDI = 1.1.

IR (ATR): $\tilde{\nu}$[cm^{-1}] = 2962 (CH_3), 2098 (N_3), 1261 (Si-CH_3), 1018 (Si-O).

Azidobutyl-terminated polymer ($PDMS_{Bu}$-N_3):

^{1}H-NMR (250 MHz, $CDCl_3$): δ[ppm] = 3.27 (t, J = 6.8 Hz, 2H), 1.64 (m, 2H), 1.49-1.40 (m, 2H), 1.35-1.29 (m, 4H), 0.89 (t, J = 6.9 Hz, 3H), 0.60-0.53 (m, 4H), 0.08 (s, 566H).

SEC (THF, PS standards): Batch 1: $\overline{M_n}$ = 10000 g/mol, $\overline{M_w}$ = 11000 g/mol, PDI = 1.1; Batch 2: $\overline{M_n}$ = 10000 g/mol, $\overline{M_w}$ = 10500 g/mol, PDI = 1.1; Batch 3: $\overline{M_n}$ = 9500 g/mol, $\overline{M_w}$ = 10500 g/mol, PDI = 1.1.

IR (ATR): $\tilde{\nu}$[cm^{-1}] = 2962 (CH_3), 2098 (N_3), 1261 (Si-CH_3), 1020 (Si-O).

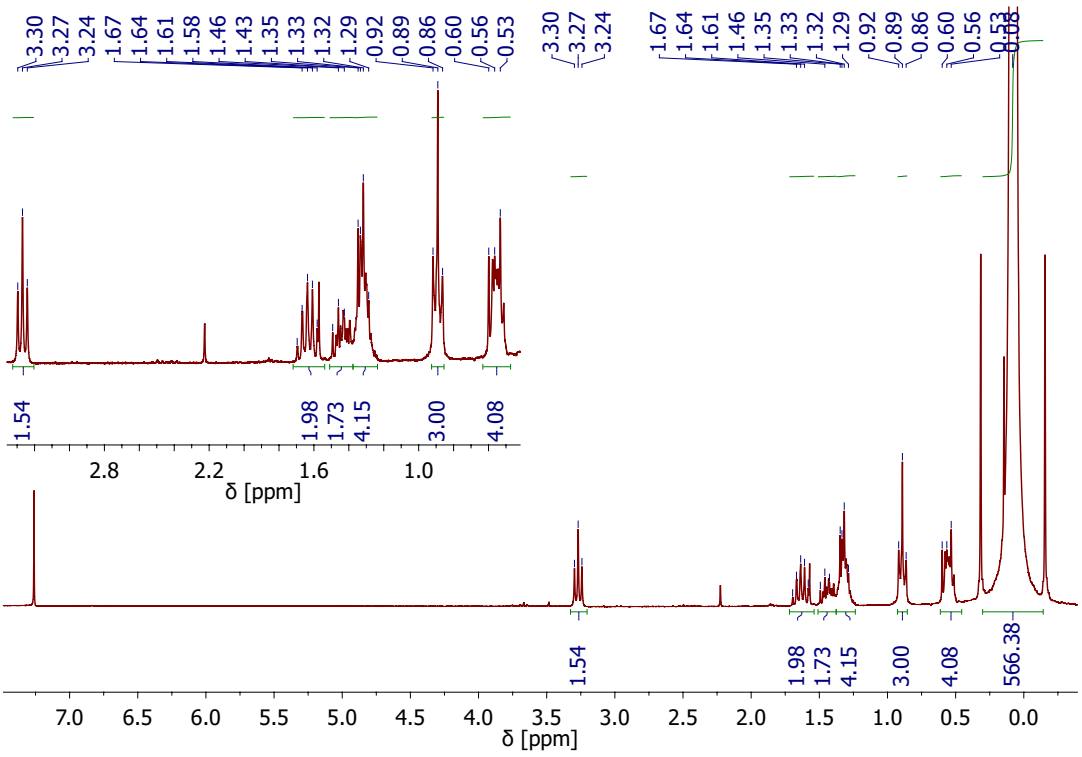

Figure 7.2: ^{1}H-NMR spectrum of purified **PDMS$_{Bu}$-N$_3$** (room temperature, $CDCl_3$).

P3HT-*b*-PDMS

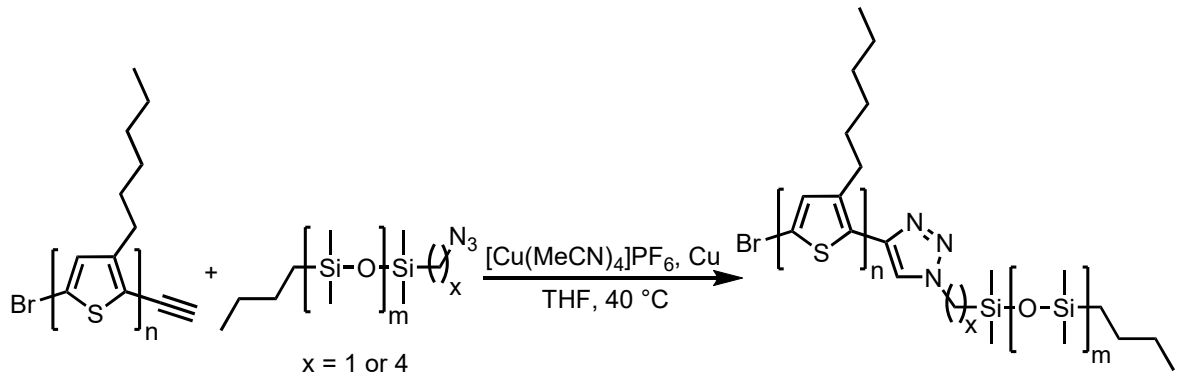

P3HT-alkyne (51 mg) and the respective **PDMS-N$_3$** (291 mg) were dissolved in 4 mL of dry THF under argon in a *Schlenk* tube. Copper powder (66 mg, 1.0 mmol) was added and the solution was degassed by four cycles of freeze-pump-thaw. $Cu(MeCN)_4PF_6$ (10 mg, 0.03 mmol) was dissolved in 1 mL of degassed THF in a separate vial under

careful exclusion of air and the solution was added to the reaction mixture *via* syringe. The flask was then sealed and the reaction was allowed to progress for 96 h at 40 °C. Methanol was slowly added in several small portions until precipitation of a dark red solid occurred at which point the addition was immediately stopped to exclude precipitation of unreacted **PDMS-N$_3$** homopolymer. The red precipitate was collected by centrifugation, washed three times with pure MeOH and dried in a vacuum oven at 40 °C. In the case of azidomethyl-terminated **PDMS** only small amounts of block copolymer were found due to polymer cleavage. For azidobutyl-terminated **PDMS** the soft polymer was found to consist of a mixture of small amounts of **P3HT-alkyne** homopolymer and a main fraction of block copolymer **P3HT-*b*-PDMS$_{Bu}$** which was further purified by passing over a preparative SEC column.

Yield: 9 mg.

^{1}H-NMR (250 MHz, CDCl$_3$): δ[ppm] = 7.59 (s), 6.98 (s, 1H), 2.81 (m, 2H), 1.71-1.36 (m, 8H), 0.91 (m, 3H), 0.07 (s, 26H).

SEC (THF, PS standards): $\overline{M_n}$ = 17000 g/mol, $\overline{M_w}$ = 22000 g/mol, PDI = 1.3.

7.2.2 Side-chain π-extended Polythiophenes

3-Bromo-2,2'-bithiophene (3-BrT$_2$)

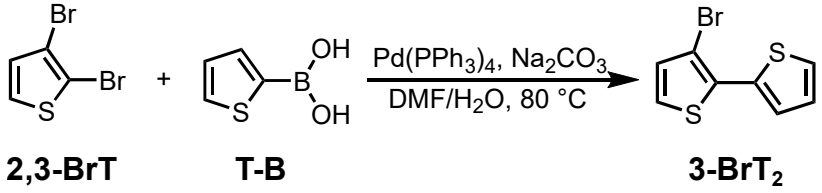

2,3-Dibromothiophene (**2,3-BrT**, 3.00 g, 12.4 mmol, 1 eq), thiophen-2-ylboronic acid (**T-B**, 1.74 g, 13.6 mmol, 1.1 eq) and aqueous Na_2CO_3 solution (1.0 M, 36 mL, 36.0 mmol, 2.9 eq) were added to 240 mL of DMF and the mixture was degassed by argon bubbling for 40 min. $Pd(PPh_3)_4$ (1.14 g, 9.9 mmol, 0.08 eq) was added and the mixture heated to 80 °C under argon for 4 h. After cooling to rt, Et_2O and water were added, the phases separated and the aqueous phase extracted with Et_2O three times. The ether phases were combined, dried over Na_2SO_4 and the solvent removed *in vacuo*. The residue was purified *via* column chromatography (silica, cyclohexane) to obtain the pure product **3-BrT$_2$**.

Yield: 1.95 g (8.0 mmol, 65%).

^{1}H-NMR (250 MHz, $CDCl_3$): δ[ppm] = 7.42 (dd, J = 3.7 Hz, 1.2 Hz, 1H), 7.36 (dd, J = 5.2 Hz, 1.2 Hz, 1H), 7.19 (d, J = 5.4 Hz, 1H), 7.09 (dd, J = 5.2 Hz, 3.7 Hz, 1H), 7.02 (d, J = 5.4 Hz, 1H).

2-(2-Ethylhexyl)thiophene (TC6C2)

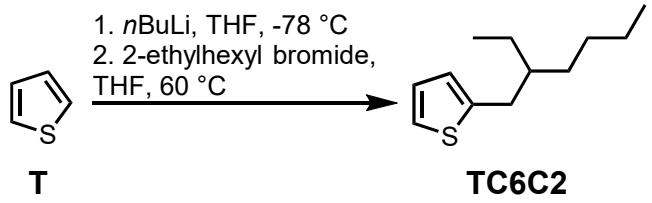

T **TC6C2**

Thiophene (**T**, 11.95 g, 142.0 mmol, 1 eq) was dissolved in 120 mL of dry THF and cooled to -78 °C. *n*BuLi (2.5 M in hexane, 12.5 mL, 70.0 mmol, 0.5 eq) was added dropwise and the mixture was stirred at the same temperature for 2 h. 2-Ethylhexyl bromide (13.52 g, 70.0 mmol, 0.5 eq) was added dropwise and the mixture heated to 60 °C for 12 h. The mixture was diluted with 100 mL of Et_2O and washed with water and brine. The phases were separated, the organic phase dried and the solvent removed *in vacuo*. The crude product was further purified by vacuum distillation (10 mbar, 105 °C) to obtain the title compound **TC6C2** as a colorless oil which slowly decomposed under atmospheric conditions.

Yield: 7.81 g (39.8 mmol, 57%).

^{1}H-NMR (250 MHz, $CDCl_3$): δ[ppm] = 7.11 (dd, J = 5.1 Hz, 1.2 Hz, 1H), 6.92 (dd, J = 5.1 Hz, 3.4 Hz, 1H), 6.76 (dd, J = 3.4 Hz, 1.1 Hz, 1H), 2.76 (d, J = 6.8 Hz, 2H), 1.63-1.53 (m, 1H), 1.39-1.25 (m, 8H), 0.89 (t, J = 7.4 Hz, 6H).

2-(2-Ethylhexyl)-5-pinacolatoborylthiophene (TC6C2-B)

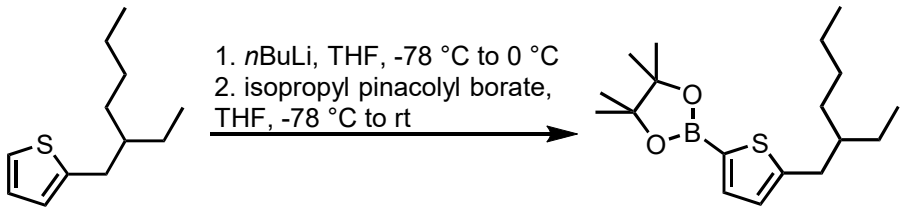

TC6C2 **TC6C2-B**

2-(2-Ethylhexyl)thiophene (**TC6C2**, 7.50 g, 38.2 mmol, 1 eq) was dissolved in 100 mL of dry THF and the mixture cooled to -78 °C. *n*BuLi (2.5 M in hexane, 18.3 mL, 45.6 mmol,

1.2 eq) was added dropwise and the mixture stirred for 10 min at the same temperature. The solution was allowed to warm to 0 °C in an ice bath, stirred for 30 min and again cooled to -78 °C. Isopropyl pinacolyl borate (8.48 g, 45.6 mmol, 1.2 eq) was added dropwise. The mixture was allowed to warm to 0 °C in an ice bath and then to rt and stirred at this temperature overnight. The solvent was removed *in vacuo*, the residue was taken up in CH_2Cl_2 and the solution washed with brine. The organic phase was dried and the solvent was removed *in vacuo* to obtain a slightly orange oil of **TC6C2-B** containing approximately 5% of starting material (^{1}H-NMR analysis), which was used in the next step without further purification.

Yield: 7.58 g (23.5 mmol, 63%).

^{1}H-NMR (250 MHz, $CDCl_3$): δ[ppm] = 7.47 (d, J = 3.4 Hz, 1H), 6.84 (d, J = 3.4 Hz, 1H), 2.79 (d, J = 6.6 Hz, 2H), 1.64-1.54 (m, 1H), 1.33 (s, 12H), 1.32-1.24 (m, 8H), 0.90-0.84 (m, 6H).

5”-(2-Ethylhexyl)-2,2’:3’,2”-terthiophene (3TC6C2)

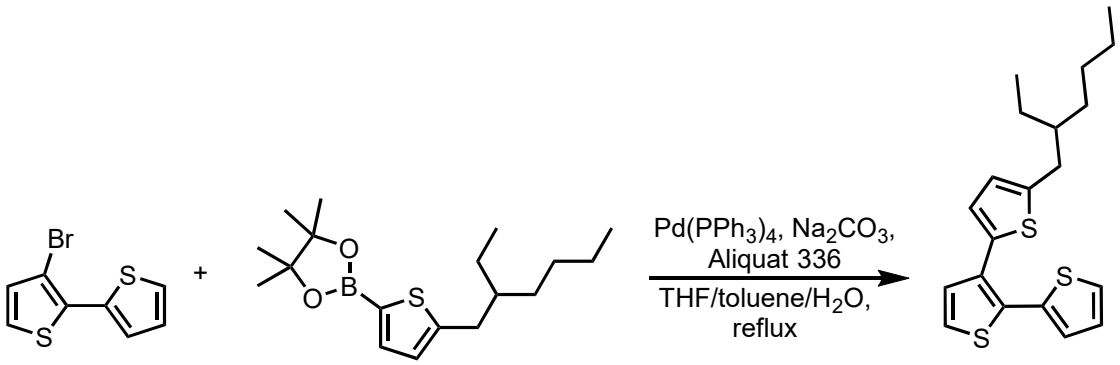

A mixture of 53 mL of dry THF and 53 mL of dry toluene was degassed by argon bubbling for 40 min. 2 mL of the mixture were transferred to a separate *Schlenk* flask and stored under argon for later use. 3-Bromo-2,2’-bithiophene (**3-BrT_2**, 1.90 g, 7.7 mmol, 1 eq), 2-(2-ethylhexyl)-5-pinacolatoborylthiophene (**TC6C2-B**, 3.72 g, 11.6 mmol, 1.5 eq), aqueous Na_2CO_3 solution (2.0 M, 19.5 mL, 39.0 mmol, 5 eq) and *Aliquat 336* (1.56 g, 3.9 mmol, 0.5 eq) were added and the mixture was again degassed for 20 min. $Pd(PPh_3)_4$ (624 mg, 0.54 mmol, 0.07 eq) was dissolved in the earlier prepared degassed solvent mixture inside a glove box and the solution was added to the reaction mixture *via* syringe. The mixture was heated to reflux for 36 h under argon, cooled to rt and diluted with Et_2O. The solution was washed with water and brine, the phases separated and the organic phase

dried over Na_2SO_4. The solvent was removed *in vacuo* and the residue purified by column chromatography (silica, cyclohexane) to obtain the title compound **3TC6C2** as a grey-white, highly viscous oil.

Yield: 2.60 g (7.2 mmol, 94%).

^{1}H-NMR (250 MHz, $CDCl_3$): δ[ppm] = 7.30 (dd, J = 5.1 Hz, 1.2 Hz, 1H), 7.25 (d, J = 5.3 Hz, 1H), 7.14 (d, J = 5.3 Hz, 1H), 7.14-7.12 (m, 1H), 7.01 (dd, J = 5.1 Hz, 3.6 Hz, 1H), 6.84 (d, J = 3.5 Hz, 1H), 6.63 (d, J = 3.5 Hz, 1H), 2.71 (d, J = 6.7 Hz, 2H), 1.59-1.50 (m, 1H), 1.39-1.24 (m, 8H), 0.87 (t, J = 7.4 Hz, 6H).

^{13}C-NMR (63 MHz, $CDCl_3$): δ[ppm] = 144.94, 135.31, 135.09, 132.79, 130.87, 129.87, 127.96, 127.25, 126.73, 126.17, 125.28, 124.51, 41.48, 34.18, 32.45, 28.98, 25.67, 23.15, 14.30, 10.99.

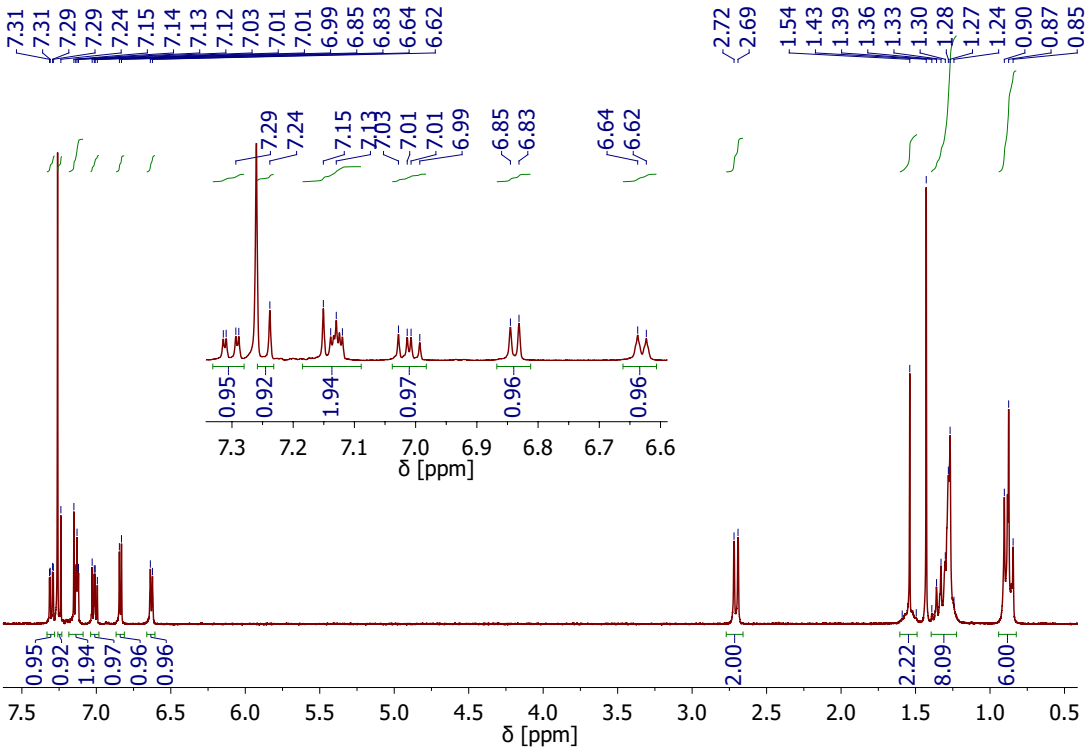

Figure 7.3: ^{1}H-NMR spectrum of purified **3TC6C2** (room temperature, $CDCl_3$)

.

5-Bromo-5”-(2-ethylhexyl)-2,2’:3’,2”-terthiophene (3TC6C2Br)

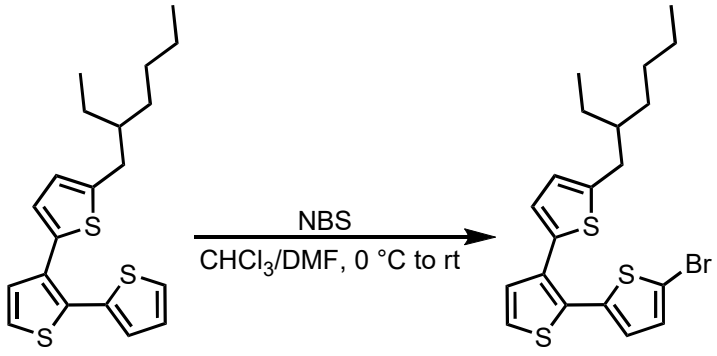

3TC6C2 **3TC6C2Br**

5”-(2-Ethylhexyl)-2,2’:3’,2”-terthiophene (**3TC6C2**, 2.38 g, 6.6 mmol, 1 eq) was dissolved in 12 mL of $CHCl_3$ and the solution was cooled to 0 °C in an ice bath. NBS (1.18 g, 6.6 mmol, 1 eq) in 12 mL of DMF was added slowly and the mixture was allowed to warm slowly to rt in the melting ice bath. After stirring at rt for two days the solution was washed five times with water and two times with brine, the organic phase was dried and the solvent removed. The residue was purified by column chromatography (silica, cyclohexane) to yield the title compound **3TC6C2Br** as a yellow-green, viscous oil.
Yield: 2.21 g (5.0 mmol, 76%).
^{1}H-NMR (250 MHz, $CDCl_3$): δ[ppm] = 7.25 (d, J = 5.3 Hz, 1H), 7.11 (d, J = 5.3 Hz, 1H), 6.96 (d, J = 3.8 Hz, 1H), 6.89 (d, J = 3.8 Hz, 1H), 6.86 (d, J = 3.5 Hz, 1H), 6.66 (d, J = 3.5 Hz, 1H), 2.72 (d, J = 6.8 Hz, 2H), 1.61-1.51 (m, 1H), 1.40-1.26 (m, 8H), 0.89 (t, J = 7.3 Hz, 6H).
^{13}C-NMR (63 MHz, $CDCl_3$): δ[ppm] = 145.45, 137.01, 134.47, 133.08, 130.21, 130.04, 129.99, 127.98, 126.61, 125.44, 124.79, 113.26, 41.50, 34.21, 32.45, 28.98, 25.68, 23.16, 14.32, 11.03.
HRMS (EI^+): calcd for $[M]^+$ m/z = 438.0145, found m/z = 438.0139.

Sample polymerization procedure for P3TC6C2

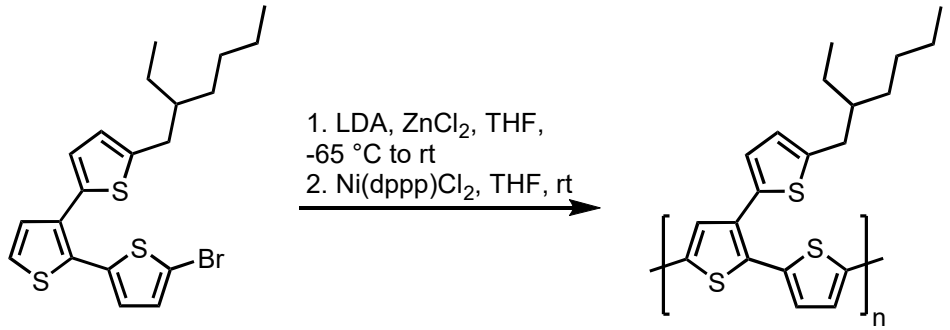

3TC6C2Br **P3TC6C2**

$ZnCl_2$ (anhydrous beads, 681 mg, 5.0 mmol) was dissolved in 5 mL of dry THF inside a glove box to produce a 1.0 M solution. 5-Bromo-5"-(2-ethylhexyl)-2,2':3',2"-terthiophene (**3TC6C2Br**, 488 mg, 1.1 mmol, 1 eq) was dissolved in 10 mL of dry THF under argon and the solution cooled to -65 °C. LDA (1.0 M in THF/hexane, 1.1 mL, 1.1 mmol, 1 eq) was added dropwise and the mixture was stirred for 1 h at the same temperature while turning slightly violet. The prepared $ZnCl_2$ solution (1.2 mL, 1.2 mmol, 1.1 eq) was added dropwise and the mixture turned orange-yellow. The solution was stirred for 20 min at -65 °C, allowed to warm to rt and kept at this temperature for another 30 min. The reaction mixture was stirred vigorously and $Ni(dppp)Cl_2$ (30 mg, 0.055 mmol, 0.05 eq) was added quickly. The mixture developed a deep violet color indicating the formation of polymer chains and stirring was continued for another 15 min. 4 M aqueous HCl solution (5 mL, 20 mmol, 18.2 eq) was added to the highly viscous mixture to quench the polymerization followed by the addition of 50 mL of MeOH to precipitate the polymer. The precipitate was collected *via* centrifugation followed by repeated washing with MeOH. The polymer **P3TC6C2** was purified by *Soxhlet* fractionation with acetone (washing fraction, neglected), chloroform and chlorobenzene. The remaining undissolved solid was found to be completely insoluble in all tested solvents.

Yield: $CHCl_3$ fraction: 35 mg (0.098 mmol, 9%), CB fraction: 45 mg (0.125 mmol, 11%).

^{1}H-NMR (700 MHz, TCE-d2, 100 °C): δ[ppm] = 7.34-7.28 (m), 7.18-7.12 (m), 7.05-6.92 (m), 6.77-6.71 (m), 2.83 (br), 1.66-1.37 (m), 0.96 (br).

SEC (1,2,4-trichlorobenzene, 160 °C, PS standards): $CHCl_3$ fraction: $\overline{M_n}$ = 7500 g/mol, $\overline{M_w}$ = 14000 g/mol, PDI = 1.9; CB fraction: $\overline{M_n}$ = 10000 g/mol, $\overline{M_w}$ = 20000 g/mol, PDI = 2.0.

7.2.3 Cationic and Anionic Conjugated Polyelectrolytes

3-(6-Bromohexyl)thiophene (3BrHT)

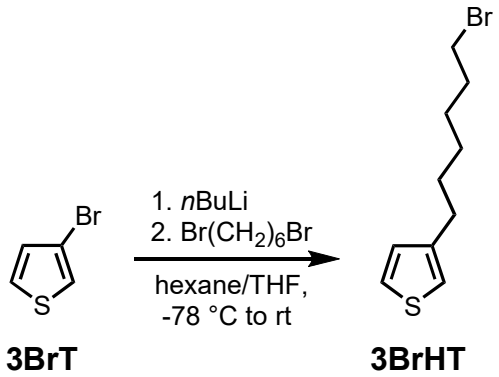

3-Bromothiophene (**3BrT**, 6.0 mL, 64.0 mmol, 1 eq) was dissolved in 150 mL of dry, degassed hexane in a dry *Schlenk* flask under argon and the solution was cooled down to -78 °C. *n*BuLi (1.6 M in hexane, 38.1 mL, 61.0 mmol, 0.95 eq) was added dropwise and the mixture was stirred for an additional 15 min. 15 mL of dry THF were added slowly *via* syringe. After 80 min a white precipitate of the lithiate had formed. The clear supernatant was removed *via* cannula to remove unreacted starting materials and other impurities and a mixture of dry hexane and THF (10:1, 115 mL) was added to the precipitate. 1,6-Dibromohexane (98.1 mL, 637.7 mmol, 10.0 eq) was then added quickly and the solution was allowed to warm to rt. After stirring for an additional 2 h, saturated $NaHCO_3$ solution was added to quench the reaction, the mixture was diluted with diethyl ether and the phases separated. The organic phase was washed with water and brine, dried and the solvent was removed to yield a viscous oil. The main part of the excess 1,6-dibromohexane was removed by vacuum distillation. Due to similar boiling points of this impurity and **3BrHT** approximately 33 w% (determined by NMR spectroscopy) of 1,6-dibromohexane remained in the crude product mixture. This mixture was used without further purification in the next bromination step to facilitate purification due to an increased boiling point of the brominated product.

Yield (determined from NMR of crude product): 8.64 g (35.0 mmol, 55%).

^{1}H-NMR (250 MHz, $CDCl_3$): δ[ppm] = 7.24 (dd, J = 4.9 Hz, 3.0 Hz, 1H), 6.94-6.92 (m, 2H), 3.41 (t, J = 6.8 Hz, 2H), 2.64 (t, J = 7.6 Hz, 2H), 1.90-1.83 (m, 2H), 1.68-1.61 (m, 2H), 1.53-1.33 (m, 4H).

2,5-Dibromo-3-(6-bromohexyl)thiophene (3BrHTBr$_2$)

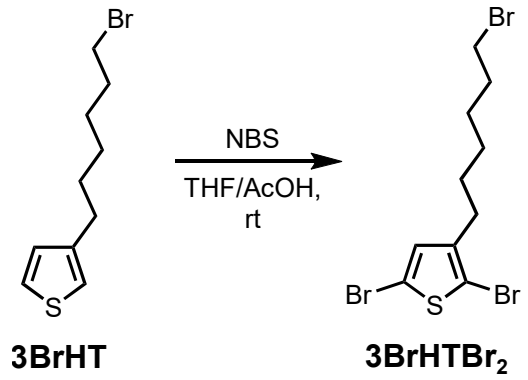

3-(6-Bromohexyl)thiophene (**3BrHT**, crude product, 33 w% 1,6-dibromohexane, 2.64 g, 10.7 mmol, 1 eq) was dissolved in a mixture of THF (25 mL) and acetic acid (25 mL). NBS (4.77 g, 26.8 mmol, 2.5 eq) was added and the solution was stirred for 2 h at rt under the exclusion of light. Saturated $NaHCO_3$ solution and Et_2O were added, the phases separated and the organic phase washed with water and brine. The solvent was removed *in vacuo* to yield an orange oil which was further purified by repeated column chromatography (silica, ethyl acetate:cyclohexane = 1:10) and heating under vacuum to remove traces of 1,6-dibromohexane. The title compound **3BrHTBr$_2$** was obtained as a colorless oil.

Yield: 2.70 g (6.7 mmol, 63%).

^{1}H-NMR (250 MHz, $CDCl_3$): δ[ppm] = 6.77 (s, 1H), 3.41 (t, J = 6.8 Hz, 2H), 2.52 (t, J = 7.6 Hz, 2H), 1.92-1.81 (m, 2H), 1.62-1.25 (m, 6H).

^{13}C-NMR (63 MHz, $CDCl_3$): δ[ppm] = 142.76, 131.02, 110.59, 108.22, 34.03, 32.78, 29.50, 29.43, 28.30, 28.02.

HRMS (EI$^+$): calcd for $[M]^+$ m/z = 401.8288, found m/z = 401.8284.

A two-step sequence similar to the synthesis of 2,5-dibromo-3-(6-bromohexyl)thiophene (**3BrHTBr$_2$**) was used by *Dr. Roman Tkachov* for the synthesis of **3BrHTBrI**. First, 3-(6-bromohexyl)thiophene (**3BrHT**, 2.50 g, 10.1 mmol, 1 eq) was brominated with NBS (1.80 g, 10.1 mmol, 1 eq) in 50 mL of THF for 2 h and the product obtained by column chromatography (silica, ethyl acetate:hexane = 5:95). Iodination was then carried out in a 1:1 mixture of $CHCl_3$ (30 mL) and acetic acid (30 mL) with NIS (2.39 g, 10.6 mmol, 1.05 eq) at rt overnight and the product **3BrHTBrI** was obtained by column chromatography (silica, ethyl acetate:hexane = 5:95).

Yield: 2.34 g (5.2 mmol, 51%).

^{1}H-NMR (250 MHz, $CDCl_3$): δ[ppm] = 6.96 (s, 1H), 3.41 (t, J = 6.8 Hz, 2H), 2.53 (t, J = 7.6 Hz, 2H), 1.92-1.80 (m, 2H), 1.62-1.25 (m, 6H).

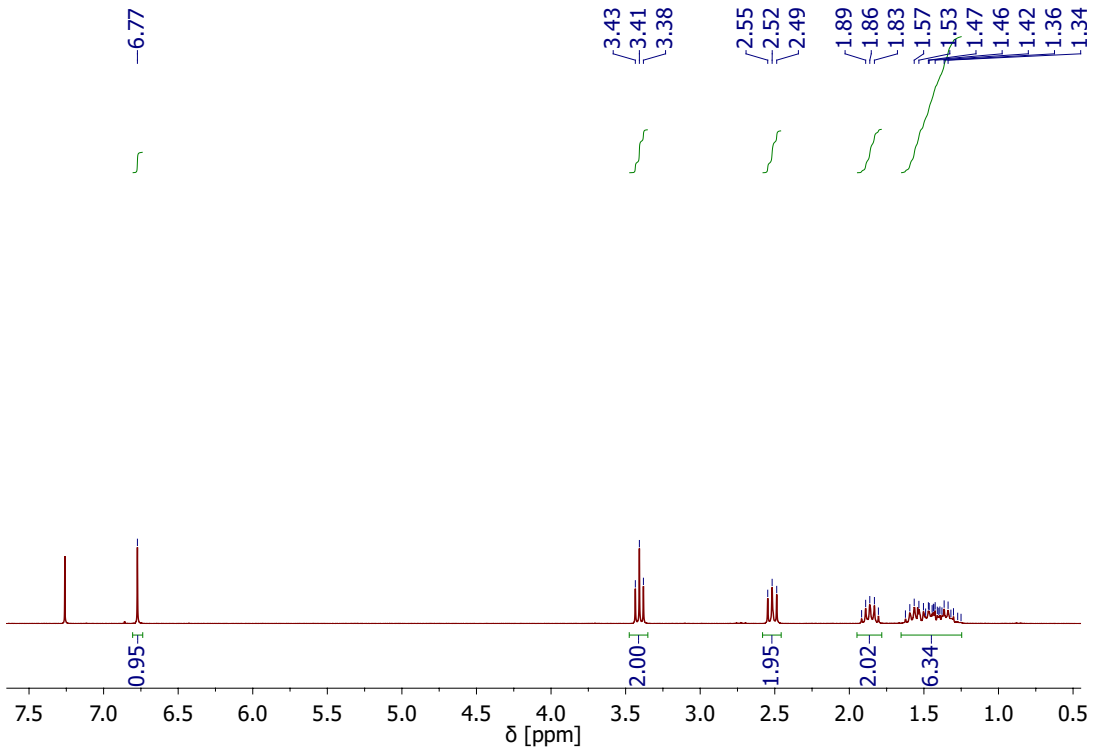

Figure 7.4: ^{1}H-NMR spectrum of purified **3BrHTBr$_2$** (room temperature, $CDCl_3$).

Sample polymerization procedure for precursor polymer P3BrHT

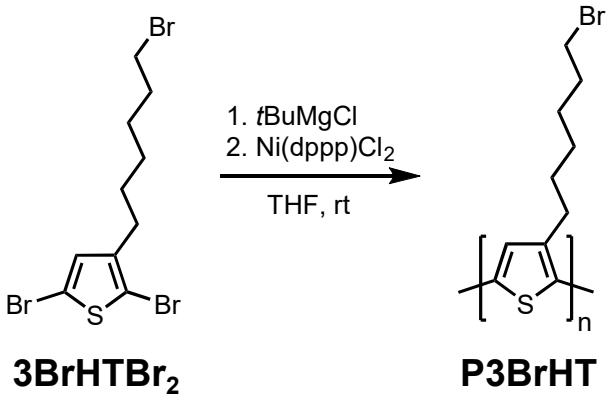

2,5-Dibromo-3-(6-bromohexyl)thiophene (**3BrHTBr$_2$**, 1.01 g, 2.5 mmol, 1 eq) was dissolved in dry THF (5 mL) under argon. *t*Butylmagnesium chloride (2.0 M in Et_2O, 1.25 mL, 2.5 mmol, 1 eq) was added dropwise. After stirring at rt for 2 h the mixture was diluted with 20 mL of dry THF and Ni(dppp)Cl_2 (13 mg, 0.024 mmol, 0.01 eq) was added in one portion as fast as possible under vigorous stirring. The mixture turned orange-red within

seconds indicating formation of polymer chains. After stirring for 15 min at rt the polymer solution was poured into an excess of methanol to precipitate the product which was then collected by centrifugation. Side products and oligomer impurities were removed by repeated *Soxhlet* purification with methanol and ethyl acetate to obtain the pure polymer **P3BrHT** as a dark red powder. Polymerization of 2-bromo-3-(6-bromohexyl)-5-iodothiophene (**3BrHTBrI**) was carried out by *Dr. Roman Tkachov* under similar conditions using Ni(dppe)Cl_2 (0.005 eq) as the catalyst.
Yield: 270 mg, (1.1 mmol, 44%).
^{1}H-NMR (250 MHz, $CDCl_3$): δ[ppm] = 6.98 (s, 1H), 3.46-3.40 (m, 2H), 2.85-2.79 (m, 2H), 1.92-1.87 (m, 2H), 1.76-1.70 (m, 2H), 1.49 (m, 4H).
IR (ATR): $\tilde{\nu}$[cm^{-1}] = 2921 (C-H).
SEC (THF, PS standards): Batch 1: $\overline{M_n}$ = 8000 g/mol, $\overline{M_w}$ = 13000 g/mol, PDI = 1.6; Batch 2: $\overline{M_n}$ = 15000 g/mol, $\overline{M_w}$ = 18000 g/mol, PDI = 1.2; Batch 3: $\overline{M_n}$ = 23000 g/mol, $\overline{M_w}$ = 31000 g/mol, PDI = 1.3.

Sample polymerization procedure for PTIm-Br

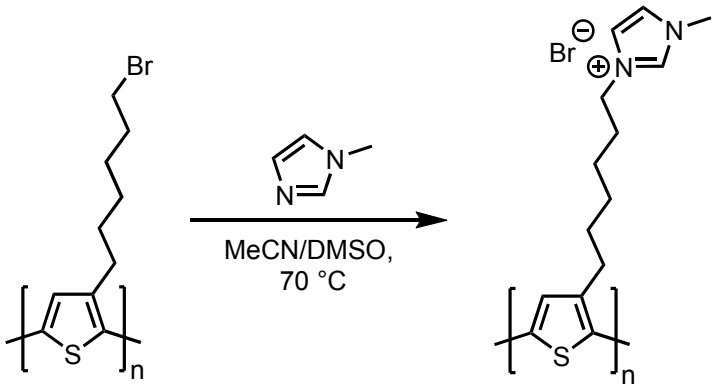

P3BrHT **PTIm-Br**

P3BrHT (8 kg/mol, 70 mg, 0.29 mmol of repeating units, 1 eq) was added to 3 mL of a 10:1 mixture of acetonitrile and DMSO to form a suspension. 1-Methylimidazole (234 mg, 2.9 mmol, 10 eq) was added and the mixture was heated to 70 °C for 48 h during which the quaternization reaction lead to the dissolution of the newly formed polyelectrolyte in the solvent mixture. After cooling to rt the solution was dropped into an excess of THF to precipitate the crude polymer product which was collected by centrifugation and washed repeatedly with THF, Et_2O and toluene. Drying at 40 °C under vacuum afforded the conjugated polyelectrolyte **PTIm-Br** as a dark powder.

Yield: 73 mg (0.22 mmol, 76%).
^{1}H-NMR (250 MHz, DMSO-d6): δ[ppm] = 9.35 (s, 1H), 7.86 (s, 1H), 7.75 (s, 1H), 7.20 (s, 1H), 4.21 (m, 2H), 3.87 (s, 3H), 2.93-2.63 (m, 2H), 1.89-1.73 (m, 2H), 1.73-1.52 (m, 2H), 1.52-1.23 (m, 4H).
IR (ATR): $\tilde{\nu}$[cm^{-1}] = 3378 (H_2O), 3076 (Im-H), 2921 (C-H), 1560 (C=N).

Sample polymerization procedure for PTS-TBA

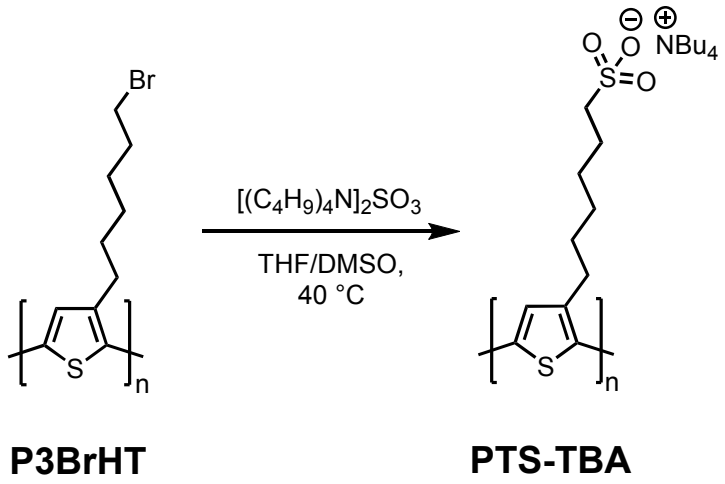

P3BrHT **PTS-TBA**

PTS-TBA was synthesized by *Dr. Roman Tkachov*. **P3BrHT** (15 kg/mol, 100 mg, 0.41 mmol of repeating units, 1 eq) was dissolved in THF (27 mL) at 40 °C and the mixture was degassed by argon bubbling for 20 min. Tetrabutylammonium sulfite (1.0 M in DMSO, 4.05 mL, 4.05 mmol, 9.9 eq) was added and the mixture was kept at 40 °C for 24 h. Water was added and the reaction mixture was dialyzed (*Spectra/Por* membrane, MW cutoff = 3500 Da) against ultrapure water for 10 d to purify the polymer. The solvent was removed *in vacuo* and the polymer **PTS-TBA** was freeze-dried to obtain a dark powder. A 2nd batch was synthesized from **P3BrHT** (23 kg/mol) employing the same reaction conditions.
Yield: 180 mg (0.37 mmol, 90%).
^{1}H-NMR (250 MHz, THF-d8/D_2O = 2:1): δ[ppm] = 7.03 (s, 1H), 3.19-3.13 (m, 8H), 2.85-2.63 (m, 4H), 1.77-1.49 (m, 12H), 1.49-1.25 (m, 12H), 0.93-0.87 (t, J = 7.3 Hz, 12H).
IR (ATR): $\tilde{\nu}$[cm^{-1}] = 3429 (H_2O), 2921 (C-H).
EA: [%] calcd for quantitative functionalization: C, 63.76; H, 10.50; N, 2.86; O, 9.80; S, 13.09; found C, 61.68; H, 9.66; N, 2.59; S, 13.26.

7.2.4 Conjugated Redox Polymers

3-Chloromethylthiophene (3CMT)

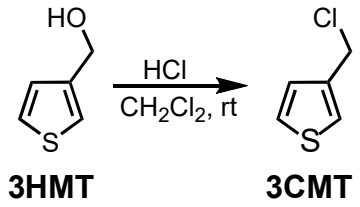

Thiophene-3-methanol (**3HMT**, 15.0 g, 131.4 mmol, 1 eq) was dissolved in 330 mL of CH_2Cl_2 and conc. aqueous HCl (37%, 330 mL, 3.90 mol, 30 eq) was added. The mixture was stirred at room temperature for 10 h. The aqueous phase was extracted two times with CH_2Cl_2. The organic phases were washed with water, two times with saturated $NaHCO_3$ solution and again with water. After drying over Na_2SO_4 and removal of the solvent *in vacuo*, the product **3CMT** was obtained as a colorless oil which slowly degraded at room temperature while developing a brownish color. The compound was thus immediately used in the next step without further purification.
Yield: 16.54 g (124.6 mmol, 95%).
^{1}H-NMR (250 MHz, $CDCl_3$): δ[ppm] = 7.34-7.29 (m, 2H), 7.13 (d, J = 4.8 Hz), 4.63 (s, 2H).

Triisopropyl-(4-thiophen-yl-but-1-inyl)-silane (3TBT)

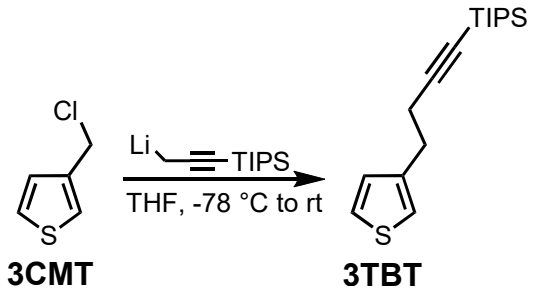

1-(Triisopropylsilyl)-1-propyne (10.26 g, 52.2 mmol, 1 eq) was dissolved in 250 mL of dry THF under an argon atmosphere. The mixture was cooled to -78 °C and *n*BuLi (1.6 M in hexane, 34.2 mL, 54.8 mmol, 1.05 eq) was added dropwise. The mixture was stirred for 2 h after which 3-chloromethylthiophene (**3CMT**, 6.90 g, 52.2 mmol, 1 eq) was added. The reaction mixture was further stirred for 15 h at room temperature and then quenched by addition of water. The phases were separated and the aqueous phase was extracted

three times with diethyl ether. The organic phases were washed with water and brine, dried over Na_2SO_4 and the solvent was removed *in vacuo*. The crude product mixture was further purified by column chromatography (silica, CH_2Cl_2:cyclohexane = 5:95) to obtain the title compound **3TBT** as a clear oil.

Yield: 7.97 g (27.3 mmol, 52%).

^{1}H-NMR (250 MHz, $CDCl_3$): δ[ppm] = 7.24 (dd, J = 4.9 Hz, 2.9 Hz, 1H), 7.03-6.99 (m, 2H), 2.88 (t, J = 7.3 Hz, 2H), 2.55 (t, J = 7.3 Hz, 2H), 1.09-0.97 (m, 21H).

^{13}C-NMR (63 MHz, $CDCl_3$): δ[ppm] = 141.16, 128.18, 125.35, 120.92, 108.30, 81.13, 29.92, 21.44, 18.72, 11.39.

HRMS (ESI^+): calcd for $[M+Na]^+$ m/z = 315.1573, found m/z = 315.1579.

(4-(2,5-Dibromothiophen-3-yl)-but-1-inyl)-triisopropylsilane (3TBTBr$_2$)

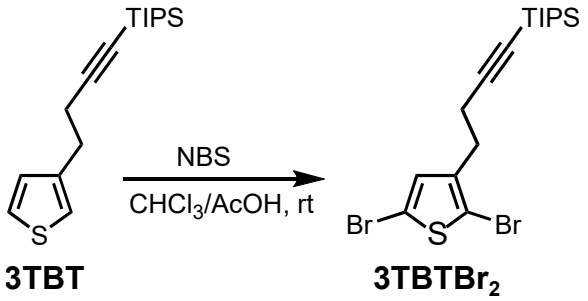

3TBT **3TBTBr$_2$**

Triisopropyl-(4-thiophen-yl-but-1-inyl)-silane (**3TBT**, 7.97 g, 27.3 mmol, 1 eq) was dissolved in 100 mL of a 1:1 mixture of glacial acetic acid and chloroform. NBS (9.70 g, 54.5 mmol, 2 eq) was added and the mixture was stirred in the dark for 3 h. More NBS (6.79 g, 38.2 mmol, 1.4 eq) was added and the bromination reaction was allowed to proceed for 60 h at room temperature until TLC analysis showed full conversion of the starting material to the dibrominated product. The reaction was quenched by addition of water, the phases separated and the aqueous phase was extracted two times with chloroform. The organic phases were washed with water and saturated $NaHCO_3$ solution, dried over Na_2SO_4 and the solvent was evaporated. The crude product mixture was further purified by column chromatography (silica, petroleum ether) and the clean product **3TBTBr$_2$** obtained as a slightly yellowish liquid.

Yield: 7.71 g (17.3 mmol, 63%).

^{1}H-NMR (250 MHz, $CDCl_3$): δ[ppm] = 6.94 (s, 1H), 2.75 (t, J = 7.0 Hz, 2H), 2.51 (t, J = 7.0 Hz, 2H) 1.10-0.94 (m, 21H).

^{13}C-NMR (63 MHz, $CDCl_3$): δ[ppm] = 140.96, 131.39, 110.53, 108.96, 107.07, 82.07, 28.80, 20.15, 18.71, 11.37.

HRMS (EI$^+$): calcd for $[M]^+$ $m/z = 447.9891$, found $m/z = 447.9880$.

2,5-Dibromo-3-hexylthiophene (3HTBr$_2$)

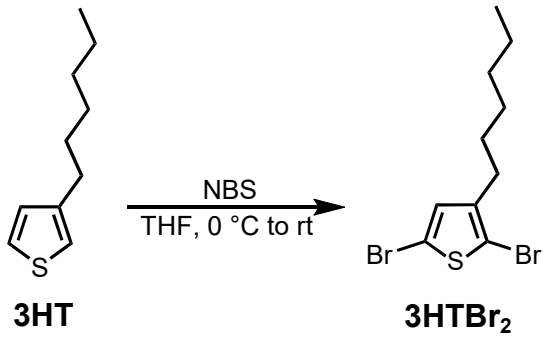

3-Hexylthiophene (**3HT**, 15.0 g, 89.1 mmol, 1 eq) was dissolved in 150 mL of dry THF and cooled to 0 °C. NBS (39.6 g, 222.5 mmol, 2.5 eq) was added and the mixture stirred under the exclusion of light at 0 °C for 2 h. At this point the conversion was found to be incomplete by TLC. The reaction was further stirred in the dark at rt overnight until TLC indicated nearly quantitative conversion of the monobrominated compound to the desired product. The reaction mixture was then diluted with diethyl ether and saturated $NaHCO_3$ solution was added. The layers were separated and the organic layer was washed two times with water and one time with brine, dried over Na_2SO_4 and the solvent removed *in vacuo*. The crude product mixture was further purified by column chromatography (silica, cyclohexane) to obtain the desired compound **3HTBr$_2$** as a slightly orange oil.
Yield: 24.2 g (74.2 mmol, 83%).
^{1}H-NMR (250 MHz, CDCl$_3$): δ[ppm] = 6.78 (s, 1H), 2.51 (t, $J = 7.6$ Hz, 2H), 1.60-1.48 (m, 2H), 1.37-1.27 (m, 6H), 0.92-0.86 (t, $J = 6.6$ Hz, 3H).
^{13}C-NMR (63 MHz, CDCl$_3$): δ[ppm] = 143.15, 131.11, 110.44, 108.06, 31.71, 29.70, 29.63, 28.93, 22.71, 14.22.
HRMS (EI$^+$): calcd for $[M]^+$ $m/z = 323.9183$, found $m/z = 323.9176$.

Sample polymerization procedure for P(3HT-*co*-3TBT)

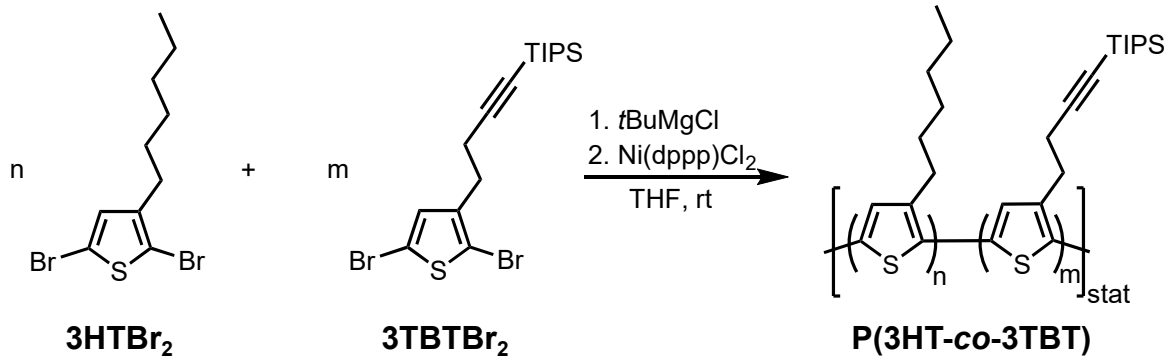

[4-(2,5-Dibromothiophen-3-yl)-but-1-inyl]-triisopropylsilane (**3TBTBr$_2$**, 540 mg, 1.2 mmol, 0.3 eq) and 2,5-dibromo-3-hexylthiophene (**3HTBr$_2$**, 913 mg, 2.8 mmol, 0.7 eq) were dissolved in 4 mL of dry THF under an argon atmosphere. A solution of *t*BuMgCl (2.0 M in Et_2O, 2.0 mL, 4.0 mmol, 1 eq) was added *via* syringe. After stirring at room temperature for 2 h the mixture was diluted to a total volume of 20 mL with dry THF. After addition of the catalyst Ni(dppp)Cl_2 (21.6 mg, 0.04 mmol, 0.01 eq) the mixture was allowed to react for 2 h at room temperature. The polymer **P(3HT-*co*-3TBT)** was precipitated into methanol, collected by centrifugation and dried in a vacuum oven at 50 °C overnight.
Yield: 394 mg.
^{1}H-NMR (250 MHz, $CDCl_3$): δ[ppm] = 7.07 (s), 6.98 (s), 3.08 (br), 2.80 (br), 2.66 (br), 1.71 (br), 1.36 (br), 1.04 (br), 0.91 (br).
^{13}C-NMR (63 MHz, $CDCl_3$): δ[ppm] = 140.04, 137.58, 133.84, 130.64, 128.75, 107.87, 81.68, 31.86, 30.68, 29.63, 29.43, 29.05, 22.82, 21.08, 18.79, 14.29, 11.44.
SEC (THF, PS standards): Batch 1 (3HT/3TBT = 0/100): $\overline{M_n}$ = 9500 g/mol, $\overline{M_w}$ = 18000 g/mol, PDI = 1.9; Batch 2 (3HT/3TBT = 41/59): $\overline{M_n}$ = 18000 g/mol, $\overline{M_w}$ = 29000 g/mol, PDI = 1.6; Batch 3 (3HT/3TBT = 55/45): $\overline{M_n}$ = 9000 g/mol, $\overline{M_w}$ = 13000 g/mol, PDI = 1.4; Batch 4 (3HT/3TBT = 67/33): $\overline{M_n}$ = 18500 g/mol, $\overline{M_w}$ = 29000 g/mol, PDI = 1.6; Batch 5 (3HT/3TBT = 73/27): $\overline{M_n}$ = 18000 g/mol, $\overline{M_w}$ = 23000 g/mol, PDI = 1.3; Batch 6 (3HT/3TBT = 91/9): $\overline{M_n}$ = 21000 g/mol, $\overline{M_w}$ = 40500 g/mol, PDI = 1.9.
IR (ATR): $\tilde{\nu}$[cm^{-1}] = 2174 (alkyne).

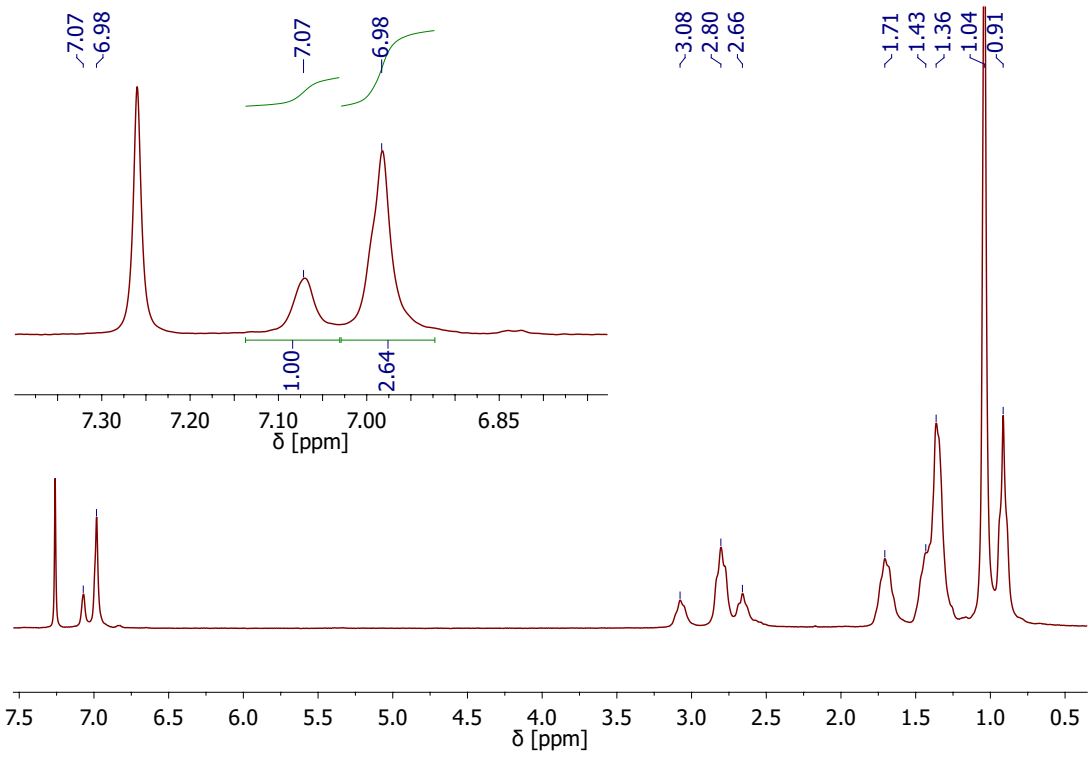

Figure 7.5: ^{1}H-NMR spectrum of purified **P(3HT-*co*-3TBT)**, batch 5 (room temperature, $CDCl_3$).

4-Nitrotriphenylamine (TPA-NO_2)

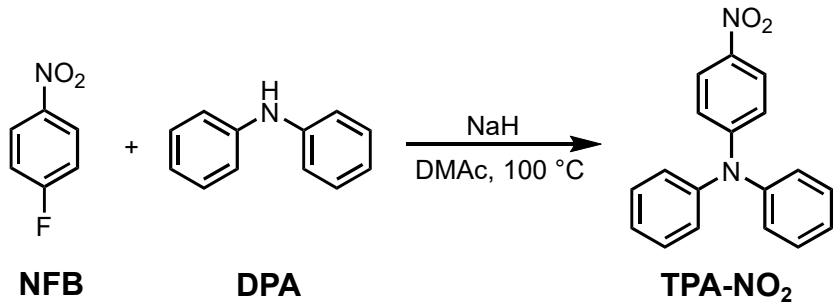

Diphenylamine (**DPA**, 5.00 g, 29.6 mmol, 1 eq) and NaH (1.11 g, 46.0 mmol, 1.6 eq) were suspended in 30 mL of DMAc. The suspension was stirred at room temperature for 30 min and then cooled to 0 °C in an ice bath. 4-Fluoronitrobenzene (**NFB**, 5.00 g, 35.5 mmol, 1.2 eq) in 30 mL of DMAc was added slowly at this temperature and the mixture was heated to 100 °C and stirred for 1 h. The reaction was quenched by pouring into dilute aqueous HCl. Recrystallization of the crude product from a 1:1 mixture of water and

isopropanol and subsequent purification *via* column chromatography (silica, petroleum ether:CH_2Cl_2 = 2:1) yielded the title compound **TPA-NO$_2$** as an orange crystalline solid.
Yield: 6.91 g (23.8 mmol, 81%).
^{1}H-NMR (250 MHz, CDCl$_3$): δ[ppm] = 8.04 (d, J = 9.4 Hz, 2H), 7.40-7.34 (m, 4H), 7.24-7.17 (m, 6H), 6.92 (d, J = 9.4 Hz, 2H).
^{13}C-NMR (63 MHz, CDCl$_3$): δ[ppm] = 153.59, 145.75, 140.24, 130.04, 126.63, 125.85, 125.57, 118.22.
HRMS (ESI$^+$): calcd for $[M+Na]^+$ m/z = 313.0947, found m/z = 313.0953.

4-Aminotriphenylamine (TPA-NH$_2$)

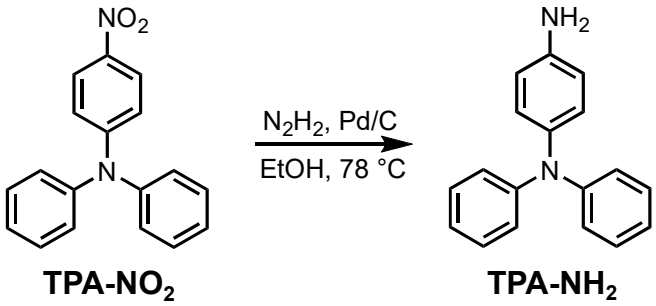

A mixture of 4-nitrotriphenylamine (**TPA-NO$_2$**, 2.00 g, 6.9 mmol, 1 eq) and palladium on carbon (10 w%, 0.10 g, 0.01 eq) in 14 mL of ethanol was heated to reflux. After careful addition of hydrazine monohydrate (2.1 mL, 42.6 mmol, 6.2 eq) *via* syringe the mixture was stirred under reflux overnight. The mixture was cooled down to room temperature, the catalyst removed by filtration and the resulting clear solution poured into water to precipitate the product **TPA-NH$_2$**. The white crystalline solid was collected by suction filtration and dried in a vacuum oven at 50 °C overnight.
Yield: 1.31 g (5.0 mmol, 72%).
^{1}H-NMR (250 MHz, CDCl$_3$): δ[ppm] = 7.23-7.16 (m, 4H), 7.04-6.89 (m, 8H), 6.65 (d, J = 8.7 Hz, 2H), 3.60 (s, 2H).
^{13}C-NMR (63 MHz, CDCl$_3$): δ[ppm] = 148.36, 142.29, 139.51, 129.13, 127.80, 122.76, 121.70, 116.66.
HRMS (ESI$^+$): calcd for $[M+H]^+$ m/z = 261.1386, found m/z = 261.1388.

4-Azidotriphenylamine (TPA-N_3)

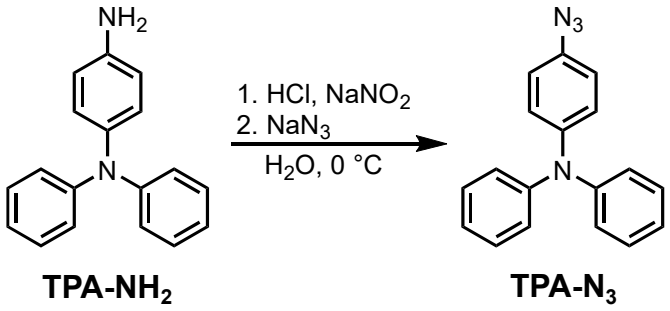

4-Aminotriphenylamine (**TPA-NH_2**, 660 mg, 2.5 mmol, 1 eq) was dissolved in a mixture of conc. HCl (37%, 0.5 mL) and water (6.6 mL) and the mixture was cooled down to 0 °C in an ice bath. The diazonium salt of the compound was formed by slow addition of a solution of sodium nitrite (185 mg, 2.7 mmol, 1.1 eq) in 2.6 mL of water which caused a significant color change of the reaction mixture to orange-red. After stirring the reaction for an additional hour at 0 °C, NaN_3 (198 mg, 3.9 mmol, 1.2 eq) in 2.6 mL of water was added slowly. The mixture was allowed to react for an additional hour. The product was extracted from the solution with CH_2Cl_2 and the organic phase was washed with water, saturated $NaHCO_3$ solution, water and brine and dried over Na_2SO_4. After removal of the solvent *in vacuo* the crude product mixture was purified by column chromatography (silica, cyclohexane:CH_2Cl_2 = 2:1) to obtain the title compound **TPA-N_3** as a white solid. Since **TPA-N_3** degrades to a variety of colored products under UV light, it should be purified, stored and handled in the dark.

Yield: 661 mg (2.3 mmol, 77%).

^{1}H-NMR (250 MHz, CD_2Cl_2): δ[ppm] = 7.28-7.22 (m, 4H), 7.09-6.99 (m, 8H), 6.93 (d, J = 9.0 Hz, 2H).

^{13}C-NMR (63 MHz, $CDCl_3$): δ[ppm] = 147.74, 145.12, 134.24, 129.43, 125.68, 124.08, 122.98, 120.01.

HRMS (ESI^+): calcd for $[M+H]^+$ m/z = 287.1291, found m/z = 287.1293.

IR (ATR): $\tilde{\nu}$[cm^{-1}] = 2079 (N_3).

6-Bromo-N-(4-(diphenylamino)phenyl)hexanamide (spTPA-Br)

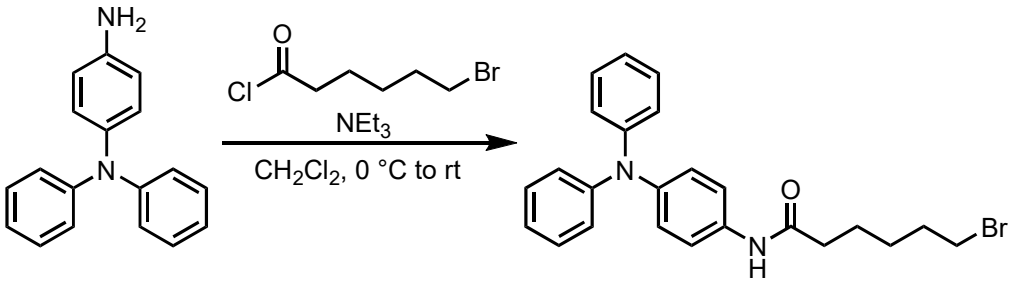

TPA-NH$_2$ **spTPA-Br**

6-Bromohexanoyl chloride (0.29 mL, 1.9 mmol, 1 eq) was dissolved in 8 mL of dichloromethane and cooled to 0 °C in an ice bath. 4-Aminotriphenylamine (**TPA-NH$_2$**, 500 mg, 1.9 mmol, 1 eq) and triethylamine (0.27 mL, 1.9 mmol, 1 eq) in 38 mL of dichloromethane were added dropwise by syringe. The ice bath was removed and the solution stirred for 12 h at room temperature. It was diluted with Et_2O and washed two times with saturated ammonium chloride solution, water and brine, dried over Na_2SO_4 and the solvent was removed *in vacuo*. The crude product was further purified *via* column chromatography (silica, CH_2Cl_2) to obtain the product **spTPA-Br** as a colorless oil which crystallized slowly to a white solid upon standing at room temperature.

Yield: 583 mg (1.3 mmol, 70%).

^{1}H-NMR (250 MHz, CD_2Cl_2): δ[ppm] = 7.40 (d, J = 8.6 Hz, 2H), 7.27-7.20 (m, 5H), 7.05-6.96 (m, 8H), 3.44 (t, J = 6.9 Hz, 2H), 2.34 (t, J = 7.6 Hz, 2H), 1.96-1.84 (m, 2H), 1.79-1.67 (m, 2H), 1.57-1.45 (m, 2H).

^{13}C-NMR (63 MHz, $CDCl_3$): δ[ppm] = 170.94, 147.87, 144.31, 133.05, 129.32, 125.17, 123.90, 122.67, 121.26, 37.44, 33.74, 32.57, 27.87, 24.82.

HRMS (ESI$^+$): calcd for $[M+Na]^+$ m/z = 459.1042, found m/z = 459.1036.

6-Azido-N-(4-(diphenylamino)phenyl)hexanamide (spTPA-N_3)

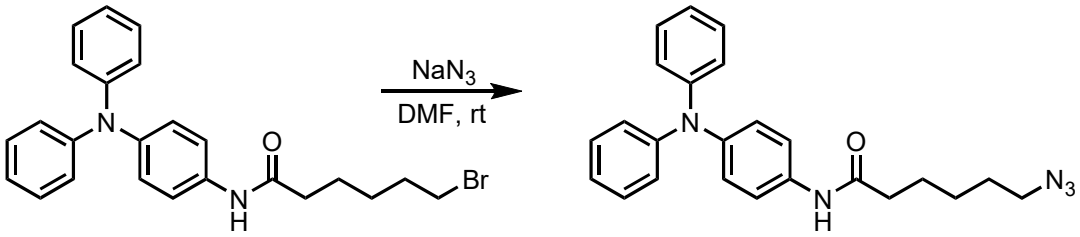

spTPA-Br **spTPA-N_3**

6-Bromo-N-(4-(diphenylamino)phenyl)hexanamide (**spTPA-Br**, 400 mg, 0.91 mmol, 1 eq) and sodium azide (310 mg, 4.77 mmol, 5.2 eq) were suspended in 8 mL of dry DMF inside a glove box. The mixture was stirred at room temperature for 16 h during which precipitation of NaBr took place. The suspension was then poured into 100 mL of brine. The resulting mixture was extracted two times with EtOAc. The combined organic phases were washed with water eight times, dried over Na_2SO_4 and concentrated *in vacuo*. The crude mixture was further purified by column chromatography (silica, CH_2Cl_2) and the product **spTPA-N_3** obtained as a colorless oil which crystallized very slowly under storage at -24 °C.

Yield: 353 mg (0.88 mmol, 97%).

^{1}H-NMR (250 MHz, CD_2Cl_2): δ[ppm] = 7.40 (d, J = 8.6 Hz, 2H), 7.27-7.20 (m, 5H), 7.07-6.96 (m, 8H), 3.29 (t, J = 6.9 Hz, 2H), 2.33 (t, J = 7.5 Hz, 2H), 1.79-1.61 (m, 4H), 1.50-1.41 (m, 2H).

^{13}C-NMR (63 MHz, $CDCl_3$): δ[ppm] = 170.94, 147.86, 144.29, 133.08, 129.32, 125.17, 123.89, 122.66, 121.23, 51.36, 37.45, 28.76, 26.48, 25.19.

HRMS (ESI^+): calcd for $[M+Na]^+$ m/z = 422.1951, found m/z = 422.1958.

IR (ATR): $\tilde{\nu}$[cm^{-1}] = 2094 (N_3), 1654 (C=O).

Polymer analogous functionalizations (PT-TPA and PT-spTPA)

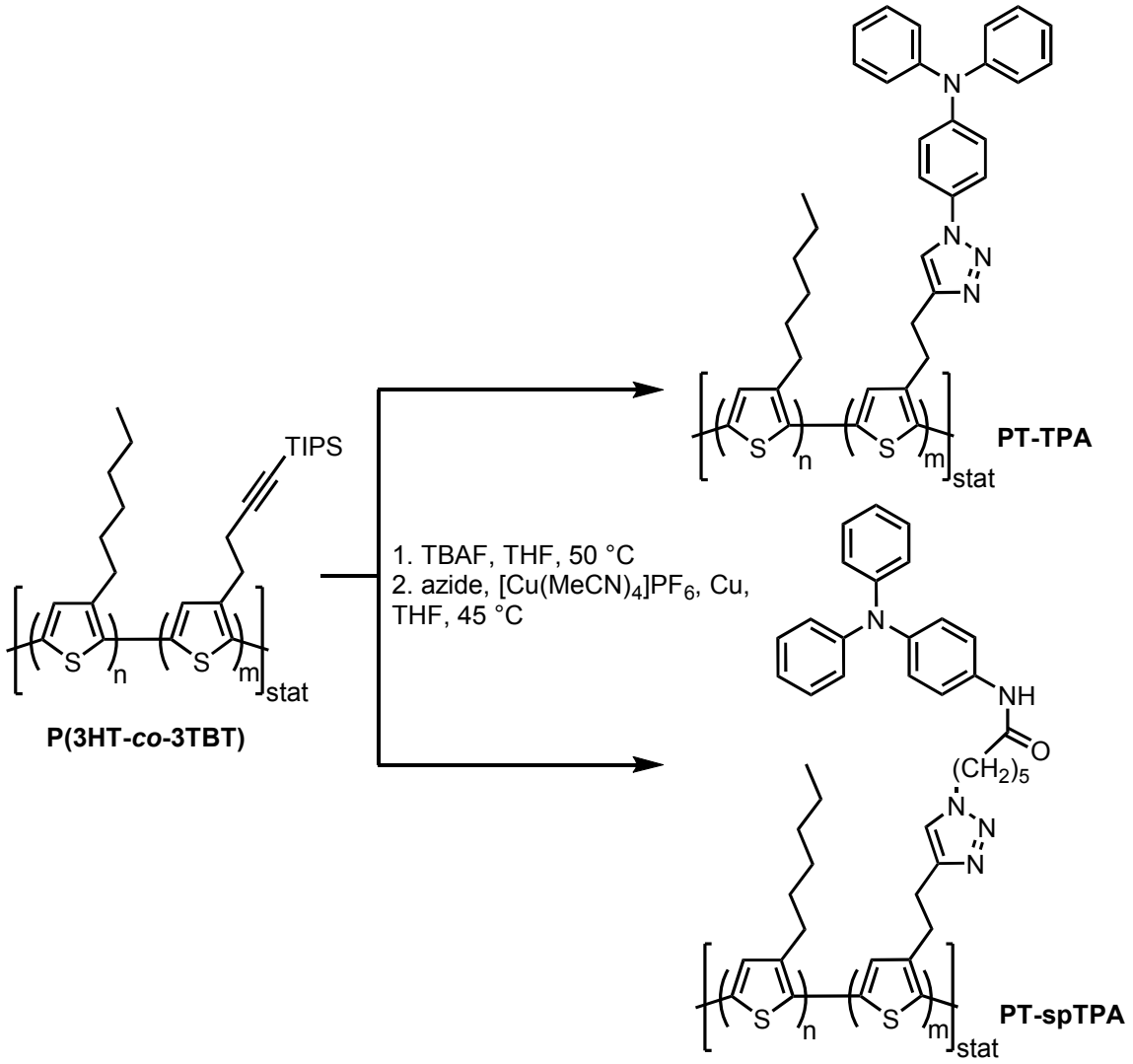

P(3HT-*co*-3TBT) (73/27 mol%, 100 mg, 0.16 mmol of alkyne groups, 1 eq) was dissolved in 20 mL of dry THF and TBAF solution (1.0 M in THF, 0.8 mL, 0.8 mmol, 5 eq) was added *via* syringe. A slight color change from bright orange to orange-red occurred instantly. After stirring for 1 h at 50 °C the mixture was cooled down to rt. Chloroform and water were added and the layers separated. The aqueous layer was extracted two times with chloroform and the combined organic phases were washed with water four times. After drying the organic phases over Na_2SO_4, the solvent was evaporated. The resulting solid was dissolved in 20 mL of dry THF and transferred into a *Schlenk* tube. Copper powder (10 mg, 0.16 mmol, 1 eq) and the respective **TPA** azide compound (0.32 mmol, 2 eq) were added and the mixture was degassed by four cycles of freeze-pump-thaw. $[Cu(MeCN)_4]PF_6$

(59 mg, 0.16 mmol, 1 eq) was added under a constant stream of argon. The *Schlenk* tube was sealed and the mixture heated to 45 °C for 68 h. The solution was diluted by addition of chloroform and washed three times with water to dissolve any gel-like particles. The organic phase was dried over Na_2SO_4 and passed over a short aluminium oxide column to remove residual copper salts. The crude polymer product was collected by precipitation in MeOH and purified by *Soxhlet* extraction with MeOH, EtOAc and $CHCl_3$. The chloroform fraction was collected. Residual small molecule impurities were separated by preparative SEC.

PT-TPA:

Yield: 55 mg.

^{1}H-NMR (250 MHz, $CDCl_3$): δ[ppm] = 7.69-7.48 (br), 7.26-6.98 (br), 3.41 (br), 3.22 (br), 2.78 (br), 1.68 (br), 1.35 (br), 0.91 (br).

^{13}C-NMR (63 MHz, $CDCl_3$): δ[ppm] = 148.36, 147.28, 140.04, 133.83, 131.33, 129.61, 128.76, 124.94, 123.78, 123.47, 121.71, 31.85, 30.66, 29.61, 29.41, 22.80, 14.29.

SEC (THF, PS standards): $\overline{M_n}$ = 21000 g/mol, $\overline{M_w}$ = 26000 g/mol, PDI = 1.2.

EA: [%] calcd for quantitative functionalization: C, 72.63; H, 6.76; N, 6.05; S, 13.85; Br, 0.71; found C, 71.13; H, 6.77; N, 5.97; S, 13.01.

PT-spTPA:

Yield: 75 mg.

^{1}H-NMR (250 MHz, $CDCl_3$): δ[ppm] = 7.39 (br), 7.17 (br), 6.98 (br), 4.28 (br), 3.14 (br), 2.79 (br), 2.25 (br), 1.86 (br), 1.68 (br), 1.34 (br), 0.90 (br).

^{13}C-NMR (63 MHz, $CDCl_3$): δ[ppm] = 147.87, 140.07, 129.29, 128.75, 125.14, 123.82, 122.58, 121.21, 31.85, 30.67, 29.62, 29.42, 22.81, 14.29.

SEC (THF, PS standards): Batch 1 (3HT/3TBT = 73/27): $\overline{M_n}$ = 24500 g/mol, $\overline{M_w}$ = 30500 g/mol, PDI = 1.2; Batch 2 (3HT/3TBT = 91/9): $\overline{M_n}$ = 28500 g/mol, $\overline{M_w}$ = 48500 g/mol, PDI = 1.7.

4-(4-(2-(2,5-Dibromothiophen-3-yl)ethyl)-1H-1,2,3-triazol-1-yl)-N,N-diphenylaniline (T-TPA)

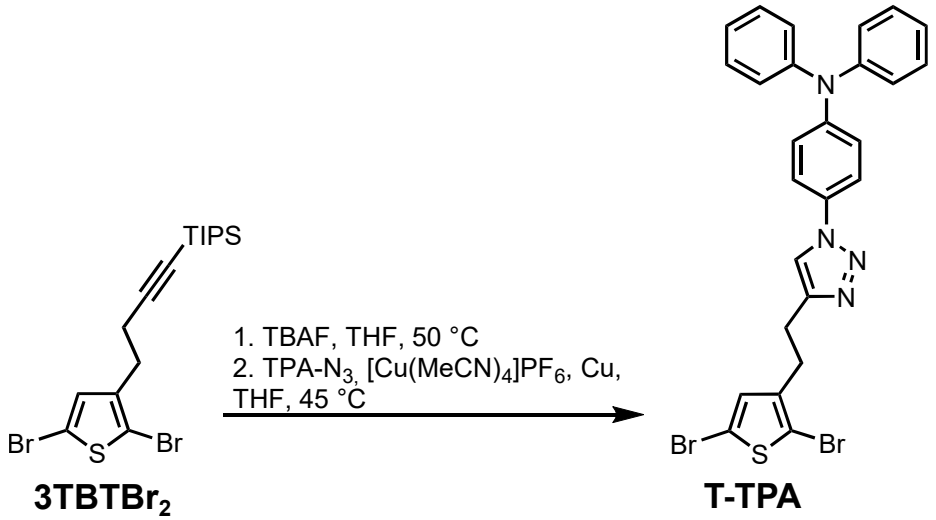

[4-(2,5-Dibromothiophen-3-yl)-but-1-inyl]-triisopropylsilane (**3TBTBr$_2$**, 280 mg, 0.62 mmol, 1 eq) was dissolved in 10 mL of dry THF and TBAF solution (1.0 M in THF, 3.1 mL, 3.1 mmol, 5 eq) was added. The mixture was heated to 50 °C for 2 h and cooled down to rt. The solution was diluted with $CHCl_3$ and washed four times with water. The organic phase was dried over Na_2SO_4 and the solvent removed *in vacuo*. The residue was dissolved in 10 mL of dry THF. 4-Azidotriphenylamine (**TPA-N$_3$**, 194 mg, 0.68 mmol, 1.1 eq) and copper powder (20 mg, 0.31 mmol, 0.5 eq) were added and the solution was degassed by four cycles of freeze-pump-thaw. $[Cu(MeCN)_4]PF_6$ (115 mg, 0.31 mmol, 0.5 eq) was added under argon, the vial was sealed and the mixture heated to 45 °C for 24 h. The copper catalyst was removed by filtration over basic aluminium oxide. The crude product was further purified by column chromatography on silica. First a solvent mixture of cyclohexane:CH_2Cl_2 = 1:1 was used to wash several side products from the column while the strongly fluorescent model compound **T-TPA** was found to elute very slowly. The solvent was then changed to 100% CH_2Cl_2 to isolate the title compound.

Yield: 267 mg (0.46 mmol, 74%).

^{1}H-NMR (250 MHz, CD_2Cl_2): δ[ppm] = 7.61 (s, 1H), 7.51 (d, J = 9.4 Hz, 2H), 7.34-7.27 (m, 4H), 7.16-7.05 (m, 8H), 6.86 (s, 1H), 3.07-2.92 (m, 4H).

^{13}C-NMR (63 MHz, $CDCl_3$): δ[ppm] = 148.49, 147.30, 146.95, 141.46, 131.28, 131.16, 130.98, 129.83, 129.41, 125.22, 124.76, 124.08, 123.64, 123.28, 122.50, 121.83, 121.68, 121.05, 120.25, 119.44, 118.65, 110.89, 109.02, 29.32, 25.79.

HRMS (ESI$^+$): calcd for $[M+Na]^+$ m/z = 600.9668, found m/z = 600.9677.

EA: [%] calcd for $C_{26}H_{20}Br_2N_4S$: C, 53.81; H, 3.47; N, 9.65; S, 5.52; Br, 27.54; found C, 53.00; H, 3.44; N, 9.35; S, 5.32.

7.2.5 Mannose-functionalized Polythiophenes

3'-Bromopropyl-2,3,4,6-tetra-O-acetyl-α-D-mannopyranoside (Man-OAc$_4$-PrBr)

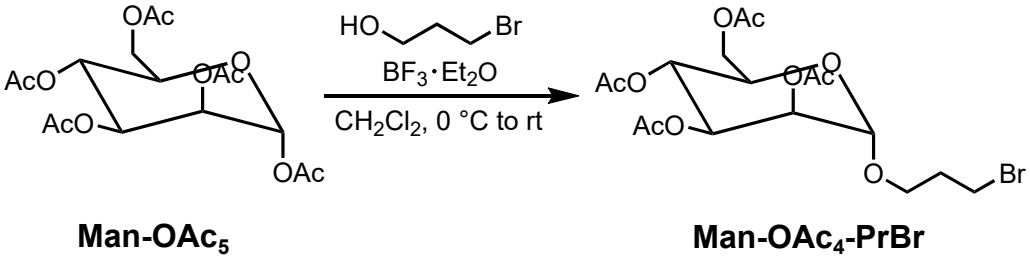

Man-OAc$_5$ **Man-OAc$_4$-PrBr**

1,2,3,4,6-Penta-O-acetyl-α-D-mannose (**Man-OAc$_5$**, 4.68 g, 12.0 mmol, 1 eq) and 3-bromopropanol (1.63 mL, 18.0 mmol, 1.5 eq) were dissolved in 50 mL of dry dichloromethane at 0 °C under argon. $BF_3{\cdot}Et_2O$ (4.43 mL, 35.9 mmol, 3 eq) was added slowly *via* syringe. The mixture was stirred at rt for 16 h and poured into an excess of 5% aqueous $NaHCO_3$ solution. The layers were separated, the organic layer was washed with $NaHCO_3$ solution and water, dried and the solvent evaporated. The residue was purified by column chromatography (silica, petroleum ether:EtOAc = 1:1) to obtain the product **Man-OAc$_4$-PrBr** as a pale yellow oil.

Yield: 2.43 g (5.2 mmol, 43%).

^{1}H-NMR (250 MHz, $CDCl_3$): δ[ppm] = 5.34-5.27 (m, 2H), 5.25-5.23 (m, 1H), 4.83 (d, J = 1.6 Hz, 1H), 4.29 (dd, J = 12.2 Hz, 5.3 Hz, 1H), 4.13 (dd, J = 12.3 Hz, 2.4 Hz, 1H), 4.04-3.97 (m, 1H), 3.95-3.86 (m, 1H), 3.62-3.50 (m, 3H), 2.18-2.07 (m, 2H), 2.16 (s, 3H), 2.11 (s, 3H), 2.05 (s, 3H), 2.00 (s, 3H).

^{13}C-NMR (63 MHz, $CDCl_3$): δ[ppm] = 170.81, 170.22, 170.08, 169.87, 97.79, 69.62, 69.20, 68.81, 66.18, 65.65, 62.57, 32.12, 30.62, 21.04, 20.92, 20.86, 20.84.

HRMS (ESI$^+$): calcd for $[M+Na]^+$ m/z = 491.0523, found m/z = 491.0541.

3'-Azidopropyl-2,3,4,6-tetra-O-acetyl-α-D-mannopyranoside (Man-OAc$_4$-PrN$_3$)

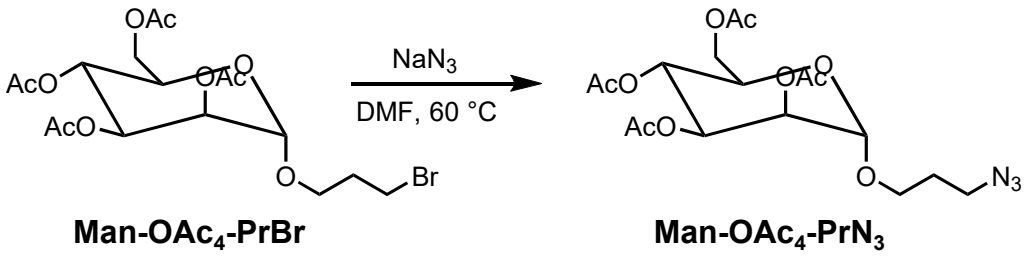

Man-OAc$_4$-PrBr **Man-OAc$_4$-PrN$_3$**

3'-Bromopropyl-2,3,4,6-tetra-O-acetyl-α-D-mannopyranoside (**Man-OAc$_4$-PrBr**, 2.20 g, 4.7 mmol, 1 eq) was dissolved in 40 mL of anhydrous DMF inside a glove box and NaN_3 (1.52 g, 23.5 mmol, 5 eq) was added. The mixture was stirred at 60 °C overnight upon which NaBr precipitated and then cooled to rt. Most of the solvent was evaporated and the residue dissolved in CH_2Cl_2. The organic phase was washed five times with water, dried and the solvent removed *in vacuo*. The residue was further purified by column chromatography (silica, petroleum ether:EtOAc = 1:1) to obtain the title compound **Man-OAc$_4$-PrN$_3$** as a white solid.

Yield: 1.78 g (4.1 mmol, 87%).

^{1}H-NMR (250 MHz, $CDCl_3$): δ[ppm] = 5.35-5.27 (m, 2H), 5.25-5.23 (m, 1H), 4.81 (d, J = 1.5 Hz, 1H), 4.28 (dd, J = 12.2 Hz, 5.4 Hz, 1H), 4.12 (dd, J = 12.3 Hz, 2.5 Hz, 1H), 4.00-3.94 (m, 1H), 3.86-3.77 (m, 1H), 3.57-3.48 (m, 1H), 3.43 (t, J = 6.5 Hz, 2H), 2.16 (s, 3H), 2.11 (s, 3H), 2.05 (s, 3H), 2.00 (s, 3H), 1.95-1.85 (m, 2H).

^{13}C-NMR (63 MHz, $CDCl_3$): δ[ppm] = 170.77, 170.20, 170.06, 169.87, 97.77, 69.62, 69.15, 68.78, 66.25, 64.98, 62.62, 48.22, 28.77, 21.04, 20.87, 20.85, 20.84.

HRMS (ESI$^+$): calcd for $[M+Na]^+$ m/z = 454.1432, found m/z = 454.1416.

IR (ATR): $\tilde{\nu}$[cm^{-1}] = 2106 (N_3), 1732 (C=O).

3'-Azidopropyl-α-D-mannopyranoside (Man-PrN$_3$)

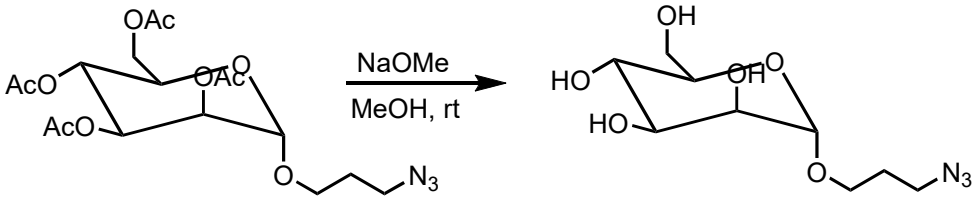

Man-OAc$_4$-PrN$_3$ **Man-PrN$_3$**

For deprotection of the alcohol groups 3'-azidopropyl-2,3,4,6-tetra-O-acetyl-α-D-mannopyranoside (**Man-OAc$_4$-PrN$_3$**, 500 mg, 1.2 mmol, 1 eq) was dissolved in 7 mL of dry MeOH and treated with a solution of NaOMe in dry MeOH (0.87 M, prepared from 200 mg Na and 10 mL MeOH, 0.5 mL, 0.4 mmol, 0.33 eq). The mixture was stirred for 30 min at rt and then acidified to pH~6 by adding an excess of ion exchange resin (*Dowex Marathon C*, H^+ form). The resin was filtered off and the title compound **Man-PrN$_3$** was obtained as a highly viscous, colorless oil by evaporation of the solvent.

Yield: 278 mg (1.1 mmol, 92%).

^{1}H-NMR (250 MHz, MeOD): δ[ppm] = 4.75 (d, J = 1.6 Hz, 1H), 3.87-3.79 (m, 3H), 3.74-3.69 (m, 1H), 3.67-3.66 (m, 1H), 3.64-3.57 (m, 1H), 3.54-3.46 (m, 2H), 3.44-3.38 (m, 2H), 1.91-1.81 (m, 2H).

^{13}C-NMR (63 MHz, MeOD): δ[ppm] = 101.66, 74.74, 72.62, 72.16, 68.56, 65.37, 62.90, 49.55, 29.94.

HRMS (ESI$^-$): calcd for [M-H]$^-$ m/z = 262.1045, found m/z = 262.1037.

IR (ATR): $\tilde{\nu}$[cm^{-1}] = 3367 (OH), 2098 (N_3).

2-(2-(2-Iodoethoxy)ethoxy)ethan-1-ol (I-OEG-OH)

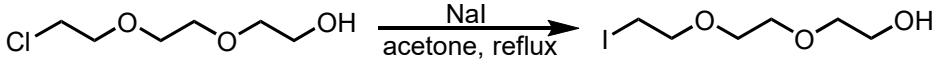

Cl-OEG-OH **I-OEG-OH**

2-(2-(2-Chloroethoxy)ethoxy)ethan-1-ol (**Cl-OEG-OH**, 5.00 g, 29.7 mmol, 1 eq) was dissolved in 33 mL of acetone and sodium iodide dihydrate (27.65 g, 148.7 mmol, 5 eq) was added. The mixture was heated to reflux for 24 h and then allowed to cool to rt. The solvent was removed *in vacuo* and the residue was taken up in water and extracted three times with Et_2O (15 mL). The organic layers were dried over $MgSO_4$, filtered and evaporated to dryness to yield the product **I-OEG-OH** which was used in the next step without further purification.

Yield: 7.18 g (27.6 mmol, 93%).
^{1}H-NMR (250 MHz, $CDCl_3$): δ[ppm] = 3.80-3.61 (m, 10H), 3.27 (t, J = 6.8 Hz, 2H), 2.26 (t, J = 6.1 Hz, 1H).

3'-(2-(2-(2-Azidoethoxy)ethoxy)ethoxy)-α-D-mannopyranoside (Man-OEGN_3)

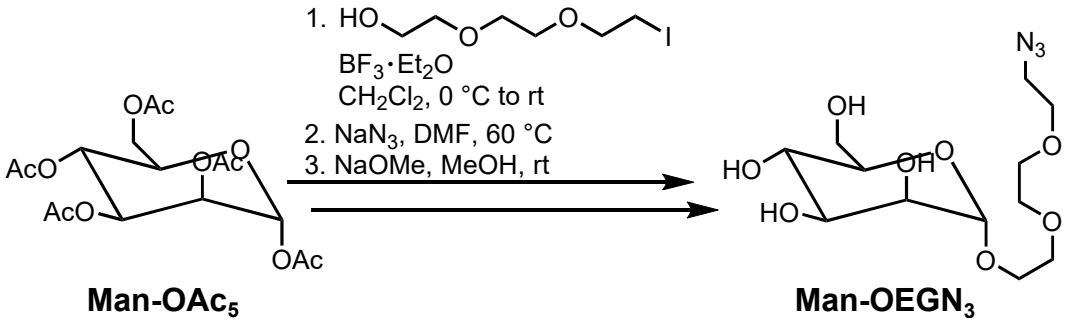

Attachment of 2-(2-(2-iodoethoxy)ethoxy)ethan-1-ol (**I-OEG-OH**) to 1,2,3,4,6-penta-O-acetyl-α-D-mannose (**Man-OAc$_5$**), iodide-azide exchange and deprotection of the alcohol groups were carried out in a three-step reaction sequence under similar conditions to the synthesis of 3'-azidopropyl-α-D-mannopyranoside (**Man-PrN_3**).

3'-(2-(2-(2-Iodoethoxy)ethoxy)ethoxy)-2,3,4,6-tetra-O-acetyl-α-D-mannopyranoside (Man-OAc$_4$-OEGI):
Yield: 1.68 g (2.9 mmol, 57%).
^{1}H-NMR (250 MHz, $CDCl_3$): δ[ppm] = 5.39-5.34 (m, 1H), 5.32-5.25 (m, 2H), 4.88 (d, J = 1.6 Hz, 1H), 4.30 (dd, J = 12.4 Hz, 5.2 Hz, 1H), 4.13-4.03 (m, 2H), 3.87-3.66 (m, 10H), 3.27 (t, J = 6.8 Hz, 2H), 2.16 (s, 3H), 2.10 (s, 3H), 2.04 (s, 3H), 1.99 (s, 3H).
^{13}C-NMR (63 MHz, $CDCl_3$): δ[ppm] = 170.82, 170.19, 170.94, 169.86, 97.87, 72.11, 70.86, 70.37, 70.22, 69.73, 69.21, 68.55, 67.56, 66.30, 62.57, 21.06, 20.93, 20.90, 20.84, 3.12.
HRMS (ESI$^+$): calcd for $[M+Na]^+$ m/z = 613.0752, found m/z = 613.0740.
3'-(2-(2-(2-Azidoethoxy)ethoxy)ethoxy)-2,3,4,6-tetra-O-acetyl-α-D-mannopyranoside (Man-OAc$_4$-OEGN_3):
Yield: 1.33 g (2.6 mmol, 88%).
^{1}H-NMR (250 MHz, $CDCl_3$): δ[ppm] = 5.39-5.34 (m, 1H), 5.32-5.24 (m, 2H), 4.87 (d, J = 1.4 Hz, 1H), 4.29 (dd, J = 12.5 Hz, 5.2 Hz, 1H), 4.12-4.03 (m, 2H), 3.87-3.65 (m, 10H), 3.40 (t, J = 5.1 Hz, 2H), 2.15 (s, 3H), 2.10 (s, 3H), 2.04 (s, 3H), 1.99 (s, 3H).
^{13}C-NMR (63 MHz, $CDCl_3$): δ[ppm] = 170.84, 170.19, 170.04, 169.87, 97.86, 70.94, 70.84, 70.24, 70.20, 69.71, 69.21, 68.54, 67.55, 66.29, 62.55, 50.81, 21.05, 20.90, 20.85, 20.84.

HRMS (ESI$^+$): calcd for $[M+Na]^+$ $m/z = 528.1800$, found $m/z = 528.1804$.

3'-(2-(2-(2-Azidoethoxy)ethoxy)ethoxy)-α-D-mannopyranoside (Man-OEGN$_3$):

Yield: 563 mg (1.7 mmol, 76%).

^{1}H-NMR (250 MHz, MeOD): δ[ppm] = 4.80 (d, J = 1.6 Hz, 1H), 3.88-3.81 (m, 3H), 3.78-3.53 (m, 13H), 3.38 (t, J = 5.0 Hz, 2H).

^{13}C-NMR (63 MHz, MeOD): δ[ppm] = 101.75, 74.60, 72.56, 72.12, 71.71, 71.55, 71.44, 71.21, 68.59, 67.78, 62.93, 51.76.

HRMS (ESI$^+$): calcd for $[M+Na]^+$ $m/z = 360.1377$, found $m/z = 360.1379$.

IR (ATR): $\tilde{\nu}$[cm^{-1}] = 3392 (OH), 2108 (N_3), 1080 (C-O).

Polymer analogous functionalization for PT-Man

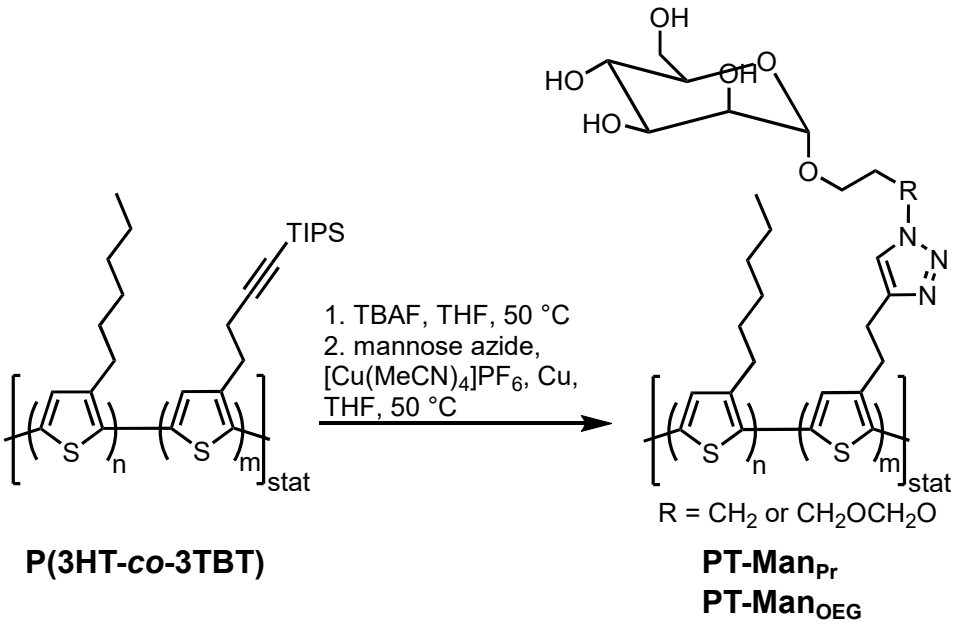

P(3HT-*co*-3TBT) (67/33 mol%, 100 mg, 0.16 mmol of alkyne groups, 1 eq) was dissolved in 20 mL of dry THF and a solution of TBAF (1.0 M in THF, 0.8 mL, 0.8 mmol, 5 eq) was added. The solution was stirred at 50 °C for 1 h, cooled to rt and diluted with water and $CHCl_3$. The layers were separated and the organic layer was washed with water and brine, dried over $MgSO_4$ and the solvent was removed *in vacuo*. The residue was dissolved in 20 mL of anhydrous THF, transferred to a *Schlenk* tube and Cu powder (10 mg, 0.16 mmol, 1 eq) as well as 3'-azidopropyl-α-D-mannopyranoside (**Man-PrN$_3$**, 64 mg, 0.24 mmol, 1.5 eq) were added. The mixture was degassed by several cycles of freeze-pump-thaw and $[Cu(MeCN)_4]PF_6$ (60 mg, 0.16 mmol, 1 eq) was added under a stream of argon. The

Schlenk tube was sealed and heated to 50 °C for 3 d. The solvent was evaporated and MeOH was added to the flask. The solid polymer **PT-Man$_{Pr}$** was scratched from the wall of the flask under MeOH, collected by filtration and further purified by *Soxhlet* extraction with MeOH and EtOAc. The dried product was found to be only soluble in 2:1 to 1:1 mixtures of *ortho*-dichlorobenzene and DMSO. Ultrasonication at 80 °C was needed to dissolve the main part of the polymer and residual insoluble material was removed by filtration of the solution before film deposition.

Yield: 73 mg.

IR (ATR): $\tilde{\nu}$[cm^{-1}] = 3367 (OH).

EA: [%] calcd for quantitative functionalization: C, 60.82; H, 7.13; N, 5.75; O, 13.14; S, 13.16; found C, 46.79; H, 5.59; N, 3.83; S, 13.18.

Functionalization with 3'-(2-(2-(2-azidoethoxy)ethoxy)ethoxy)-α-D-mannopyranoside (**Man-OEGN$_3$**, 132 mg, 0.4 mmol, 1.5 eq) was carried out under similar conditions with **P(3HT-*co*-3TBT)** (73/27 mol%, 200 mg, 0.26 mmol of alkyne groups, 1 eq). The product **PT-Man$_{OEG}$** was fully soluble in 5:1 mixtures of *ortho*-dichlorobenzene and DMSO at rt.

Yield: 21 mg.

^{1}H-NMR (250 MHz, *o*DCB-d4:DMSO-d6 = 5:1): δ[ppm] = 7.19 (br), 5.28-3.16 (m), 3.56 (br), 2.90 (br), 1.73 (br), 1.42 (br), 1.27 (br), 0.88 (br).

IR (ATR): $\tilde{\nu}$[cm^{-1}] = 3311 (OH).

List of Abbreviations

$\overline{M_n}$	Number-average Molecular Weight
$\overline{M_w}$	Weight-average Molecular Weight
*o*DCB	*ortho*-Dichlorobenzene
1-CN	1-Chloronapthalene
2PP	Two-point Probe
3HT	3-Hexylthiophene
3T	2,2':3',2"-Terthiophene
3TBT	(4-(thiophen-3-yl)-but-1-inyl)-triisopropylsilane
4PP	Four-point Probe
AFM	Atomic Force Microscopy
ATR	Attenuated Total Reflection
CB	Chlorobenzene
CDSA	Crystallization-driven Self-assembly
CI	Chemical Ionization
Con A	Concanavalin A
CP	Conjugated/Conducting Polymer
CPE	Conjugated Polyelectrolyte
CRP	Conjugated/Conducting Redox Polymer
CuAAC	Copper(I) Catalyzed Alkyne-Azide Cycloaddition
CV	Cyclic Voltammetry
D_3	Hexamethylcyclotrisiloxane
DCTB	*trans*-2-(3-(4-*tert*-Butylphenyl)-2-methyl-2-propenylidene)malononitrile
DIPEA	N,N-diisopropylethylamine
DMAc	Dimethylacetamide
dppp	1,3-Bis(diphenylphosphino)propane
DSC	Differential Scanning Calorimetry
EA	Elemental Analysis
EGOFET	Electrolyte-gated Organic Field Effect Transistor
EI	Electron Impact (Ionization)
EPR	Electron Paramagnetic Resonance (Spectroscopy)
eq	Equivalents
EQCM	Electrochemical Quartz Crystal Microbalance
EQE	External Quantum Efficiency
ESI	Electrospray Ionization

F_4TCNQ	2,3,5,6-Tetrafluoro-7,7,8,8-tetracyanoquinodimethane
Fc	Ferrocene
FRET	Förster Resonance Energy Transfer
GRIM	Grignard Metathesis (Polymerization)
HH	Head-to-Head
HOMO	Highest Occupied Molecular Orbital
HSA	Human Serum Albumin
HT	Head-to-Tail
HTL	Hole-transport Layer
IR	Infrared (Spectroscopy)
ITO	Indium Tin Oxide
KCTP	Kumada Chain Transfer Polymerization
LCAO	Linear Combination of Atomic Orbitals
LPS	Lipopolysaccharide
LUMO	Lowest Unoccupied Molecular Orbital
MALDI-TOF	Matrix Assisted Laser Desorption Ionization Time of Flight
MISFET	Metal-Insulator-Semiconductor Field Effect Transistor
MS	Mass Spectrometry
NIR	Near Infrared
NMR	Nuclear Magnetic Resonance (Spectroscopy)
ODTS	Octadecyltrichlorosilane
OECT	Organic Electrochemical Transistor
OFET	Organic Field Effect Transistor
OLED	Organic Light Emitting Diode
OPV	Organic Photovoltaics
OSC	Organic Semiconductor, Organic Solar Cell
P3AT	Poly(3-alkylthiophene)
P3BrHT	Poly(3-(6-bromohexyl)thiophene)
P3HT	Poly(3-hexylthiophene)
P3TCxCy	Alkylthiophene-substituted polythiophenes, x and y denote the alkyl chain branch lengths
PAc	Polyacetylene
PANI	Polyaniline
PBS	Phosphate-buffered saline
PCBM	Phenyl-C61-butyric acid methyl ester
PCE	Power Conversion Efficiency

PDI ..... Polydispersity Index
PDMS ..... Poly(dimethylsiloxane)
PEDOT ..... Poly(3,4-ethylenedioxythiophene)
PF ..... Polyfluorene
PL ..... Photoluminescence
PPP ..... Poly(*para*-phenylene)
PPV ..... Poly(*para*-phenylene vinylene)
PPy ..... Polypyrrole
PSS ..... Poly(styrene sulfonate)
PT ..... Polythiophene
PT-Man ..... α-D-mannosyl-functionalized Polythiophenes
PT-spTPA ..... TPA-functionalized Polythiophene, with alkyl spacer
PT-TPA ..... TPA-functionalized Polythiophene, without alkyl spacer
PTIm-Br ..... Poly(3-(6-(1-methylimidazolium-3-yl)hexyl)thiophene-2,5-diyl), bromide salt
PTS-TBA ..... Poly(6-(thiophene-3-yl)hexane-1-sulfonate), tetrabutylammonium salt
RFID ..... Radio-Frequency Identification
SEC ..... Size Exclusion Chromatography
TBAF ..... Tetrabutylammonium fluoride
TCB 1,2,4-Trichlorobenzene
TEM ..... Transmission Electron Microscopy
TEMPO 2,2,6,6-Tetramethylpiperidinyloxyl
TGA ..... Thermogravimetric Analysis
TIPS ..... Triisopropylsilyl
TLC ..... Thin Layer Chromatography
TPA ..... Triphenylamine
TPB ..... Tetraphenylbenzidine
TT ..... Tail-to-Tail
UV/Vis ..... Ultraviolet/Visible Light (Spectroscopy)
WAXS ..... Wide Angle X-ray Scattering
XRD ..... X-ray Diffraction

Bibliography

[1] T. A. Skotheim, J. R. Reynolds, *Handbook of Conducting Polymers*, CRC Press, **2007**.

[2] D. S. Chung, D. H. Lee, J. W. Park, J. Jang, S. Nam, Y.-H. Kim, S.-K. Kwon, C. E. Park, *Org. Electron.* **2009**, *10*, 1041.

[3] J. Qian, X. Li, D. J. Lunn, J. Gwyther, Z. M. Hudson, E. Kynaston, P. A. Rupar, M. A. Winnik, I. Manners, *J. Am. Chem. Soc.* **2014**, *136*, 4121.

[4] T. V. Richter, PhD thesis, University of Freiburg, Germany, **2011**.

[5] T. V. Richter, C. H. Braun, S. Link, M. Scheuble, E. J. W. Crossland, F. Stelzl, U. Würfel, S. Ludwigs, *Macromolecules* **2012**, *45*, 5782.

[6] M. Scheuble, PhD thesis, University of Stuttgart, Germany, **2015**.

[7] M. Scheuble, Y. M. Gross, D. Trefz, M. Brinkmann, J. T. López Navarrete, M. C. Ruiz Delgado, S. Ludwigs, *Macromolecules* **2015**, *48*, 7049.

[8] B. Liu, G. C. Bazan, *Conjugated Polyelectrolytes*, Wiley-VCH Verlag GmbH & Co. KGaA, **2012**.

[9] J. C. Brendel, M. M. Schmidt, G. Hagen, R. Moos, M. Thelakkat, *Chem. Mater.* **2014**, *26*, 1992.

[10] D. Bondarev, J. Zedník, I. Šloufová, A. Sharf, M. Procházka, J. Pfleger, J. Vohlídal, *J. Polym. Sci. Part A Polym. Chem.* **2010**, *48*, 3073.

[11] R. Merkle, P. Gutbrod, P. Reinold, M. Katzmaier, R. Tkachov, J. Maier, S. Ludwigs, *Polymer* **2017**, *132*, 216.

[12] T. L. Benanti, A. Kalaydjian, D. Venkataraman, *Macromolecules* **2008**, *41*, 8312.

[13] P. Reinold, K. Bruchlos, S. Ludwigs, *Polym. Chem.* **2017**, *8*, 7351.

[14] K.-Y. Pu, J. Shi, L. Wang, L. Cai, G. Wang, B. Liu, *Macromolecules* **2010**, *43*, 9690.

[15] H. Toss, C. Suspène, B. Piro, A. Yassar, X. Crispin, L. Kergoat, M.-C. Pham, M. Berggren, *Org. Electron.* **2014**, *15*, 2420.

[16] N. Armaroli, V. Balzani, *Energy Environ. Sci.* **2011**, *4*, 3193.

[17] N. Armaroli, V. Balzani, *Angew. Chemie Int. Ed.* **2007**, *46*, 52.

[18] K. B. Tokarska, N. P. Gillett, A. J. Weaver, V. K. Arora, M. Eby, *Nat. Clim. Change* **2016**, *6*, 851.

[19] M. Z. Jacobson, *Energy Environ. Sci.* **2009**, *2*, 148.

[20] P. Gerland, A. E. Raftery, H. Ševčíková, N. Li, D. Gu, T. Spoorenberg, L. Alkema, B. K. Fosdick, J. Chunn, N. Lalic, G. Bay, T. Buettner, G. K. Heilig, J. Wilmoth, *Science* **2014**, *346*, 234.

[21] M. Ivanova, *Glob. Policy* **2016**, *7*, 411.

[22] P. Poizot, F. Dolhem, *Energy Environ. Sci.* **2011**, *4*, 2003.

[23] R. R. Søndergaard, M. Hösel, F. C. Krebs, *J. Polym. Sci. Part B Polym. Phys.* **2013**, *51*, 16.

[24] T. Song, W. Rim, S. Park, Y. Kim, G. Yang, H. Kim, S. Baek, J. Jung, B. Kwon, S. Cho, H. Jung, Y. Choo, J. Choi, *IEEE J. Solid-State Circuits* **2017**, *52*, 240.

[25] W. J. Parak, F. C. Simmel, A. W. Holleitner, *Nanotechnology*, Wiley-VCH Verlag GmbH & Co. KGaA, **2010**.

[26] T. Ito, H. Shirakawa, S. Ikeda, *J. Polym. Sci. Polym. Chem. Ed.* **1974**, *12*, 11.

[27] H. Shirakawa, E. J. Louis, A. G. MacDiarmid, C. K. Chiang, A. J. Heeger, *J. Chem. Soc. Chem. Commun.* **1977**, 578.

[28] C. K. Chiang, C. R. Fincher, Y. W. Park, A. J. Heeger, H. Shirakawa, E. J. Louis, S. C. Gau, A. G. MacDiarmid, *Phys. Rev. Lett.* **1977**, *39*, 1098.

[29] C. K. Chiang, M. A. Druy, S. C. Gau, A. J. Heeger, E. J. Louis, A. G. MacDiarmid, Y. W. Park, H. Shirakawa, *J. Am. Chem. Soc.* **1978**, *100*, 1013.

[30] Y. Chujo, *Conjugated Polymer Synthesis*, Wiley-VCH Verlag GmbH & Co. KGaA, **2010**.

[31] M. Rehahn, *Chemie unserer Zeit* **2003**, *37*, 18.

[32] R. S. Mulliken, *Science* **1967**, *157*, 13.

[33] P. A. Cox, *The Electronic Structure of Solids*, Oxford University Press, **1987**.

[34] H. Shirakawa, T. Ito, S. Ikeda, *Makromol. Chem.* **1978**, *179*, 1565.

[35] W. Tremel, R. Seshadri, E. Finckh, *Chemie unserer Zeit* **2001**, *35*, 42.

[36] S. Roth, H. Bleier, *Adv. Phys.* **1987**, *36*, 385.

[37] J. Heinze, B. A. Frontana-Uribe, S. Ludwigs, *Chem. Rev.* **2010**, *110*, 4724.

[38] J. L. Bredas, G. B. Street, *Acc. Chem. Res.* **1985**, *18*, 309.

[39] D. Ofer, R. M. Crooks, M. S. Wrighton, *J. Am. Chem. Soc.* **1990**, *112*, 7869.

[40] I. E. Jacobs, E. W. Aasen, J. L. Oliveira, T. N. Fonseca, J. D. Roehling, J. Li, G. Zhang, M. P. Augustine, M. Mascal, A. J. Moulé, *J. Mater. Chem. C* **2016**, *4*, 3454.

[41] P. Pingel, D. Neher, *Phys. Rev. B* **2013**, *87*, 115209.

[42] W. Gao, A. Kahn, *Appl. Phys. Lett.* **2001**, *79*, 4040.

[43] J. B. Torrance, J. J. Mayerle, K. Bechgaard, B. D. Silverman, Y. Tomkiewicz, *Phys. Rev. B* **1980**, *22*, 4960.

[44] D. A. Dixon, J. C. Calabrese, J. S. Miller, *J. Phys. Chem.* **1989**, *93*, 2284.

[45] F. Jäckel, U. G. E. Perera, V. Iancu, K.-F. Braun, N. Koch, J. P. Rabe, S.-W. Hla, *Phys. Rev. Lett.* **2008**, *100*, 126102.

[46] D. T. Duong, C. Wang, E. Antono, M. F. Toney, A. Salleo, *Org. Electron.* **2013**, *14*, 1330.

[47] D. T. Scholes, S. A. Hawks, P. Y. Yee, H. Wu, J. R. Lindemuth, S. H. Tolbert, B. J. Schwartz, *J. Phys. Chem. Lett.* **2015**, *6*, 4786.

[48] C. M. Cardona, W. Li, A. E. Kaifer, D. Stockdale, G. C. Bazan, *Adv. Mater.* **2011**, *23*, 2367.

[49] G. Zotti, *Synth. Met.* **1998**, *97*, 267.

[50] R. R. Chance, J. L. Brédas, R. Silbey, *Phys. Rev. B* **1984**, *29*, 4491.

[51] L. Beverina, G. A. Pagani, M. Sassi, *Chem. Commun.* **2014**, *50*, 5413.

[52] C. Enengl, S. Enengl, S. Pluczyk, M. Havlicek, M. Lapkowski, H. Neugebauer, E. Ehrenfreund, *ChemPhysChem* **2016**, *17*, 3830.

[53] J. Yamamoto, Y. Furukawa, *J. Phys. Chem. B* **2015**, *119*, 4788.

[54] M. Skompska, A. Szkurłat, *Electrochim. Acta* **2001**, *46*, 4007.

[55] W. Ten Hoeve, H. Wynberg, E. E. Havinga, E. W. Meijer, *J. Am. Chem. Soc.* **1991**, *113*, 5887.

[56] J. Lawrence, E. Goto, J. M. Ren, B. McDearmon, D. S. Kim, Y. Ochiai, P. G. Clark, D. Laitar, T. Higashihara, C. J. Hawker, *J. Am. Chem. Soc.* **2017**, *139*, 13735.

[57] S. Ludwigs, *P3HT Revisited - From Molecular Scale to Solar Cell Devices*, Springer, **2014**.

[58] S. Samitsu, T. Shimomura, S. Heike, T. Hashizume, K. Ito, *Macromolecules* **2008**, *41*, 8000.

[59] T. Adachi, J. Brazard, R. J. Ono, B. Hanson, M. C. Traub, Z.-Q. Wu, Z. Li, J. C. Bolinger, V. Ganesan, C. W. Bielawski, D. A. Vanden Bout, P. F. Barbara, *J. Phys. Chem. Lett.* **2011**, *2*, 1400.

[60] M. Trznadel, A. Pron, M. Zagorska, R. Chrzaszcz, J. Pielichowski, *Macromolecules* **1998**, *31*, 5051.

[61] C. Yang, F. P. Orfino, S. Holdcroft, *Macromolecules* **1996**, *29*, 6510.

[62] F. C. Spano, J. Clark, C. Silva, R. H. Friend, *J. Chem. Phys.* **2009**, *130*.

[63] F. C. Spano, C. Silva, *Annu. Rev. Phys. Chem.* **2014**, *65*, 477.

[64] R. R. Schaller, *IEEE Spectr.* **1997**, *34*, 52.

[65] H. Klauk, *Chem. Soc. Rev.* **2010**, *39*, 2643.

[66] M. C. Hamilton, S. Martin, J. Kanicki, *Chem. Mater.* **2004**, *16*, 4699.

[67] H. Sirringhaus, P. J. Brown, R. H. Friend, M. M. Nielsen, K. Bechgaard, B. M. W. Langeveld-Voss, A. J. H. Spiering, R. A. J. Janssen, E. W. Meijer, P. Herwig, D. M. de Leeuw, *Nature* **1999**, *401*, 685.

[68] A. Babel, S. A. Jenekhe, *Synth. Met.* **2005**, *148*, 169.

[69] H. Koezuka, A. Tsumura, T. Ando, *Synth. Met.* **1987**, *18*, 699.

[70] H.-R. Tseng, H. Phan, C. Luo, M. Wang, L. A. Perez, S. N. Patel, L. Ying, E. J. Kramer, T.-Q. Nguyen, G. C. Bazan, A. J. Heeger, *Adv. Mater.* **2014**, *26*, 2993.

[71] J. E. Mark, *Polymer Data Handbook*, Oxford University Press, **1999**.

[72] M. P. Walser, W. L. Kalb, T. Mathis, B. Batlogg, *Appl. Phys. Lett.* **2009**, *95*, 233301.

[73] U. Zschieschang, F. Letzkus, J. N. Burghartz, H. Klauk, *IEEE Trans. Nanotechnol.* **2017**, *16*, 837.

[74] A. Facchetti, *Mater. Today* **2007**, *10*, 28.

[75] C. Suspène, B. Piro, S. Reisberg, M.-C. Pham, H. Toss, M. Berggren, A. Yassar, G. Horowitz, *J. Mater. Chem. B* **2013**, *1*, 2090.

[76] B. Piro, D. Wang, D. Benaoudia, A. Tibaldi, G. Anquetin, V. Noël, S. Reisberg, G. Mattana, B. Jackson, *Biosens. Bioelectron.* **2017**, *92*, 215.

[77] T. Cramer, A. Campana, F. Leonardi, S. Casalini, A. Kyndiah, M. Murgia, F. Biscarini, *J. Mater. Chem. B* **2013**, *1*, 3728.

[78] J. Rivnay, S. Inal, A. Salleo, R. M. Owens, M. Berggren, G. G. Malliaras, *Nat. Rev. Mater.* **2018**, *3*, 17086.

[79] J. Rivnay, S. Inal, B. A. Collins, M. Sessolo, E. Stavrinidou, X. Strakosas, C. Tassone, D. M. Delongchamp, G. G. Malliaras, *Nat. Commun.* **2016**, *7*, 11287.

[80] A. Laiho, L. Herlogsson, R. Forchheimer, X. Crispin, M. Berggren, *Proc. Natl. Acad. Sci.* **2011**, *108*, 15069.

[81] J. T. Mabeck, G. G. Malliaras, *Anal. Bioanal. Chem.* **2005**, *384*, 343.

[82] Y.-J. Cheng, S.-H. Yang, C.-S. Hsu, *Chem. Rev.* **2009**, *109*, 5868.

[83] S. Allard, M. Forster, B. Souharce, H. Thiem, U. Scherf, *Angew. Chemie Int. Ed.* **2008**, *47*, 4070.

[84] M. Goll, A. Ruff, E. Muks, F. Goerigk, B. Omiecienski, I. Ruff, R. C. González-Cano, J. T. Lopez Navarrete, M. C. Ruiz Delgado, S. Ludwigs, *Beilstein J. Org. Chem.* **2015**, *11*, 335.

[85] Y. Xia, K. Sun, J. Ouyang, *Adv. Mater.* **2012**, *24*, 2436.

[86] C. Qiu, J. Wang, S. Mao, W. Guo, S. Cheng, Y. Wang, *Polym. Adv. Technol.* **2010**, *21*, 651.

[87] K. Leo, *Elementary Processes in Organic Photovoltaics*, Springer, **2017**.

[88] B. T. McGrail, A. Sehirlioglu, E. Pentzer, *Angew. Chemie Int. Ed.* **2015**, *54*, 1710.

[89] R. Kroon, D. A. Mengistie, D. Kiefer, J. Hynynen, J. D. Ryan, L. Yu, C. Müller, *Chem. Soc. Rev.* **2016**, *45*, 6147.

[90] M. Scheuble, M. Goll, S. Ludwigs, *Macromol. Rapid Commun.* **2015**, *36*, 115.

[91] Z. Zhang, J. Wang, *J. Mater. Chem.* **2012**, *22*, 4178.

[92] R. D. McCullough, *Adv. Mater.* **1998**, *10*, 93.

[93] J. Roncali, *Chem. Rev.* **1992**, *92*, 711.

[94] K. Yoshino, S. Hayashi, R.-I. Sugimoto, *Jpn. J. Appl. Phys.* **1984**, *23*, L899.

[95] T. Yamamoto, K. Sanechika, A. Yamamoto, *J. Polym. Sci. Polym. Lett. Ed.* **1980**, *18*, 9.

[96] R. L. Elsenbaumer, K. Y. Jen, R. Oboodi, *Synth. Met.* **1986**, *15*, 169.

[97] R. S. Loewe, P. C. Ewbank, J. Liu, L. Zhai, R. D. McCullough, *Macromolecules* **2001**, *34*, 4324.

[98] R. D. McCullough, R. D. Lowe, *J. Chem. Soc. Chem. Commun.* **1992**, 70.

[99] R. D. McCullough, R. D. Lowe, M. Jayaraman, D. L. Anderson, *J. Org. Chem.* **1993**, *58*, 904.

[100] I. Osaka, R. D. McCullough, *Acc. Chem. Res.* **2008**, *41*, 1202.

[101] T. A. Chen, R. D. Rieke, *J. Am. Chem. Soc.* **1992**, *114*, 10087.

[102] R. S. Loewe, S. M. Khersonsky, R. D. McCullough, *Adv. Mater.* **1999**, *11*, 250.

[103] R. H. Lohwasser, M. Thelakkat, *Macromolecules* **2011**, *44*, 3388.

[104] R. Miyakoshi, A. Yokoyama, T. Yokozawa, *J. Am. Chem. Soc.* **2005**, *127*, 17542.

[105] E. L. Lanni, A. J. McNeil, *Macromolecules* **2010**, *43*, 8039.

[106] M. P. Bhatt, H. D. Magurudeniya, P. Sista, E. E. Sheina, M. Jeffries-El, B. G. Janesko, R. D. McCullough, M. C. Stefan, *J. Mater. Chem. A* **2013**, *1*, 12841.

[107] M. C. Iovu, E. E. Sheina, R. R. Gil, R. D. McCullough, *Macromolecules* **2005**, *38*, 8649.

[108] Y. Geng, L. Huang, S. Wu, F. Wang, *Sci. China Chem.* **2010**, *53*, 1620.

[109] Y. Li, G. Vamvounis, S. Holdcroft, *Macromolecules* **2002**, *35*, 6900.

[110] X. Chen, B. Gholamkhass, X. Han, G. Vamvounis, S. Holdcroft, *Macromol. Rapid Commun.* **2007**, *28*, 1792.

[111] L. Zhai, R. L. Pilston, K. L. Zaiger, K. K. Stokes, R. D. McCullough, *Macromolecules* **2003**, *36*, 61.

[112] J. M. Lobez, T. L. Andrew, V. Bulović, T. M. Swager, *ACS Nano* **2012**, *6*, 3044.

[113] H. C. Kolb, M. G. Finn, K. B. Sharpless, *Angew. Chemie Int. Ed.* **2001**, *40*, 2004.

[114] V. V. Rostovtsev, L. G. Green, V. V. Fokin, K. B. Sharpless, *Angew. Chemie Int. Ed.* **2002**, *41*, 2596.

[115] M. Meldal, *Macromol. Rapid Commun.* **2008**, *29*, 1016.

[116] M. Meldal, C. W. Tornøe, *Chem. Rev.* **2008**, *108*, 2952.

[117] D. Fournier, R. Hoogenboom, U. S. Schubert, *Chem. Soc. Rev.* **2007**, *36*, 1369.

[118] D. Díaz Díaz, *Macromol. Symp.* **2015**, *358*, 10.

[119] A. Cernat, M. Tertiș, C. Cristea, R. Săndulescu, *Int. J. Electrochem. Sci.* **2015**, *10*, 6324.

[120] S. Halila, M. Manguian, S. Fort, S. Cottaz, T. Hamaide, E. Fleury, H. Driguez, *Macromol. Chem. Phys.* **2008**, *209*, 1282.

[121] M. J. Isaacman, K. A. Barron, L. S. Theogarajan, *J. Polym. Sci. Part A Polym. Chem.* **2012**, *50*, 2319.

[122] S. Fleischmann, K. Hinrichs, U. Oertel, S. Reichelt, K. Eichhorn, B. Voit, *Macromol. Rapid Commun.* **2008**, *29*, 1177.

[123] T. Rambarran, F. Gonzaga, M. A. Brook, *Macromolecules* **2012**, *45*, 2276.

[124] S. Yamamoto, H. Yasuda, H. Ohkita, H. Benten, S. Ito, S. Miyanishi, K. Tajima, K. Hashimoto, *J. Phys. Chem. C* **2014**, *118*, 10584.

[125] H. J. Kim, M. Skinner, H. Yu, J. H. Oh, A. L. Briseno, T. Emrick, B. J. Kim, R. C. Hayward, *Nano Lett.* **2015**, *15*, 5689.

[126] C. Enders, S. Tanner, W. H. Binder, *Macromolecules* **2010**, *43*, 8436.

[127] M. G. Mohamed, C.-C. Cheng, Y.-C. Lin, C.-W. Huang, F.-H. Lu, F.-C. Chang, S.-W. Kuo, *RSC Adv.* **2014**, *4*, 21830.

[128] B. C. Englert, S. Bakbak, U. H. F. Bunz, *Macromolecules* **2005**, *38*, 5868.

[129] H. J. Kim, K. Paek, H. Yang, C. H. Cho, J. S. Kim, W. Lee, B. J. Kim, *Macromolecules* **2013**, *46*, 8472.

[130] Z. Li, R. J. Ono, Z.-Q. Wu, C. W. Bielawski, *Chem. Commun.* **2011**, *47*, 197.

[131] M. Urien, H. Erothu, E. Cloutet, R. C. Hiorns, L. Vignau, H. Cramail, *Macromolecules* **2008**, *41*, 7033.

[132] R. H. Lohwasser, M. Thelakkat, *Macromolecules* **2012**, *45*, 3070.

[133] A. Britze, V. Möllmann, G. Grundmeier, H. Luftmann, D. Kuckling, *Macromol. Chem. Phys.* **2011**, *212*, 679.

[134] A. E. Javier, S. N. Patel, D. T. Hallinan, V. Srinivasan, N. P. Balsara, *Angew. Chemie Int. Ed.* **2011**, *50*, 9848.

[135] U. Mansfeld, C. Pietsch, R. Hoogenboom, C. R. Becer, U. S. Schubert, *Polym. Chem.* **2010**, *1*, 1560.

[136] J. Park, H. C. Moon, J. K. Kim, *J. Polym. Sci. Part A Polym. Chem.* **2013**, *51*, 2225.

[137] T. K. Kunz, M. O. Wolf, *Polym. Chem.* **2011**, *2*, 640.

[138] B. Koo, E. M. Sletten, T. M. Swager, *Macromolecules* **2015**, *48*, 229.

[139] P. Paoprasert, J. W. Spalenka, D. L. Peterson, R. E. Ruther, R. J. Hamers, P. G. Evans, P. Gopalan, *J. Mater. Chem.* **2010**, *20*, 2651.

[140] D. Meng, J. Sun, S. Jiang, Y. Zeng, Y. Li, S. Yan, J. Geng, Y. Huang, *J. Mater. Chem.* **2012**, *22*, 21583.

[141] L. Zhao, X. Pang, R. Adhikary, J. W. Petrich, Z. Lin, *Angew. Chemie Int. Ed.* **2011**, *50*, 3958.

[142] J. Jung, X. Pang, C. Feng, Z. Lin, *Langmuir* **2013**, *29*, 8086.

[143] J. U. Lind, T. S. Hansen, A. E. Daugaard, S. Hvilsted, T. L. Andresen, N. B. Larsen, *Macromolecules* **2011**, *44*, 495.

[144] H.-B. Bu, G. Götz, E. Reinold, A. Vogt, S. Schmid, J. L. Segura, R. Blanco, R. Gómez, P. Bäuerle, *Tetrahedron* **2011**, *67*, 1114.

[145] R. Huisgen, *Proc. Chem. Soc.* **1961**, 357.

[146] V. O. Rodionov, V. V. Fokin, M. G. Finn, *Angew. Chemie Int. Ed.* **2005**, *44*, 2210.

[147] J. E. Hein, V. V. Fokin, *Chem. Soc. Rev.* **2010**, *39*, 1302.

[148] Y. Mai, A. Eisenberg, *Chem. Soc. Rev.* **2012**, *41*, 5969.

[149] U. Scherf, S. Adamczyk, A. Gutacker, N. Koenen, *Macromol. Rapid Commun.* **2009**, *30*, 1059.

[150] A. de Cuendias, R. C. Hiorns, E. Cloutet, L. Vignau, H. Cramail, *Polym. Int.* **2010**, *59*, 1452.

[151] M. Jeffries-El, G. Sauvé, R. D. McCullough, *Macromolecules* **2005**, *38*, 10346.

[152] M. C. Iovu, M. Jeffries-El, E. E. Sheina, J. R. Cooper, R. D. McCullough, *Polymer* **2005**, *46*, 8582.

[153] E. Kaul, V. Senkovskyy, R. Tkachov, V. Bocharova, H. Komber, M. Stamm, A. Kiriy, *Macromolecules* **2010**, *43*, 77.

[154] A. Smeets, K. van den Bergh, J. de Winter, P. Gerbaux, T. Verbiest, G. Koeckelberghs, *Macromolecules* **2009**, *42*, 7638.

[155] C.-A. Dai, W.-C. Yen, Y.-H. Lee, C.-C. Ho, W.-F. Su, *J. Am. Chem. Soc.* **2007**, *129*, 11036.

[156] J. B. Gilroy, D. J. Lunn, S. K. Patra, G. R. Whittell, M. A. Winnik, I. Manners, *Macromolecules* **2012**, *45*, 5806.

[157] C. N. Kempf, K. A. Smith, S. L. Pesek, X. Li, R. Verduzco, *Polym. Chem.* **2013**, *4*, 2158.

[158] S. K. Patra, R. Ahmed, G. R. Whittell, D. J. Lunn, E. L. Dunphy, M. A. Winnik, I. Manners, *J. Am. Chem. Soc.* **2011**, *133*, 8842.

[159] P. Kumari, M. K. Bera, S. Malik, B. K. Kuila, *ACS Appl. Mater. Interfaces* **2015**, *7*, 12348.

[160] T. C. Kendrick, B. Parbhoo, J. W. White in, John Wiley & Sons, Ltd, **1989**.

[161] E. Song, B. Kang, H. H. Choi, D. H. Sin, H. Lee, W. H. Lee, K. Cho, *Adv. Electron. Mater.* **2016**, *2*, 1500250.

[162] S. Lee, H. Jeon, M. Jang, K.-Y. Baek, H. Yang, *ACS Appl. Mater. Interfaces* **2015**, *7*, 1290.

[163] F. Carpi, G. Gallone, F. Galantini, D. De Rossi, *Adv. Funct. Mater.* **2008**, *18*, 235.

[164] E. L. Kynaston, O. E. C. Gould, J. Gwyther, G. R. Whittell, M. A. Winnik, I. Manners, *Macromol. Chem. Phys.* **2015**, *216*, 685.

[165] M. Zhang, P. A. Rupar, C. Feng, K. Lin, D. J. Lunn, A. Oliver, A. Nunns, G. R. Whittell, I. Manners, M. A. Winnik, *Macromolecules* **2013**, *46*, 1296.

[166] K. Tsuchiya, K. Ando, T. Shimomura, K. Ogino, *Polymer* **2016**, *92*, 125.

[167] E. J. W. Crossland, K. Tremel, F. Fischer, K. Rahimi, G. Reiter, U. Steiner, S. Ludwigs, *Adv. Mater.* **2012**, *24*, 839.

[168] C. Xia, X. Fan, J. Locklin, R. C. Advincula, A. Gies, W. Nonidez, *J. Am. Chem. Soc.* **2004**, *126*, 8735.

[169] M. Scheuble, T. V. Richter, M. Goll, S. Link, J. T. López Navarrete, A. Ruff, M. C. Ruiz Delgado, S. Ludwigs, *Polym. Chem.* **2014**, *5*, 6824.

[170] T. V. Richter, S. Link, R. Hanselmann, S. Ludwigs, *Macromol. Rapid Commun.* **2009**, *30*, 1323.

[171] S. Link, T. Richter, O. Yurchenko, J. Heinze, S. Ludwigs, *J. Phys. Chem. B* **2010**, *114*, 10703.

[172] H.-J. Wang, C.-P. Chen, R.-J. Jeng, *Materials* **2014**, *7*, 2411.

[173] Y. Li, Y. Zou, *Adv. Mater.* **2008**, *20*, 2952.

[174] H.-J. Wang, C.-W. Chou, C.-P. Chen, Y.-H. Chen, R.-H. Lee, R.-J. Jeng, *J. Mater. Chem. A* **2013**, *1*, 8950.

[175] C. Y. Kuo, Y. C. Huang, C. Y. Hsiow, Y. W. Yang, C. I. Huang, S. P. Rwei, H. L. Wang, L. Wang, *Macromolecules* **2013**, *46*, 5985.

[176] C.-Y. Yu, B.-T. Ko, C. Ting, C.-P. Chen, *Sol. Energy Mater. Sol. Cells* **2009**, *93*, 613.

[177] H.-W. Lin, W.-Y. Lee, C. Lu, C.-J. Lin, H.-C. Wu, Y.-W. Lin, B. Ahn, Y. Rho, M. Ree, W.-C. Chen, *Polym. Chem.* **2012**, *3*, 767.

[178] H.-C. Wu, Y.-C. Lai, Y.-C. Chiu, W.-Y. Lee, W.-C. Chen, *Macromol. Chem. Phys.* **2014**, *215*, 638.

[179] C. Lu, H. C. Wu, Y. C. Chiu, W. Y. Lee, W. C. Chen, *Macromolecules* **2012**, *45*, 3047.

[180] J.-W. Park, D. H. Lee, D. S. Chung, D.-M. Kang, Y.-H. Kim, C. E. Park, S.-K. Kwon, *Macromolecules* **2010**, *43*, 2118.

[181] H. Cha, J. W. Park, D. S. Chung, T. K. An, Y.-H. Kim, S.-K. Kwon, C. E. Park, *J. Mater. Chem.* **2012**, *22*, 15141.

[182] K. Takagi, C. Torii, Y. Yamashita, *J. Polym. Sci. Part A Polym. Chem.* **2009**, *47*, 3034.

[183] G. Sini, M. Schubert, C. Risko, S. Roland, O. P. Lee, Z. Chen, T. V. Richter, D. Dolfen, V. Coropceanu, S. Ludwigs, U. Scherf, A. Facchetti, J. M. J. Fréchet, D. Neher, *Adv. Energy Mater.* **2018**, *8*, 1702232.

[184] J. Mei, Z. Bao, *Chem. Mater.* **2014**, *26*, 604.

[185] H. Jiang, P. Taranekar, J. R. Reynolds, K. S. Schanze, *Angew. Chemie Int. Ed.* **2009**, *48*, 4300.

[186] L. Zhai, R. D. McCullough, *Adv. Mater.* **2002**, *14*, 901.

[187] J. Liang, K. Li, B. Liu, *Chem. Sci.* **2013**, *4*, 1377.

[188] R. Zhan, B. Liu, *Chem. Rec.* **2016**, *16*, 1715.

[189] Y. Liu, K. Ogawa, K. S. Schanze, *J. Photochem. Photobiol. C Photochem. Rev.* **2009**, *10*, 173.

[190] A. Duarte, K.-Y. Pu, B. Liu, G. C. Bazan, *Chem. Mater.* **2011**, *23*, 501.

[191] Y. Ikenoue, Y. Saida, M.-A. Kira, H. Tomozawa, H. Yashima, M. Kobayashi, *J. Chem. Soc. Chem. Commun.* **1990**, 1694.

[192] G. Zotti, S. Zecchin, G. Schiavon, A. Berlin, G. Pagani, A. Canavesi, *Chem. Mater.* **1997**, *9*, 2940.

[193] M. S. Freund, B. A. Deore, *Self-Doped Conducting Polymers*, John Wiley & Sons, Ltd, **2007**.

[194] A. O. Patil, Y. Ikenoue, F. Wudl, A. J. Heeger, *J. Am. Chem. Soc.* **1987**, *109*, 1858.

[195] A. O. Patil, Y. Ikenoue, N. Basescu, N. Colaneri, J. Chen, F. Wudl, A. J. Heeger, *Synth. Met.* **1987**, *20*, 151.

[196] Y. Ikenoue, J. Chiang, A. O. Patil, F. Wudl, A. J. Heeger, *J. Am. Chem. Soc.* **1988**, *110*, 2983.

[197] A. Gutacker, S. Adamczyk, A. Helfer, L. E. Garner, R. C. Evans, S. M. Fonseca, M. Knaapila, G. C. Bazan, H. D. Burrows, U. Scherf, *J. Mater. Chem.* **2010**, *20*, 1423.

[198] C. A. Cutler, M. Bouguettaya, T.-S. Kang, J. R. Reynolds, *Macromolecules* **2005**, *38*, 3068.

[199] S. Kim, J. Jackiw, E. Robinson, K. S. Schanze, J. R. Reynolds, J. Baur, M. F. Rubner, D. Boils, *Macromolecules* **1998**, *31*, 964.

[200] S. Shi, F. Wudl, *Macromolecules* **1990**, *23*, 2119.

[201] R. D. McCullough, P. C. Ewbank, R. S. Loewe, *J. Am. Chem. Soc.* **1997**, *119*, 633.

[202] A. Viinikanoja, J. Lukkari, T. Ääritalo, T. Laiho, J. Kankare, *Langmuir* **2003**, *19*, 2768.

[203] H.-A. Ho, M. Boissinot, M. G. Bergeron, G. Corbeil, K. Doré, D. Boudreau, M. Leclerc, *Angew. Chemie* **2002**, *114*, 1618.

[204] C. Xue, F. Cai, H. Liu, *Chem. Eur. J.* **2008**, *14*, 1648.

[205] S. Kazim, J. Pfleger, M. Procházka, D. Bondarev, J. Vohlídal, *J. Colloid Interface Sci.* **2011**, *354*, 611.

[206] T. Ghoos, J. Brassinne, C.-A. Fustin, J.-F. Gohy, M. Defour, N. van den Brande, B. van Mele, L. Lutsen, D. J. Vanderzande, W. Maes, *Polymer* **2013**, *54*, 6293.

[207] J. Leger, M. Berggren, S. Carter, *Iontronics*, CRC Press, **2010**.

[208] J. H. Seo, A. Gutacker, Y. Sun, H. Wu, F. Huang, Y. Cao, U. Scherf, A. J. Heeger, G. C. Bazan, *J. Am. Chem. Soc.* **2011**, *133*, 8416.

[209] H. Zhou, Y. Zhang, C.-K. Mai, S. D. Collins, T.-Q. Nguyen, G. C. Bazan, A. J. Heeger, *Adv. Mater.* **2014**, *26*, 780.

[210] S. Inal, J. Rivnay, P. Leleux, M. Ferro, M. Ramuz, J. C. Brendel, M. M. Schmidt, M. Thelakkat, G. G. Malliaras, *Adv. Mater.* **2014**, *26*, 7450.

[211] D. Khodagholy, J. Rivnay, M. Sessolo, M. Gurfinkel, P. Leleux, L. H. Jimison, E. Stavrinidou, T. Herve, S. Sanaur, R. M. Owens, G. G. Malliaras, *Nat. Commun.* **2013**, *4*, 2133.

[212] A. P.-Z. Clark, A. J. Cadby, C. K.-F. Shen, Y. Rubin, S. H. Tolbert, *J. Phys. Chem. B* **2006**, *110*, 22088.

[213] M. I. Arroyo-Villan, G. A. Diaz-Quijada, M. S. A. Abdou, S. Holdcroft, *Macromolecules* **1995**, *28*, 975.

[214] Z. Gu, Y.-J. Bao, Y. Zhang, M. Wang, Q.-D. Shen, *Macromolecules* **2006**, *39*, 3125.

[215] L. Chen, S. Xu, D. McBranch, D. Whitten, *J. Am. Chem. Soc.* **2000**, *122*, 9302.

[216] M. Knaapila, L. Almásy, V. M. Garamus, C. Pearson, S. Pradhan, M. C. Petty, U. Scherf, H. D. Burrows, A. P. Monkman, *J. Phys. Chem. B* **2006**, *110*, 10248.

[217] M. Knaapila, R. C. Evans, A. Gutacker, V. M. Garamus, N. K. Székely, U. Scherf, H. D. Burrows, *Soft Matter* **2011**, *7*, 6863.

[218] M. Monteserín, H. D. Burrows, A. J. M. Valente, V. M. M. Lobo, R. Mallavia, M. J. Tapia, I. X. García-Zubiri, R. E. Di Paolo, A. L. Maçanita, *J. Phys. Chem. B* **2007**, *111*, 13560.

[219] R. Yang, A. Garcia, D. Korystov, A. Mikhailovsky, G. C. Bazan, T.-Q. Nguyen, *J. Am. Chem. Soc.* **2006**, *128*, 16532.

[220] A. Garcia, T.-Q. Nguyen, *J. Phys. Chem. C* **2008**, *112*, 7054.

[221] G. Inzelt, *Classification of Electrochemically Active Polymers*, Springer, **2012**.

[222] R. Gracia, D. Mecerreyes, *Polym. Chem.* **2013**, *4*, 2206.

[223] M. Yao, H. Senoh, T. Sakai, T. Kiyobayashi, *J. Power Sources* **2012**, *202*, 364.

[224] C. Su, Y. Ye, L. Xu, C. Zhang, *J. Mater. Chem.* **2012**, *22*, 22658.

[225] K. Nakabayashi, H. Mori, *Int. J. Polym. Sci.* **2012**, *2012*, 1.

[226] M. Sommer, S. M. Lindner, M. Thelakkat, *Adv. Funct. Mater.* **2007**, *17*, 1493.

[227] H. Nishide, T. Suga, *Interface* **2005**, *14*, 32.

[228] T. Janoschka, M. D. Hager, U. S. Schubert, *Adv. Mater.* **2012**, *24*, 6397.

[229] Y. Liang, Z. Tao, J. Chen, *Adv. Energy Mater.* **2012**, *2*, 742.

[230] Z. Song, H. Zhou, *Energy Environ. Sci.* **2013**, *6*, 2280.

[231] E. F. Dalton, N. A. Surridge, J. C. Jernigan, K. O. Wilbourn, J. S. Facci, R. W. Murray, *Chem. Phys.* **1990**, *141*, 143.

[232] J. B. Torrance, *Acc. Chem. Res.* **1979**, *12*, 79.

[233] O. Yurchenko, J. Heinze, S. Ludwigs, *ChemPhysChem* **2010**, *11*, 1637.

[234] L. Nyholm, G. Nyström, A. Mihranyan, M. Strømme, *Adv. Mater.* **2011**, *23*, 3751.

[235] Y. Liang, Z. Chen, Y. Jing, Y. Rong, A. Facchetti, Y. Yao, *J. Am. Chem. Soc.* **2015**, *137*, 4956.

[236] C. Karlsson, H. Huang, M. Strømme, A. Gogoll, M. Sjödin, *RSC Adv.* **2015**, *5*, 11309.

[237] A. Cravino, N. S. Sariciftci, *J. Mater. Chem.* **2002**, *12*, 1931.

[238] J. Roncali, *Chem. Soc. Rev.* **2005**, *34*, 483.

[239] M. Chen, M. Li, H. Wang, S. Qu, X. Zhao, L. Xie, S. Yang, *Polym. Chem.* **2013**, *4*, 550.

[240] J. L. Segura, R. Gómez, R. Blanco, E. Reinold, P. Bäuerle, *Chem. Mater.* **2006**, *18*, 2834.

[241] S. S. Zhu, T. M. Swager, *Adv. Mater.* **1996**, *8*, 497.

[242] S. S. Zhu, R. P. Kingsborough, T. M. Swager, *J. Mater. Chem.* **1999**, *9*, 2123.

[243] G. Zotti, G. Schiavon, S. Zecchin, A. Berlin, G. Pagani, A. Canavesi, *Synth. Met.* **1996**, *76*, 255.

[244] K.-S. Park, S. B. Schougaard, J. B. Goodenough, *Adv. Mater.* **2007**, *19*, 848.

[245] R. H. Lohwasser, G. Gupta, P. Kohn, M. Sommer, A. S. Lang, T. Thurn-Albrecht, M. Thelakkat, *Macromolecules* **2013**, *46*, 4403.

[246] J. Shen, H. Masaoka, K. Tsuchiya, K. Ogino, *Polym. J.* **2008**, *40*, 421.

[247] B. J. Holliday, T. M. Swager, *Chem. Commun.* **2005**, 23.

[248] D. Trefz, A. Ruff, R. Tkachov, M. Wieland, M. Goll, A. Kiriy, S. Ludwigs, *J. Phys. Chem. C* **2015**, *119*, 22760.

[249] O. Yurchenko, D. Freytag, L. zur Borg, R. Zentel, J. Heinze, S. Ludwigs, *J. Phys. Chem. B* **2012**, *116*, 30.

[250] S. Grigalevicius, B. Zhang, Z. Xie, M. Forster, U. Scherf, *Org. Electron.* **2011**, *12*, 2253.

[251] H. John, R. Bauer, P. Espindola, P. Sonar, J. Heinze, K. Müllen, *Angew. Chemie Int. Ed.* **2005**, *44*, 2447.

[252] J. Alvarez, L. Sun, R. M. Crooks, *Chem. Mater.* **2002**, *14*, 3995.

[253] S.-H. Hsiao, H.-M. Wang, *J. Polym. Sci. Part A Polym. Chem.* **2016**, *54*, 2476.

[254] P. Taranekar, C. Huang, T. M. Fulghum, A. Baba, G. Jiang, J.-Y. Park, R. C. Advincula, *Adv. Funct. Mater.* **2008**, *18*, 347.

[255] T. Fulghum, S. M. A. Karim, A. Baba, P. Taranekar, T. Nakai, T. Masuda, R. C. Advincula, *Macromolecules* **2006**, *39*, 1467.

[256] A. Maity, M. Biswas, *J. Appl. Polym. Sci.* **2006**, *100*, 819.

[257] S. Inaoka, R. Advincula, *Macromolecules* **2002**, *35*, 2426.

[258] J. K. Feng, Y. L. Cao, X. P. Ai, H. X. Yang, *J. Power Sources* **2008**, *177*, 199.

[259] W. Ni, J. Cheng, X. Li, G. Gu, L. Huang, Q. Guan, D. Yuan, B. Wang, *RSC Adv.* **2015**, *5*, 9221.

[260] C. Su, F. Yang, L. Ji, L. Xu, C. Zhang, *J. Mater. Chem. A* **2014**, *2*, 20083.

[261] J. Kim, H.-S. Park, T.-H. Kim, S. Y. Kim, H.-K. Song, *Phys. Chem. Chem. Phys.* **2014**, *16*, 5295.

[262] D. T. McQuade, A. E. Pullen, T. M. Swager, *Chem. Rev.* **2000**, *100*, 2537.

[263] M. J. Marsella, T. M. Swager, *J. Am. Chem. Soc.* **1993**, *115*, 12214.

[264] R. P. Kingsborough, T. M. Swager, *Adv. Mater.* **1998**, *10*, 1100.

[265] T. Malinski, A. Ciszewski, J. R. Fish, L. Czuchajowski, *Anal. Chem.* **1990**, *62*, 909.

[266] I.-B. Kim, A. Dunkhorst, J. Gilbert, U. H. F. Bunz, *Macromolecules* **2005**, *38*, 4560.

[267] Y. Liu, K. S. Schanze, *Anal. Chem.* **2008**, *80*, 8605.

[268] H. A. Ho, M. Leclerc, *J. Am. Chem. Soc.* **2003**, *125*, 4412.

[269] C. Li, M. Numata, M. Takeuchi, S. Shinkai, *Angew. Chemie Int. Ed.* **2005**, *44*, 6371.

[270] A. C. Carreon, W. L. Santos, J. B. Matson, R. C. So, *Polym. Chem.* **2014**, *5*, 314.

[271] J. Rubio-Magnieto, A. Thomas, S. Richeter, A. Mehdi, P. Dubois, R. Lazzaroni, S. Clément, M. Surin, *Chem. Commun.* **2013**, *49*, 5483.

[272] A. Herland, K. P. R. Nilsson, J. D. M. Olsson, P. Hammarström, P. Konradsson, O. Inganäs, *J. Am. Chem. Soc.* **2005**, *127*, 2317.

[273] A. Emge, P. Bäuerle, *Synth. Met.* **1999**, *102*, 1370.

[274] N. Sharon, H. Lis, *Science* **1972**, *177*, 949.

[275] R. Lotan, G. L. Nicolson, *Biochim. Biophys. Acta* **1979**, *559*, 329.

[276] T. K. Chowdhury, A. K. Weiss, *Concanavalin A*, Plenum Press, **1975**.

[277] G. L. Bratthauer, *Immunocytochemical Methods and Protocols*, **2010**.

[278] Z. Shen, M. Huang, C. Xiao, Y. Zhang, X. Zeng, P. G. Wang, *Anal. Chem.* **2007**, *79*, 2312.

[279] V. Ladmiral, G. Mantovani, G. J. Clarkson, S. Cauet, J. L. Irwin, D. M. Haddleton, *J. Am. Chem. Soc.* **2006**, *128*, 4823.

[280] J. J. Lundquist, E. J. Toone, *Chem. Rev.* **2002**, *102*, 555.

[281] D. Diwan, K. Shinkai, T. Tetsuka, B. Cao, H. Arai, T. Koyama, K. Hatano, K. Matsuoka, *Molecules* **2017**, *22*, 157.

[282] R. L. Phillips, I.-B. Kim, L. M. Tolbert, U. H. F. Bunz, *J. Am. Chem. Soc.* **2008**, *130*, 6952.

[283] J. Shi, L. Cai, K.-Y. Pu, B. Liu, *Chem. Asian J.* **2010**, *5*, 301.

[284] L. Wang, G. Fang, L. Li, D. Cao, *Sensors Actuators B Chem.* **2016**, *229*, 47.

[285] O. A. Loaiza, P. J. Lamas-Ardisana, E. Jubete, E. Ochoteco, I. Loinaz, G. Cabanero, I. Garcia, S. Penades, *Anal. Chem.* **2011**, *83*, 2987.

[286] H. Seto, S. Kamba, T. Kondo, M. Hasegawa, S. Nashima, Y. Ehara, Y. Ogawa, Y. Hoshino, Y. Miura, *ACS Appl. Mater. Interfaces* **2014**, *6*, 13234.

[287] S.-C. Luo, E. A. B. Kantchev, B. Zhu, Y. W. Siang, H.-H. Yu, *Chem. Commun.* **2012**, *48*, 6942.

[288] F. Ma, A. Rehman, H. Liu, J. Zhang, S. Zhu, X. Zeng, *Anal. Chem.* **2015**, *87*, 1560.

[289] J. E. Carlé, B. Andreasen, T. Tromholt, M. V. Madsen, K. Norrman, M. Jørgensen, F. C. Krebs, *J. Mater. Chem.* **2012**, *22*, 24417.

[290] J. W. Rumer, I. McCulloch, *Mater. Today* **2015**, *18*, 425.

[291] T. Suga, H. Konishi, H. Nishide, *Chem. Commun.* **2007**, 1730.

[292] T. J. Prosa, M. J. Winokur, J. Moulton, P. Smith, A. J. Heeger, *Macromolecules* **1992**, *25*, 4364.

[293] R. Noriega, J. Rivnay, K. Vandewal, F. P. V. Koch, N. Stingelin, P. Smith, M. F. Toney, A. Salleo, *Nat. Mater.* **2013**, *12*, 1038.

[294] R. J. Kline, M. D. McGehee, E. N. Kadnikova, J. Liu, J. M. J. Fréchet, M. F. Toney, *Macromolecules* **2005**, *38*, 3312.

[295] A. Rodrigues, M. C. R. Castro, A. S. F. Farinha, M. Oliveira, J. P. C. Tomé, A. V. Machado, M. M. M. Raposo, L. Hilliou, G. Bernardo, *Polym. Test.* **2013**, *32*, 1192.

[296] Z. Wu, A. Petzold, T. Henze, T. Thurn-Albrecht, R. H. Lohwasser, M. Sommer, M. Thelakkat, *Macromolecules* **2010**, *43*, 4646.

[297] V. Ho, B. W. Boudouris, R. A. Segalman, *Macromolecules* **2010**, *43*, 7895.

[298] S. V. Meille, V. Romita, T. Caronna, A. J. Lovinger, M. Catellani, L. Belobrzeckaja, *Macromolecules* **1997**, *30*, 7898.

[299] M. Halik, H. Klauk, U. Zschieschang, G. Schmid, C. Dehm, M. Schütz, S. Maisch, F. Effenberger, M. Brunnbauer, F. Stellacci, *Nature* **2004**, *431*, 963.

[300] E. Stavrinidou, P. Leleux, H. Rajaona, D. Khodagholy, J. Rivnay, M. Lindau, S. Sanaur, G. G. Malliaras, *Adv. Mater.* **2013**, *25*, 4488.

[301] A. Malti, J. Edberg, H. Granberg, Z. U. Khan, J. W. Andreasen, X. Liu, D. Zhao, H. Zhang, Y. Yao, J. W. Brill, I. Engquist, M. Fahlman, L. Wågberg, X. Crispin, M. Berggren, *Adv. Sci.* **2016**, *3*, 1500305.

[302] E. F. Palermo, H. L. van der Laan, A. J. McNeil, *Polym. Chem.* **2013**, *4*, 4606.

[303] J. H. Ortony, R. Q. Yang, J. Z. Brzezinski, L. Edman, T.-Q. Nguyen, G. C. Bazan, *Adv. Mater.* **2008**, *20*, 298.

[304] A. M. Glaudell, J. E. Cochran, S. N. Patel, M. L. Chabinyc, *Adv. Energy Mater.* **2015**, *5*, 1401072.

[305] Q. Zhang, Y. Sun, W. Xu, D. Zhu, *Adv. Mater.* **2014**, *26*, 6829.

[306] A. Veysel Tunc, A. De Sio, D. Riedel, F. Deschler, E. Da Como, J. Parisi, E. von Hauff, *Org. Electron.* **2012**, *13*, 290.

[307] L. Ma, W. H. Lee, Y. D. Park, J. S. Kim, H. S. Lee, K. Cho, *Appl. Phys. Lett.* **2008**, *92*, 63310.

[308] J. Webster, *Electrical Measurement, Signal Processing, and Displays*, CRC Press, **2003**.

[309] C. Wang, D. T. Duong, K. Vandewal, J. Rivnay, A. Salleo, *Phys. Rev. B* **2015**, *91*, 85205.

[310] C.-K. Mai, T. Arai, X. Liu, S. L. Fronk, G. M. Su, R. A. Segalman, M. L. Chabinyc, G. C. Bazan, *Chem. Commun.* **2015**, *51*, 17607.

[311] C.-K. Mai, R. A. Schlitz, G. M. Su, D. Spitzer, X. Wang, S. L. Fronk, D. G. Cahill, M. L. Chabinyc, G. C. Bazan, *J. Am. Chem. Soc.* **2014**, *136*, 13478.

[312] A. Berlin, G. Schiavon, S. Zecchin, G. Zotti, *Synth. Met.* **2001**, *119*, 153.

[313] E. J. Corey, C. Rücker, *Tetrahedron Lett.* **1982**, *23*, 719.

[314] B. J. Kim, Y. Miyamoto, B. Ma, J. M. J. Fréchet, *Adv. Funct. Mater.* **2009**, *19*, 2273.

[315] K. Lu, Y. Guo, Y. Liu, C.-A. Di, T. Li, Z. Wei, G. Yu, C. Du, S. Ye, *Macromolecules* **2009**, *42*, 3222.

[316] J. Lee, H. Han, J. Lee, S. C. Yoon, C. Lee, *J. Mater. Chem. C* **2014**, *2*, 1474.

[317] J. W. Rumer, R. S. Ashraf, N. D. Eisenmenger, Z. Huang, I. Meager, C. B. Nielsen, B. C. Schroeder, M. L. Chabinyc, I. McCulloch, *Adv. Energy Mater.* **2015**, *5*, 1401426.

[318] B. A. G. Hammer, M. A. Reyes-Martinez, F. A. Bokel, F. Liu, T. P. Russell, R. C. Hayward, A. L. Briseno, T. Emrick, *ACS Appl. Mater. Interfaces* **2014**, *6*, 7705.

[319] N. Cho, H.-L. Yip, J. A. Davies, P. D. Kazarinoff, D. F. Zeigler, M. M. Durban, Y. Segawa, K. M. O'Malley, C. K. Luscombe, A. K.-Y. Jen, *Adv. Energy Mater.* **2011**, *1*, 1148.

[320] B. Liu, R.-Q. Png, L.-H. Zhao, L.-L. Chua, R. H. Friend, P. K. H. Ho, *Nat. Commun.* **2012**, *3*, 1321.

[321] F. Ouhib, M. Tomassetti, J. Manca, F. Piersimoni, D. Spoltore, S. Bertho, H. Moons, R. Lazzaroni, S. Desbief, C. Jerome, C. Detrembleur, *Macromolecules* **2013**, *46*, 785.

[322] Y. Sun, S.-C. Chien, H.-L. Yip, Y. Zhang, K.-S. Chen, D. F. Zeigler, F.-C. Chen, B. Lin, A. K.-Y. Jen, *Chem. Mater.* **2011**, *23*, 5006.

[323] W.-F. Su, R.-T. Chen, Y. Chen, *J. Polym. Sci. Part A Polym. Chem.* **2011**, *49*, 352.

[324] F.-J. Kahle, I. Bauer, P. Strohriegl, A. Köhler, *J. Polym. Sci. Part B Polym. Phys.* **2017**, *55*, 112.

[325] C. Huang, G. Jiang, R. Advincula, *Macromolecules* **2008**, *41*, 4661.

[326] R. Ravindranath, P. K. Ajikumar, S. Bahulayan, N. B. M. Hanafiah, A. Baba, R. C. Advincula, W. Knoll, S. Valiyaveettil, *J. Phys. Chem. B* **2007**, *111*, 6336.

[327] O. I. Negru, M. Grigoras, *J. Polym. Res.* **2015**, *22*, 637.

[328] A. Palma-Cando, U. Scherf, *Macromol. Chem. Phys.* **2016**, *217*, 827.

[329] A. Palma-Cando, G. Brunklaus, U. Scherf, *Macromolecules* **2015**, *48*, 6816.

[330] M. I. Mangione, R. A. Spanevello, A. Rumbero, D. Heredia, G. Marzari, L. Fernandez, L. Otero, F. Fungo, *Macromolecules* **2013**, *46*, 4754.

[331] Z.-G. Zhang, S. Zhang, J. Min, C. Chui, J. Zhang, M. Zhang, Y. Li, *Macromolecules* **2012**, *45*, 113.

[332] W.-Y. Lee, T. Kurosawa, S.-T. Lin, T. Higashihara, M. Ueda, W.-C. Chen, *Chem. Mater.* **2011**, *23*, 4487.

[333] Q. Zhang, Z. Ning, H. Tian, *Dyes and Pigments* **2009**, *81*, 80.

[334] A. Wolf, E. Moulin, J.-J. Cid, A. Goujon, G. Du, E. Busseron, G. Fuks, N. Giuseppone, *Chem. Commun.* **2015**, *51*, 4212.

[335] A. A. Accurso, M. Delaney, J. O'Brien, H. Kim, P. M. Iovine, D. D. Díaz, M. G. Finn, *Chem. Eur. J.* **2014**, *20*, 10710.

[336] K. Yuan Chiu, T. Xiang Su, J. Hong Li, T.-H. Lin, G.-S. Liou, S.-H. Cheng, *J. Electroanal. Chem.* **2005**, *575*, 95.

[337] G. Zotti, R. Salmaso, M. C. Gallazzi, R. A. Marin, *Chem. Mater.* **1997**, *9*, 791.

[338] H. J. Ahonen, J. Lukkari, J. Kankare, *Macromolecules* **2000**, *33*, 6787.

[339] M. Skompska, R. Holze, J. Mieczkowski, R. Holze, J. Heinze, *J. Electroanal. Chem.* **2005**, *577*, 9.

[340] I. D. V. Ingram, D. J. Tate, A. V. S. Parry, R. S. Sprick, M. L. Turner, *Appl. Phys. Lett.* **2014**, *104*, 153304.

[341] K. Walzer, B. Maennig, M. Pfeiffer, K. Leo, *Chem. Rev.* **2007**, *107*, 1233.

[342] A. Siove, D. Adès, *Polymer* **2004**, *45*, 4045.

[343] J.-H. Wu, G.-S. Liou, *ACS Appl. Mater. Interfaces* **2015**, *7*, 15988.

[344] H.-Y. Lin, G.-S. Liou, *J. Polym. Sci. Part A Polym. Chem.* **2009**, *47*, 285.

[345] K. Väkiparta, M. Reghu, M. R. Andersson, J. Moulton, T. Taka, *Solid State Commun.* **1993**, *87*, 619.

[346] B. Ren, M. Wang, J. Liu, J. Ge, X. Zhang, H. Dong, *Green Chem.* **2015**, *17*, 1390.

[347] C.-W. Huang, F.-C. Chang, Y.-L. Chu, C.-C. Lai, T.-E. Lin, C.-Y. Zhu, S.-W. Kuo, *J. Mater. Chem. C* **2015**, *3*, 8142.

[348] I. Strzemińska, S. Sainte Rose Fanchine, G. Anquetin, S. Reisberg, V. Noël, M. C. Pham, B. Piro, *Biosens. Bioelectron.* **2016**, *81*, 131.

[349] W. L. F. Armarego, C. Chai, *Purification of Laboratory Chemicals*, Butterworth-Heinemann, **2009**.

[350] G. R. Fulmer, A. J. M. Miller, N. H. Sherden, H. E. Gottlieb, A. Nudelman, B. M. Stoltz, J. E. Bercaw, K. I. Goldberg, *Organometallics* **2010**, *29*, 2176.

[351] W. Kaim, J. Fiedler, *Chem. Soc. Rev.* **2009**, *38*, 3373.

[352] S. A. DiBenedetto, A. Facchetti, M. A. Ratner, T. J. Marks, *Adv. Mater.* **2009**, *21*, 1407.